UNIVERSITAT ROVIRA I VIRGILI

ESTABLISHMENT OF A FULLY AUTOMATIZED MICROFLUIDIC PLATFORM FOR THE SCREENING AND CHARACTERIZATION OF NOVEL HEPATITIS B VIRUS CAPSID ASSEMBLY MODULATORS

Tamás Vermes

ADVERTIMENT. L'accés als continguts d'aquesta tesi doctoral i la seva utilització ha de respectar els drets de la persona autora. Pot ser utilitzada per a consulta o estudi personal, així com en activitats o materials d'investigació i docència en els termes establerts a l'art. 32 del Text Refós de la Llei de Propietat Intel·lectual (RDL 1/1996). Per altres utilitzacions es requereix l'autorització prèvia i expressa de la persona autora. En qualsevol cas, en la utilització dels seus continguts caldrà indicar de forma clara el nom i cognoms de la persona autora i el títol de la tesi doctoral. No s'autoritza la seva reproducció o altres formes d'explotació efectuades amb finalitats de lucre ni la seva comunicació pública des d'un lloc aliè al servei TDX. Tampoc s'autoritza la presentació del seu contingut en una finestra o marc aliè a TDX (framing). Aquesta reserva de drets afecta tant als continguts de la tesi com als seus resums i índexs.

ADVERTENCIA. El acceso a los contenidos de esta tesis doctoral y su utilización debe respetar los derechos de la persona autora. Puede ser utilizada para consulta o estudio personal, así como en actividades o materiales de investigación y docencia en los términos establecidos en el art. 32 del Texto Refundido de la Ley de Propiedad Intelectual (RDL 1/1996). Para otros usos se requiere la autorización previa y expresa de la persona autora. En cualquier caso, en la utilización de sus contenidos se deberá indicar de forma clara el nombre y apellidos de la persona autora y el título de la tesis doctoral. No se autoriza su reproducción u otras formas de explotación efectuadas con fines lucrativos ni su comunicación pública desde un sitio ajeno al servicio TDR. Tampoco se autoriza la presentación de su contenido en una ventana o marco ajeno a TDR (framing). Esta reserva de derechos afecta tanto al contenido de la tesis como a sus resúmenes e índices.

WARNING. Access to the contents of this doctoral thesis and its use must respect the rights of the author. It can be used for reference or private study, as well as research and learning activities or materials in the terms established by the 32nd article of the Spanish Consolidated Copyright Act (RDL 1/1996). Express and previous authorization of the author is required for any other uses. In any case, when using its content, full name of the author and title of the thesis must be clearly indicated. Reproduction or other forms of for profit use or public communication from outside TDX service is not allowed. Presentation of its content in a window or frame external to TDX (framing) is not authorized either. These rights affect both the content of the thesis and its abstracts and indexes.

UNIVERSITAT
ROVIRA i VIRGILI

Establishment of a fully automatized microfluidic platform for the screening and characterization of novel Hepatitis B virus capsid assembly modulators

---

Tamás Vermes

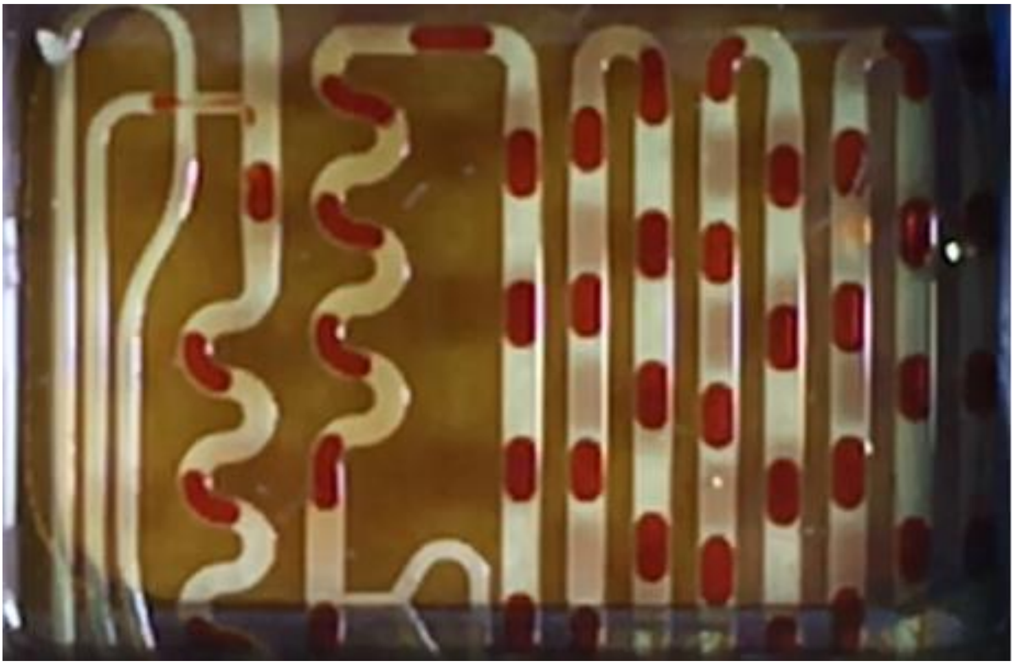

DOCTORAL THESIS
2021

The thesis is the result of VIRO-FLOW Industrial Doctorate Programme. This project was supported by a research grant from the European Union’s Horizon 2020 research and innovation program under the Marie Sklodowska-Curie grant agreement No. 766058.

Establishment of a fully automatized microfluidic platform for the screening and characterization of novel Hepatitis B virus capsid assembly modulators

Doctoral Thesis by

Tamás Vermes

Developed under the supervision of

Prof. Miquel A. Pericàs Brondo

Dr. Helmut Buschmann

Departament de Química Analítica i Química Orgànica (URV)

Institute of Chemical Research of Catalonia (ICIQ)

UNIVERSITAT
ROVIRA i VIRGILI
ICIQ Institute of Chemical Research of Catalonia

Tarragona

2021

UNIVERSITAT ROVIRA I VIRGILI

ICIQ
Institut
Català
d'Investigació
Química

Prof. Miquel A. Pericàs Brondo, Group Leader of the Institute of Chemical Research of Catalonia (ICIQ) and,

Dr. Helmut Buschmann, Lecturer of University of Aachen (RWTH Aachen University) in the field of Medicinal Chemistry and Drug Discovery for Master and PhD Students.

STATE, that the present Doctoral Thesis entitled: "**Establishment of a fully automatized microfluidic platform for the screening and characterization of novel Hepatitis B virus capsid assembly modulators"**, presented by Tamás Vermes to receive the degree of Doctor, has been carried out under our supervision at the Institute of Chemical Research of Catalonia (ICIQ) and at AiCuris Anti-infective Cures AG.

Tarragona, 27 October 2021

PhD Thesis Supervisor

Prof. Miquel A. Pericàs Brondo

PhD Thesis Co-supervisor

Dr. Helmut Buschmann

[I STATE PAGE]

Acknowledgments

To work in the VIRO-FLOW project was an extraordinary chance to grow in subject-specific and on a personal level. In this sense, I would like to firstly thank the two scientific supervisors **Dr. Helmut Buschmann** and **Prof. Dr. Pericas**, for leading and managing the project with their excellent expertise in their respective scientific topics.

Furthermore, I would like to sincerely thank **Dr. Andreas Urban** for being an excellent mentor during the Ph.D. providing scientific leadership with high expertise. It was always a delight having discussions with him, be it at scientific or non-scientific subjects. Special thanks also go to **Dr. Esther Alza** and **Dr. Thomas Goldner** for the great support by organizing tremendous amounts of excellence courses for the students and their guidance in good scientific practices.

I would also like to mention the Fluigent team (Jena) for their support with microfluidic devices and **Dr. Thomas Henkel, Dr. Mark Keplinski** for all the help with the microfluidic chips and theoretical insights.

My gratitude also goes to my fellow VIRO-FLOW students, **Dr. Justine Raymond** and **Dr. Elene Detta**, with whom I shared good and difficult times during the project. The work would not have been such an experience without the cheerful and hardworking colleges from Dr. Andreas' research group, including **Dr. Angelica Corcuera, Ilva Leckebusch, Stolle Katharina, and Wiebke Schultze,** relentlessly helping with practical advice. The same can be said to the new friends from Prof. Dr. Pericas's group, including **Dr. Patricia Llanes, Dr. Marco M. Mastandrea, Dr. Parijat Borah, Dr. Leijie Zhou, Dr. Moreshwar Chaudhari, Nicola Zanda, Stefania Perulli, Adrian J. Brenes Rucinski,** and **Arianna Brandolese**. Despite being from a different scientific topic, the working atmosphere and team spirit were energizing and welcoming. I am truly grateful to have shared these 1.5 years with these colleges during and, especially, after work.

Furthermore, I would like to thank many friends whom I had the chance to meet during this journey, including those of Wuppertal, particularly **Christiane and Damian Bartocha**, **Anastasia Harmanza, René Neuhoff, Sascha Pfeiffer, Angelica Schneider**. I am grateful for all the joyful moments we spent together in nature, during Nightfever, or just by hanging out. These were partly the most valuable memories made and a constant source of joy and vitality.

Of course, I must mention **Rosa Vidal Durán** and her family displaying the warmest and most sincere hospitality one can imagine. I am deeply grateful for the long discussions, the travels and mountain biking, the incredible events. Special thanks also go to **Albert Font Aldaz** and **Leonard Bock**, two special friends in good and bad situations alike.

Most of all, I would like to thank **Charlotte Ruppenthal**, who was always supportive with words and deeds on a daily basis. I would not want to miss any of the time we spent together. Finally, the thank goes to **Zoltán Vermes** and **Ildikó Vermes**, who supported me during the whole Ph.D. despite their current situation. Without their selflessness, I could not have completed the here presented work.

Summary

In its current form, drug discovery faces major challenges due to the constant erosion of earnings per drug resulting from a reduction in new FDA approvements combined with the steadily rising development costs. In order to reduce the development costs, multiple enabling technologies have been developed. Among them the integrated microfluidic screening platforms with feedback mechanism showed promising results by accelerating the hit-to-lead development cycle from several weeks required for conventional synthesis, shipping and screening to a few hours. In order to obtain suitable equipment, several modular devices were obtained, tested, and finally connected into a single system. The harmonization and automation were performed using workflows written in Microfluidic Automation Tool (MAT). Finally, evaluation protocols were written for the fluorescence and reflection data in KNIME, allowing the calculation of Z'-factor, standard deviations, dilution curves, and robust half-maximal effective concentrations (EC_{50} values) (Chapter III). Hepatitis B virus (HBV) core protein (HBc) was selected as primary target due to the continuing demand for a functional cure to help address the economic and social challenges imposed by the chronic HBV disease. An existing HBc assembly assay was adapted to the microfluidic setup, using inflow dilution with convection dominated Taylor Aris Dispersion (TAD), rotate-split-and-recombine mixing, and fluorescence readout. Based on high-resolution dose response curves, EC_{50s} were calculated at unexplored early kinetics of under 1 min. Furthermore, CAM-induced HBc assembly kinetics were measured for the first time at residence times down to 5 s post-mixing. The kinetic data permitted rapid categorization of CAMs according to their mode of actions (Chapter IV). Lastly, droplet microfluidics were used to eleminate further TAD mediated dilution had post mixing. Early results in droplets showed that mixing of HBc and reagents prior to encapsidation is necessary to prevent HBc's adsorption to the droplet-droplet interface. Finally, the system was complemented with a liquid handling system (LHS) as an interface between the microfluidics and 96 microtiter wells. This upgrade allows construction of a semi-automated synthesis/ screening system representing a novel approach to reduce cycle times and costs in early-stage drug discovery.

Index

List of Abbreviations

°C	Degree Celsius
aa	Amino acid
ADME-T	Adsorption distribution metabolism excretion and toxicity
Amp	Ampicillin
aSEC	Analytical size-exclusion chromatography
ASO	Antisense oligonucleotides
CAM	Capsid Assembly Modulators
CAM-A	Capsid Assembly Modulators-Abridged
CAM-N	Capsid Assembly Modulators-Normal
Ca	Chloramphenicol
Cb	Carbenicillin
CCMV	Cowpea chlorotic mottle virus
Cdk2	Cyclin-dependent kinase 2
COC	Cyclic olefin copolymer
COSY	COrrelated SpectroscopY
CMC	Critical micelle concentration
CP	Continuous phase
CTD	C-terminal domain
DBT	Dibenzothiazepinecarboxamide
DCM	Dichloromethane
DD	Drug Discovery
DLS	Dynamic light scattering
DNA	Deoxyribonucleic acid
DP	Disperse phase
dsDNA	double-stranded DNA
EC_{50}	Half-maximal effective concentration
EDTA	Ethylenediaminetetraacetic acid
EMA	European Medicines Agency
ESR	Early-stage researcher
FA	Fluorescence anisotropy
FCS	Fluorescence correlation spectroscopy
FDA	Food and Drug Administration
FITC	Fluorescein isothiocyanate
FLIM	fluorescence lifetime imaging
FRET	Fluorescence resonance energy transfer
FW	Forward primer
g	Gramm
h	Hour
HAP	Heteroaryldihydropyrimidine
HBc	Hepatitis B Core protein
HBV	Hepatitis B Virus
HCMV	Human Cytomegalovirus
HIV	Human immunodeficiency virus
HPLC	High-performance liquid chromatography
HTS	High throughput screening
IC_{50}	Half maximal inhibitory concentration

ID	Inner diameter
IPTG	Isopropyl β-D-1-thiogalactopyranoside
IFNα	Interferon alpha-1
KHz	Kilohertz
l	Liter
L	Length
LBDD	Ligand-based drug design
LED	Light-emitting diodes
LHS	Liquid handling system
Log P	Octanol-water partition coefficient
M	Molar
MAT	Microfluidic Automation Tool
mg	Milligramm
MI	Mixing Index
Min	Minute
ml	Milliliter
mm	Millimeter
mM	Millimolar
ms	Millisecond
MS	Mass spectrometry
MW	Molecular weight
Na	Nucleoside analogs
NAGE	Native Agarose Gel Electrophoresis
ng	Nanogramm
nl	Nanoliter
NMR	Nuclear Magnetic Resonance
nm	Nanometer
nM	Nano Molar
ns	Nanosecond
NTD	N-terminal domain
OD	Outer diameter
PAGE	Polyacrylamide gel electrophoresis
PC	Polycarbonate
PCR	Polymerase chain reaction
Pe	Pelect number
PEEK	Polyether ether ketone
PEG	Polyethylene glycol
PFA	Perfluoroalkoxy alkanes
PFPA	Perfluorinated Polyether
pKa	Acid dissociation constant
pgRNA	Pregenomic RNA
PN	Product number
PPA	Phenylpropenamide
R&D	Research and development
Re	Reynold number
RFU	Relative fluorescence unit
RT	Reverse transcriptase
RNAi	RNA interference
RNA	Ribonucleic acid
s	Seconds

SAV	Surface-to-volume area
SAR	Structural activity relationship
SARS-CoV-2	Severe acute respiratory syndrome coronavirus 2
SBA	Sulfamoylbenzamide
SBDD	Structure-based drug design
SDS	Sodium dodecyl sulfate
SRPK	Serine/ arginine protein kinase
TAD	Taylor Aris Dispersion
TOCSY	TOtal Correlated SpectroscopY
TRFA	Time-Resolved Fluorescence Anisotropic
ROSAR	Rotate Split And Recombine
RT	Reverse transcriptase
RW	Reverse primer
QSAR	Quantitative structure-activity relationships
WHO	World Health Organization
µ-TAS	Micro total analysis system
µl	Microliter
µm	Micrometer

Chapter I.

Introduction

I.1 The Drug Discovery process

I.1.1 History of Drug Development

In its earliest stages, drug discovery (DD) was based solely on natural products to combat pathogens and heal human diseases.[1,2] During the 20th century, striking advances were achieved in chemistry, redefining the subject's understanding by Avogadro's atomic hypothesis.[3] At the same time, DD was improved by technical, technological, and analytical developments. Some of the major findings were the isolation and purification of active ingredients (API), such as morphine[4] and penicillin,[5] and later the development of high-performance liquid chromatography (HPLC), nuclear magnetic resonance (NMR), mass spectrometry and crystallography. These advances supported the chemical modifications of extracted natural APIs, greatly improving the generation of half-synthetic and synthetic compounds with enhanced efficiency.

In addition, improvements in microbiology and biochemistry allowed the determination of genes involved in a disease, their cloning, expression, and finally, their characterization. Based on the bacterial targets as well as human-related enzymes and cellular receptors screening methods were developed. The intercommunication of new chemical entries' synthesis and subsequent testing against the biological determined disease targets led to rational drug design. Furthermore, microbiological advances enabled the harvesting and cultivation of human cell lines, used to test the effectivity, toxicity, ADME (absorption, distribution, metabolism, and excretion) characteristics, initial metabolism, and drug penetration properties.[6] Moreover, biotechnological advances led to the research of new drug types, including monoclonal antibodies and recombinant proteins.[3] Lastly, the technological advances made in hardware and software development over the last 60 years enabled the implementation of *in silico* methods to the rational DD process.[7,8] In particular, the testing of potential chemical entities against drug targets using computational methods, called virtual screening, offered an inexpensive, fast, and simple way for the identification of novel lead structures.

I.1.2 The modern Drug Discovery process

At the end of the 20th century, the DD process known today was established, which can be categorized into rational design, including structure-based drug design (SBDD), ligand-based drug design (LBDD), and high-throughput screening approaches (HTS).

In a SBDD, the early stages of the DD process include the target (gene, enzyme, receptor) characterization, hit generation, and optimization. For a protein target, the structure is evaluated using X-ray crystallography, electron microscopy, *CO*rrelated *S*pectroscop*Y* (COSY), or *TO*tal Correlated *S*pectroscop*Y* (TOCSY) NMR. It is of uppermost importance that the target is associated with the disease (target validity), can produce a measurable response after drug application (druggability), and is simply integrated into a novel screening or biochemical HTS formats (assayability).[9] Afterward, *in silico* or *in vitro* libraries with more extensive compounds are screened to determine optimal biological activity measured in half-maximal inhibitory concentration (IC_{50}) or half-maximal effective concentration (EC_{50}) values. Usually, this is performed in a combination of biochemical primary assay screens and an orthogonal phenotypic counter screen.[10] Knowing the target's structure facilitates the research process considerably but is not a necessity. LBDD starts with one or multiple compounds with known activity to establish pharmacophore instead of the target's structure before improving the compound's activity in further screening approaches.[11]

Since the 1990s, the biochemical HTS assays were performed in standardized microtiter plate formats combined with automated setups.[12–16] Depending on the assay's size, the wells were set to 96-well plate (200 µl), 384-well plate (50-70 µl), and 1,536-well plates (5–10 µl) with the latter being able to screen up to 100,000 compounds per day.[17–19] The trend in the biochemical HTS was to work with homogenous formats instead of the time and resource-consuming heterogeneous assays, which drastically increased the throughput.[20] In order to operate a biochemical HTS screening, it is essential to validate the assay prior to use by determining false negatives and positives. Suppose the rate of false negatives are above 2 %, in that case the assay has to be adjusted by either optimizing the technical setup or the assays condition, including buffer composition, pH-values, temperature, and compound concentration.[21–23] Major drawbacks of biochemical assays are the deviations of the protein target from its natural conformation, which is dependent on the expression system, and the time required for the expression and purification.[24] Furthermore, a biochemical assay is a highly artificial environment that often leads to misinterpreted compound activity due to lipophilicity and the neglection of off-target activity.[25] Nonetheless, HTS was the most successful method in the development of novel drugs according to the number of clinical successes and is still the major method to identify novel leads.[26] Aside from biochemical HTS, phenotypic high-throughput screening (HTS) approaches were applied in many cases in which neither the structure nor active ligands are known. The primary benefit of this format is its ability to provide activity values in a biological system without any pre-knowledge. However, cellular cultures were often complicated and laborious to execute, limiting their general use.[27] The phenotypic screening can be performed target-directed (known cellular target) or target-blind. In the former, the cell viability is monitored, which represents a straightforward methodology to determine the compounds' activity independent of specific biochemical pathways. The target-directed phenotypic assays are more expensive and time-consuming to culture but can provide information on the compound's in a cellular environment providing further information on ADME-T properties.[28]

Upon discovering promising hits during targeted design or HTS, structural activity relationships (SAR) are evaluated. To generate smaller, more targeted libraries, advanced computational methods can be used to develop quantitative structure-activity relationships (QSAR) adopted as a guideline for new synthetical modifications. Meanwhile, initial and improved hits are evaluated in phenotypic assays to determine efficiency, solubility, permeability (log P), acidity or basicity (pKa), drug-drug interactions, metabolism properties, and overall drug-likeness according to Lipinski’s rule of 5.[29] A hit with increased efficiency and ADME-T properties is nominated to a lead compound which will undergo further testings in a preclinical setting, including animal trials that evaluate pharmacological and pharmacokinetic profiles and the selectivity for the biological target.

Finally, the successful leads can enter the clinical trials, which are rigorously supervised and regulated to ensure activity and prevent critical adverse effects. The process is built upon three successive phases: phase I executed on a smaller, healthy group has the main function to detect early side effects and drug toxicity. In Phase II, the drug candidate is administered to a larger group of participants suffering the tested disease, and data is collected to determine drug efficiency. Finally, comprehensive testing is performed in phase III on several thousand participants from different genders, ethnicities, and age groups to obtain a complete picture of the drug's effects on a diverse population. The development of a drug usually requires more than 10 years, with an approval rate of 15.3 % for the lead and 10.4 % for the secondary indications.[12] Most drug candidates fail due to lack of efficacy in the intended disease indication, with secondary causes lying in safety profile and ADME properties.[12,30] Given the high failure rate, the resulting median cost of developing a new drug has been estimated to be $985 million, with an average cost of $1.3 billion, showcasing the importance of improvements of the DD process.[31]

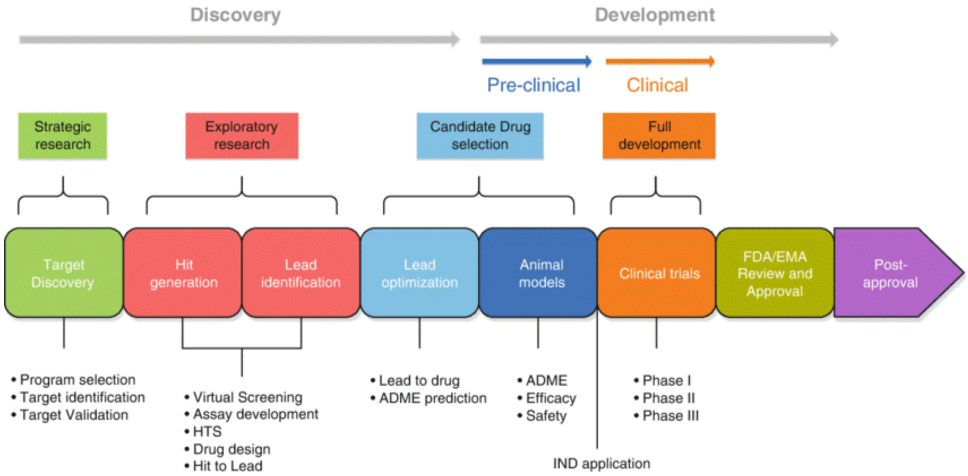

Figure 1: The targeted DD process from target identification to drug approval. The process is built up from the research and development stage (Target identification, hit generation, and lead generation), the pre-clinical studies, and the clinical trials (Phase I, Phase II, and Phase III). Drugs successfully going through the process are approved by the FDA before the lunch on the market. Individual time and cost requirements vary in each process, but the rough estimations are displayed above each step.[1]

---

[1] *Reprinted by permission from [SPRINGER NATURE LICENSE]: [Springer Nature] [Springer eBook][Medicinal Biotechnology for Disease Modeling, Clinical Therapy, and Drug Discovery and Development, Robin Duelen, Marlies Corvelyn, Ilaria Tortorella et al.], [COPYRIGHT: 5162901297650] (2019)[32]

I.1.3 Major challenges and limitations of Drug Discovery

Despite the novel technologies and improvements, the number of FDA-approved drugs has been constantly decreasing since 1990, while research and development costs have kept climbing (Eroom's law).[12,31] The constant decrease in earnings per drug was further hollowed for the pharmaceutical industries due to financial losses from the expiration of patents, increasing environmental regulations, and a cost-constrained healthcare system.[33] Consequently, the DD's business model as it is known today might lead to failure, hampering the novel discoveries of drugs and impact public healthcare as well.[31,33]

Defining a clear solution is very challenging given that the DD process is a multidimensional, chaotic system with nonlinear behaviors errors, and only incomplete predictability. The resulting errors are usually based on incomplete data ending in challenging interpretations.[34] Furthermore, some criticize the regulatory hurdles, increased complexity, and unbalanced regulatory risk-benefit assessments leading to early project termination.[12] Indeed, no other industry is as strongly regulated as the food or health industry which is understandable given the drawbacks of falsely administered drugs or overlook of side effects during the development. One of the most prominent examples was Thalidomide, administered in West Germany in 1957 against morning sickness. The drug taken by pregnant women soon led to the rise of many birth defects.[35] Moreover, various other drugs, for example, diethylstilbestrol,[36] fenfluramine,[37] terfenadine,[38] were recalled through the last 70 years due to severe adverse effects. Learning from the past and implementing the knowledge to an overall improved regulatory risk-benefit assessment could in itself lead to an improved success rate.[12]

In infectious diseases, a combination of regulatory and research-oriented problems is found. New antibiotics rose fast in the first half of the 20th century, but with the brand-new compounds, different resistance strains arose. The resulting strong regulations of these medicaments, which were made to slow the resistance development against novel antibiotics, also rendered the research in

---

this area highly unprofitable.[39,40] Simultaneously many drugs research projects were focused on viral infections, such as human immunodeficiency virus (HIV), HBV, bubonic plague, and smallpox. Recently the emerging zoonotic coronavirus (SARS-CoV-2), which caused the COVID-19 pandemic, showcased the urgency for fast responses to this ubiquitous threat that requires improvements in the discovery process.[41]

I.1.4 Developments and improvements of modern Drug Discovery using enabling technologies

The high demand in the DD's acceleration, cost reduction, quality improvements, and accuracy in detecting early false positive or false negative hits led to the simultaneous developments of enabling technologies.[33] The notable improvements in the last two decades are attributed to *in silico* methodologies, including artificial intelligence and machine learning, improvements in medicinal chemistry, and enabling technologies.[30,34] In medicinal chemistry, various novel diverse oriented synthesis methods were produced to analyze diverse functional groups, stereochemistries, and frameworks, which is essential given the vast cardinality of the chemical space with approximately 10^{30}–10^{60} drug-like molecules.[30,42] Meanwhile, function-oriented synthesis strategies allowed the easier generation of focused libraries and were often employed in the hit-to-lead development cycle.[30]

Labeling technologies and improvements in screening methodology underwent great optimizations toward miniaturization and automation.[43,44] The main goal of miniaturized systems was to decrease analysis time and sample consumption which led to both economic and ecological benefits. Furthermore, the smaller assay formats also allowed a more rigorous control over physical parameters, such as heat-/ mass transfer, electric or optic reactions, and pressure leading to novel opportunities and increased safety for handling unknown compounds.[44] Automation further increases the efficiency of DD by the high speed of execution, parallelization, lower error rates and reduced risks of false positives or negatives, lower consumption of materials, and more precise handling.[43,45]

These benefits improved decision making, especially for the hit to lead candidates, and reduced human labor and exposition to dangerous chemicals.[43]

As for the screening approaches homogeneous and heterogeneous enzymatic assays were developed in microplates, microarrays, and microfluidic devices.[44,46] The microtiter plate assays have proven successful due to their specificity, sensitivity, robustness, and reproducibility. However, the decrease in volume to surface in smaller wells limited the miniaturization of microplates due to increased handling difficulties and the faster evaporation of the compounds. Micro and especially nanoarrays overcame conventional microtiter plates' scale and density limitations and can reach densities down to thousands of spots/cm^2. As a result, nanoarrays can perform multiplex measurements combined with a rapid screening at a nanoscopic scale.[46] Another assay format discussed in the following chapters is microfluidic assays, which are likewise able to handle nanoliter samples in a 3D environment.[47]

I.2 Microfluidic systems as novel enabling technologies and their current implementations

The groundbreaking development of micro total analysis systems (µTAS) in 1990 and later the micro-electro-mechanical-systems (MEMS) led to the implementation of microfluidics into chemistry and biochemistry. This revolutionized novel, innovative methodologies with distinct benefits given the platform's inherent properties.[46,48–51] According to the fluid generation and handling, microfluidics are categorized into continuous flow and droplet flow formats. Both are performed within small enclosed platforms, providing the previously described advantages of miniaturization, such as reduced sample consumption, higher throughput, and the option of straightforward parallelization and automation with versatility and speed.[43,46] The smaller volumes of microfluidic systems are also ideal for run-away reactions, hazardous reagents, photochemistry, and electrochemistry.[52] The lower detection volume allows improved fluorescence-based readouts, resulting in high volume-to-background ratios similar to confocal setups.[53,54] Additionally, the increased surface-to-volume ratios permit higher control over physical parameters, such as temperature, pressure, mass transfer, and evaporation. In this assay formats this results in readouts with higher selectivity, increased data resolution, and better reproducibility.[55] In an automated setup, the feedback mechanism of MEMS or µTAS is also used to fastly adjust the reaction conditions for the multistep synthesis process and improvements of novel compounds in an iterative manner.[56] The adaptation of biochemical assays in continuous flow allows higher analytical reliability, and thus, better prediction of drug profiles. In contrast to the usual 8 data points obtained from a well-titer format assay, microfluidic assays can measure high-resolution-dose response curves of compounds with up to 10,000 data points from a single measurement using similar amounts of samples.[43,57–59] Indeed, microfluidic assays were able to depict complex concentration-activity relationships based on high-resolution dose response curves contrary to standard assay formats.[43] Moreover, reaction kinetics can be evaluated at a couple of seconds post mixing, allowing the evaluation of enzymatic kinetic reactions and fast biochemical processes.[26,37,38,45,46]

I.2.1 Droplet microfluidics

Droplet-based microfluidics is a rapidly growing interdisciplinary field combining biochemistry, chemistry, microsystem engineering, material sciences, as well as physics to develop novel assay formats. This method relies on the generation of monodisperse droplets of the fluid of interest called disperse phase (DP) compartmentalized in an immiscible fluid (continuous phase/ CP) which further increases the difficulty compared to continuous flow. The DP's spatial and chemical separation into small droplets of the size of a few femtoliters to nanoliters allows the mixing of reagents within ms due to miniaturization and Tayler flow within droplets. Furthermore, compartmentalization prevents the parabolic dilution of the reagents, as would be the case for continuous Hagen-Poiseulle flow and thereby the measurement of independent data points.[60,61] Therefore, droplet microfluidics is suitable for the determination of reaction kinetics based on the direct correlation between the droplet's traveled distance and reaction time (Figure 2).[62,63] The unique features of this methodology led to its implementation into various fields such as protein crystallization,[64] PCR,[65] antibody screening,[65] cells screening,[65–67], enzymatic screening,[67,68] nanoparticle synthesis,[64] sortings of droplets of different solutions, organic aqueous phase extraction, antibiotic screening, enzyme evolution,[69–71], drug delivery[72] and drug screening and combinatorial screening.[65]

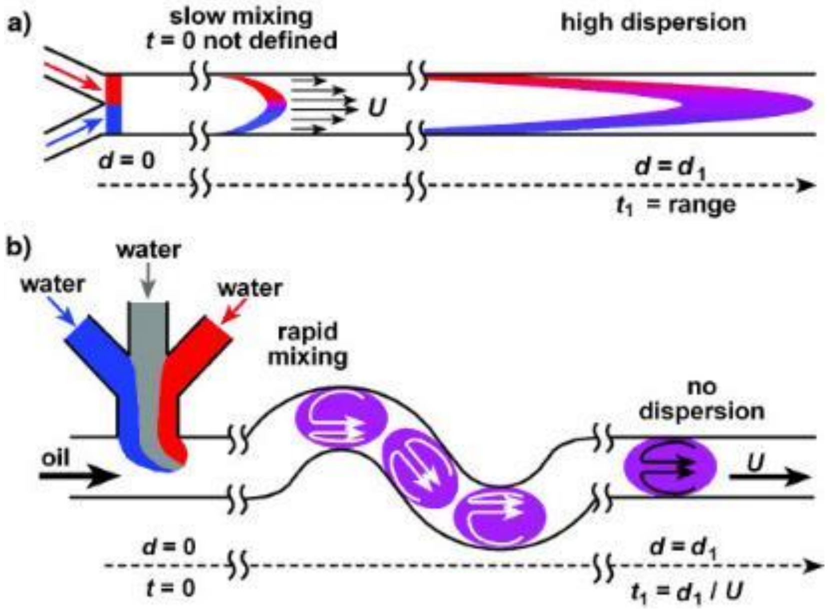

Figure 2: A) Parabolic shift of a continuous flow due to an increasing flow rate gradient towards the middle of a channel in laminar co-flows settings. **B**) Compartmentalization of the DP prevents TAD mediated dilution and leads to enhanced mixing within ms.[2]

The ideal droplet-based microfluidics assay strives for a high to ultra-high throughput, monodispersity of the droplets with a preferably low variation in droplet sizes (bellow 3 %), and a good reproducibility coupled to high resistance against external physical perturbations. Parameters with the highest impact on performance are the microreactor's design and the materials used for the fabrication, the choice of surfactants and carrier oils, and the flow rates.[72]

---

[2] Reprinted by permission from John Wiley and Sons [Angewandte Chemie)] (A Microfluidic System for Controlling Reaction Networks in Timet, Rustem F. Ismagilov, Joshua D. Tice, Helen Song), [COPYRIGHT: 5162900609668] (2003).[63]

I.2.2 Application of microfluidic systems in Drug Discovery

Microfluidic systems have been integrated into all the different drug discovery stages,[45] including drug screening assays,[73] chemical synthesis,[74] protein crystallization,[75] cell counting, [76] DNA sequencing, [77] and enzymatic assays. [46,77–82] The novel method contributed to an entirely new approach in tackling the early detection of false positive or negative hits: organ on a chip model. The 3D microchips are designed to represent given organs in the body, including all physical, chemical, and cellular stimuli, thereby accurately mimicking human physiology and delivering more accurate information on the drug's pharmacophoric profile.[83] The successful implementation of this technology could also reduce issues with species-species variations and animal models.[84,85] For example, Volker et al. developed a liver on a chip model with long-living stable hepatocytes arranged in a 3D manner to analyze long-term drug-induced liver injuries.[85] Biopsies can also be examined in microfluidic platforms, as shown with the screening of drug combinations in two genetically different pancreatic cell lines.[86]

Another vital application of microfluidic systems are the point of care applications. Digital microfluidics advanced recently in this field, showing high flexibility, multiplex, and parallel operations in compact mobile platforms, including all basic fluid operations and automation required for integrated systems.[87] Self-contained microfluidic systems are also well known for their compact size and highly sensitive quantitative diagnostic readouts, making them ideal in peripheral regions that are generally unreachable with common tools.[88]

Lastly, applications in advanced drug delivery systems emerged, including the multifunctional drug carrier's fabrication from polymers and the delivery of small quantities of drugs to the targeted tissue.[89] In particular, µTAS is ideal for hit-to-lead development, eliminating temporal and spatial hurdles between synthesis and screening. Automated operations with an implemented synthesis of compound libraries, screening, and evaluation with a rapid feedback cycle minimize the gap between synthesis and biochemical evaluation, thereby accelerating the research process during the hit to lead development stage.[43]

Indeed, numerous systems primarily based on microfluidics were developed to optimize the hit-to-lead development cycle in academia and research faculties with implementations to certain companies such as AbbVie and Cyclofluidic.[49,51,81,82,90–92] Bimbisar et al. developed an integrated platform to synthesize, screen automatically, and evaluate the activities of Abi kinase inhibitors based on activity prediction using Random-Forest regression to generate novel entities with improved pIC_{50} under 8 within just 21 compounds.[93] A captivating work was presented by Oliver j Miller et al. in developing a highly precise droplet-based microfluidic system that can screen up to 10,000 data points per compound with very low consumption, allowing the generation of high-precision dose-response curves valuable to detect untypical protein activities. The assay was evaluated by screening 704 compounds against tyrosine phosphatase 1B, successfully identifying potent inhibitors.[58] Different cellular-based high throughput screening assays were developed as well using perfusion flow mode and droplet modes.[94] Simultaneously, many integrated platforms were developed for several protein targets.[95] Several examples are the binders of polycomb protein EED with a library turnaround time between 24-36 h,[90] b-secretase BACE1 with a complete cycle time of only 1 h per compound,[96] the serine protease hepsin using the CyclOps synthesis-to-screen platform[97], and xanthine-derived dipeptidyl peptidase 4 with a full synthesis-screening cycle time of 24 h.[98]

Despite the several success stories, the full integration of the molecular design cycle into the DD has not yet been applied on a broader scale. The main reason was the lower versatility of chemical synthesis in microfluidic format, the proper scoring and production, and the optimization of promising molecules in an adaptive learning cycle. Hence, novel automated systems are developed to improve the microstructure and cost-efficiency in a more widespread spectrum.

I.2.3 The VIRO-FLOW projects aim at microfluidic systems

The development of novel µTAS systems is a challenging and multidisciplinary task which many novel joint projects try to improve. One of these projects was the VIRO-FLOW project, founded in 2017 as a collaboration between the chemical research faculty ICIQ and the pharmaceutical company AiCuris Anti-infective Cures AG. KG. The ITN-EID programme was providing high-level training for 3 early-stage researchers in a network of experts with the focus on developing innovative HBV inhibitors and optimizing the hit-to-lead cycle by designing a fully automated continuous flow platform.[99] This process involved the drug synthesis in flow with inline detection of the compounds chemical and biochemical activity. The main objective was to use the obtained data and automatically evaluate them to calculate the most fitting structures for the subsequent synthetic cascade. Furthermore, the automatization of the combined chemical and biochemical processes will lead to an iterative optimization cycle of biochemical activity for the newly generated compounds. In this multidisciplinary project, the central part of this work was the development of the microfluidic platform for the inflow testing of novel anti-HBV compounds against the HBc as the primary target.

I.3 Capsid assembly assay as an ideal target for inflow screening

I.3.1 Hepatitis B Virus epidemiology and disease process

HBV remains a top health priority worldwide, with currently over 296 million people chronically infected. It is still a devastating cause of morbidity and mortality, accounting for more than 820,000 deaths per year.[100] Its geographic distribution is worldwide, with the lowest prevalence in North and South America and the highest one in the Western Pacific region with 116 million and Africa with 81 million infected people leading to an immense burden on the local individuals and the healthcare system.[100] The global distribution of the virus is traceable with the local distribution of the 10 different genotypes of HBV (A-J).[101]

On a cellular level, the infection is caused by a hepatotropic enveloped DNA virus from the Hepadnaviridae.[105] The 3.2 kb long partial double-stranded dsDNA in infectious viruses are found in the form of a relaxed circular construct (rcDNA), which is coding for four partially overlapping reading frames: viral polymerase, HBc, the HBx protein, and the surface protein, which has three size variations (large (L), Medium (M), and small (S)) (Figure 3).

Figure 3: HBV genome scripts coding for the four protein constructs, including the preC protein (orange), the viral polymerase (light green), the three surface protein subunits (blue), and finally, the X protein (dark green).[3]

The life cycle of HBV is shown in (Figure 4). During the infection of a hepatocyte, the HBsAg glycoprotein binds reversibly to heparan sulfate proteoglycans on the cell surface, and the larger surface proteins (L) interact with the sodium taurocholate co-transporting polypeptide, which in turn initiates the viral internalization.[106,107] The virus loses its lipid envelop, and the tetrachediracal virus particle build from 120 or 90 core proteins is transported to the nucleus due to a nuclear transportation signal on the core protein. Next, the capsid disassembles, releasing the rcDNA into the nucleus where the host's DNA repair system closes it to the covalently closed circular DNA (cccDNA). This cccDNA forms a minichromosome by binding with histones H3 and H4 to initiate transcription of the pregenomic RNA (pgRNA), which functions as the HBc and the viral template polymerase. After transcription, the viral pgRNA is transported to the cytosol, where the viral reverse polymerases and HBc protein are translated using host-specific enzymes.[108] Next, one viral polymerase binds to templates of pgRNA using its 5'stem-loop structure (ε). The RNA-

---

[3] Reprinted by permission from [SPRINGER NATURE LICENSE]: [Springer Nature] [Nature Reviews Disease Primers] [Hepatitis B virus infection, Man-Fung Yuen et al.], [COPYRIGHT: 5162340846648] (2018).[102]

Polymerase complex, in turn, functions as a nucleation factor for the HBc core protein, initiating the assembly of infectious immature particles.[109] To complete the virus maturation process, the viral polymerase starts the reverse transcription process of the pgRNA to rcDNA involving priming and template shifts with the support of the core protein to which the RNA is bound.[110] In the final viral particle, the electrical and density change of the DNA template triggers exposure of the HBc's c-terminus, which is recognized by the host cell as a signal for initiating the virus secretion. In this last step, the 42 nm viral particle binds to surface proteins in the endoplasmic reticulum and is secreted or recycled to the cell nucleus to maintain the cccDNA levels. Interestingly, depending on the disease progression, around 10 % of the viral particles contain double-stranded linear DNA, which is more easily integrated into the host genome upon infection.[111] Aside from the virus, many 17-25 nm enveloped spherical empty subviral particles (90 % of total secretion), called Dane particles, are also secreted, probably functioning as a decoy for the immune system as described above.[102,112]

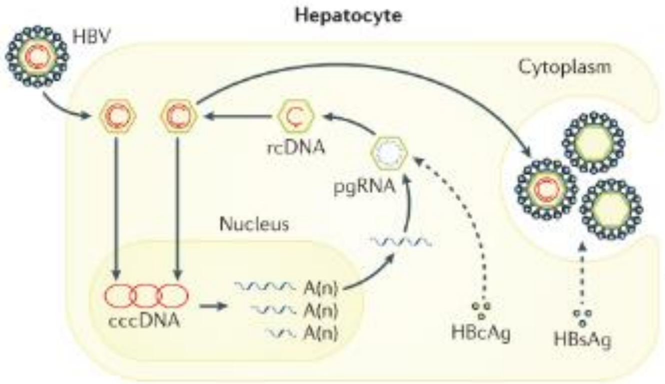

Figure 4: HBV life cycle. The virus life cycle includes the uptake, rcDNA release in the nucleus and its repair to cccDNA, transcription of the pgRNA in the nucleus, translation of the polymerase and the HBc protein, encapsidation of the pgRNA-polymerase construct in a newly assembled HBc capsid, the recycling of rcDNA to maintain the cccDNA pool or the release of viral particles.[4]

The transmission is commonly achieved by droplet infection of body fluids, including blood, saliva, sperm, or other body fluids during sex or birth.[100] After infection, a coordinated immune response is often hampered by HBV using several mechanisms. First, HBV releases a high amount of empty subviral

---

[4] Reprinted by permission from [SPRINGER NATURE LICENSE]: [Springer Nature] [Nature Reviews Disease Primers] [Hepatitis B virus infection, Man-Fung Yuen et al.], [COPYRIGHT: 5162340846648] (2018)[102]

particles containing HBsAg, which can mislead the adaptive immunity resulting in a T cell anergy and depletion. Many of the viral sub-particles showed interactions with host immune signaling pathways such as nuclear factor-kB and mitogen-activated protein kinase pathways, cytokine secretion, and TLR signaling. Furthermore, the HBx protein of the virus can inhibit proteasome-based degradation of viral proteins. Lastly, interferon-stimulated gene transcription can also be impaired by viral responses.[102] Hence, after an acute infection, around 5 % of adult cases and 95 % of infants or young children failed to clear the virus, and the disease progresses to chronic liver infections.[100] During the chronic HBV development, the patients suffer from recurring high-grade liver infections, which is around 15-30 % of the patients leading to liver fibrosis and cirrhosis, caused by the host's immune system trying to eradicate the virus, that can progress to decompensated liver disease and hepatocellular carcinoma in around 40 % of the cases.[102,103] In many cases, these advanced liver damages lead to the need for a liver transplant before liver failure.[104]

I.3.2 Current anti-HBV drugs

Despite a safe and 98-100 % effective vaccine, there is no global eradication of HBV within reach. Hence, the Global Hepatitis Health Sector Strategy declared the ambition to eliminate HBV as a public health threat by 2030 with a functional cure by the HBV surface antigen seroclearance.[100] The current treatment of HBV chronic infection consists of viral replication inhibitors and immune modulators. Immune modulators which are currently used are polyethylene glycol-Interferon-alpha-2a (PEG-IFNα-2a) and IFNα-2b, possessing antiviral and immune-modulating properties. They currently offer a 10 % chance of complete cure, require prolonged treatment, and can be associated with severe side effects, including malaise, fever, thyrotoxic features, and depression, which strongly limits their utilization.[113] Reverse transcriptase inhibitors for HBV are nucleotide or nucleotide analogs (NA), including lamivudine, adefovir dipivoxil, telbivudine, entecavir, TDF, and tenofovir alafenamide, with the last three offering the best potency and resistance rates. NA can effectively suppress virus replication, and in long treatment, they can reverse liver cirrhosis and prevent hepatocomal canceroma. [114,115] However, NA requires a continued to lifelong treatment with a significant number of resistance development.[116,117] Furthermore, even though NAs have minimal adverse effects and are quite economical, the success rate for complete clearance with 3-11 % seroconversion for HBsAg is fairly low.[118]

Combined therapies of NA and immune modulators displayed higher success rates in some studies. According to Marcellin et al., the combination of PEG-IFNα with TDF ended in a higher HBsAg seroclearance of 9.1 % compared to the individual treatments with the same constraints.[119] Still, other studies failed to find a positive effect in combined therapies; hence more work is required to find the correct combined therapies for the given viral variants.[120] Other unsettling findings have been reported, including mutations and vaccine escape mutations in Africa, especially in HBV-HIV cohost, emphasizing the need for a rapid and innovative response to the virus.[121] Overall, it is essential to develop a functional cure, preferably on novel viral targets.[122–124]

I.3.3 HBV core protein as a promising target

Due to the small genome with a limited number of open reading frames, only a few viral targets can be exploited to inhibit viral replication and cure chronic HBV infection. In this regard, host-specific drugs were introduced, such as APOBEC3 cytidine deaminases and Glucosidase inhibitor derivatives.[125] Furthermore, inventive drugs have been developed targeting the different stages of the virus life cycle, including virus entry inhibitors, cccDNA directed therapeutic approaches, RNA interference (RNAi/ antisense oligonucleotides) approaches, and capsid assembly modulators (CAMs) targeting the HBc.[125–127]

In this context, the 21 kDa HBV core protein is an attractive target for novel antiviral therapies. It is essential for the HBV life cycle participating in the viral DNA release at the cell nucleus, transcription of the viral RNA, encapsidation of the viral polymerase, suppression of initiate immunity and the reverse transcription of the RNA to relaxed circular DNA (rcDNA) inside the HBc capsid.[123,124] Furthermore, the core protein has no significant homology to any host protein, thereby reducing the risk of unwanted side- or adverse effects. Finally, as fine adjusted polymeric assembly complexes, HBc is opted for viral replication and hence is likely to suppress mutations due to the dominant sensitivity of the wildtype protein.[128,129]

Structure-wise, the HBc itself contains 183 to 185 amino acids depending on the genotype and is organized in two distinct domains. The N-terminal domain (NTD) composed of residues 1-149 is essential for the capsid assembly forming the outer shell. This domain is formed of 5 α-helices, of which two are perpendicular to the final capsid and are reversed for the dimer-dimer interface while the other three lay in plain and form the hydrophobic interactions between HBc homodimers.[123] An important feature of the HBc capsid built from the N-terminal domains is the highly dynamic structure with conformation variations and melting of secondary structures.[130] The C-terminal domain (CTD), is built up from the remaining 34-36 residues and is composed of four clusters of three to four arginine residues, seven serines, and one threonine typically structured toward the interior of the capsid.[112,123] These residues are essential for the packaging of the pgRNA HBV polymerase complex, binding of host proteins such as protein kinase C, serine/ arginine protein kinase (SRPK), and cyclin-dependent kinase 2 (Cdk2), and later the reverse transcription of the pgRNA to the rcDNA in the capsid.[131] Furthermore, by phosphorylation and dephosphorylation of the arginine residues, the capsid switches the maturation signal necessary for the envelopment and secretion of the virus.[112,132] The CTD is extremely basic due to the arginine clusters leading to a challenging recombinant expression and purification of a full-length HBc sequence in *E. coli*.[133,134] For this reason, the C-terminal truncated version cp149 is frequently used to study capsid assembly and screen for CAMs.[135]

The majority of the HBc protein is composed of 120 (36 nm-diameter) HBc compact homo-dimers in 95 % with a smaller portion (5 %) assembling from 90 dimers (32 nm-diameter) into capsids following T=4 or T=3 symmetry.[112,136,137] The structure of the assembled product follows fivefold isohedrical vertices with hexagonal arrangements of dimers. A T=4 capsid has four quasi-equivalent subunits nominated A, B, C, D, of which two structurally different dimer pairs are formed AB and CD.[112,138] The dimer-dimer interface is hydrophobic, driven by the previously described two α-helical hairpins of the adjacent monomers resulting in a four-helix bundle (Figure 5).[139]

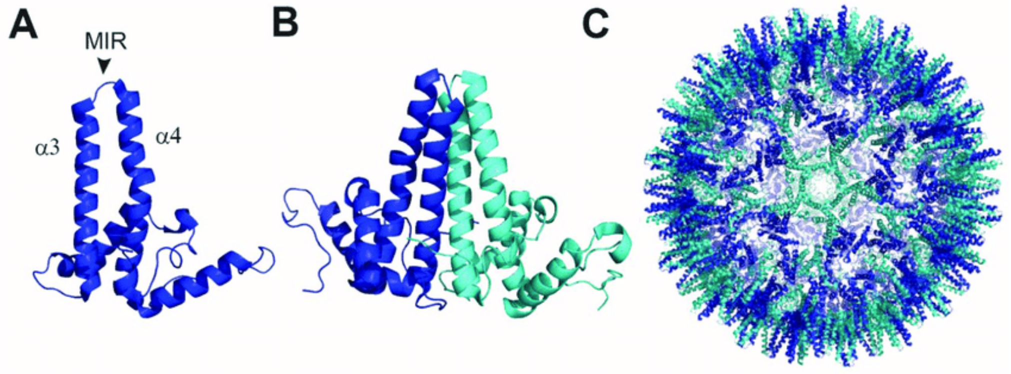

Figure 5: Structure of HBc core protein (A), HBc dimers (B), and HBc capsid (C). Under physiological conditions, the HBc proteins dimerize using the α3 and α4 helical secondary structures. The other three orthogonal α helices build the hydrophobic interface, which is required to assemble HBc dimers to the HBc capsids.[5]

---

[5] . Reprinted by permission from [Creative Commons Attribution License]: [Viruses] [Virus-Like Particle Vaccines] [Virus-Like Particles and Nanoparticles for Vaccine Development against HCMV, Michela Perotti and Laurent Perez.], (2020).[140]

The capsid assembly from the HBc dimers is governed by entropy-driven weak interactions of -3 to -4 kcal.[141] The main impact factors on capsid assembly are the ionic strength, pH of the solution, temperature, HBc concentration, and the presence of CAMs due to allosteric activation of the HBc protein.[142–146] The reaction is induced by the burial of the approximately 75 % hydrophobic surface area at the HBc interdimer contacts (approx. 1700 A),[112] leading to a controlled, multivalent assembly with the possibility to edit incorrectly associated proteins thermodynamically.[134,145,147] From a kinetic point of view, the assembly has a sigmoidal curve starting with slow rate-limiting nucleation steps, followed by a steady-state elongation step consisting of the fast addition of new dimers HBc dimers and finalized by closed distinct capsids (Equation 1, and Figure 6).[134,142,145,147] During the steady-state of the assembly, nuclei and capsid intermediates continually form parallelly, leading to a multitude of reactions simultaneously instead of a strict procedure.[145] The depletion of dimers (kinetic traps) during the assembly is prevented by both the weak hydrophobic interactions between dimers and the rate-limiting nucleation step. Indeed attempts to accelerate the nucleation step to increase assembly kinetic often lead to kinetic traps or errors in the capsid lattice.[146,147] Once assembled, the capsids follow a strong hysteresis allowing them to maintain integrity at unfavorable assembly conditions. This “breathing” of the capsid is essential for releasing the rcDNA at the right conditions.[148] Furthermore, the dynamic structure of the HBc capsid allows transient exposure of the CTD domain essential for viral secretion following the reverse transcription of the viral pgRNA.[149]

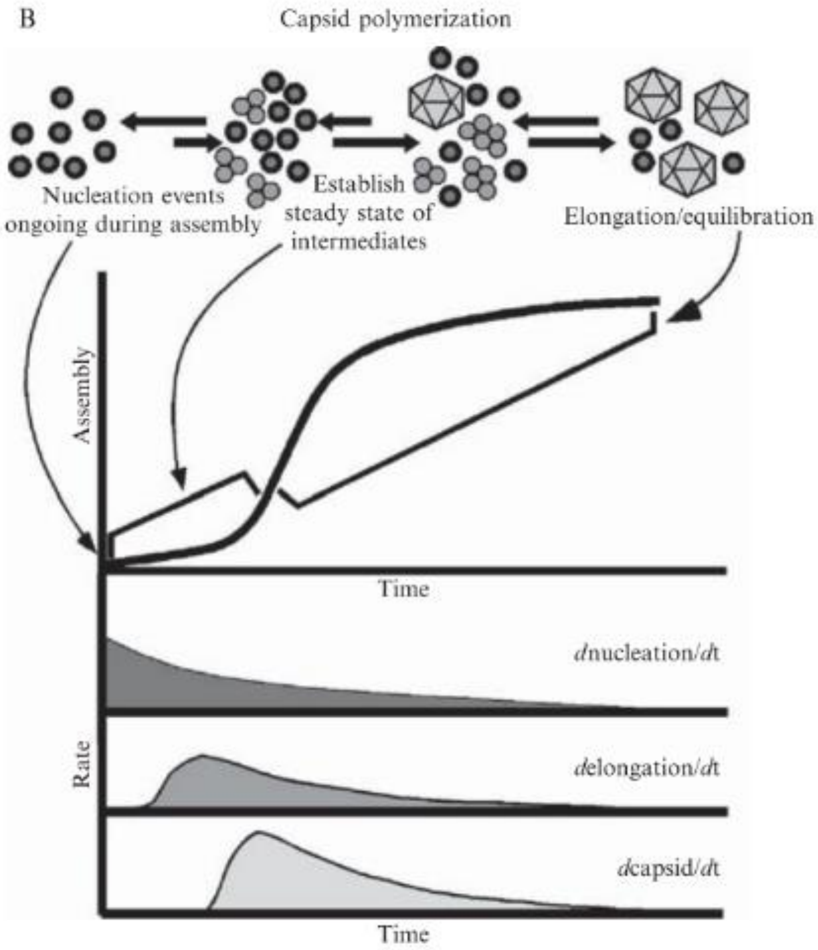

Figure 6: HBV capsid assembly with the nucleation, steady-state, and elongation reactions. The three processes, including nucleation elongation and capsid formation, are subsequent. However, since each capsid needs the nucleation and elongation process individually, the overall reaction is a sum of all these reactions running parallelly.[6]

$$K_{capsid} = \frac{[Capsid]}{[Capsid]^{120}}$$

Equation 1: HBV capsid assembly kinetics. The prominent exponent leads to a pseudocritical concentration at which rapid assembly occurs.

---

[6] Reprinted by permission from [ELSEVIER LICENSE]: [Elsevier Books] [Methods in Enzymology] [Chapter 14 The Thermodynamics of Virus Capsid Assembly, Sarah Katen, Adam Zlotnick.], [COPYRIGHT: 5180150611084] (2009).[145]

I 4 Objectives

The VIRO-FLOW project aims to integrate the advantages of continuous flow chemistry with *in vitro* microfluidic bioassay technologies for the fast and efficient discovery of novel and innovative inhibitors of HBV. As part of the project, the presented work was focused on developing an automated microfluidic system for the inflow synthesis, purification, and testing of novel anti-HBV compounds. The primary target for the inflow adaptation was the pleitropic HBc, given its multifunctionality in the virus life cycle combined with fast assembly properties. To achieve this, the specific objectives for each chapter were the following:

- **Chapter II**: Evaluation and generation of various methods to differentiate the mode of action of novel CAMs in an economical, reproducible, and accurate manner.
- **Chapter III:** Selection and evaluation of the most fitting devices for the microfluidic system and its subsequent automation.
- **Chapter IV**: Adaptation of the CAM-mediated HBc assembly to continuous flow format and inflow measurements of dose-response curves and kinetics. With the obtained data, the EC_{50} values were calculated, and the CAMs mode of action was determined.
- **Chapter V:** Droplet microfluidics were evaluated as a suitable assay format for the HBc capsid assembly assay.

I 5 Reference

1. Thomford, N. E. *et al.* Natural products for drug discovery in the 21st century: Innovations for novel drug discovery. *Int. J. Mol. Sci.* **19**, (2018).
2. Katz, L. & Baltz, R. H. Natural product discovery: past, present, and future. *J. Ind. Microbiol. Biotechnol.* **43**, 155–176 (2016).
3. Drews, J. Drug discovery: A historical perspective. *Science (80-.).* **287**, 1960–1964 (2000).
4. Sertürner, F. W. Über das Morphium , eine neue falzfähige Grundlnge, und die Mekonsäure, als Hauptbestandtheile des Opiums. *Ann. Phys.* (1817).
5. A., F. On the antibacterial action of cultures of a Penicilliwn with special reference to their useful isolation ofE. influenme. *Br. J. Exp. Pathol.* **10**, 226–36 (1929).
6. Jaroch, K., Jaroch, A. & Bojko, B. Cell cultures in drug discovery and development: The need of reliable in vitro-in vivo extrapolation for pharmacodynamics and pharmacokinetics assessment. *J. Pharm. Biomed. Anal.* **147**, 297–312 (2018).
7. Kapetanovic, I. M. Computer-aided drug discovery and development (CADDD): In silico-chemico-biological approach. *Chem. Biol. Interact.* **171**, 165–176 (2008).
8. Rifaioglu, A. S. *et al.* Recent applications of deep learning and machine intelligence on in silico drug discovery: Methods, tools and databases. *Brief. Bioinform.* **20**, 1878–1912 (2019).
9. Gashaw, I., Ellinghaus, P., Sommer, A. & Asadullah, K. What makes a good drug target? *Drug Discov. Today* **17**, S24–S30 (2012).
10. Inglese, J. *et al.* High-throughput screening assays for the identification of chemical probes. *Nat. Chem. Biol.* **3**, 466–479 (2007).
11. KM Merz Jr, D Ringe, C. R. *Drug design: structure-and ligand-based approaches*. (2010).
12. M., Hay, D.W., Thomas, J.L., Craighead., EconomidesJ., Rosenthal. Clinical development success rates for investigational drugs. *Nat. Biotechnol.* **32**, 40–51 (2014).
13. Bibette, J. Gaining confidence in high-throughput screening. *Proc. Natl. Acad. Sci. U. S. A.* **109**, 649–650 (2012).
14. Noah, J. New developments and emerging trends in high-throughput screening methods for lead compound identification. *Int. J. High Throughput Screen.* 141 (2010).
15. Dick Basu A S, K. The Importance of Microplate Standardization. *J. Biomol. Screen.* (1999).
16. SLAS. ANSI/SLAS Microplate Standards. https://www.slas.org/education/ansi-slas-microplate-standards/ (2021).
17. Hodder, P., Mull, R., Cassaday, J., Berry, K. & Strulovici, B. Miniaturization of intracellular calcium functional assays to 1536-well plate format using a fluorometric imaging plate reader. *J. Biomol. Screen.* **9**, 417–426 (2004).
18. Hertzberg, R. P. & Pope, A. J. High-throughput screening: New technology for the 21st century. *Curr. Opin. Chem. Biol.* **4**, 445–451 (2000).
19. MacArron, R. *et al.* Impact of high-throughput screening in biomedical research. *Nat. Rev. Drug Discov.* **10**, 188–195 (2011).
20. England, E. *et al.* Application of the mirrorball high-sensitivity cytometer to multiplexed assays for antibody drug discovery. *J. Biomol. Screen.* **20**, 536–544 (2015).
21. Neumann, B. *et al.* High-throughput RNAi screening by time-lapse imaging of live human cells. *Nat. Methods* **3**, 385–390 (2006).
22. Motabar, O. *et al.* A new resorufin-based α-glucosidase assay for high-throughput screening. *Anal. Biochem.* **390**, 79–84 (2009).
23. Macarró, R. & Hertzberg, R. P. Design and implementation of high throughput screening assays. *Mol. Biotechnol.* **47**, 270–285 (2011).
24. Netzer, W. J. & Hartl, F. U. Recombination of protein domains facilitated by co-translational

folding in eukaryotes. *Nature* **388**, 343–349 (1997).

25. Keserü, G. M. & Makara, G. M. The influence of lead discovery strategies on the properties of drug candidates. *Nat. Rev. Drug Discov.* **8**, 203–212 (2009).

26. Hert, J., Irwin, J. J., Laggner, C., Keiser, M. J. & Shoichet, B. K. Quantifying biogenic bias in screening libraries. *Nat. Chem. Biol.* **5**, 479–483 (2009).

27. Oeljeklaus, J., Kaschani, F. & Kaiser, M. Streamlining chemical probe discovery: Libraries of 'fully functionalized' small molecules for phenotypic screening. *Angew. Chemie - Int. Ed.* **52**, 1368–1370 (2013).

28. Zheng, W., Thorne, N. & McKew, J. C. Phenotypic screens as a renewed approach for drug discovery. *Drug Discov. Today* **18**, 1067–1073 (2013).

29. Christopher A. Lipinski", Franco Lombardo, Beryl W. Dominy, P. J. F. Experimental and computational approaches to estimate solubility and permeability in drug discovery and development settings. *Adv. Drug Deliv. Rev.* (1996).

30. Hingorani, A. D. *et al.* Improving the odds of drug development success through human genomics: modelling study. *Sci. Rep.* **9**, 1–25 (2019).

31. Wouters, O. J., McKee, M. & Luyten, J. Estimated Research and Development Investment Needed to Bring a New Medicine to Market, 2009-2018. *JAMA - J. Am. Med. Assoc.* **323**, 844–853 (2020).

32. Duelen, R. *et al. Medicinal Biotechnology for Disease Modeling, Clinical Therapy, and Drug Discovery and Development*. *Introduction to Biotech Entrepreneurship: From Idea to Business* (2019).

33. Paul, S. M. *et al.* How to improve RD productivity: The pharmaceutical industry's grand challenge. *Nat. Rev. Drug Discov.* **9**, 203–214 (2010).

34. Schneider, G. Automating Drug Discovery. **17**, (2018).

35. Lenz, W. & Knapp, K. Die Thalidomid-Embryopathie. *Dtsch. Medizinische Wochenschrift* **87**, 1232–1242 (1962).

36. Giusti, R. M., Iwamoto, K. & Hatch, E. E. Diethylstilbestrol revisited: A review of the long-term health effects. *Ann. Intern. Med.* **122**, 778–788 (1995).

37. Heide M. Connolly, M.D., Jack L. Crary, M.D., Michael D. McGoon, M.D., Donald D. Hensrud, M.D., M.P.H. Brooks S. Edwards, M.D., William D. Edwards, M.D., and Hartzell V. Schaff, M. D. Valvular Heart Disease Associated With Fenfluramine-Phentermine. *N. Engl. J. Med.* 581–588 (1997).

38. Woosley, R. L., Chen, Y., Freiman, J. P. & Gillis, R. A. Mechanism of the Cardiotoxic Actions of Terfenadine. *JAMA J. Am. Med. Assoc.* **269**, 1532–1536 (1993).

39. Mohr, K. I. History of Antibiotics Research. *Springer Int.* 435 (2016)

40. Tacconelli, E. *et al.* Discovery, research, and development of new antibiotics: the WHO priority list of antibiotic-resistant bacteria and tuberculosis. *Lancet Infect. Dis.* **18**, 318–327 (2018).

41. Ghosh, A. K., Brindisi, M., Shahabi, D., Chapman, M. E. & Mesecar, A. D. Drug Development and Medicinal Chemistry Efforts toward SARS-Coronavirus and Covid-19 Therapeutics. *ChemMedChem* **15**, 907–932 (2020).

42. Schreiber, S. L., Ciba, M. & Schreiber, S. L. Target-Oriented and Diversity-Oriented Organic Synthesis in Drug Discovery. (2000).

43. Schneider, G. Automating drug discovery. *Nat. Rev. Drug Discov.* **17**, 97–113 (2018).

44. Ríos, Á. & Zougagh, M. Modern qualitative analysis by miniaturized and microfluidic systems. *TrAC - Trends Anal. Chem.* **69**, 105–113 (2015).

45. Nys, G. & Fillet, M. Microfluidics contribution to pharmaceutical sciences: From drug discovery to post marketing product management. *J. Pharm. Biomed. Anal.* **159**, 348–362 (2018).

46. Pereira, S. A. P., Dyson, P. J. & Saraiva, M. L. M. F. S. Miniaturized technologies for high-throughput drug screening enzymatic assays and diagnostics – A review. *TrAC - Trends Anal.*

Chem. **126**, 115862 (2020).

47. Fleming, G. S. & Beeler, A. B. Integrated Drug Discovery in Continuous Flow. *J. Flow Chem.* **7**, 124–128 (2017).

48. Reyes, D. R., Iossifidis, D., Auroux, P. & Manz, A. Micro Total Analysis Systems . 1 . Introduction , Theory , and Technology. **74**, 2623–2636 (2002).

49. Lee, S. J. & Lee, S. Y. Micro total analysis system (μ-TAS) in biotechnology. *Appl. Microbiol. Biotechnol.* **64**, 289–299 (2004).

50. Manz, A., Graber, N. & Widmer, H. M. Miniaturized total chemical analysis systems: A novel concept for chemical sensing. *Sensors Actuators B. Chem.* **1**, 244–248 (1990).

51. Dittrich, P. S., Tachikawa, K. & Manz, A. Micro total analysis systems. Latest advancements and trends. *Anal. Chem.* **78**, 3887–3907 (2006).

52. Bogdan, A. R. & Dombrowski, A. W. Emerging Trends in Flow Chemistry and Applications to the Pharmaceutical Industry. *J. Med. Chem.* **62**, 6422–6468 (2019).

53. Măriuţa, D. *et al.* Miniaturization of fluorescence sensing in optofluidic devices. *Microfluidics and Nanofluidics* vol. 24 (2020).

54. Dittrich, P. S. & Manz, A. Single-molecule fluorescence detection in microfluidic channels-the Holy Grail in μtAS? *Anal. Bioanal. Chem.* **382**, 1771–1782 (2005).

55. Plutschack, M. B., Pieber, B., Gilmore, K. & Seeberger, P. H. The Hitchhiker's Guide to Flow Chemistry â¥. *Chem. Rev.* **117**, 11796–11893 (2017).

56. Reizman, B. J. & Jensen, K. F. Feedback in Flow for Accelerated Reaction Development. *Acc. Chem. Res.* **49**, 1786–1796 (2016).

57. Whitesides, G. M. The origins and the future of microfluidics. *Nature* **442**, 368–373 (2006).

58. Miller, O. J. *et al.* High-resolution dose-response screening using droplet-based microfluidics. *Proc. Natl. Acad. Sci. U. S. A.* **109**, 378–383 (2012).

59. Werner, M. *et al.* Seamless integration of dose-response screening and flow chemistry: Efficient generation of structure-activity relationship data of β-secretase (BACE1) inhibitors. *Angew. Chemie - Int. Ed.* **53**, 1704–1708 (2014).

60. Seemann, R., Brinkmann, M., Pfohl, T. & Herminghaus, S. Droplet based microfluidics. *Reports Prog. Phys.* **75**, (2012).

61. Michelle R. Bringer, Cory J. Gerdts, Helen Song, J. D. T. and R. F. I. Microfluidic systems for chemical kinetics. *Phil. Trans. R. Soc. Lond. A* 1087–1104 (2004).

62. Ismagilov, R. F. A Microfluidic System for Controlling Reaction N. *AngewandteChemie* 791–796 (2003).

63. Helen Song, Joshua D. Tice, and R. F. I. A Microfluidic System for Controlling Reaction Networks in Time**. *Angew. CHem. Int..* **42**, 767 (2003).

64. Song, H., Chen, D. L. & Ismagilov, R. F. Reactions in droplets in microfluidic channels. *Angew. Chemie - Int. Ed.* **45**, 7336–7356 (2006).

65. Shembekar, N., Chaipan, C., Utharala, R. & Merten, C. A. Droplet-based microfluidics in drug discovery, transcriptomics and high-throughput molecular genetics. *Lab on a Chip* vol. 16 1314–1331 (2016).

66. Lagus, T. P. & Edd, J. F. A review of the theory, methods and recent applications of high-throughput single-cell droplet microfluidics. *J. Phys. D. Appl. Phys.* **46**, (2013).

67. Rosenfeld, L., Lin, T., Derda, R. & Tang, S. K. Y. Review and analysis of performance metrics of droplet microfluidics systems. *Microfluid. Nanofluidics* **16**, 921–939 (2014).

68. Mazutis, L. *et al.* Multi-step microfluidic droplet processing: Kinetic analysis of an in vitro translated enzyme. *Lab Chip* **9**, 2902–2908 (2009).

69. Agresti, J. J. *et al.* Ultrahigh-throughput screening in drop-based microfluidics for directed evolution. *Proc. Natl. Acad. Sci. U. S. A.* **107**, 4004–4009 (2010).

70. Chiu, F. W. Y. & Stavrakis, S. High-throughput droplet-based microfluidics for directed evolution of enzymes. *Electrophoresis* **40**, 2860–2872 (2019).

71. Payne, E. M., Holland-Moritz, D. A., Sun, S. & Kennedy, R. T. High-throughput screening by droplet microfluidics: Perspective into key challenges and future prospects. *Lab Chip* **20**, 2247–2262 (2020).

72. Shang, L., Cheng, Y. & Zhao, Y. Emerging Droplet Microfluidics. *Chem. Rev.* **117**, 7964–8040 (2017).

73. Tsui, J. H., Lee, W., Pun, S. H., Kim, J. & Kim, D. H. Microfluidics-assisted in vitro drug screening and carrier production. *Adv. Drug Deliv. Rev.* **65**, 1575–1588 (2013).

74. Yang, C. *et al.* High throughput computing based distributed genetic algorithm for building energy consumption optimization. *Energy Build.* **76**, 92–101 (2014).

75. Ferreira, J., Castro, F., Rocha, F. & Kuhn, S. Protein crystallization in a droplet-based microfluidic device: Hydrodynamic analysis and study of the phase behaviour. *Chem. Eng. Sci.* **191**, 232–244 (2018).

76. Hassan, U. & Bashir, R. Electrical cell counting process characterization in a microfluidic impedance cytometer. *Biomed. Microdevices* **16**, 697–704 (2014).

77. Clausell-Tormos, J., Griffiths, A. D. & Merten, C. A. An automated two-phase microfluidic system for kinetic analyses and the screening of compound libraries. *Lab Chip* **10**, 1302–1307 (2010).

78. Wu, J., He, Z., Chen, Q. & Lin, J. M. Biochemical analysis on microfluidic chips. *TrAC - Trends Anal. Chem.* **80**, 213–231 (2016).

79. Neužil, P., Giselbrecht, S., Länge, K., Huang, T. J. & Manz, A. Revisiting lab-on-a-chip technology for drug discovery. *Nat. Rev. Drug Discov.* **11**, 620–632 (2012).

80. Lee, D. W., Lee, M. Y., Ku, B. & Nam, D. H. Automatic 3D cell analysis in high-throughput microarray using micropillar and microwell chips. *J. Biomol. Screen.* **20**, 1178–1184 (2015).

81. Perrin, D., Frémaux, C., Besson, D., Sauer, W. H. B. & Scheer, A. A microfluidics-based mobility shift assay to discover new tyrosine phosphatase inhibitors. *J. Biomol. Screen.* **11**, 996–1004 (2006).

82. Wright, B. D. *et al.* Development of a high-throughput screening assay to identify inhibitors of the lipid kinase PIP5K1C. *J. Biomol. Screen.* **20**, 655–662 (2015).

83. Benam, K. H. *et al.* Engineered in vitro disease models. *Annu. Rev. Pathol. Mech. Dis.* **10**, 195–262 (2015).

84. Skardal, A., Shupe, T. & Atala, A. Organoid-on-a-chip and body-on-a-chip systems for drug screening and disease modeling. *Drug Discov. Today* **21**, 1399–1411 (2016).

85. Lauschke, V. M., Hendriks, D. F. G., Bell, C. C., Andersson, T. B. & Ingelman-Sundberg, M. Novel 3D Culture Systems for Studies of Human Liver Function and Assessments of the Hepatotoxicity of Drugs and Drug Candidates. *Chem. Res. Toxicol.* **29**, 1936–1955 (2016).

86. Eduati, F. *et al.* A microfluidics platform for combinatorial drug screening on cancer biopsies. *Nat. Commun.* **9**, (2018).

87. Samiei, E., Tabrizian, M. & Hoorfar, M. A review of digital microfluidics as portable platforms for lab-on a-chip applications. *Lab Chip* **16**, 2376–2396 (2016).

88. Boyd-Moss, M., Baratchi, S., Di Venere, M. & Khoshmanesh, K. Self-contained microfluidic systems: A review. *Lab Chip* **16**, 3177–3192 (2016).

89. Riahi, R. *et al.* Microfluidics for advanced drug delivery systems. *Curr. Opin. Chem. Eng.* **7**, 101–112 (2015).

90. Baranczak, A. *et al.* Integrated Platform for Expedited Synthesis-Purification-Testing of Small Molecule Libraries. *ACS Med. Chem. Lett.* **8**, 461–465 (2017).

91. Parry, D. M. Closing the Loop: Developing an Integrated Design, Make, and Test Platform for Discovery. *ACS Med. Chem. Lett.* **10**, 848–856 (2019).

92. Samiei, E., Tabrizian, M. & Hoorfar, M. A review of digital microfluidics as portable platforms

for lab-on a-chip applications. *Lab Chip* **16**, 2376–2396 (2016).

93. Desai, B. *et al.* Rapid discovery of a novel series of Abl kinase inhibitors by application of an integrated microfluidic synthesis and screening platform. *J. Med. Chem.* **56**, 3033–3047 (2013).

94. Du, G., Fang, Q. & den Toonder, J. M. J. Microfluidics for cell-based high throughput screening platforms-A review. *Anal. Chim. Acta* **903**, 36–50 (2016).

95. Baumann, M. Integrating continuous flow synthesis with in-line analysis and data generation. *Org. Biomol. Chem.* **16**, 5946–5954 (2018).

96. Werner, M. *et al.* Seamless integration of dose-response screening and flow chemistry: Efficient generation of structure-activity relationship data of β-secretase (BACE1) inhibitors. *Angew. Chemie - Int. Ed.* **53**, 1704–1708 (2014).

97. Pant, S. M. *et al.* Design, Synthesis, and Testing of Potent, Selective Hepsin Inhibitors via Application of an Automated Closed-Loop Optimization Platform. *J. Med. Chem.* **61**, 4335–4347 (2018).

98. Czechtizky, W. *et al.* Integrated synthesis and testing of substituted xanthine based DPP4 inhibitors: Application to drug discovery. *ACS Med. Chem. Lett.* **4**, 768–772 (2013).

99. Supervisor, D. H. B. (AiCuris) – *et al.* Viro Flow. http://www.viro-flow.eu/.

100. Hepatitis B. https://www.who.int/news-room/fact-sheets/detail/hepatitis-b.

101. Sunbul, M. Hepatitis B virus genotypes: Global distribution and clinical importance. *World J. Gastroenterol.* **20**, 5427–5434 (2014).

102. Yuen, M. F. *et al.* Hepatitis B virus infection. *Nat. Rev. Dis. Prim.* **4**, 1–21 (2018).

103. Giovanna, F., Bortolotti, F. & Francesco, D. Natural history of chronic hepatitis B: Special emphasis on disease progression and prognostic factors. *J. Hepatol.* **48**, 335–352 (2008).

104. Flemming, J. A., Kim, W. R., Brosgart, C. L. & Terrault, N. A. Reduction in liver transplant wait-listing in the era of direct-acting antiviral therapy. *Hepatology* **65**, 804–812 (2017).

105. Seitz, S., Urban, S., Antoni, C. & Böttcher, B. Cryo-electron microscopy of hepatitis B virions reveals variability in envelope capsid interactions. *EMBO J.* **26**, 4160–4167 (2007).

106. Sureau, C. & Salisse, J. A conformational heparan sulfate binding site essential to infectivity overlaps with the conserved hepatitis B virus a-determinant. *Hepatology* **57**, 985–994 (2013).

107. Ni, Y. *et al.* Hepatitis B and D viruses exploit sodium taurocholate co-transporting polypeptide for species-specific entry into hepatocytes. *Gastroenterology* **146**, 1–14 (2014).

108. Newbold, J. E. *et al.* The covalently closed duplex form of the hepadnavirus genome exists in situ as a heterogeneous population of viral minichromosomes. *J. Virol.* **69**, 3350–3357 (1995).

109. Bartenschlager, R. & Schaller, H. Hepadnaviral assembly is initiated by polymerase binding to the encapsidation signal in the viral RNA genome. *EMBO J.* **11**, 3413–3420 (1992).

110. Glebe, D. & Bremer, C. The molecular virology of hepatitis B virus. *Semin. Liver Dis.* **33**, 103–112 (2013).

111. Tu, T., Budzinska, M. A., Shackel, N. A. & Urban, S. HBV DNA integration: Molecular mechanisms and clinical implications. *Viruses* **9**, (2017).

112. Venkatakrishnan, B. & Zlotnick, A. The Structural Biology of Hepatitis B Virus: Form and Function. *Annu. Rev. Virol.* **3**, 429–451 (2016).

113. Lampertico, P. *et al.* Randomised study comparing 48 and 96 weeks peginterferon α-2a therapy in genotype D HBeAg-negative chronic hepatitis B. *Gut* **62**, 290–298 (2013).

114. Marcellin, P. *et al.* Regression of cirrhosis during treatment with tenofovir disoproxil fumarate for chronic hepatitis B: A 5-year open-label follow-up study. *Lancet* **381**, 468–475 (2013).

115. Lai, C. L. & Yuen, M. F. Prevention of hepatitis B virus-related hepatocellular carcinoma with antiviral therapy. *Hepatology* **57**, 399–408 (2013).

116. Chevaliez, S., Hézode, C., Bahrami, S., Grare, M. & Pawlotsky, J. M. Long-term hepatitis B surface antigen (HBsAg) kinetics during nucleoside/nucleotide analogue therapy: Finite

treatment duration unlikely. *J. Hepatol.* **58**, 676–683 (2013).

117. Cho, J. Y. *et al.* Long-term hepatitis B surface antigen (HBsAg) kinetics during entecavir treatment in Korean patients—Functional cure unlikely. *J. Viral Hepat.* **27**, 951–954 (2020).

118. Nijampatnam, B. & Liotta, D. C. Recent advances in the development of HBV capsid assembly modulators. *Curr. Opin. Chem. Biol.* **50**, 73–79 (2019).

119. Marcellin, P. *et al.* Combination of Tenofovir Disoproxil Fumarate and Peginterferon α-2a Increases Loss of Hepatitis B Surface Antigen in Patients with Chronic Hepatitis B. *Gastroenterology* **150**, 134-144.e10 (2016).

120. Bourlière, M. *et al.* Effect on HBs antigen clearance of addition of pegylated interferon alfa-2a to nucleos(t)ide analogue therapy versus nucleos(t)ide analogue therapy alone in patients with HBe antigen-negative chronic hepatitis B and sustained undetectable plasma hepatitis. *Lancet Gastroenterol. Hepatol.* **2**, 177–188 (2017).

121. Mokaya, J. *et al.* A systematic review of hepatitis B virus (HBV) drug and vaccine escape mutations in Africa: A call for urgent action. *PLoS Negl. Trop. Dis.* **12**, 1–24 (2018).

122. Selzer, L. & Zlotnick, A. Assembly and release of hepatitis B virus. *Cold Spring Harb. Perspect. Med.* **5**, 1–18 (2015).

123. Zlotnick, A. *et al.* Core protein: A pleiotropic keystone in the HBV lifecycle. *Antiviral Res.* **121**, 82–93 (2015).

124. Diab, A., Foca, A., Zoulim, F., Durantel, D. & Andrisani, O. The diverse functions of the hepatitis B core/capsid protein (HBc) in the viral life cycle: Implications for the development of HBc-targeting antivirals. *Antiviral Res.* **149**, 211–220 (2018).

125. Grimm, D., Thimme, R. & Blum, H. E. HBV life cycle and novel drug targets. *Hepatol. Int.* **5**, 644–653 (2011).

126. Volz, T. *et al.* The entry inhibitor Myrcludex-B efficiently blocks intrahepatic virus spreading in humanized mice previously infected with hepatitis B virus. *J. Hepatol.* **58**, 861–867 (2013).

127. Kang, L. *et al.* Anti-HBV drugs: Progress, unmet needs, and new hope. *Viruses* **7**, 4960–4977 (2015).

128. Tanner, E. J. *et al.* Dominant drug targets suppress the emergence of antiviral resistance. *Elife* **3**, 1–16 (2014).

129. Tan, Z., Maguire, M. L., Loeb, D. D. & Zlotnick, A. *Genetically Altering the Thermodynamics and Kinetics of Hepatitis B Virus Capsid Assembly Has Profound Effects on Virus Replication in Cell Culture*. *Journal of Virology* vol. 87 (2013).

130. Hilmer, J. K., Zlotnick, A. & Bothner, B. Conformational Equilibria and Rates of Localized Motion within Hepatitis B Virus Capsids. *J. Mol. Biol.* **375**, 581–594 (2008).

131. Zlotnick, A. *et al.* Localization of the C terminus of the assembly domain of hepatitis B virus capsid protein: Implications for morphogenesis and organization of encapsidated RNA. *Proc. Natl. Acad. Sci. U. S. A.* **94**, 9556–9561 (1997).

132. Perlman, D. H., Berg, E. A., O'Connor, P. B., Costello, C. E. & Hu, J. Reverse transcription-associated dephosphorylation of hepadnavirus nucleocapsids. *Proc. Natl. Acad. Sci. U. S. A.* **102**, 9020–9025 (2005).

133. Wingfield, P. T., Stahl, S. J., Williams, R. W. & Steven1, A. C. Hepatitis core Antigen produced in Escherichia coli. *Biochemistry* **34**, 4919–4932 (1995).

134. Ceres, P. & Zlotnick, A. Weak protein-protein interactions are sufficient to drive assembly of hepatitis B virus capsids. *Biochemistry* **41**, 11525–11531 (2002).

135. Stray, S. J., Johnson, J. M., Kopek, B. G. & Zlotnick, A. An in vitro fluorescence screen to identify antivirals that disrupt hepatitis B virus capsid assembly. *Nat. Biotechnol.* **24**, 358–362 (2006).

136. Böttcher, B., Wynne, S. A. & Crowther, R. A. Determination of the fold of the core protein of hepatitis B virus by electron cryomicroscopy. *Nature* **386**, 88–91 (1997).

137. Crowther, R. A. *et al.* Three-dimensional structure of hepatitis B virus core particles determined by electron cryomicroscopy. *Cell* **77**, 943–950 (1994).

138. Qazi, S., Schlicksup, C. J., Rittichier, J., Vannieuwenhze, M. S. & Zlotnick, A. An Assembly-Activating Site in the Hepatitis B Virus Capsid Protein Can Also Trigger Disassembly. *ACS Chem. Biol.* **13**, 2114–2120 (2018).

139. Zheng, C. L., Fu, Y. M., Xu, Z. X., Zou, Y. & Deng, K. Hepatitis B virus core protein dimer-dimer interface is critical for viral replication. *Mol. Med. Rep.* **19**, 262–270 (2019).

140. Perotti, M. & Perez, L. Virus-like particles and nanoparticles for vaccine development against HCMV. *Viruses* **12**, 1–17 (2019).

141. Zlotnick, A. Are weak protein-protein interactions the general rule in capsid assembly? *Virology* **315**, 269–274 (2003).

142. Zlotnick, A., Johnson, J. M., Wingfield, P. W., Stahl, S. J. & Endres, D. A theoretical model successfully identifies features of hepatitis B virus capsid assembly. *Biochemistry* **38**, 14644–14652 (1999).

143. Stray, S. J., Ceres, P. & Zlotnick, A. Zinc ions trigger conformational change and oligomerization of hepatitis B virus capsid protein. *Biochemistry* **43**, 9989–9998 (2004).

144. Kegel, W. K. & Van Der Schoot, P. Competing hydrophobic and screened-coulomb interactions in hepatitis B virus capsid assembly. *Biophys. J.* **86**, 3905–3913 (2004).

145. Katen, S. & Zlotnick, A. *Chapter 14 The Thermodynamics of Virus Capsid Assembly*. *Methods in Enzymology* vol. 455 (Elsevier Inc., 2009).

146. Lutomski, C. A. *et al.* Multiple Pathways in Capsid Assembly. *J. Am. Chem. Soc.* **140**, 5784–5790 (2018).

147. Zlotnick, A. & Mukhopadhyay, S. Virus assembly, allostery and antivirals. *Trends Microbiol.* **19**, 14–23 (2011).

148. Singh, S. & Zlotnick, A. Observed hysteresis of virus capsid disassembly is implicit in kinetic models of assembly. *J. Biol. Chem.* **278**, 18249–18255 (2003).

149. Bothner, B., Dong, X. F., Bibbs, L., Johnson, J. E. & Siuzdak, G. Evidence of viral capsid dynamics using limited proteolysis mass spectrometry. *J. Biol. Chem.* **273**, 673–676 (1998).

Chapter II.

Analysis and development of novel techniques for the screening of CAM's mode of action

II.1 Introduction

The first assay considered for the adaptation of inflow analysis was the HBc capsid assembly assay introduced by Zlotnick.[1] Capsid assembly has not seen many applications in the microfluidic format despiting displaying promising characteristics including faster kinetics, homogeneous assay formats, and a strong sensitivity towards CAM.[2,3] Furthermore CAMs display multifunctionality in the virus lifecycle and activity against both wildtype and nucleotide analog resistant HBV strains.[4]

These compound classes are categorized into two classes based on their mode of action: capsid assembly modulator-aberrant (CAM-A) and capsid assembly modulators-normal (CAM-N).[5] Both types of CAM bind to the same pocket as allosteric modulators at the dimer-dimer interface, which mainly consists of non-polar amino acids. However, CAM-A and CAM-N are located in different quasi-equivalent locations leading to the assembly polymorphism.[6,7] CAM-N compounds stabilize protein-protein interactions, accelerating the spontaneous self-assembly of nucleocapsids and prevent the encapsidation of the viral pgRNA-polymerase complex. The resulting capsids assemble without viral DNA and are non-infectious.[5,8–12] On the other hand, CAM-A distorts the dimer-dimer binding geometry and misdirects the assembly, resulting in defect capsids aggregating to larger protein constructs. Contrary to the regular capsids, these structures are prone to proteasomal degradation and intracellular clearance.[8,13–16] The exact molecular mechanism leading to the different morphologies of the CAM assembled products is not yet entirely understood.[17] However, it is known that the -2 kcal/mol stronger association energy in the case of CAM-A also accelerates the assembly reaction, which often leads to kinetic traps by enhancing the nucleation step of the assembly process.[18–20] Furthermore, changing the biophysical environment of the assembly reaction has also shown a substantial impact on the assembly reaction. While HAPs lead to the formation of aggregates at weaker association energies, the presence of higher NaCl concentrations prevented this effect leading to morphological intact capsid formations.[21] Finally, some CAMs were found not only to accelerate assembly but simultaneously disassemble HBc capsids in a dose-dependent manner. One plausible explanation was that while these compounds were locally supporting the assembly, the slightly shifted binding angle led to an overall "straining" and destabilization of the capsid.[22,23]

Since the first discovery of BAY 41-4109 (CAM-A) in 2003, a substantial amount of work was invested in the development of novel CAMs. BAY 41-4109 inhibits HBV DNA replication in HepG2.2.15 cell lines with an EC_{50} of 0.054 µM.[24] Furthermore, it sustained virological response in an *in vivo* HBV mouse model, with a reduction of both serum HBV DNA levels and HBV antigens (HBeAg and HBsAg), making BAY 41-4109 a favorable candidate.[16] Despite its initial toxicological profile *in vivo,* HAP-based CAM-As were never given up due to their unique mode of action, leading to the research of bioavailable HAPs and culminating in the administration of BAY 41-4109, RO-7049389, GLS4JHS to clinical trials.[16,25,26]

Many further studies were performed based on the structure-based virtual screening with the Kwon HAP_R01 ligand leading to further findings.[27] The next class of CAMs characterized were phenylpropenamides with the two potent compounds AT130 and AT-61, that selectively inhibited viral pgRNA packaging in earlier studies but formed regular capsids instead of the aberrant ones.[28] Shortly after, the sulfamoylbenzamides (SBA) were identified from high throughput screening approaches as CAM-N.[26,29] SBA represents the chemical CAM class with the highest number of compounds, including recently KR-26556. [30] Aside from these three large CAM classes, several other types were classified and investigated over the last 20 years, including benzamide derivatives,[31] dibenzothiazepine (DBT1),[22] pyridazinone derivative,[32] pyrazolyl-thiazoles,[8] pyrazolo piperidine,[33] phenylpropenamides,[5] sulfamoylpyrroloamides (SPAs), glyoxamide-pyrrolamides,[8] dibenzo-thiazepin-2-ones,[8] phenylpiperidine-3-carboxamides,[34] isothiafludin[31] ZW-1841, and ZW-1847,[27] glyoxamide derivatives,[35] GLP-26,[35] and indole-2-carboxamides.[4] Even though no CAM has yet been approved as a drug, several compounds are currently in clinical trials, including AB-423/ AB-506, JNJ6379/ JNJ0440, CAM-N JNJ-56136379,[36] NVR 3-778,[26] ABi-H0731/ ABi-

H2158, NZ-4, RG7907, QL-007 and the CAM-A type compounds BAY 41-4109, RO-7049389, GLS4JHS.[26]

There is still an unmet medical need to discover novel, efficacious CAM scaffolds HBV drugs with an altered mode of action. In this sense, this chapter focuses on evaluating and improving various analytical methods to facilitate the CAMs and their mode of actions recognition.

II.2 Aim of the work

One of the objectives of VIRO-FLOW was the optimization of HBc assembly assays. In this chapter, several analytical methods were evaluated and tested to determine the CAM's mode of action in a fast, economical, reproducible, and accurate manner. Three different procedures were envisioned to update the HBc assembly assay: Size-dependent filtration, CAM-A selective proteolytic degradation, and CAM-A selective disassembly. Furthermore, the target protein in the assay was varied by employing CAM-A or CAM-N selective CP150C mutant, including the mutation, expression, and purification of the new targets. With these CP150C variants, a CAM-A or -N specific HBc assay could be developed. As alternatives to the microtiter formats, biophysical methods were employed with the focus on three different methods: dynamic light scattering (DLS), fluorescence anisotropy (FA), and fluorescence correlation spectroscopy (FCS). In the end, the objective was to distinguish the CAMs' mode of action based on the protein products' homogeneity, light intensity, size distribution, and Brownian motion.

II.3 Methods

Table 1: Overview of materials used in chapter II. More details and materials are listed in the respective subchapters.

	Chemicals/ equipment	**CAS number, providor, article number**
Chemicals	Fluorescein isothiocyanate (FITC)	Merck, Buchs, Switzerland CAS: 518-47-8
	5,6-Carboxyfluorescein	Merck, Buchs, Switzerland CAS: 72088-94-9
	50 mM HEPES buffer ph 7.4	Merck, Buchs, Switzerland CAS: 7365-45-9
	NaCl	Merck, Buchs, Switzerland CAS: 7647-14-5
	Tetradecane	Merck, Buchs, Switzerland CAS: 629-59-4
	$SPAN_{20}$	Merck, Buchs, Switzerland CAS: 1338-39-2
	FC770	Merck, Buchs, Switzerland CAS: 1093615-61-2
	SBA	Synthesized as described in Corcuera et al.[8]
	JNJ 56136349	Synthesized as described in Corcuera et al.[8,36]
	BAY 41-4109	Synthesized at Bayer AG Wuppertal Germany
	GLS4	Synthesized at Vandyck
	CP150-BO (3 µM)	Expressed, purified, and labeled at AiCuris Anti-infective Cures AG, Wuppertal, Germany (Experiment HBV 2019-74)
Consumable materials	Assay Plate, 384 Well, Low Volume, Black Round Bottom	Corning Incorporated, Kaiserslautern, Germany Product Number 4514
	Microplate, 96 Well, PS, U-BOTTOM, CLEAR	Greiner Bio-One GmbH, Solingen, Germany Product number: M0812-100EA
Laboratory equipment	ClARIOstar	BMG Labtech, Ortenberg, Germany SN: 01044
	BIOHIT 300 µl Handpipet	VWR international GmbH, Darmstadt, Germany SN: 227481
	HAMILTON MICROLAB STAR	Hamilton Germany GmbH, Gräfelfing, Germany SN: 00423
	Integra 12.5 µl Pipets	VWR international GmbH, Darmstadt, Germany SN: 6006558

II.3.1 Mutagenesis of CAM selective CP150C proteins

Table 2: Materials and consumables used for the selective mutagenesis of the CAM selective CP150C dimers.

	Chemicals/ equipment	**CAS number, providor, article number**
Antibiotics	Ampicillin (amp) (Stock solution) (100 mg/ml)	VWR Life Science, Bruchsal, Germany For 2 ml Solve 200 mg amp in 2 ml H_2O
	Chloramphenicol (Ca) (Stock solution) (35 mg/ml)	Carl Roth GmbH & Co. KG, Karlsruhe, Germany For 2 ml Solve 70 mg Ca in 2 ml 100 % EtOH
Various stock solutions	Isopropyl β-D-1-thiogalactopyranoside (IPTG) (10 mM)	Merck, Buchs, Switzerland Solve 4.76 mg IPTG in 2 ml H_2O
	X-Gal (2 %)	Merck, Buchs, Switzerland For 2 ml Solve 20 mg X-Gal in 2 ml DMF
Media	LB-Stock solution	For 400 ml 16 g Difco^{TM} LB AGAR, Miller (REF 244520) Solve in 400 ml purified water Autoclave the medium
	LB-amp-Agar	300 ml LB-Agar medium were melted using the microwave 300 µl amp (100 mg/ml) were added
	SOC Medium	ThermoFischer SCIENTIFIC GmbH, Darmstadt, Germany Catalog number: 15544034
Plasmids / Vectors	pET CP150C (9 ng/µl)	AiCuris Anti-infective Cures AG, Wuppertal, Germany [8]
	pUC18	Merck, Buchs, Switzerland CAS Number: 9007-49-2
	pWhitescript	Merck, Buchs, Switzerland
QuickChange Lightning Site-Directed Mutagenesis Kit	QuickChange Lightning Enzyme	Agilent Technologies, Inc, Frankfurth am Main, Germany
	10x QuikChange Lightning buffer	Agilent Technologies, Inc, Frankfurth am Main, Germany
	dNTP mix	Agilent Technologies, Inc, Frankfurth am Main, Germany
	QuikSolution reagent	Agilent Technologies, Inc, Frankfurth am Main, Germany
	*Dpn*I restriction enzyme	Agilent Technologies, Inc, Frankfurth am Main, Germany
	pWhitescript 4.5 kb control plasmid	Agilent Technologies, Inc, Frankfurth am Main, Germany (5 ng/µl)
	Forward Primer (FW) Primer 1	5’-CCA TGA TTA CGC CAA GCG CGC AAT TAA CCC TCA C-3’
	Reverse Primer (RW) Primer 2	5’-GTG AGG GTT AAT TGC GCG CTT GGC GTA ATC ATG G-3’
	XL10-Gold ultracompetent cells	Agilent Technologies, Inc, Frankfurth am Main, Germany Catalog number: 200315
	XL10-Gold ß-mercaptoethanol mix (ß-ME)	Agilent Technologies, Inc, Frankfurth am Main, Germany Catalog number: 200517

	pUC18 control plasmid (0.1 ng/µl in TE buffer)	Agilent Technologies, Inc, Frankfurth am Main, Germany Catalog number: SD0051
Primers (Conc: 100 µM)	Primer 3 5' CP150C_D29G	5’-TCC GAG CGT TCG TGG TCT GCT GGA TAC CG-3’
	Primer 4 3'CP150C_D29 G	5’-CGG TAT CCA GCA GAC CAC GAA CGC TCG GA-3’
	Primer 5 5' CP150C_L30F	5’-GAG CGT TCG TGA TCT GTT CGA TAC CGC AGC AGC AC-3’
	Primer 6 3' CP150C_L30F	5’-GTG CTG CTG CGG TAT CGA ACA GAT CAC GAA CGC TC-3’
	Primer 7 5' CP150C_T33P	5’-CGT TCG TGA TCT GCT GGA TCC GGC AGC AGC ACT-3’
	Primer 8 3' CP150C_T33P	5’-AGT GCT GCT GCC GGA TCC AGC AGA TCA CGA ACG-3’
	Primer 3 V124G forward Primer (Conc: 100 µM)	5’-CTG GTT AGC TTT GGT GGT TGG ATT CGT ACC CCT C-3’
	Primer 4 V124G reverse Primer (Conc: 100 µM)	GAG GGG TAC GAA TCC AAC CAC CAA AGC TAA CCA G-3’
	Primer 3 T33N Forward Primer (Conc: 100 µM)	5’-CGT TCG TGA TCT GCT GGA TAA CGC AGC AGC AC-3’
	Primer 4 T33N Reverse Primer (Conc: 100 µM)	5’-GTG CTG CTG CGT TAT CCA GCA GAT CAC GAA CG-3’
	Primer 5 T109I Forward Primer (Conc: 100 µM)	5’-CAT ATT TCA GCA CTG ATC TTT GGT CGT GAA ACC G-3’
	Primer 6 T109I Reverse Primer (Conc: 100 µM)	5’-CGG TTT CAC GAC CAA AGA TCA GTG CTG AAA TAT G-3’

Mutant Strand Synthesis Reaction (Thermal Cycling)

The solutions' preparation and reactions' execution were performed according to Agilent’s instructions. The pET CP150C, coding for the truncated CP150C protein, was diluted to a concentration of 9 ng/µl. Next, the primers synthesized by Metabion (Table 1 and Table 2) were solved in dd H_2O to a final concentration of 100 µM, and initial PCR reactions were prepared in thin-walled tubes with various primer concentrations to determine the optimal reaction settings (Table 3). Finally, the PCR cycles were performed according to Table 4. The best performance was mostly obtained using 50 ng pET CP150C concentrations used in all future experiments.

Table 3: Composition of the samples and controls for the mutagenesis.

Substances	**pWhitescript mutagenesis control**	**Negative control (H_2O)**	**Sample 4**	**Sample 3**	**Sample 2**	**Sample 1**
10xReaction buffer	5 µl	5 µl	5 µl	5 µl	5 µl	5 µl
Plasmid	5 µl pWhitscript 4.5 kb	5 µl H_2O	**100 ng** 11 µl pET CP150C	**50 ng** 5.5 µl pET CP150C	**25 ng** 2.7 µl pET CP150C	**10 ng** 1.1 µl pET CP150C
Oligonucleotide control primer fw	1.25 µl (125 ng) primer 1	1.25 µl (125 ng) primer 3	1.25 µl primer 3	1.25 µl primer 3	1.25 µl primer 3	1.25 µl primer 3
Oligonucleotide control primer rw	1.25 µl (125 ng) primer 2	1.25 µl primer 4	1.25 µl primer 4	1.25 µl primer 4	1.25 µl primer 4	1.25 µl primer 4
dNTP mix	1 µl	1 µl	1 µl	1 µl	1 µl	1 µl
QuickSolution reagent	1.5 µl	1.5 µl	1.5 µl	1.5 µl	1.5 µl	1.5 µl
ddH$_2$O (fill up to 50 µl)	34 µl	34 µl	28 µl	33.5 µl	36.3 µl	37.9 µl
QuickChange Lightning Enzyme	1 µl	1 µl	1 µl	1 µl	1 µl	1 µl

Table 4: Program used for the PCR in Table 3.

Segment	**Cycles**	**Temperature**	**Time**
1	1	95 °C	2 min
2	18	95 °C	20 s
		60 °C	10 s
		68 °C	30 s/kb plasmid length (3 min)
3	1	68 °C	5 min
4	1	4 °C	hold

The products were evaluated with a *Dpn*I restriction analysis, followed by a 1.5 % agarose gel plotting before and after *Dpn*I. Successfully mutated plasmids were transformed into *E. coli* XL150-Gold ultracompetent cells using heat pulse transformation in a 42 °C water bath for 30 s. After 1 h incubation in SOC medium, the bacteria were spread on LB-amp agar plates containing amp (100 mg/ml) and Ca (35 mg/ml) and further incubated for 17 h. Following two days of the growing period, up to 6 colonies per mutant were picked and incubated in the liquid media at 37 °C and 200 rpm overnight. Small amounts of Plasmid DNA were harvested from the cultures with the QuickLyse Miniprep kit according to the manufacturer's description. The DNA was sequenced by GATC Biotech, verifying the nucleotide substitution, which was verified by the alignment between the mutants. Hence one replicate per mutant was chosen for further DNA amplification repeating the transformation, incubation, and harvesting steps described above on a larger scale.

II.3.2 Expression of CAM selective CP150C proteins in *E. coli* Rosetta2 (DE3) competent cells

Table 5: Materials and consumables used in the expression of the CAM selective CP150C mutants.

	Chemicals/ equipment	**CAS number, industry, article number**
Antibiotics	Ampicillin (stock solution) (100 mg/ml)	VWR Life Science, Bruchsal, Germany LOT 17F295303
	Chloramphenicol (stock solution) (35 mg/ml)	Carl Roth GmbH & Co. KG, Karlsruhe, Germany For 2 ml Solve 70 mg chloramphenicol in 2 ml 100 % EtOH ArtN: 6295.2
	Carbenicillin (cb) (stock solution) (100 mg/ml)	Carl Roth GmbH & Co. KG, Karlsruhe, Germany For 2 ml Solve 200 mg cb in 2 ml H_2O LOT: 700150G
Various stock solutions	IPTG (1 M)	Merck, Buchs, Switzerland CAS 367-93-1
	X-Gal (2 %)	Merck, Buchs, Switzerland For 2 ml Solve 20 mg X-Gal in 2 ml DMF CAS: 7240-90-6
	50 % Glucose solution	Merck, Buchs, Switzerland For 500 ml Solve 250 g Glucose in 500 ml H_2O CAS: 50-99-7
Media	LB-Stock solution (4x1 l in 2 l Falcon tube)	Merck, Buchs, Switzerland For 1 l 10 g Difco^{TM} LB AGAR, Miller (REF 244520) Solve in 1 l purified water Autoclave the medium
	LB-Amp-Agar	Merck, Buchs, Switzerland 300 ml LB-Agar medium were melted using the microwave 300 µl amp (100 mg/ml) were added
	SOC Medium	ThermoFischer SCIENTIFIC GmbH, Darmstadt, Germany catalog number: 15544034
Plasmids/ Vectors	pET CP150C V124G (420 ng/µl)	II.3.2 Expression of CAM selective CP150C proteins in *E. coli* Rosetta2 *(*DE3*)* competent cells
	pET CP150C T109I (113 ng/µl)	
Cells	Rosetta^{TM} 2(DE3) Singles^{TM} Competent	Novagen Inc, Wisconsin, USA LOT M00008379
Centrifuges	SORVALL RC 3C HPlus Rotortyp: HG000A/HBBG	ThermoFischer SCIENTIFIC GmbH, Darmstadt, Germany
	Rotortyp: JA-10, JA-17	

E. coli Rosetta2 (DE3) is a BL21 derivate designed to enhance the expression of eukaryotic proteins that require rarely used codons in *E. coli*. This cell line carries 7 rare codons on a Ca resistance plasmid and a chromosomal copy of the

T7 RNA polymerase gene under the control of the *lac*UV5 promotor. Therefore, it is suitable to express proteins from pET vectors by induction with IPTG. Hence, the synthesized pET CP150C mutant constructs were transformed into the *E. coli* DE3 expression cell line using a heat pulse at 42 °C for 30 s according to the description of the cell lines.

Following the transformation, the bacteria were spread on preheated LB-cam (35 µg/ml)-amp (100 µg/ml) agar plates and were incubated for 14 h at 37 °C. Next, precultures were prepared by inoculating two 4 ml LB medium containing 35 µl/ml ca, and 100 µl/ml cb, respectively. After 8 h incubation at 37 °C, 1 ml of the preculture were used to inoculate 2x100 ml LB-medium (35 µl/ml ca/ 100 µl/ml CB) overnight cultures which were further incubated at 37 °C/200 rpm for 14 h.

Finally, LB media was prepared with the respective antibiotics and glucose (100 µg/µl Cb, 35 µg/µl Ca, 2 % Glucose), which was inoculated with the overnight cultures to an OD of 0.1 (around 30 ml of the overnight cultures respectively). The bacteria were kept at 37 °C, 120 rpm until an OD of around 0.5 was reached signaling that the bacteria reached the logarithmic growth phase. The protein expression was induced with 2 ml 1 M IPTG (2 mM final concentration), and the cultures were further incubated at 37 °C, 120 rpm for 3 h. Finally, the cells were harvested and centrifuged at 5,000 g, 4 °C for 20 min. The supernatant was discarded, and the pellets were resolved in remaining LB media and transferred into 50 ml falcon tubes which were centrifuged again for 20 min at 5,000 g, 4 °C. The final pellets containing the protein of interest were stored at -80 °C until purification.

II.3.3 Purification of CAM selective CP150C proteins using a series of size exclusion- and affinity columns

Table 6: Materials and consumables used for the purification of the CAM selective CP150c mutants.

	Materials and consumables	**Composition/ location /company**
Chemicals/ Protein used for the biochemical assay	Ammonium sulfate (up to 40 % saturation)	Merck, Buchs, Switzerland CAS: 7783-20-2 At 4 °C 0.23 g AS/ml
	$CaCl_2$	Merck, Buchs, Switzerland CAS: 10043-52-4
	EDTA	Merck, Buchs, Switzerland CAS 6381-92-6
	DTT	Merck, Buchs, Switzerland CAS: 3483-12-3
	HEPES buffer 50 mM HEPES, pH 7.5 5 mM DTT	For 1.8 l 90 ml HEPES, pH 7.5 1.38 g DTT 1.71 l ddH_2O CAS (HEPES): 7365-45-9
	Tris buffer	Merck, Buchs, Switzerland Catalog number: 3535773
	5 M NaCl	Merck, Buchs, Switzerland For 50 ml 14.61 g NaCl Fill up to 50 ml with 50 mM HEPES.
	$NaCO_3$	Merck, Buchs, Switzerland CAS: 207-838-8
	Mercaptoethanol	Merck, Buchs, Switzerland CAS: 60-24-2
	Urea 2 M	Merck, Buchs, Switzerland CAS: 200-315-5 2.09 g per 10 ml solution under constant stirring on ice
	Urea 8 M	Merck, Buchs, Switzerland Add 5.57 g urea per 10 ml solution under constant stirring on ice
Buffers	**Buffer A** 100 mM Tris, pH 7.5 100 mM NaCl 2 mM DTT Filter-sterilized	For 1 l 100 mL 1 M Tris, pH 7.5 20 mL 5 M NaCl 0.309 g DTT 880 mL ddH_2O
	Buffer N, pH 9.6 50 mM $NaHCO_3$ 5 mM DTT Filter-sterilized	For 5 L 21 g $NaHCO_3$ 3.86 g DTT 4.99 l ddH_2O 8-10 mL 10 M NaOH
	HEPES buffer 50 mM HEPES pH 7.5 5 mM DTT	Merck, Buchs, Switzerland For 1.8 l 90 ml HEPES, pH 7.5 1.38 g DTT Fill up with ddH_2O
	Cell lysis buffer Qproteome Bacterial Protein Prep Kit, QIAGEN 37900	QIAGEN, Hilden, Germany 10 mL lysis buffer 100 uL lysozyme (60 mg lysozyme + 600 uL lysis buffer) + 10 uL benzonase

Laboratory equipment	ÄKTA System	Amersham Biosciences Europe GmbH, Freiburg im Breisgau, Germany SN: 18130000-001241
	Sephacryl^{TM} S-300 HR	Merck, Buchs, Switzerland (lot 10217242)
	CaptoCore700	Merck, Buchs, Switzerland (GE17-5481-01)
	Stirred cell 400 ml	Merck, Buchs, Switzerland Amicon CN: UFSC40001
Consumable materials	Lysis buffer QIAGEN	QIAGEN, Hilden, Germany SKU 60-00050-11
	Ultrafiltration Discs Ultracel 10 KDa	Corning Incorporated, Kaiserslautern, Germany Millipore 13642
Chemicals, consumable materials used for sodium dodecyl sulfate (SDS)-polyacrylamide gel electrophoresis (PAGE)	MES-SDS Running buffer (20x)	Alfa Aesar GmbH & Co KG, Karlsruhe, Germany (LOT: U19C512)
	MES-SDS running buffer (1x)	For 2 l 100 ml MES-SDS Running Buffer (20x) 1900 ml H_2O
	NuPAGE^{TM} 4-12 % Bis-Tris Gel	Invitrogen, Waltham, USA (LOT: 18022671)
	NuPAGE^{R} LDS Sample Buffer (4x)	Invitrogen, Waltham, USA (LOT: 1771590)
	SeeBluePlus2 Prestained Standard	Invitrogen, Waltham, USA (LOT: 1929090)
	Comassie Stain Solution 1x Solution	Bio-Rad Laboratories, Feldkirchen, Germany 63722A

The *E. coli* pellets obtained from the protein expressions were lysed with Qproteome Bacterial Lysis buffer from QIAGEN according to the manufacturer's description. The broken-down cell pellets were resuspended in 250 ml Lysis buffer and incubated on ice for 30 min. Undesired components and membrane proteins were removed with centrifugation at 14,000 g, 4 °C for 30 min with JA-12 centrifuge head, and the proteins in the supernatant (70 ml) were salted out by adding ammonium sulfate (0.23 g AS/ml) under slow stirring at 4 °C with a final incubation for 1 h. The obtained muddy solution was centrifuged at 25,000 g, 4 °C for 1 h with JA-17 centrifuge to gain the protein pellets.

Pellets were resuspended in buffer A until an OD280 between 6-8 was reached**.** The resulting solutions were centrifuged at 25,000 g, 4 °C for 15 min with a JA-17 centrifuge head. The supernatant was filtered (0.45 µm filter) and loaded onto the preequilibrated (with 2x5 volume buffer A) CaptoCore 700 column. The assembled capsids were separated in the affinity column using the ÄKTA 10 S system. After every column chromatography, the sample's UV spectrum at

280 nm was analyzed to find the protein peaks of interest. Furthermore, the presence of the protein in the peak fractions was verified using sodium dodecyl sulfate - polyacrylamide gel electrophoresis (SDS-PAGE). (Figure 7 and Figure 8). After the cross-validation, the first two fractions (A1 and A2) containing the protein of interest were pooled and dialyzed overnight at 4 °C in buffer N.

The CP150C capsids from the pooled fractions were disassembled using 4.8 g Urea which was added slowly to the 23 ml protein solution collected from the dialysis. After 1.5 h of incubation on ice, the protein solution was filtered (0.45 µm filter) and loaded onto the preequilibrated Sephacryl S300 column. The purification program was used with a Sephacryl S300 1 l F950 column, buffer N, flowrates of 3 ml/min, and a pressure Limit 0.77 MPa (Figure 9 and Figure 10). Again, the presence of CP150C in peak fractions was validated with SDS-PAGE (Figure 11). The peak fractions containing the main volumes of CP150C were pooled, and the resulting solution was concentrated with two Amicon Centricons (10 MWCO) until a final concentration of 5.7 mg/ml and a volume of 24.5 ml was reached, followed by final dialysis in HEPES buffer overnight at 4 °C.

The two-column chromatography steps were repeated a second time (Figure 12 to Figure 15) to increase the proportion of assembly competent proteins. After completing the purification protocol, 28 ml of CP150C (wildtype) with a 1.7 mg/ml concentration were obtained.

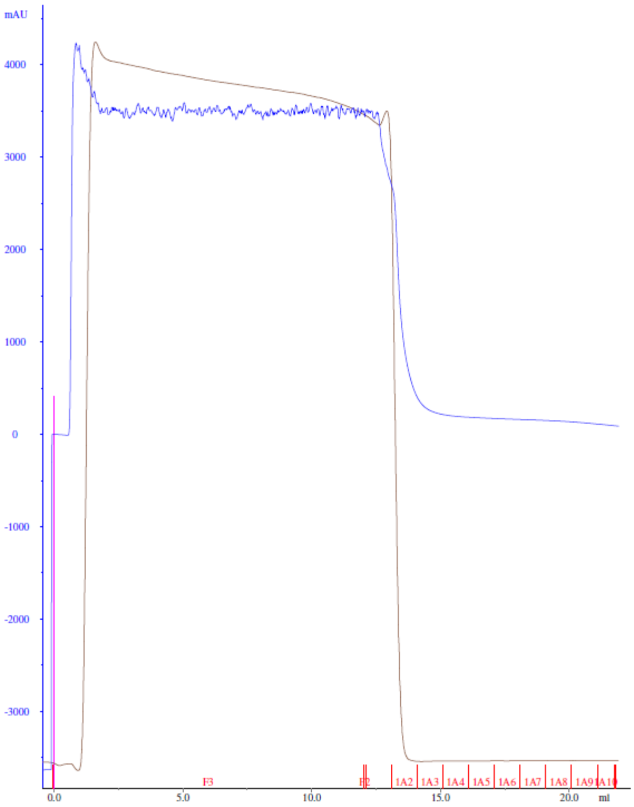

Figure 7 Elution profile of CP150C capsids from the first CaptoCore700 column. The absorption of the protein was displayed in mAU (blue graph) determined by UV absorption at a wavelength of 280 nm. Protein fractions were aliquoted in 1 ml samples which are displayed on the x-axis marked by red letters. The sample injection is marked purple at 0 ml. Approximately 19 ml protein solution was eluted using Tris buffer (pH 7.5) with 100 mM NaCl and 2 mM DTT at room temperature.

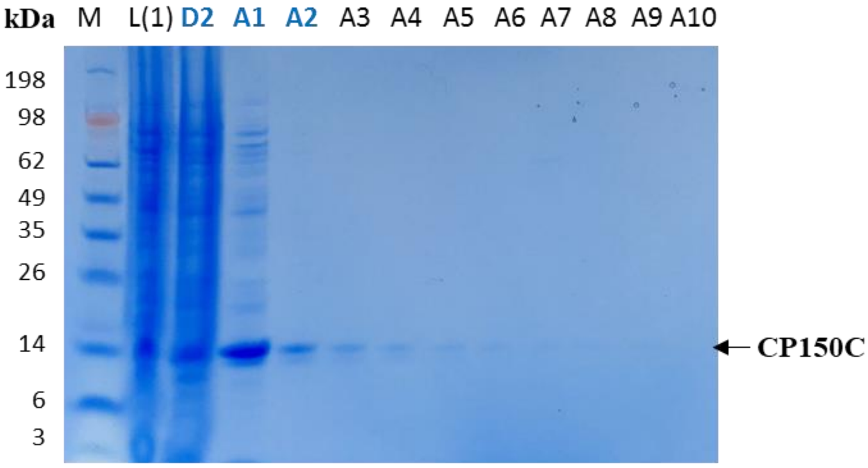

Figure 8 SDS-PAGE analysis of the different fractions from the first CaptoCore700 column. M: Molecular weight marker. Line L(1): Loading sample. Line D2= flow through, Line A1-A10: Sample Fractions. According to the Coomassie blue staining fractions D2-A2 (marked blue) exhibited the highest protein concentration at the 14 kDa marker and were pooled together.

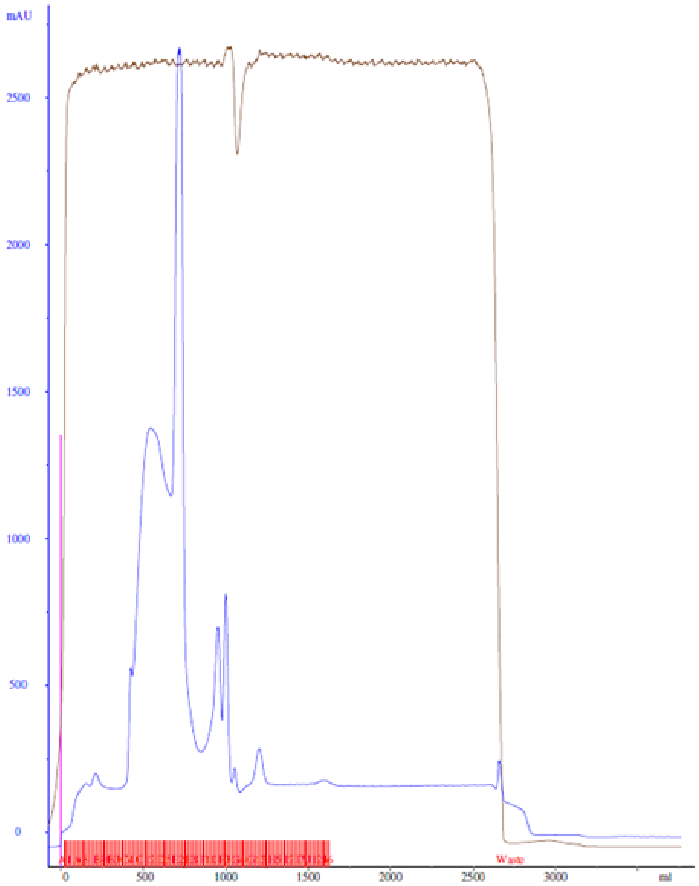

Figure 9 Elution profile of CP150C dimers from the first Sephacryl$^{\text{TM}}$ S300 HR column. The absorption of the protein was displayed in mAU (blue graph) determined by UV absorption at a wavelength of 280 nm. Protein fractions were aliquoted in 2 ml samples which are displayed on the x-axis marked by red letters. The sample injection is marked purple at 0 ml. Approximately 104 ml protein solution was eluted using $NaHCO_3$ buffer (pH 9.6) with 5 mM DTT at 4 °C.

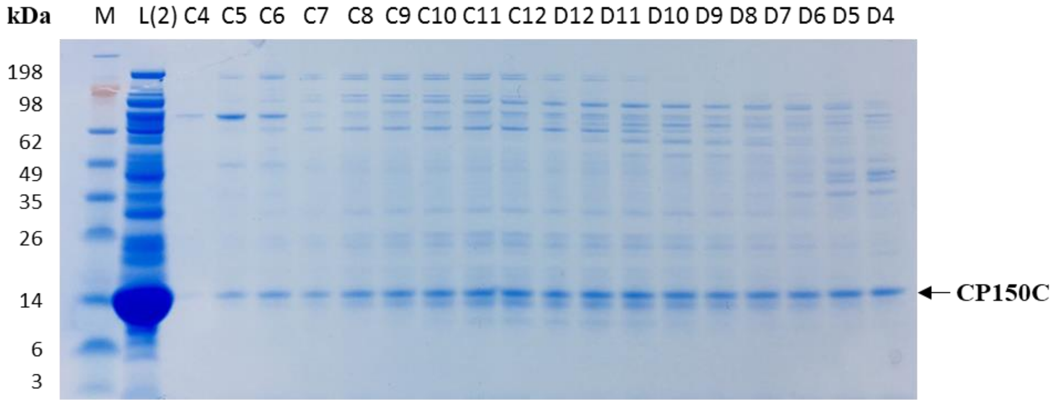

Figure 10 SDS-PAGE analysis of the different fractions from the First Sephacryl$^{\text{TM}}$ S300 HR column. M: Molecular weight marker. Line L(2): Loading sample, Line C4-D4: Sample Fractions. Displayed are the first 18 fractions with yet clear contamination of other cellular proteins. Therefore, these fractions were disregarded. In Figure 11 the remaining fractions are displayed containing the CP150C protein.

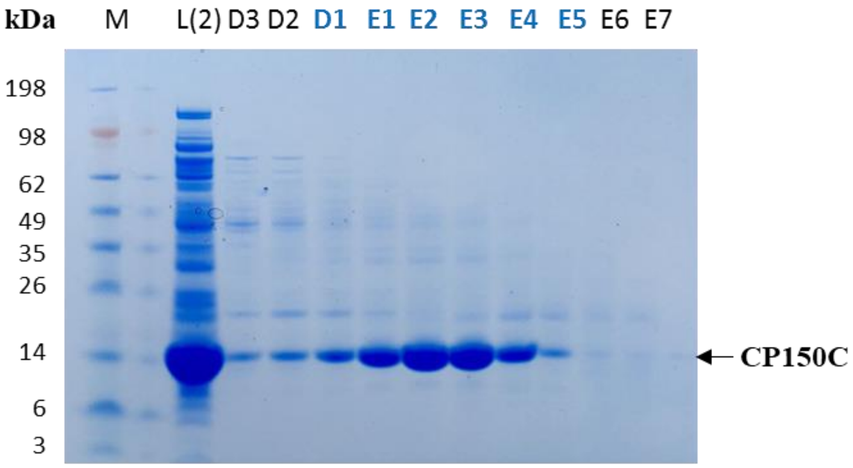

Figure 11 SDS-PAGE analysis of the different fractions from the First Sephacryl™ S300 HR column. M: Molecular weight marker. Line L(2): Loading sample, Line D3-E7: Sample Fractions. According to the Coomassie blue staining fractions D1-E5 (marked blue) exhibited the highest protein concentration at the 14 kDa marker and were pooled together.

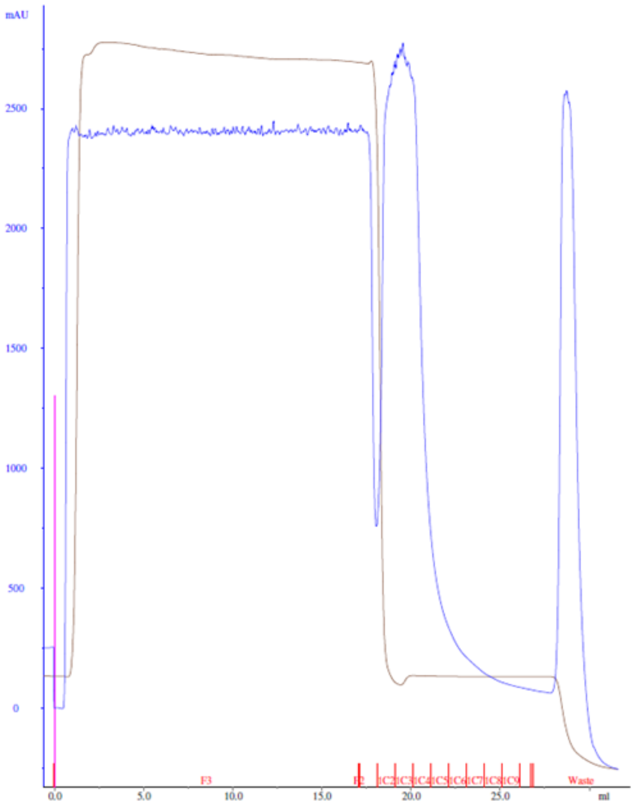

Figure 12 Elution profile of CP150C capsids from the second CaptoCore700 column.
The absorption of the protein was displayed in mAU (blue graph) determined by UV absorption at a wavelength of 280 nm. Protein fractions were aliquoted in 1 ml samples which are displayed on the x-axis marked by red letters. The sample injection is marked purple at 0 ml. Approximately 24 ml protein solution was eluted using Tris buffer (pH 7.5) with 100 mM NaCl and 2 mM DTT at room temperature.

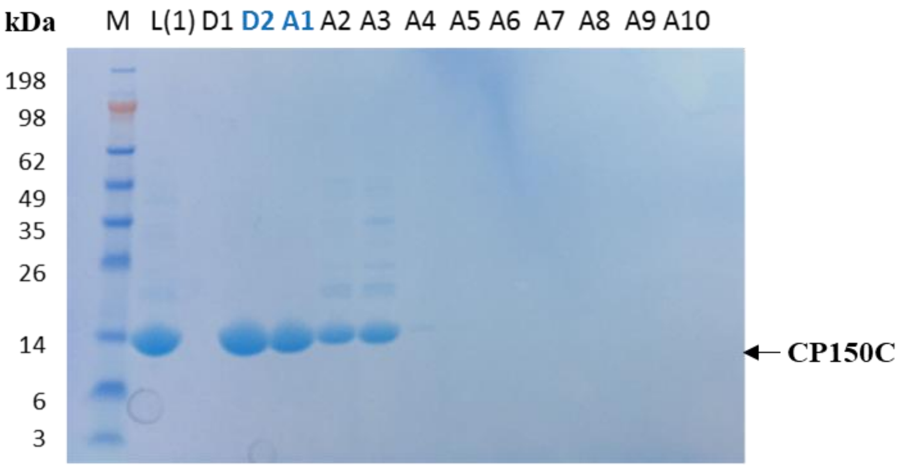

Figure 13: SDS-PAGE analysis of the different fractions from the Second CaptoCore700 column M: Molecular weight marker. Line L(1): Loading sample. Line D1: Solvent flow through. Line D2= Sample flow through, Line A1-A10: Sample Fractions. According to the Coomassie blue staining fractions D2-A2 (marked blue) exhibited the highest protein concentration at the 14 kDa marker and were pooled together.

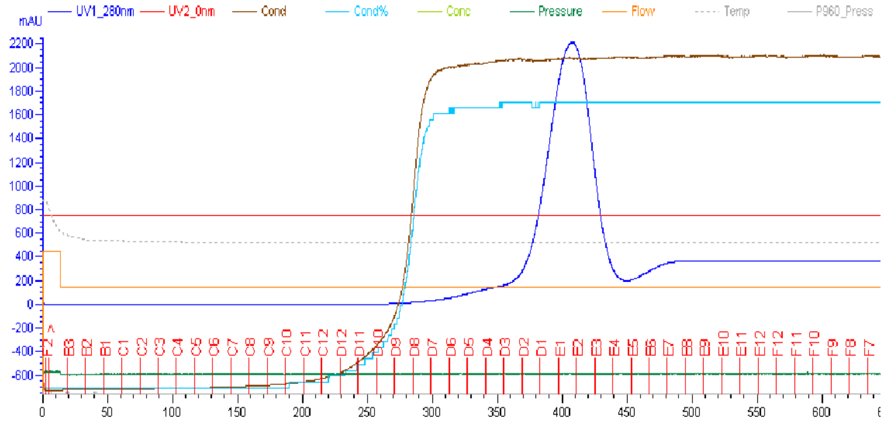

Figure 14: Elution profile of CP150C dimers from the second Sephacryl^{TM} S300 HR column. The absorption of the protein was displayed in mAU (blue graph) determined by UV absorption at a wavelength of 280 nm. Protein fractions were aliquoted in 2 ml samples which are displayed on the x-axis marked by red letters. Approximately 112 ml protein solution was eluted using $NaHCO_3$ buffer (pH 9.6) with 5 mM DTT at 4 °C.

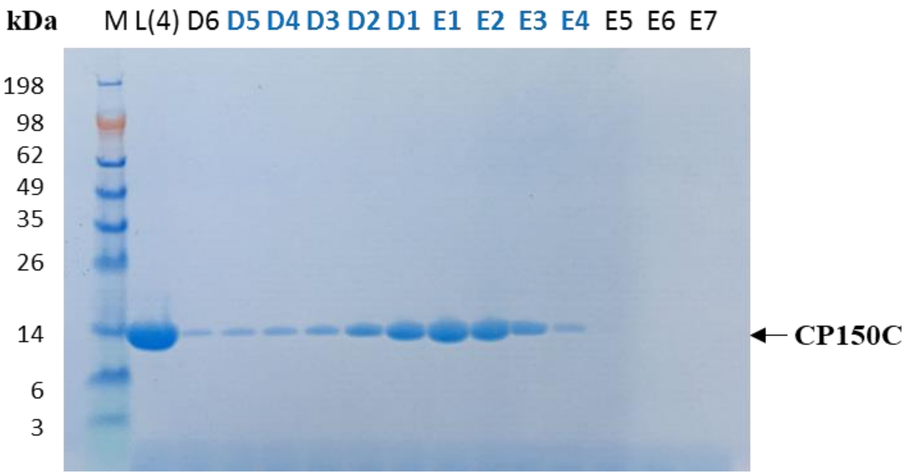

Figure 15: SDS-PAGE analysis of the different fractions from the Second Sephacryl^{TM} S300 HR column. M: Molecular weight marker. Line L(1): Loading sample, Line D6-E7: Sample Fractions. According to the Coomassie blue staining fractions D5-E4 (marked blue) exhibited the highest protein concentration at the 14 kDa marker and were pooled together.

Given the high consensus between the amino acid sequence of the mutants and the CP150C protein, it was assumed that differences in size and physical properties should be minimal. Therefore, the standard CP150C purification protocol was used for the mutants. However, since during the initial purification only insignificant amounts of protein were purified several novel protocols were developed and evaluated.

Cell lysis and HBV-CP150C-F110I purification from inclusion bodies by a multistep dialysis

For the purification of the two HBV-CP150C mutants F110I and P25S, several different purification methods were evaluated. The lysis of the bacterial pellets was performed as described above until the first centrifugation step at 14,000 g, 4 °C for 30 min in UZ. The location of the CP150-BO mutants was determined by analyzing the contents of the supernatant and the cell pellets. First, to harvest protein dimers from the pellets, multistep urea dialysis was performed. The pellets were solved in 160 ml dissociation buffer (8 M urea, 200 mM NaCl, 50 mM sodium carbonate, 10 mM 2-mercaptoethanol, pH 9.5) and incubated overnight at 4 °C. In the next step, the solution was dialyzed in a 2 M urea buffer (2 M urea, 200 mM NaCl, 50 mM sodium carbonate, 10 mM 2-

mercaptoethanol, pH 9.5) for 4.5 h at 4 °C followed by a final dialysis in a 0.5 M urea buffer (0.5 M urea, 150 mM NaCl, 100 mM TRIS, 2 mM DTT, 1 mM EDTA, 10 mM $CaCl_2$ pH 9.5) for 4.5 h at 4 °C. Lastly, the urea was completely removed via dialysis in a Tris buffer (100 mM Tris, 150 mM NaCl, 1 mM EDTA, 10 mM $CaCl_2$ pH9.5) overnight at 4 °C. A Sorensen buffer system was prepared to solubilize the proteins, and the 0.5 mg/ml proteins were added to 1.8 ml of the buffer solution, respectively. After incubation at 30 °C for 1 h, the samples were pelleted using a centrifuge at 13,000 g for 1 h.

Ammonium sulfate precipitation of HBV-CP150C-F110I from inclusion bodies and the cytosol

The handling of the protein was performed constantly at 4 °C to prevent denaturation. The precipitation from the cytosol was performed using ammonium sulfate 36.8 g (0.23 g AS/ml), which was added slowly (over 30 min) to the dialyzed cell pellet solution under constant stirring. The solution was incubated for 1 h, and the proteins were pelleted with centrifugation at 25,000 g, for another 1 h with the ultracentrifuge. The obtained protein pellets were stored over 4 days. Afterward, the proteins of interest could not be precipitated from the inclusion bodies nor from the cytosol using 40 % ammonium sulfate. Therefore, the concentration of ammonium sulfate was increased stepwise to find the right conditions for HBV-CP150C-F110I precipitation. Sample solutions (2 ml) were prepared from the supernatants of the 40 % ammonium sulfate precipitations (dialyzed cell pellets and lysed cell supernatants), and ammonium sulfate was added slowly under constant stirring for 1 h. Finally, the proteins were pelleted by centrifugation at 13,900 g for 1 h and analyzed using SDS-gel. Upon determining optimal concentrations, the proteins were salted out.

II.3.4 Labelling of the CP150C protein

Table 7: Materials and consumables used for the labelling of the CP150C dimers.

	Materials and consumables	**Composition/ location/ company**
Chemicals/ Protein	**CP150C**	AiCuris Anti-infective Cures AG, Wuppertal, Germany
	DTT 1 M	Merck, Buchs, Switzerland CAS: 3483-12-3 Für 100 µl 15.43 mg DTT Fill up to 100 µl with 50 mM HEPES.
	BODIPY-FL	ThermoFischer SCIENTIFIC GmbH, Darmstadt, Germany
	50 mM HEPES buffer, pH 7.4	Merck, Buchs, Switzerland 500 mM HEPES buffer diluted 1:10 in H_2O.
Laboratory equipment	**DeNovix Photometer**	DeNovix, Wilmington, USA (SN: S5MN82)
Consumable materials	**PD10-Desalting column**	GE Healthcare Information Technologies GmbH & Co. KG, Dornstadt, Germany

The cysteine truncated N-terminal assembly domain of the HBc protein was labeled with the fluorescence dye BODIPY-FL (CP150-BO) for the capsid assembly assay. The labeling process was performed at 4 °C given the temperature sensitivity of CP150-BO. The first step was the reduction of the disulfide bonds between the terminal cysteine groups by slowly adding a freshly prepared 1 M DTT solution until reaching a 20 mM DTT concentration in the dimer solution. Meanwhile, two PD10-desalting columns were equilibrated with 3x5 ml HEPES pH 7.4, followed by adding 2.5 ml of the CP150C solution to each column, respectively. After the complete absorption of the dimers, the protein was eluted using 3.5 ml HEPES (pH 7.4), thereby separating the samples from DTT. Directly after the purification, the labeling was started by slowly adding (over 25 min) BODIPY-FL to the protein under constant stirring at 4 °C. The reaction was incubated overnight at 4 °C to allow the completion of the reaction, and excessive BODIPY-FL was removed with centrifugation at 14,000 rpm/4 °C for 10 min. The supernatant (protein) was collected in new Eppendorf tubes while three PD10-desalting columns were equilibrated with 3x5 ml HEPES pH 7.4 followed by the loading of 2.5 ml CP150-BO on each PD-desalting column. Finally, the Proteins were eluted with 3.5 ml HEPES pH 7.4, resulting in 10 ml CP150-BO with final concentrations of 20-15 µmol and labeling efficacy between 1.6 and 1.8.

II.3.5 High-Throughput Screening using 384 microtiter well format

All the reaction steps involving handling the light-sensitive labeled CP150-BO were carried out under yellow light. The transfer of the proteins, compounds, and salts to the microtiter plate was executed sequentially with multi-pipets, starting with the half logarithmic dilution ladder (2.5 µl) of the respective compound, followed by the CP150-BO proteins' (2.5 µl, final concentration 1.5 µM) addition. At the last step, the reaction is initiated automatically by increasing the NaCl concentration to 300 mM (5 µl) using the ClarioStar. The positive and negative controls were added manually instead of the 300 mM NaCl by pipetting 2.5 M NaCl or 50 mM HEPES (PH 7.4) into the respective wells after the first reaction cycle. After the initiation of the measurement, samples are excited with a fluorescence signal of the wavelength 477 nm, and the emission is measured at 530 nm until 15 min in 1 min cycles using the CLARIOstar. Percentage assembly values are normalized to CP150-BO (1.5 µM) dimers in 50 mM HEPES as the negative control, and 2.5 M NaCl-assembled CP150-BO (1.5 µM) capsids at a residence time of 5 min the positive control (Equation 2). The compound's EC_{50} values were calculated using GraphPrism7.

Equation 1): Calculation of CAM mediated percentual CP150-BO assembly based on P150-BO mixed with 50 mM HEPES as negative, and BO mixed with 2.5 M NaCl as the positive control at 5 min post mixing.

$$Percentual\ Assembly = 100 * \frac{(1 - \left(\frac{RFU\ (CP150 - BO\ mixed\ with\ CAM)}{RFU\ (CP150 - BO\ mixed\ with\ 50\ mM\ HEPES)}\right))}{(1 - \left(\frac{RFU\ (CP150 - BO\ mixed\ with\ 2M\ NaCl)}{RFU\ (CP150 - BO\ mixed\ with\ 50\ mM\ HEPES}\right)}$$

II.3.6 CAMs' activity and toxicity testings in HepAD38 cellular cultures

The CAM's activity and toxicity identification was cross evaluated using a HepAD38 cell-based high-throughput screening in 96-well formats. Each well carried a constant amount of $1.1x10^6$ HepAD38 cells and different concentrations of the respective antiviral compounds. The cells were incubated in tetracycline-free cell media for one week at 37 °C allowing the expression of HBV-related genes. After the incubation, the supernatant of the cells was collected, and the cDNA of the subviral particles was purified using the MagNA pure 96 system. The cDNA's concentration was carried out by qPCR using the LightCycler480 system. The sample preparation and initial cell incubation for the CC50's determination were executed analogously to the EC_{50} measurement using a second 96-microtiter plate. Following the 1-week incubation period, the cells were stained with PrästoBlue to verify the vitality of the HepAD38 cells and thereby the toxicity of the substances.

II.3.7 Protease mediated digestion of HBc dimers and assembly products

Table 8: Materials used for the protease mediated disassembly of HBc capsids and proteins.

	Materials and consumables	**Composition/ location/ company**
Chemicals, consumables	**AIC085300 (60 µM) (JNJ 56136379)**	For 200 µl: 10 µl 1.2 mM AIC085300 in DMSO was diluted in 190 µl 50 mM HEPES buffer (pH 7.4).
	AIC090019 (32 µM) (HAP)	Forr 200 µl: 10 µl 640 µM AIC090019 in DMSO was diluted in 190 µl 50 mM HEPES buffer (pH 7.4).
	CP150C (1.7 mg/ml)	AiCuris Anti-infective Cures AG, Wuppertal, Germany 2,936 µl for 40 reactions
	DTT 1 M	Merck, Buchs, Switzerland For 500 µl 77.15 mg DTT Fill up with 50 mM HEPES to 100 µl
	EDTA (150 mM)	Merck, Buchs, Switzerland For 1 ml 44.4 mg EDTA Fill up with 50 mM HEPES to 1 ml
	50 mM HEPES buffer, pH 7.4	Merck, Buchs, Switzerland 500 mM HEPES Buffer diluted 1:10 in H_2O
	1.2 M NaCl	For 50 ml 3.5 g NaCl Fill up with 50 mM HEPES to 50 ml
	5 M NaCl	For 50 ml 14.61 g NaCl Fill up with 50 mM HEPES to 50 ml
	Proteinase K (10 mg/ml)	Merck, Buchs, Switzerland CAS: CAS 39450-01-6 Für 150 µl 1.5 mg Proteinase K

		Fill up with 50 mM HEPES to 150 µl
Chemicals, consumables for Native agarose gel electrophoresis (NAGE)	**Agarose I**	VWR Life Science, Bruchsal, Germany Catalog number: 18300012 0.8 % m/v
	GelCode^{TM} Blue Safe Protein	ThermoFischer SCIENTIFIC GmbH, Darmstadt, Germany Catalog number: 24590
	HCl (25 %)	Merck, Buchs, Switzerland CAS: 7647-01-0
	1 M Tris, pH 8.5 Filter sterilized with 0.2 µm CA	Merck, Buchs, Switzerland Catalog number: 3535773 For 500 ml 60.55 g Tris base 15-18 ml concentrated HCl (pH adjust to 8.5) Fill up with H_2O to 500 ml
	NAGE buffer 1X 25 mM Tris, pH 8.5 19.2 mM Glycin	Für 1 l 100 ml 10X NAGE Buffer 900 ml H_2O
	NAGE buffer 10 X 250 mM Tris, pH 8.5 192 mM Glycin	Für 1 l 250 ml 1 M Tris, pH 8.5 14.4 g glycine Fill up with H_2O to 1 l
	4X sample loading buffer 240 mM Tris-CL pH 7.5 40 % (v/v) Glyzerin 0.4 % Bromphenol blau	Für 4 ml 960 µl 1 M Tris-Cl, pH 7.5 1,600 µl Glycerol 16 mg Bromphenolblau (MW:669.96) 1440 µl H_2O
Chemicals, consumables for SDS-PAGE	**MES-SDS running buffer (20 x)**	Alfa Aesar GmbH & Co KG, Karlsruhe, Germany (LOT: U19C512)
	MES-SDS running buffer (1 x)	Für 2 l 100 ml MES-SDS running Buffer (20x) 1,900 ml H_2O
	NuPAGE^{TM} 4-12 % Bis-Tris Gel	Invitrogen, Waltham, USA (LOT: 18022671)
	NuPAGE^{R} LDS Sample buffer (4 x)	Invitrogen, Waltham, USA (LOT: 1771590)
	SeeBluePlus2 Prestained Standard	Invitrogen, Waltham, USA Invitrogen (LOT: 1929090)
	GelCode Blue Safe Protein Stain	ThermoFischer SCIENTIFIC GmbH, Darmstadt, Germany Catalog number: 24594

The CP150C samples were prepared by reducing the disulfide bonds between the terminal cysteines and filtering the samples with PD10 desalting columns as described in II.3.4 Labelling of the CP150C protein. The dimers were eluted with 1.5 ml HEPES buffer (PH 7.4) and fractionated into 10 X 500 µl samples. The fractions' concentration was determined with fluorescence quantification using the DeNovix fluorometer. Samples containing the highest dimer concentrations were united, resulting in a final concentration of 1.560 mg/ml. Next, CP150C was incubated with 50 mM HEPES (CP150C dimer control), 2.5 M NaCl (HBc capsid control) or the reference compounds for 1 h followed by the addition of proteinase K in increasing concentrations (Table 9). The addition of the proteinase K was executed in a 20-second tact to allow a consistent incubation time for each sample. After the 10 min incubation at 37 °C, the reaction was stopped with the addition of 150 mM EDTA to the solutions. The results were evaluated by plotting 10 µl (2.4 µg CP150 per sample) samples on SDS-PAGE and 40 µl on native agarose gel electrophoresis (NAGE) -PAGE (11.25 µg CP150 per sample).

Table 9: Proteinase K dilution ladder used in the proteinase mediated digestion of HBc dimers and assembly products (Figure 16 and Figure 17).

Proteinase K concentration in mg/ml	10	3.2	1	0.32	0.1	0.032	0.01	0.0032	0.001
The volume of proteinase K stock in µl	(Stock solution)	48	47	48	47	48	47	48	47
HEPES 50 mM in µl	0	102	103.1	102	103.1	102	103.1	102	103.1
Total volume in µl	150	150	150	150	150	150	150	150	150

II.3.8 Detergence mediated disassembly of HBc capsids and proteins

Table 10 Materials/equipment used in the detergence mediated disassembly of HBc capsids.

	Materials and consumables	**Composition/ location/ company**
Chemicals/ Protein used for the biochemical assay	**AIC090019 (1 µM) (HAP)**	For 640 µl: 1 µl 640 µM AIC090019 in DMSO was diluted with 639 µl 50 mM HEPES buffer (pH7.4).
	AIC085300 (1.2 mM) (JNJ 56136379)	For 200 µl: 24 µl of 10 mM AIC085300 in DMSO 176 µl DMSO
	AIC090019 (640 µM) (HAP)	For 200 µl: 24 µl of 10 mM AIC090019 in DMSO 176 µl DMSO
	DMSO	Merck, Buchs, Switzerland CAS 67-68-5
	50 mM HEPES buffer, pH 7.4	Merck, Buchs, Switzerland 500 mM HEPES buffer diluted 1:10 in H_2O.
	5 M NaCl	Merck, Buchs, Switzerland For 50 ml 14.61 g NaCl

		Fill up to 50 ml with 50 mM HEPES.
	5 M NaCL + 1.1 % DMSO	For 1 ml 11 µl DMSO 989 µl 5 M NaCl
	600 mM NaCl	For 50 ml Mix 6 ml 5 M NaCl with 44 ml 50 mM HEPES buffer (PH 7.4)
	CP150-BO (9 µM)	For 468 µl 193 µl protein HBV 2018-171 275 µl 50 mM HEPES pH 7.4
Detergents tested	**SDS (0.5 %)**	Merck, Buchs, Switzerland CAS: 151-21-3 For 0.5 % solution 5 mg Solve in 1 ml 50 mM HEPES, PH 7.4
	Triton X (20 %)	Merck, Buchs, Switzerland: CAS: 9036-19-5 Mix 40 µl Triton X 100 % with 160 µl 50 mM HEPES pH 7.4
Laboratory equipment	**ClARIOstar**	BMG Labtech, Ortenberg, Germany (SN: 01044)
	BIOHIT 300 µl Handpipet	VWR Life Science, Bruchsal, Germany (SN: 227481)
	HAMILTON	Hamilton Germany GmbH, Gräfelfing, Germany (SN: 00423)
	Integra 12.5 µl Pipets	VWR Life Science, Bruchsal, Germany (SN: 6006558)
Consumable materials	**Assay Plate, 384 Well, Low Volume, Black Round Bottom**	Corning Incorporated, Kaiserslautern, Germany Product Number 4514
	Microplate, 96 Well, PS, U-BOTTOM, CLEAR	Greiner Bio-One GmbH, Solingen, Germany Product number: M0812-100EA

In the HBc assembly assay, described in II.3.5 High-Throughput Screening using 384 microtiter well format, the controls were adjusted to 0.5 % DMSO concentration to prevent DMSO mediated differences between samples in the readout. The initial assembly reaction with JNJ 56136349 and BAY 41-4109 were performed in three replicates in the 384-well formats with measurement of the capsid assembly every 90 s over 15 min. After the assembly reaction, 3 µl of the detergence dilutions were added to the mixtures and the reaction was again recorded every 90 s over 15 min. During the evaluation, the fluorescence signals of the samples were normalized on the fluorescence signal of the negative control (0 mM NaCl) and positive control (2.5 M NaCl) at 7.5 min to determine the degree of capsid assembly (Equation 2). The degree of disassembly, in turn, was determined by normalizing the samples' fluorescence signals with the negative control (0 mM NaCl) 4.5 min after the addition of the detergents. The percental disassembly was calculated by subtracting the percental assembly of the capsids before and after the addition of the detergents. The resulting data points were transferred to GraphPrism7, allowing the plotting of the percental disassembly against the detergence's concentrations and the calculations of deterngence mediated disassembly.

II.3.9 Dynamic light scattering

Table 11: Devices and samples used for dynamic light scattering mediated differentiation between HBc assembly products.

	Materials and consumables	**Composition/ location/ company**
Optical setup	**Multi-Angle light scattering**	**Wyatt**
Samples	Negative control	50 mM HEPES buffer
	CP150-BO dimers	CP150-BO in 50 mM HEPES buffer
	CP150-BO capsids	CP150-BO+ 2.5 M NaCl in 50 mM HEPES buffer
	CP150-BO aggregates	CP150-BO+ 32 µM Heteroarylpirimidine + 300 mM NaCl in 50 mM HEPES buffer

The non-labeled HBc proteins were preassembled in AiCuris and shipped to Wyatt technology. Here, the addition of fresh DTT prior assembly reactions was essential to reduce the disulfide bonds formed between the terminal cysteine of dimers. The HBc dimers, capsids, and aggregates were purified on size exclusion columns, and the mass fraction of the different assembly products was determined by utilizing the DLS from Wyatt. Following the purification, 1 ml samples were injected into the multi-angle light scattering cell, where the data was recorded according to Wyatt's manuals.

II.3.10 Fluorescence anisotropy

Table 12: Devices and samples used for fluorescence anisotropic mediated differentiation between HBc assembly products.

	Materials and consumables	**Composition/ location/ company**
Optical setup	**FluoTime 100 spectrometer**	**PicoQuant**
Samples	Negative control	50 mM HEPES buffer
	CP150-BO dimers	CP150-BO in 50 mM HEPES buffer
	CP150-BO capsids	CP150-BO + 2.5 M NaCl in 50 mM HEPES buffer
	CP150-BO aggregates	CP150-BO + 32 µM Heteroarylpirimidine + 300 mM NaCl in 50 mM HEPES buffer

Samples were incubated for 1 h prior to transport to PicoQuant. After the transport, the samples were stored at 4 °C until the experiments. The FluoTime 100 was equilibrated and used according to PicoQuants manuals. All three samples were measured based on time-correlated single-photon counting using the FluoTime 100 spectrometer from PicoQuant, and the data were evaluated with a global reconvultion analysis of the decay curves. Differences between measurements were corrected using the instrumental response function, which was determined using a 50 mM HEPES buffer. Anisotropy describes the kinetics of the process of increased random distribution of the fluorophores over time by comparing the orientation of the fluorophores at the moment of light emission (Equation 2).

$$R(t) = \frac{VV(t) - G * VH(t)}{VV(t) + 2 * G * VH(t)}$$

Equation 2: Equation for anisotropy based on the orientation of the fluorophores with respect to the configuration of the optics at the moment of light emission. VV(t): vertically oriented fluorophores at time t, VH(t): horizontally oriented fluorophores at time t, G: Instrument and wavelength-dependent correction factor.

II.3.11 Fluorescence correlation spectroscopy

Table 13: Devices and samples used for fluorescence correlation spectroscopy mediated differentiation between HBc assembly products.

	Materials and consumables	**Composition/ location/ company**
Optical setup	microtime 200 Inverse time-resolved confocal microscope	PicoQuant, Berlin, Germany
Samples	Negative control	50 mM HEPES buffer
	CP150-BO capsids	CP150-BO + 2.5 M NaCl in 50 mM HEPES buffer
	CP150-BO aggregates	CP150-BO + 32 µM Heteroarylpirimidine + 300 mM NaCl in 50 mM HEPES buffer

Samples were incubated for 1 h prior to transport to PicoQuant. After the transport, the samples were stored at 4 °C until the experiments. The MicroTime 200 was initiated, and the laser focus was calibrated using internal standards according to the manufacturer. The samples were fixed between two microscope slides for the measurement, and data was recorded over 15 min.

II.4 Results and Discussions

In the introduction the importance of the discovery of novel CAM-A like compounds was emphasised. The focus on the following work is the development and adaptation of novel methods to differentiate between CAM-A and N assembled products in an easy, reproducible, and economic matter. The initial step involved novel modifications to the 384-microtiter plate screening method while in the second part the compatibility of other biophysical methods was evaluated in order to differentiate between the CAMs.

II.4.1 Differentiation of CAMs' mode of action using the standard microtiter plate-based assay

In the fluorescence readout based 384-well microtiter plate assay standardazid in the industry, a CAM leads to the assembly of the CP150-BO dimers leading to the mutual quenching of the terminal BODIPY dyes given their proximity (II.3.5 High-Throughput Screening using 384 microtiter well format).[3] This assay was proven sensitive, accurate, and reproducible in a HTS manner. However, the differentiation between HBc aggregates, capsids, incomplete constructs, trimers of dimers or other subunits is not feasible based on the relative fluorescence signal redation which is similar in all assembly products.[3,5,37,38] Hence, even though this assay was used extensively and successfully during the screening of novel CAMs' activity, it could not distinguish between the morphology of the assembled products. Therefore, modifications were introduced by telescoping a second screening step to differentiate between the CAMs' mode of action based on the stability and size differences between the CAM-N formed capsids and the CAM-A induced aggregates.[6] In theory, the difference in size is an easy feature to distinguish the assembly products, as previously described column chromatography, but its implementation to a fluorescence based microtiter screening format was not trivial.[8] Initial plans to execute a filtration step after the first screening to remove possible aggregates and rescreen the residual proteins turned out to be impractical. The main difficulties were the filters' design for the already small assay format (384 wells) with a mash wide of under 1 µM resulting in difficulties with sample handling and back pressures. The focus on the stability variations between the assembly products were more promising. During the maturation process of hepatitis B virus particles, the encapsidated single-stranded viral RNA pgRNA is transcribed to the open circular DNA by the viral polymerase. Due to the higher charge density of the viral DNA, the capsid structure changes and becomes more unstable than an RNA containing capsid, which was observed via proteasomal degradation of the capsids.[39,40] Therefore, the hypothesis was established that hysterically stabilized empty capsids might have a higher resistance against proteolytic degradation or detergence mediated denaturation than protein aggregates, which have defects in the capsid lattice.

In the following, conditions were evaluated to selectively disassemble or digest protein aggregates while leaving the capsids intact. This could be integrated as a second step after the initial 384 well-titer-based biochemical assembly assay. In this way, the fluorescence signal quenching would be selectively reversible by dissasembeling the protein aggregates in the second screening, while the capsids and their quenched signal would remain stable.

II.4.1.1 Proteinase K digestion mediated differentiation of CAM CP150C assembly products

The proteinase K, a broad-spectrum serine protease was chosen for the following experiments. Proteinase K cuts HBc dimers in non-specific amino sequences, which was a promising start for the selective digestion of the protein aggregates' exposed regions.[39]

In the first step, the stability of assembled HBc capsids and non-assembled dimers against proteolysis were evaluated to define proteinase K concentrations leading to dimer's selective digestions and the digested products were separated using SDS-gel electrophoresis (II.3.7 Protease mediated digestion of HBc dimers and assembly products) (Figure 16). As expected, the HBc displayed higher tolerance to the protease up to a concentration of 32 µg/ml, whereas dimers were already digested at concentrations of 3.2 µg/ml. Next, new experiments were designed to investigate the difference in stability between capsids and aggregates. The initial experiment was repeated, but this time the first incubation step was conducted with 3.2 µM BAY 41-4109 with 300 mM NaCl or 6 µM glyoxamide-pyrrolamide (JNJ 56136349) with 300 mM NaCl to form protein aggregates or capsids at 10-fold EC_{50} concentrations, respectively (Figure 17).

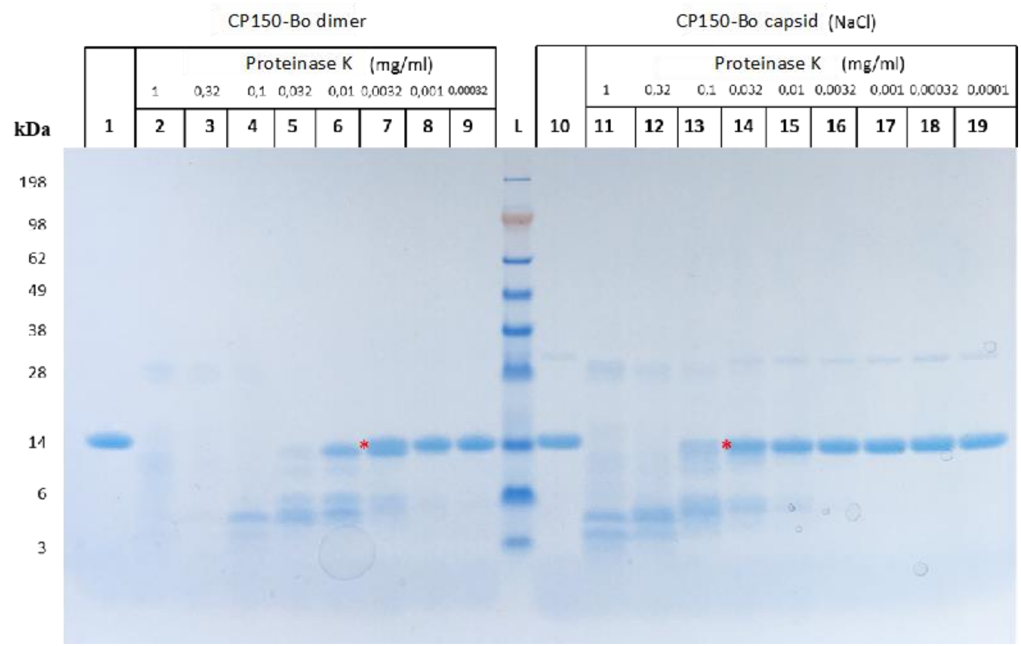

Figure 16: Proteinase K mediated degradation of CP150-BO dimers and capsids. Proteins were incubated with 2.5 M NaCl for 1 h at room temperature followed by 10 min incubation of the solutions with increasing proteinase K concentrations at 30 ªC. Line L: Standard protein ladder. Line 1 and 10: Undigested CP150C as a positive control. Line 2-9: Proteolytic degradation of CP150C dimers with increasing concentration of proteinase K. Line 11-19: Proteolytic degradation of CP150-BO capsids with increasing concentrations of proteinase K.

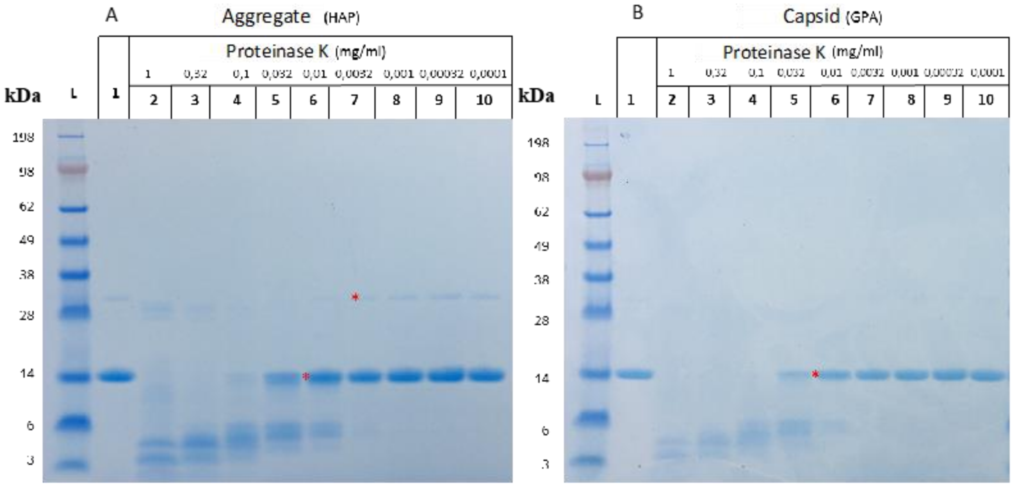

Figure 17: Proteinase K mediated degradation of BAY 41-4109 (3.2 µM) assembled CP150-BO aggregates (A) and JNJ 56136349 (6 µM) assembled capsids (B). Proteins were incubated with the compounds for 1 at room temperature followed by 10 min incubation of the solutions with increasing proteinase K concentrations at 30 °C. Line L: Standard protein ladder. Line 1: Undigested CP150C aggregates or capsids as the positive control. Line 2-10: Proteolytic degradation assembled CP150C aggregates and capsids with increasing concentration of proteinase k.

In both cases, a proteinase K concentration above 32 µg/ml led to the digestion of the products, not allowing a clear differentiation between the products wherefore this experiment was stopped.

In conclusion HBc capsids are indeed more resilient to protease-mediated disassembly than dimers. However, the initial screenings with protease K could not detect a protease concentration that would be selective for aggregates or capsids. Therefore, in future more specific proteases targeting the known exposed regions of the assembled capsids should be utilized.

II.4.1.2 CAM assembled CP150C products's differentiation based on detergence-based disassembly

In previous in-house studies, some detergents interfered with the HBc assembly reaction. Based on these findings the hysterically stable capsids could have a higher resistance to detergence-mediated disassembly than the aggregates or dimers. As a proof of concept, various Triton X or SDS concentrations were added after initial assembly to start a selective disassembly of the protein aggregates (II.3.8 Detergence mediated disassembly of HBc capsids and proteins). SDS has proven to be very potent at the disassembly of capsids and aggregates, starting at concentrations of 0.005 % and reaching complete disassembly at a concentration of around 1 % (Figure 18). In addition, no significant differences were measured in the fluorescence signals of BODIPY with and without SDS, indicating no negative impacts on the quantum yield of the dye. Unexpectedly, increasing SDS concentrations led to a higher disassembly with the JNJ 56136349 assembled capsids then with the BAY 41-4109 assembled aggregates, but the difference did not exceed 10 % in most cases. Hence the differentiation of the protein products is likely not clear, and further CAMs needs to be evaluated. Unfortunately, Triton X failed to disassemble any of the assembly products even at concentrations of around 10 %, at which further pipetting became impossible due to the high viscosity (Figure 19). Furthermore, Triton X increased the fluorescence in BODIPY samples, likely due to the separation of the linked dye molecules reducing the mutual quenching.

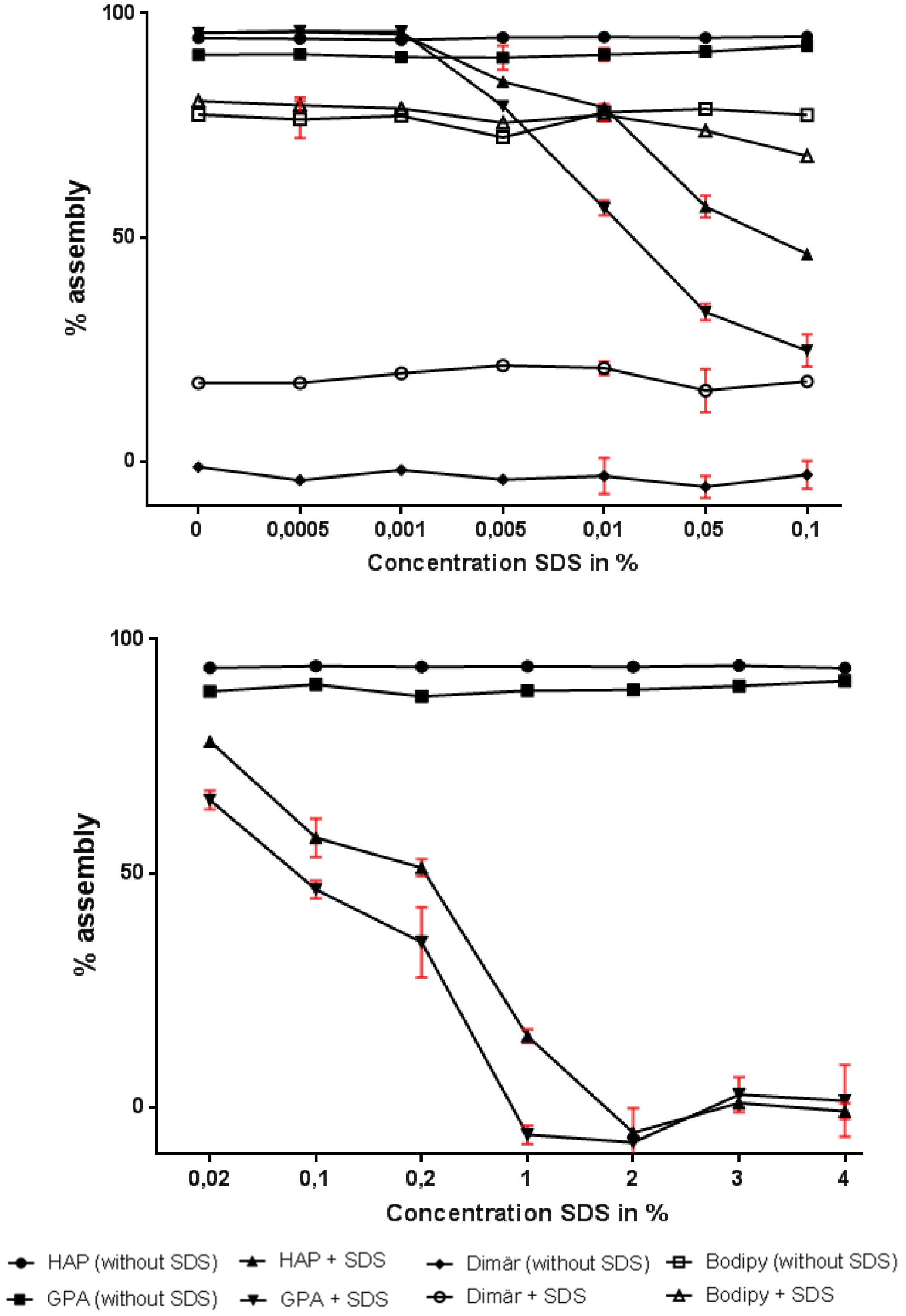

Figure 18: Percentual assembly of the BAY 41-4109/ JNJ 56136349 assembled capsids after 5 min incubation with ascending concentrations of SDS. Both BAY 41-4109 and JNJ 56136349 assembled capsids disassembled at SDS concentrations of 0.005 % and above. CP150-BO dimers were not affected by any concentration of SDS. The BODIPY-FL fluorescence signal was slightly quenched from an SDS concentration of 0.05 %.

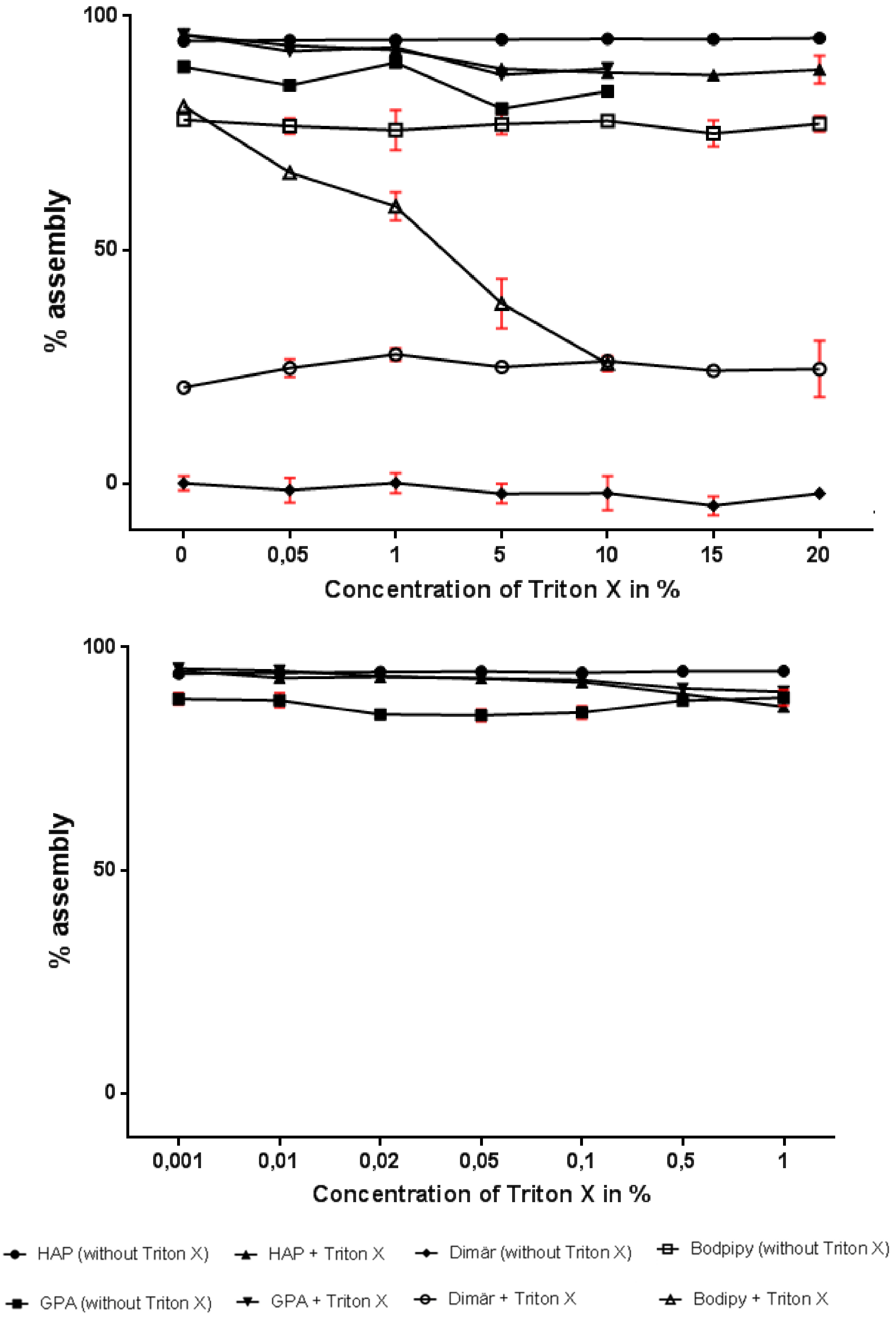

Figure 19: Percentual assembly of BAY 41-4109 or JNJ 56136349 assembled capsids after 5 min incubation with ascending Triton X concentrations. Neither HAP nor JNJ 56136349 assembled capsids disassembled at Triton X concentrations up to 10 %. CP150-BO dimers were not affected by any concentration of SDS, however, BODIPYs fluorescence signal was quenched above a Triton X concentration of 0.05 %.

In conclusion, capsid stability with SDS and TRITON-X showed mixed results. While Triton-X could not disassemble the aggregates or the capsids, SDS led to a slightly faster disassembly of the HBc capsids. However, more experiments with varying compounds and compound concentrations must be done with SDS before a precise categorization is possible. Aside from the previously mentioned factors, variations of temperature or sodium chloride concentrations could facilitate a selective disassembly.

II.4.2 Differentiation of CAMs' mode of action using selective CP150-BO mutants

As described in the general introduction, several papers, patents, and postershave been published in recent years introducing and evaluating novel CAM that showed varying activity with different CP150C mutants.[5,10,29,41–46] The differences between the tested CAM's affinity towards certain CP150C mutants could be class-specific and hence valuable for differentiating the mode of action. In this sense, the mutagenesis, expression, and purification of several CP150C mutants was executed to test their applicabilities in a mutant based biochemical assay.

II.4.2.1 Mutagenesis and expression of CAM selective CP150C proteins

During literature research, 12 possible CP150C mutant candidates were found with favorable selectivities for either CAM-A, CAM-N, or mutants with resistance towards both classes (Table 14). Starting with HBV-CP150C mutants of higher priority (F110I, T33N, and P25S), the mutagenesis was executed for all 12 variants by inserting a point mutation into the pET CP150C plasmid coding for the CP150C protein using thermal cycling PCR (II.3.1 Mutagenesis).

Table 14: Classification of the selective CP150C mutants into CAM-A, CAM-N or double resistant mutations (pocket).

Classification	CP150C mutant	FC for CAM-N (JNJ 6379	FC for CAM-A (BAY 41-4109)
CAM-A	P25S	0.4	23
	T109I	0.1	27
	R127H	3.7	>77
	F24L	0.9	7.3
	T33P	14	>67
CAM-N	F110I	13	<0.5
	V124G	>35	1.4
	T128I	11	<0.05
	L27Q	>21	3.2
Pocket	D29G	2.2	4.6
	T33N	85	>95
	L30F	9.3	14
	Y118F	6.6	6.7

The proteins were expressed using the standard expression protocol of CP150C, given the high consensus in the primary DNA sequence between the mutants and the original CP150C protein (II.3.2 Expression of CAM selective CP150C proteins in *E. coli* Rosetta2 (DE3) competent cells). Four CP150C mutant expressions were successful preformed on a larger scale for HBV-CP150C-P25S, HBV-CP150C-T33N, HBV-CP150C-V124G, and HBV-CP150C-T109I (Figure 26 to Figure 29) (II.3.2 Expression of CAM selective CP150C proteins in *E. coli* Rosetta2 (DE3) competent cells).

II.4.2.2 Purification of CAM selective CP150C proteins using a series of size exclusion- and affinity columns

Following the expression of the four mutants, the purification of HBV-CP150C-P25S and HBV-CP150C-F110I was performed using the standard CP150C purification protocol (II.3.3 Purification of CAM selective CP150C proteins using a series of size exclusion- and affinity columns). The first two standard mutant purifications from the cytosol did not obtain any products after the initial sequence of CaptoCore700 affinity column and Sephacryl^{TM} S300 HR column size exclusion chromatography. This result could be either due to the fallacious activity of the protein inhibiting the disassembly prior to the size exclusion column or difficulties with the extraction from the pelleted proteins. Indeed, after further experimentations with the purification of FC110I, target proteins were found in inclusion bodies instead of the pelleted cytosol. Therefore, to get functional proteins, the extraction of the inclusion bodies was conducted using 8 M urea, followed by the protein's gentle refolding using stepwise dialysis to decrease the urea's concentration. Unfortunatly, further attempts in stabilizing and solubilizing the recovered proteins were not successful.

In the meantime, cellular assays carrying the HBV-CP150C-F110I mutation showed a heavily impaired replication indicating that the mutation is interfering with the activity of the CP150-BO protein. The impaired cellular replications of the mutated virus combined with the accumulation of the proteins in inclusion bodies indicated a misfolded CP150-mutant in its natural form leading to the precipitation under standard conditions. In future attempts, the refolding of the proteins to a functional state with chaperons or different means could be employed, but these techniques are beyond the scope of this work.

The purification of the mutant HBV-CP150C-P25S first Sephacryl S300 column contained a protein band slightly under the protein band from the CP150C dimer. Many attempts of further columns and dialysis were performed to separate the two bands, but in all cases, nearly all the proteins were lost after the second size exclusion column.

The expression of the mutants proved to be far more challenging than initially estimated. Furthermore, Dr. Angelica Corcuera tested various mutants in cellular assays, which were showing a compound resistance rather than the anticipated class-specific resistance. Hence, even the thoroughly purified mutants could be insufficient to distinguish CAMs' mode of action leading to the termination of these experiments.

II.4.3 Analysis of CAMs’ mode of action using biophysical methods

Elaborate techniques have been utilized previously to provide information on the HBc assembly, such as dynamic light scattering,[47] size exclusion chromatography and immunofluorescence assays,[8,48] small-angle X-ray scattering,[49] time-of-flight mass spectrometry[50] and fluorescence correlation spectroscopy.[51] The feasibility of some of these techniques to differentiate between the HBc assembly products' morphology in an economic manner was assessed.

II.4.3.1 Dynamic light scattering

During a DLS measurement, monochromatic coherent light is illuminating the samples, usually generated by a laser. If the laser's wavelength is sufficiently lower than the measured particles' size, then the light is reflected according to Rayleigh scattering. The reflection that occurs from the surrounding particles has either constructive or destructive interference, thereby generating a light intensity fluctuation projected onto a screen and called a speckle pattern. Due to the Brownian motion of the particles, the reflected light intensity changes over time, leading to a temporal variation dependent on the particles' size. The temporal fluctuations of the speckle patterns in turn is evaluated with an autocorrelation function, providing information about the hydrodynamic radius, translational diffusion coefficient, and the average size and mass of the samples can be determined.[52]

Especially the average size and mass of the particles are parameters which are required to differentiate between the morphology of the HBc assembly products. Important benefits of the technology are the label-free utilization and non-invasive readout of the samples. However, dynamic light scattering can not accurately depict multimodal samples, wherefore, a purification of the particles with flow field fractionation or column chromatography prior to measurements is required. Furthermore, larger volumes of up to 1 ml samples are necessary for an accurate measurement, leading to an unwanted high sample and protein consumption. The addition of this technology as a readout for the microfluidic system was considered, and HBc aggregates, capsids, and dimers were evaluated using a multi-angle light scattering device from Wyatt (Table 15 and Table 16).

Table 15: DLS of CP150-BO dimers with and without the addition of DTT. Aside from dimers, tetramers, hexamers, and high molecular mass aggregates were found in the sample (Mw). Rh: Hydrodynamic radius, rz (nm): z-average radius. Samples with DTT added prior to the measurement consisted mainly of dimers (89 %) contrary to the No DTT samples, which also contained up to 46 % tetrameric and hexameric structures. Protein aggregates with high molar masses were found in both samples.

		Mp (kDa)	Mw (kDa)	Rh (nm)	rz (nm)	Mass fraction (%)
+5mM DTT	Dimer	32.0 ± 1.4%	32.2 ± 2.1%	-	-	89.0
	Tetramer	-	-	-	-	0.7
	Hexamer	-	-	-	-	0.1
	Aggregate	3820.6 ± 1.1%	3800.2 ± 1.1%	15.5 ± 1.7%	18.4 ± 12.2%	10.2
No DTT	Dimer	34.2 ± 3.6%	34.5 ± 4.1%	-	-	37.1
	Tetramer	70.7 ± 2.3%	70.7 ± 2.7%	-	-	16.0
	Hexamer	97.4 ± 1.9%	98.6 ± 2.2%	-	-	30.0
	Aggregate	3744.4 ± 1.7%	3640.3 ± 1.7%	15.6 ± 1.7%	16.9 ± 21.2%	15.0

Table 16: DLS of CP150-BO capsids with the addition of DTT. Aside from capsids, a small amount of high molecular mass aggregates was found in the sample (Mw). Rh: Hydrodynamic radius, rz (nm): z-average radius. CP150C assembled with 2.5 M NaCl resulted in capsids of a MW of approx. 37 kDa (up to 90 %). Aggregates of higher masses were present in the fractions to a small percentage.

	Peak	Mp (kDa)	Mw (kDa)	rz (nm)	Rh (nm)	Mass fraction (%)	Calculated mass (µg)
Sample 2 Capsid	Capsid	353.7 ± 0.2	3696.1 ± 0.2	18.3 ± 2.2	16.0 ± 1.9	90.6	4.4
	HMW	9024.1 ± 0.3	9310.0 ± 0.3	38.0± 0.8	18.2 ± 5.5	4.8	0.2
	Aggregates	12277.7 ± 0.4	21683.0 ± 0.5	54.7 ± 0.7	14.8 ± 9.6	4.6	0.2

Capsid and dimer samples were easily distinguished by the variety in the calculated molecular mass. Interestingly, without the addition of DTT before the measurement various large products formed due to the disulfide bonds at the terminal cysteines. On the other hand, the analysis of the protein aggregates was not successful likely due to the protein column used in the system preventing the large proteins from entering the solid phase. By utilizing flow field fractionation instead of a column-mediated purification, this issue could be circumvented.

In summary, DLS allowed the differentiation between dimers, capsids, and aggregates are possible. However, the extensive sample preparation required combined with the large volumes of samples needed for the detection prevent using this method for screening purposes. Initial models of the DLS as a readout system for the microfluidic system were also disregarded due to its high sample consumption.

II.4.3.2 Time resolved fluorescence anisotropic measurements

In the Time-Resolved Fluorescence Anisotropic (TRFA) measurement the samples are excited with a pulse of linearly polarized light with a wavelength of 475 nm. Fluorophores with transition vectors aligned parallel to the polarization plane of the exciting light are excited, while the ones with vectors perpendicular to the polarization plane are not. Due to Brownian rotation, the initial biased population of excited fluorophores is randomly distributed with the correlation of time. Simultaneously the fluorophores relax from the first excited state to the ground electronic state by emitting the absorbed light. Given these two parallel processes, the polarization plane of the fluorophore can be determined by the orientation of the fluorescent molecule at the time of emission.[53]

For TRFA, the standard BODIPY labeled CP150-BO proteins were used, which already had several theoretical challenges listed above. Since BODIPY was not linked by a rigid linker, a high chance existed to measure the rotation of the fluorophore on the protein instead of the rotation of the protein itself. In theory, larger proteins aggregates have a slower rotation speed than the smaller capsids, and the two should be distinguishable. Furthermore, since both carry the same fluorophore with identical decay lifetimes, more aggregates should be at the vertical position (VV) regarding the device optics at an early moment of emission than capsid. Therefore, the anisotropy for CP150-BO aggregates must be significantly lower at early moments of emission than the one from CP150-BO capsids. Unfortunatly, this tendency was not observed by comparing the measured fundamental anisotropy for protein aggregates, capsids, and dimers. Given that the fluorophores were not fixed tightly to the proteins, these results were expected. (Figure 20, Figure 21,and Table 18).

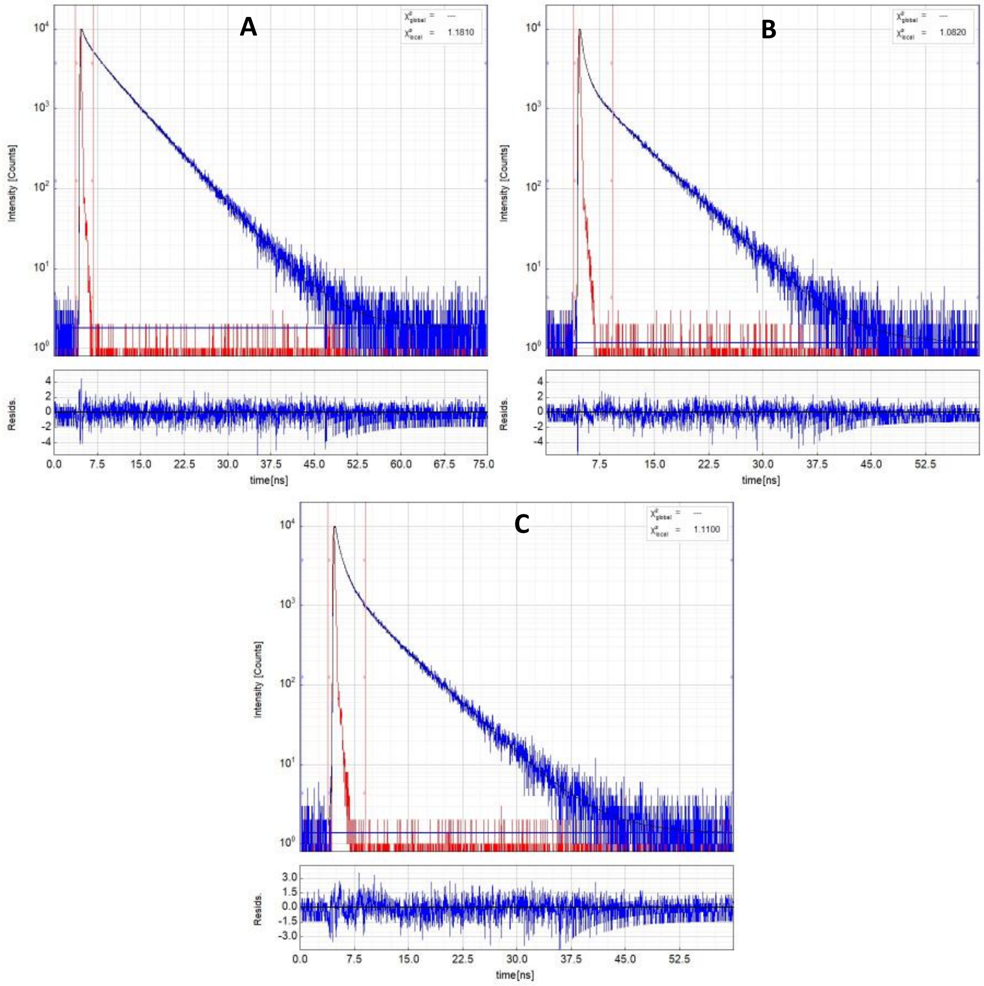

Figure 20: Polarized decays of CP150-BO dimers in 50 mM HEPES buffer (A), CP150-BO capsids in 50 mM HEPES buffer with 2.5 M NaCl (B) and of CP150-BO aggregates in 50 mM HEPES and 32 µM BAY 41-4109 and the instrument response function. The anisotropy decay curve as calculated by FluoFit is plotted at the bottom panel. In addition, an appropriate portion of r(t) was fitted to a triple exponential decay model without reconvolution. The fitted curve and the properly weighted residuals are also shown.

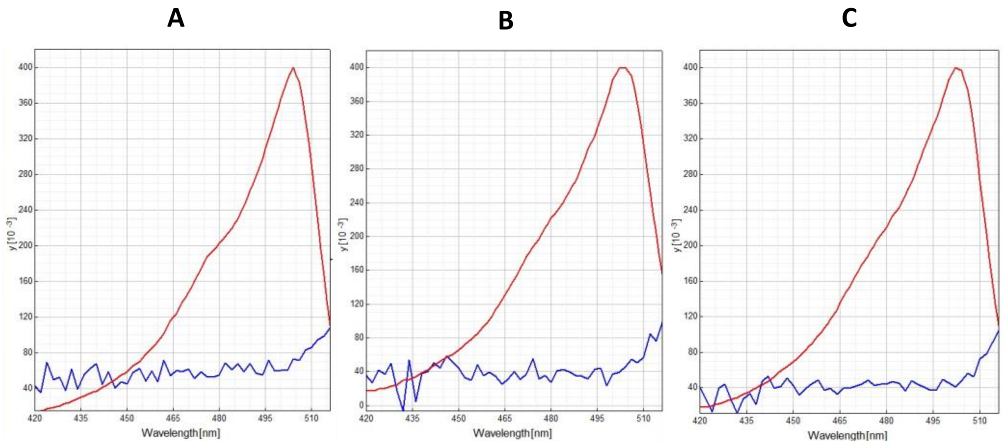

Figure 21: Emission spectrum (red) of CP150-BOdimers (A), capsids (B), and aggregates (C) as a function of the emitted wavelength after excitation with 484 nm.

By optimizing the lifetimes and rotational freedoms of the fluorophores, anisotropic measurements could be implemented to differentiate between CAM N and A assembly products. Even in this case, however, this method is not fast nor straightforward enough for a high throughput utilization, hence the third readout was attempted: Fluorescence correlation spectroscopy.

II.4.3.3 Time Resolved Fluorescence correlation spectroscopy

Fluorescence correlation spectroscopy (FCS) analyzes the temporal fluctuations of fluorescence intensities in femtoliter amounts of samples and records molecules' motion and fluorescence intensity in picomolar concentrations. Therefore, this method allows the calculation of the number of molecules, the absolute concentration in the solution, the size and shape, and the diffusion constants. Due to the large molar mass of the protein aggregates, these products should have a significantly slower diffusion constant than the much smaller capsids. These could be depicted by the qualitative measurements of the temporal fluctuation of the fluorescence intensities during a given time.[54]

Before the FCS measurements, the confocal microscope was used to take fluorescence lifetime images (FLIM) from both the JNJ 56136349 assembled protein capsids as well as the BAY 41-4109 assembled aggregates (Figure 22). Most of the observed capsids (Figure 22, B and Figure 23) had sizes around 400 nm, which is one order of magnitude greater than results obtained from literature which is around 36 nm.[55] Since FLIM methods are based on an optical confocal microscope, this blurring was expected as a result of the limited resolution in the low nm scale. While particles with similar sizes were observed in BAY 41-4109 mediated CP150-BO assembly products, large aggregates were detected as well (Figure 22 A, and Table 17). This result correlates with previously described literature sources stating that BAY 41-4109 mediated assembly of the dimer proteins produces irregularly shaped incomplete capsids (lower sized particles) that tend to clone up, forming larger aggregates.[8,44]

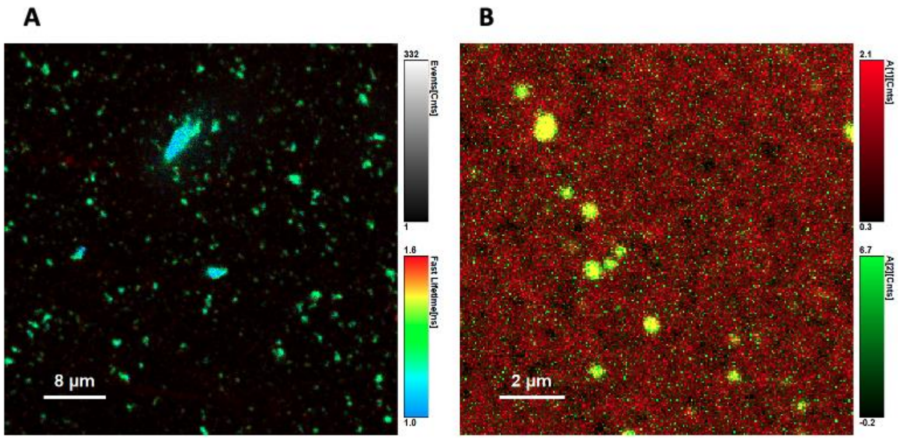

Figure 22: FLIM depiction of CP150-BO aggregates (A) and capsids (B). The intensity of the assembly products is represented according to the respective scales. While capsids were mostly homogeneous (B), CP150C aggregates displayed a large variety of sizes from under a µm up to 8 µm.

Table 17: Observed size distribution in CP150-BO capsid and aggregate particles from the FLIM pictures measured by ImageJ.

Sample	Label	FLIM depiction of JNJ 56136349 assembled protudcts in µM	FLIM depiction of BAY 41-4109 assembled smaller products in µM	FLIM depiction of BAY 41-4109 assembled larger products in µM
1	Samples	0.511	0.335	6.396
2		0.319	0.356	1.109
3		0.38	0.799	1.621
4		0.245	0.419	2.614
5		0.331	0.44	1.661
6		0.405	0.251	-
7		0.417	-	-
8		0.319	-	-
9		0.638	-	-
Evaluation	Mean	0.396	0.433	2.68
	SD	0.118	0.191	2.147
	Min	0.245	0.251	1.109
	Max	0.638	0.799	6.396

FCS was measured using a 1 µM solution of the protein aggregates and the capsids, respectively. Quantitatively a significant difference was observed between the two samples. While the autocorrelated fluorescence signal of the capsids already started to change after 0.003 s, this was only the case after approximately 450 s for the protein aggregates (Figure 23). Furthermore, strong fluctuations were observed in the latter, which could be due to the aggregates' high inhomogeneity, as shown in the FLIM spetrum.

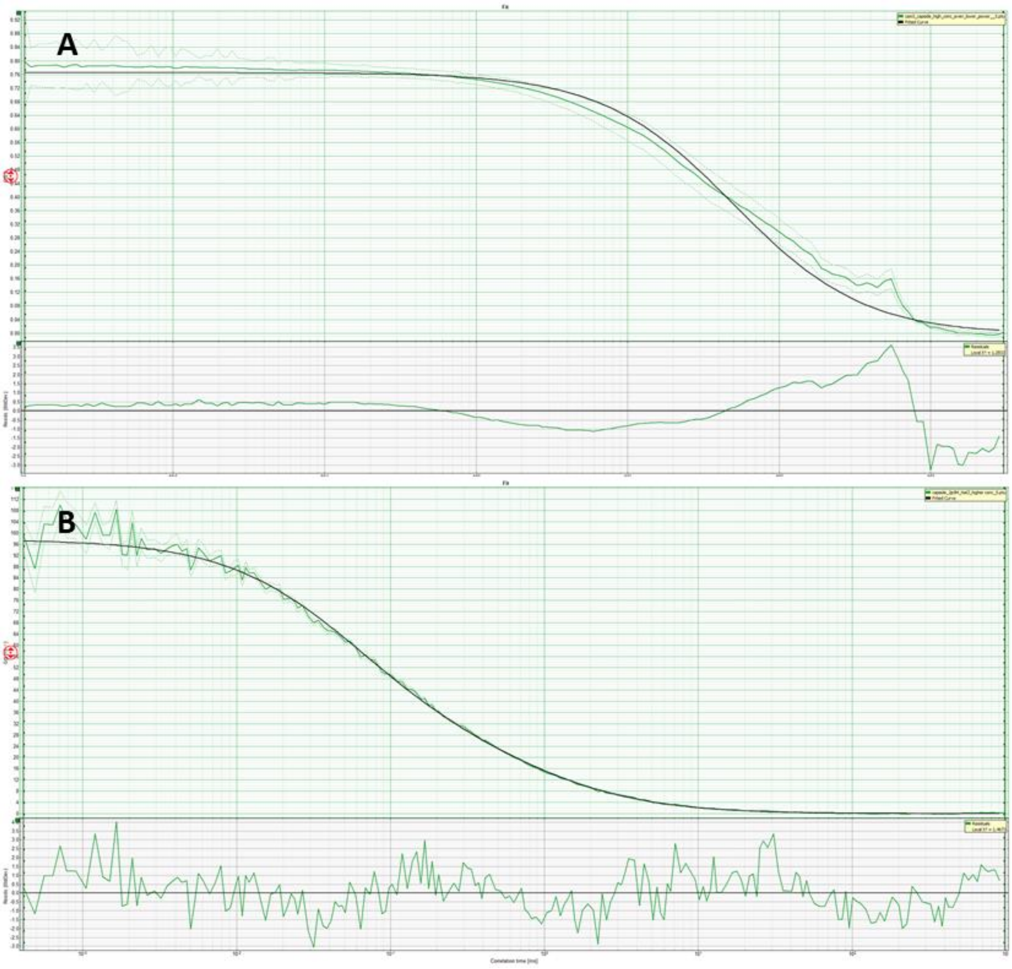

Figure 23: Fluorescence correlation curve of CP150-BO aggregates (A) (1 µM) and CP150-BO capsids (B) (1 µM). Temporal changes of the fluorescence intensities in the detection volume are evaluated with respect to their strength and duration. **(A)** Autocorrelation of this signal depicted changes starting around the second one and deviations from the standard model were measured after 450 s suggesting multiple different sized structures. **(B)** Autocorrelation started around 0,003 s and a regular standard model confirmed a strong population of smaller sized particles.

The next step was the measurement of the fluorescence intensities of the assembly species, which were depicted in a photon-counting histogram. The JNJ 56136349 assembled capsids had a uniform distribution around a relative fluorescence intensity of 0.2. Protein aggregates formed with BAY 41-4109 also followed a similar pattern but had a substantial amount of high intensity spikes up to 2.0 (Figure 21). This method was also a good indicator of the samples' homogeneity since their fluorescence intensity varied with their size.

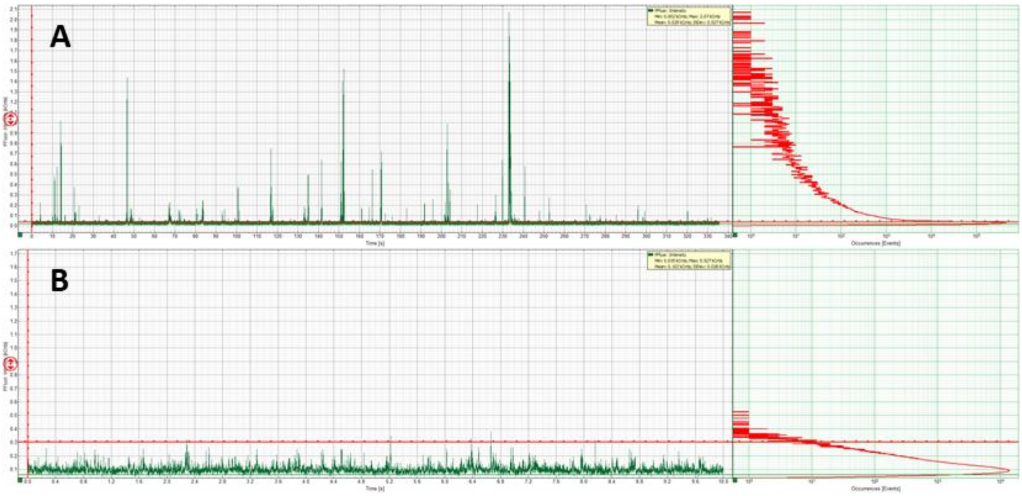

Figure 24: Photon counting histogram of CP150-BO aggregates (**A**) (10 µM) and CP150-BO capsids (**B**) (10 µM). (**A**) Measurement over 340 s showed a strong distribution around the relative intensity of 0.2, with many irregular signals picking up 2.0. (**B**) Measurement over 10 s showed regulare pattern with spike intensities around 0.2.

The results were further visualized by depicting the relative intensities of the fluorescence species against the fluorophobic lifetimes. Capsids have a relative fluorescence intensity of around 4.5 and a fluorescence lifetime of 4.5 ns. Compared to that, larger aggregates had a stronger fluorescence intensity visualized in the long tail of the fluorescence intensities in and a change in the fluorescence lifetime from approximately 5 ns to around 2 ns (Figure 25).

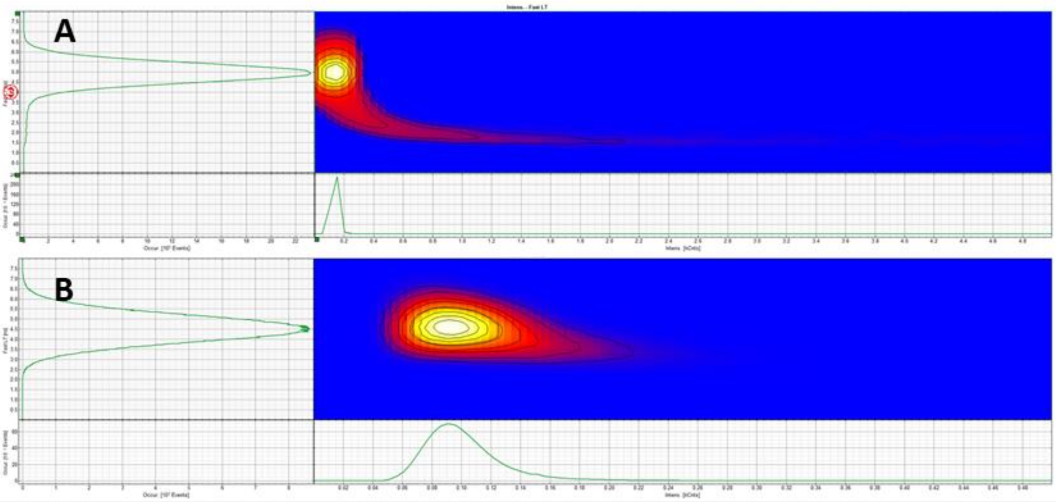

Figure 25: 2D intensity-lifetime histogram of CP150-BO aggregates (A) (1 µM) and CP150-BO capsids (B) (**100 µM)**. (**A**) Most detected species have a lower intensity of 0.2 counts and a fluorescence lifetime of around 5 ns. However, intensities spiking up to 4 kcounts and relative lifetimes of around 2.0 ns are observed as well. **(B)** Compared to A the capsids are more regularly distributed around intensities of 0.9 k counts and relative lifetimes of around 4.5 ns.

In conclusion, the most accurate method to differentiate between CAM A and N assembled products is the FCS readout system. This method successfully differentiated the between BAY 41-4109 formed CP150-BO aggregates and JNJ 56136349 assembled capsids using photon counting histogram, 2D intensity-lifetime histogram, and fluorescence correlation curves. However, highly sensitive confocal laser scanning microscope is a prerequisite for FCS measurements and the sample preparations are longer than in conventional microtiter plate methdos. Therefore, the direct integration to a screening cascade would be to cost intense. Nonetheless, further evaluation of assembly products using this method can give insights about the assembly products, as well as the mutual interaction of the fluorophores used for labeling.

II.5 Conclusion

The current standard for CAM mediated HBc assembly screening is a microtiter plate based assay that is fast, straightforward, and robust in the determination of the novel CAMs' activity (II.3.5 High-Throughput Screening using 384 microtiter well format).[3] However, in this format, it is not possible to simultaneously measure fast kinetics for all the tested compounds. Furthermore, the assay lacks the ability to differentiate between the product morphologies during capsid assembly. This information is relevant in that compounds from class A displayed interesting behavior, such as proteasomal degradation of assembly products, which could offer several benefits over the CAM-Ns.[15,18,26,38,44,56] To date, the experimental identification of CAMs' mode of action was mainly performed using thermodynamic assembly data or by analyzing the morphology of assembly products after long incubation times.[8,47–51,57]

In order to find a simple way of differentiating between A and N type CAMs, novel modifications on the microtiter assay were performed. This included three different processes which were telescoped after the first screening step to deliver information about the CAM’s mode of action in addition to the activity values already obtained. In a first attempt, a filtration step following the screening was evaluated to remove large aggregates assembled by CAM-A. A successful implementation would not change the fluorescence values of the assembled capsids while reducing the values of CAM-A assembled aggregates. However, the handling of the filter with a mesh width < 1 µm resulted in strong beackpressure and was therefore not feasable. Furthermore, there are many reports about the morphology of the CAM-A assembled capsids showing that in some cases they form tube-like aggregates but in others incomplete or damaged capsids.[8,15] In this case, there is a high possibility that damaged capsids or fragmented aggregates formed by a CAM-A pass the filter due to the smaller size leading to a misguided characterization.

In the second attempt, the selective proteinase K mediated degradation of CP150C aggregate was assessed. The literature showed that complete capsids could protect the dimers from proteolytic degradation by concealing sensitive termini.[39] At the same time, the misfolded capsids from CAM-A exposed some of these sequences, which could be utilized to selectively digest these products while maintaining the integrity of CAM-N assembled capsids.[8,57] Indeed, in initial experiments, conditions were found where the selective digestion of dimers, but not the HBc capsids was possible. However, CAM-A and CAM-N assembled products had a similar resistance towards proteinase K digestion and could not be differentiated. In future attempts, nonspecific proteases, or proteases with selectivity for a terminal sequence of the CP150C dimer, could be employed to gain the required results.

The last attempt to differentiate the CAMs'mode of action in the microtiter format was the detergence-mediated disassembly of the HBc aggregates and capsids. Therefore, various concentrations of SDS or Triton X were evaluated which were added to the reaction mixture 15 min after the assembly. As was the case with the proteinase K, a surfactant concentration was not found for the selective disassembly of either CAM products.

Consequently, a new approach was attempted by changing the target protein instead of the assay. Several HBc mutants were described showing varying sensitivity towards different CAMs.[5,29,41–44] After extensive literature research, 12 different CP150C mutants were chosen with the aim to find CAM-A and CAM-N selective mutants usable in a class-specific high-throughput screening assay. From the pET CP150C mutant constructs generated by thermal cycling PCR, four were expressed: The CAM-A resistant HBV-CP150C-P25S, the CAM-N resistance mutants HBV-CP150C-V124G and HBV-CP150C-F110I, and the double resistant mutant HBV-CP150C-T33N. Initial attempts to purify the construct were unsuccessful, and so these experiments were placed on hold due to time restrictions. Furthermore, as mentioned in II.4.2.2 Purification of CAM selective CP150C proteins using a series of size exclusion- and affinity columns, Dr. Corcuera found that the mutants displayed more of a compound than class-specific resistance in cellular assays. As such, even a successful purification and new assay based on a single CAM selective mutant would likely misinterpret the mode of action due to compound-specific variations. In this regard, the modifications of the HBc capsid assembly in microtiter format were halted.

In the next step the current state-of-the-art techniques were evaluated as potential methods to differentiate between CAM-N and-A assembled products as an alternative to the capsid assembly assay. The main methods evaluated were DLS, FA, and FCS. It was possible to successfully differentiate between capsids and protein aggregates using DLS as well as FCS, with the FCS excelling in sample preparation, time requirement, and sample consumption over DLS. Indeed, using FLIM depictions, fluorescence correlation curves, photon counting histograms, and intensity lifetime histograms, it was possible to observe clear differences between BAY 41-4109 (CAM-A) assembled aggregates and NaCl assembled capsids in regard to size, temporal changes, and sample homogeneity. While the capsids were homogeneous and had a smaller size of approximatly 0.34 µM (higher than literature value due to the sensitivity of the optical readout), the aggregates showed larger sizes with significant variations between smaller capsid like structures and larger aggregates (mean 2.7 µM with an SD over 5 measurements of 2.1 µM). Overall, FCS is an excellent methodology for HBc assembly readout; however, the high setup cost and complexity of high throughput compatibility were substantial limitations.

The differentiation between CAM-A and N mediated HBc assembly is not limited to the morphology of the assembled products. Zhou et al. showed that HAPs could alter the buried interface between dimers, thereby strengthening the assembly reaction.[44] Due to high association energies, the nucleation is enhanced resulting in a faster overall assembly reaction and the formation of kinetically trapped intermediates due to the depletion of free core protein.[58] These differences in kinetic activity could offer another way to achieve faster and more precise characterization of CAM and will be addressed later in this work (IV.4.3 CP150-BO assembly kinetics as an indicator of the mode of action of CAMs).

II.6 References

1. Stray, S. J., Johnson, J. M., Kopek, B. G. & Zlotnick, A. An in vitro fluorescence screen to identify antivirals that disrupt hepatitis B virus capsid assembly. *Nat. Biotechnol.* **24**, 358–362 (2006).
2. Zlotnick, A. *et al.* Core protein: A pleiotropic keystone in the HBV lifecycle. *Antiviral Res.* **121**, 82–93 (2015).
3. Zlotnick, A. *et al.* In vitro screening for molecules that affect virus capsid assembly (and other protein association reactions). *Nat. Protoc.* **2**, 490–498 (2007).
4. Donald Alaistair, A. U. & Susanne Bonsmann, Anita Wegert, C. G. Patent Application Publication (10) Pub . No .: US 2020/0354379 A1. **2020**, (2020).
5. Katen, S. P., Chirapu, S. R., Finn, M. G. & Zlotnick, A. Trapping of Hepatitis B Virus Capsid Assembly Intermediates by Phenylpropenamide Assembly Accelerators PPA. *ACS Chem. Biol.* **5**, 1125–1136 (2010).
6. Liu, C., Fan, G., Wang, Z., Chen, H. S. & Yin, C. C. Allosteric conformational changes of human HBV core protein transform its assembly. *Sci. Rep.* **7**, 1–9 (2017).
7. Katen, S. P., Tan, Z., Chirapu, S. R., Finn, M. G. & Zlotnick, A. Assembly-directed antivirals differentially bind quasiequivalent pockets to modify hepatitis B virus capsid tertiary and quaternary structure. *Structure* **21**, 1406–1416 (2013).
8. Corcuera, A. *et al.* Novel non-heteroarylpyrimidine (HAP) capsid assembly modifiers have a different mode of action from HAPs in vitro GPA, PT, DBT. *Antiviral Res.* **158**, 135–142 (2018).
9. Berke, J. M. *et al.* Capsid assembly modulators have a dual mechanism of action in primary human hepatocytes infected with hepatitis B virus SBA. *Antimicrob. Agents Chemother.* **61**, 1–14 (2017).
10. Incorvia, C. *(12) United States Patent*. vol. 2 (2015).
11. Rudolf, B. *et al. States Patent*. vol. 2 (2019).
12. Perni, R. B. *et al.* Phenylpropenamide derivatives as inhibitors of hepatitis B virus replication. *Bioorganic Med. Chem. Lett.* **10**, 2687–2690 (2000).
13. Bourne, C. R., Finn, M. G. & Zlotnick, A. Global Structural Changes in Hepatitis B Virus Capsids Induced by the Assembly Effector HAP1. *J. Virol.* **80**, 11055–11061 (2006).
14. Zhou, Z. *et al.* Heteroaryldihydropyrimidine (HAP) and Sulfamoylbenzamide (SBA) Inhibit Hepatitis B Virus Replication by Different Molecular Mechanisms. *Sci. Rep.* **7**, 1–12 (2017).
15. Stray, S. J. *et al.* A heteroaryldihydropyrimidine activates and can misdirect hepatitis B virus capsid assembly. *Proc. Natl. Acad. Sci. U. S. A.* **102**, 8138–8143 (2005).
16. Karl Deres, H. R.-W. Inhibition of Hepatitis B Virus Replication by Drug-Induced Depletion of Nucleocapsids. *Science (80-.).* **303**, 1829 (2003).
17. Venkatakrishnan, B. *et al.* Hepatitis B Virus Capsids Have Diverse Structural Responses to Small-Molecule Ligands Bound to the Heteroaryldihydropyrimidine Pocket. *J. Virol.* **90**, 3994–4004 (2016).
18. Bourne, C. *et al.* Small-Molecule Effectors of Hepatitis B Virus Capsid Assembly Give Insight into Virus Life Cycle. *J. Virol.* **82**, 10262–10270 (2008).
19. Hagan, M. F., Elrad, O. M. & Jack, R. L. Mechanisms of kinetic trapping in self-assembly and phase transformation. *J. Chem. Phys.* **135**, (2011).
20. Hagan, M. F. & Elrad, O. M. Understanding the concentration dependence of viral capsid assembly kinetics - The origin of the lag time and identifying the critical nucleus size. *Biophys. J.* **98**, 1065–1074 (2010).
21. Kondylis, P. *et al.* Competition between Normative and Drug-Induced Virus Self-Assembly Observed with Single-Particle Methods. *J. Am. Chem. Soc.* **141**, 1251–1260 (2019).

22. Schlicksup, C. J., Laughlin, P., Dunkelbarger, S., Wang, J. C. Y. & Zlotnick, A. Local Stabilization of Subunit-Subunit Contacts Causes Global Destabilization of Hepatitis B Virus Capsids. *ACS Chem. Biol.* **15**, 1708–1717 (2020).

23. Qazi, S., Schlicksup, C. J., Rittichier, J., Vannieuwenhze, M. S. & Zlotnick, A. An Assembly-Activating Site in the Hepatitis B Virus Capsid Protein Can Also Trigger Disassembly. *ACS Chem. Biol.* **13**, 2114–2120 (2018).

24. Deres, K. *et al.* Inhibition of hepatitis B virus replication by drug-induced depletion of nucleocapsids. *Science (80-.).* **299**, 893–896 (2003).

25. Qiu, Z. *et al.* Design and synthesis of orally bioavailable 4-methyl heteroaryldihydropyrimidine based hepatitis B virus (HBV) capsid inhibitors. *J. Med. Chem.* **59**, 7651–7666 (2016).

26. Yang, L. *et al.* Treatment of Chronic Hepatitis B Virus Infection Using Small Molecule Modulators of Nucleocapsid Assembly: Recent Advances and Perspectives. *ACS Infect. Dis.* **5**, 713–724 (2019).

27. Xie, J., Sarafianos, S. G. & Wang, Z. Capsid Assembly Modulators : Structure and Pharmacophore-Based Approaches. (2021).

28. Feld, J. J. *et al.* The phenylpropenamide derivative AT-130 blocks HBV replication at the level of viral RNA packaging. *Antiviral Res.* **76**, 168–177 (2007).

29. Ren, Y. *et al.* Discovery and optimization of benzenesulfonamides-based hepatitis B virus capsid modulators via contemporary medicinal chemistry strategies. *Eur. J. Med. Chem.* **206**, 112714 (2020).

30. Na, H. G. *et al.* Discovery of a New Sulfonamide Hepatitis B Capsid Assembly Modulator. *ACS Med. Chem. Lett.* **11**, 166–171 (2020).

31. Zhang, X. *et al.* Discovery of Novel Hepatitis B Virus Nucleocapsid Assembly Inhibitors. *ACS Infect. Dis.* **5**, 759–768 (2019).

32. Wang, Y. J. *et al.* A novel pyridazinone derivative inhibits hepatitis B virus replication by inducing genome-free capsid formation. *Antimicrob. Agents Chemother.* **59**, 7061–7072 (2015).

33. Kuduk, S. D. *et al.* Identification of a new class of HBV capsid assembly modulator. *Bioorg. Med. Chem. Lett.* **39**, 127848 (2021).

34. Pei, Y. *et al.* Discovery of New Hepatitis B Virus Capsid Assembly Modulators by an Optimal High-Throughput Cell-Based Assay. *ACS Infect. Dis.* **5**, 778–787 (2019).

35. Hepatitis, N., Capsid, B. V., Modulator, A. & Responses, P. A. crossm Potent Antiviral Responses In Vitro and in Humanized Mice. 1–12 (2020).

36. Berke, J. M. *et al.* Antiviral properties and mechanism of action studies of the hepatitis B virus capsid assembly modulator JNJ-56136379. *Antimicrob. Agents Chemother.* **64**, 1–15 (2020).

37. Böttcher, B. & Nassal, M. Structure of Mutant Hepatitis B Core Protein Capsids with Premature Secretion Phenotype. *J. Mol. Biol.* **430**, 4941–4954 (2018).

38. Schlicksup, C. J. *et al.* Hepatitis B virus core protein allosteric modulators can distort and disrupt intact capsids. *Elife* **7**, 1–24 (2018).

39. Cui, X., Ludgate, L., Ning, X. & Hu, J. Maturation-Associated Destabilization of Hepatitis B Virus Nucleocapsid. *J. Virol.* **87**, 11494–11503 (2013).

40. Selzer, L., Kant, R., Wang, J. C. Y., Bothner, B. & Zlotnick, A. Hepatitis B virus core protein phosphorylation sites affect capsid stability and transient exposure of the C-terminal domain. *J. Biol. Chem.* **290**, 28584–28593 (2015).

41. Tan, Z., Maguire, M. L., Loeb, D. D. & Zlotnick, A. *Genetically Altering the Thermodynamics and Kinetics of Hepatitis B Virus Capsid Assembly Has Profound Effects on Virus Replication in Cell Culture*. *Journal of Virology* vol. 87 (2013).

42. Wu, S. *et al.* Discovery and Mechanistic Study of Benzamide Derivatives That Modulate Hepatitis B Virus Capsid Assembly. *J. Virol.* **91**, (2017).

43. Ruan, L., Hadden, J. A. & Zlotnick, A. Assembly Properties of Hepatitis B Virus Core Protein Mutants Correlate with Their Resistance to Assembly-Directed Antivirals. *J. Virol.* **92**, (2018).

44. Zhou, Z. *et al.* Heteroaryldihydropyrimidine (HAP) and Sulfamoylbenzamide (SBA) Inhibit Hepatitis B Virus Replication by Different Molecular Mechanisms. *Sci. Rep.* **7**, 1–12 (2017).

45. VANDYCK, Koen; HACHE, Geerwin; Yvonne, Paul; Stefaan, Julien;David, Craig;ROMBOUTS, Geert; VERSCHUEREN, Wim, Gaston; RABOISSON, Pierre, Jean-Marie, B. WO 2014/184350 A1. vol. 5 (2014).

46. Suzuki, Y., Kitajima, T., Flores, A., Surgery, H. & Hospital, H. F. Oral Abstracts. *Hepatology* **72**, 1–1159 (2020).

47. Zlotnick, A., Aldrich, R., Johnson, J. M., Ceres, P. & Young, M. J. Mechanism of capsid assembly for an icosahedral plant virus. *Virology* **277**, 450–456 (2000).

48. Sauviller, S. *et al.* Development of a cellular high-content, immunofluorescent HBV core assay to identify novel capsid assembly modulators that induce the formation of aberrant HBV core structures. *J. Virol. Methods* **293**, 114150 (2021).

49. Tresset, G. *et al.* Norovirus capsid proteins self-assemble through biphasic kinetics via long-lived stave-like intermediates. *J. Am. Chem. Soc.* **135**, 15373–15381 (2013).

50. Uetrecht, C., Barbu, I. M., Shoemaker, G. K., Van Duijn, E. & Heck, A. J. R. Interrogating viral capsid assembly with ion mobility-mass spectrometry. *Nat. Chem.* **3**, 126–132 (2011).

51. Borodavka, A., Tuma, R. & Stockley, P. G. Evidence that viral RNAs have evolved for efficient, two-stage packaging. *Proc. Natl. Acad. Sci. U. S. A.* **109**, 15769–15774 (2012).

52. Stetefeld, J., McKenna, S. A. & Patel, T. R. Dynamic light scattering: a practical guide and applications in biomedical sciences. *Biophys. Rev.* **8**, 409–427 (2016).

53. Lakowicz, J. R., Cherek, H., Kuśba, J., Gryczynski, I. & Johnson, M. L. Review of fluorescence anisotropy decay analysis by frequency-domain fluorescence spectroscopy. *J. Fluoresc.* **3**, 103–116 (1993).

54. Hess, S. T., Huang, S., Heikal, A. A. & Webb, W. W. Biological and chemical applications of fluorescence correlation spectroscopy: A review. *Biochemistry* **41**, 697–705 (2002).

55. Crowther, R. A. *et al.* Three-dimensional structure of hepatitis B virus core particles determined by electron cryomicroscopy. *Cell* **77**, 943–950 (1994).

56. Berke, J. M. *et al.* Antiviral profiling of the capsid assembly modulator BAY41-4109 on full-length HBV genotype A-H clinical isolates and core site-directed mutants in vitro. *Antiviral Res.* **144**, 205–215 (2017).

57. Newman, M., Suk, F.-M., Cajimat, M., Chua, P. K. & Shih, C. Stability and Morphology Comparisons of Self-AssembledVirus-Like Particles from Wild-Type and Mutant Human Hepatitis B VirusCapsidProteins. *J. Virol.* **77**, 12950–12960 (2003).

58. Zlotnick, A., Johnson, J. M., Wingfield, P. W., Stahl, S. J. & Endres, D. A theoretical model successfully identifies features of hepatitis B virus capsid assembly. *Biochemistry* **38**, 14644–14652 (1999).

II.7 Attachments

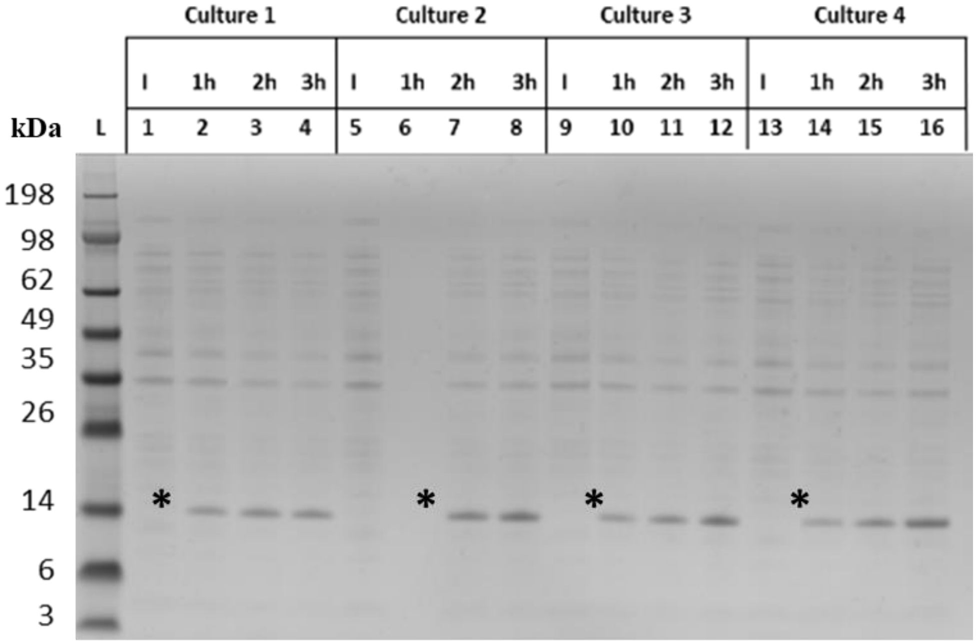

Figure 26 Protein expression of HBV-CP150C-P25S in E. coli Rosetta DE3 (SDS-PAGE): Samples were taken before induction with IPTG (I) and 1 h, 2 h and 3 h post-induction. Line L: Ladder, Line 1-4: Culture 1, Line 5-8 Culture 2, Line 9-12 Culture 3, Line 12-16 Culture 4. A new protein band was observed in every culture after induction with IPTG marked with a black asterix.

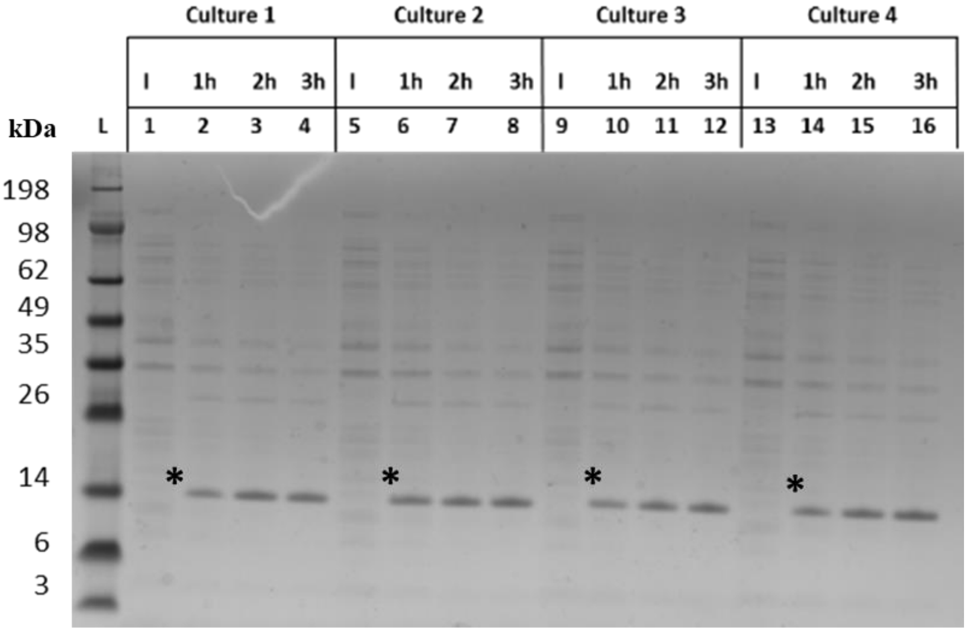

Figure 27: Protein expression of HBV-CP150C-T33N in E. coli Rosetta DE3 (SDS-PAGE): Samples were taken before induction with IPTG (I) and 1 h, 2 h and 3 h post-induction. Line L: Ladder, Line 1-4: Culture 1, Line 5-8 Culture 2, Line 9-12 Culture 3, Line 12-16 Culture 4. A new protein band was observed in every culture after induction with IPTG marked with a black asterix.

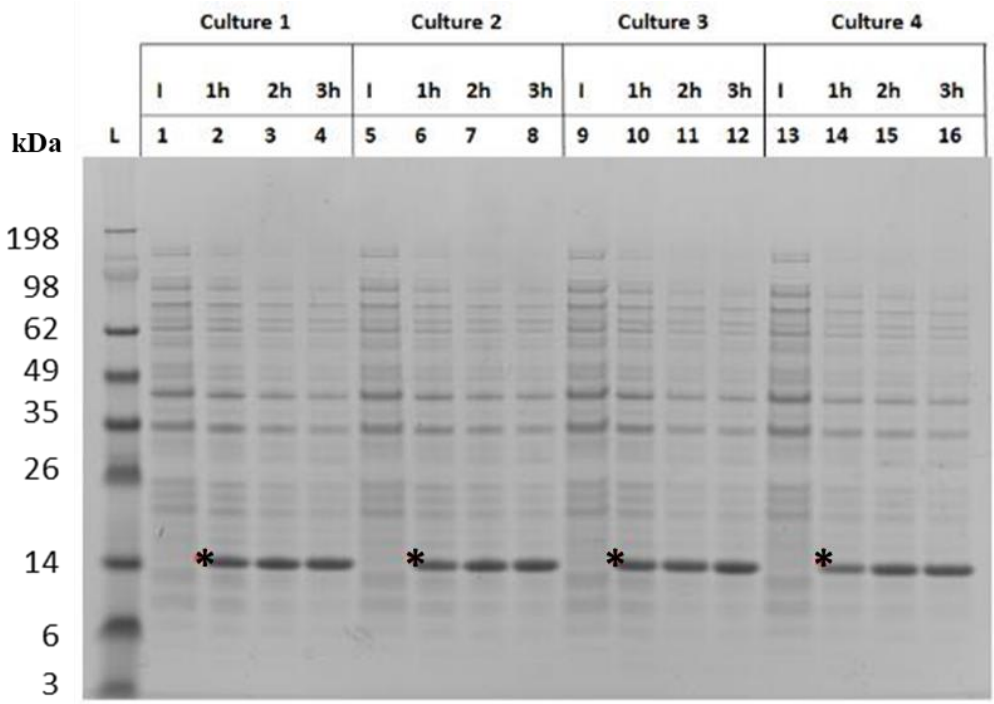

Figure 28 Protein expression of HBV-CP150C-V124G in E. coli Rosetta DE3 (SDS-PAGE) (13.12.18): Samples were taken before induction with IPTG (I) and 1 h, 2 h and 3 h post-induction. Line L: Ladder, Line 1-4: Culture 1, Line 5-8 Culture 2, Line 9-12 Culture 3, Line 12-16 Culture 4. A new protein band was observed in every culture after induction with IPTG marked with a black asterix.

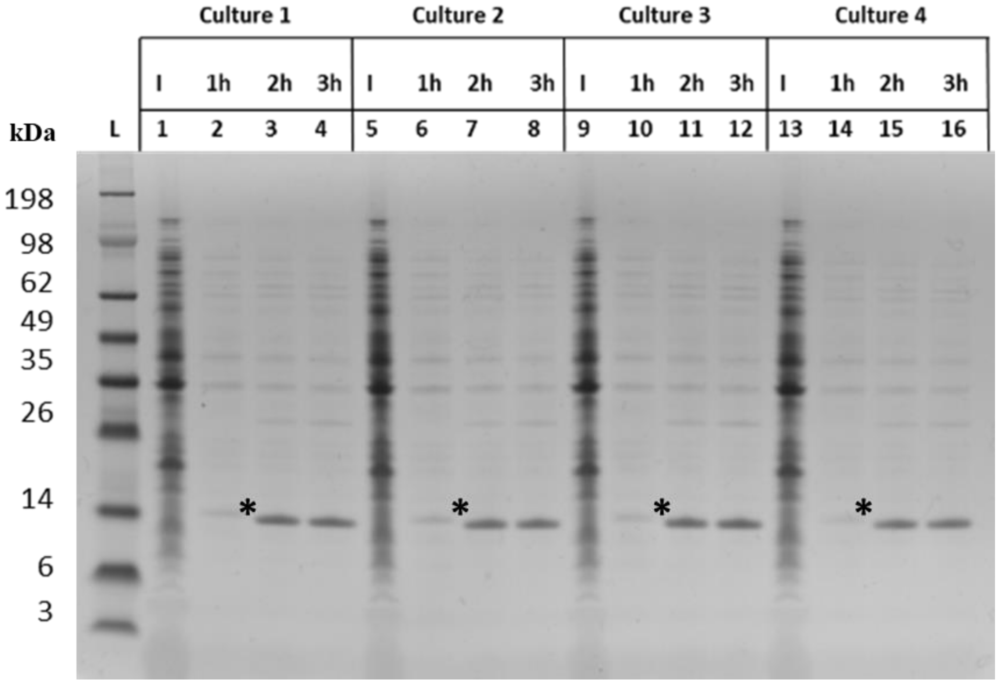

Figure 29: Protein expression of HBV-CP150C-T109I in E. coli Rosetta DE3 (SDS-PAGE) (13.12.18): Samples were taken before induction with IPTG (I) and 1 h, 2 h and 3 h post-induction. Line L: Ladder, Line 1-4: Culture 1, Line 5-8 Culture 2, Line 9-12 Culture 3, Line 12-16 Culture 4. A new protein band was observed in every culture after induction with IPTG marked with a black asterix.

Table 18: Results from the global reconvultion analysis of the decay curves for the anisotropic measurement from the CP150-BO dimers (A), capsids (B), and aggregates (C). The TRFA followed third order with the respective intensities (A1-A3) and decay times (T1- T3). In addition, fundamental anisotropy (B1), as well as the rotational correlation time (φ), were calculated.

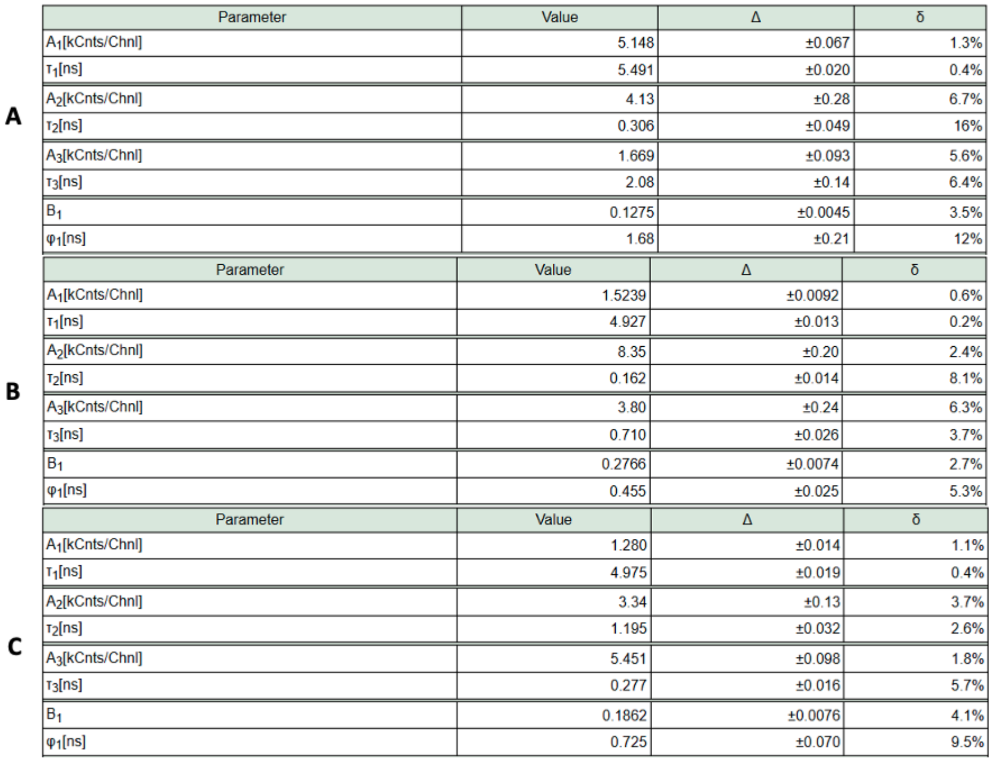

A

Parameter	Value	Δ	δ
A_1[kCnts/Chnl]	5.148	±0.067	1.3%
τ_1[ns]	5.491	±0.020	0.4%
A_2[kCnts/Chnl]	4.13	±0.28	6.7%
τ_2[ns]	0.306	±0.049	16%
A_3[kCnts/Chnl]	1.669	±0.093	5.6%
τ_3[ns]	2.08	±0.14	6.4%
B_1	0.1275	±0.0045	3.5%
φ_1[ns]	1.68	±0.21	12%

B

Parameter	Value	Δ	δ
A_1[kCnts/Chnl]	1.5239	±0.0092	0.6%
τ_1[ns]	4.927	±0.013	0.2%
A_2[kCnts/Chnl]	8.35	±0.20	2.4%
τ_2[ns]	0.162	±0.014	8.1%
A_3[kCnts/Chnl]	3.80	±0.24	6.3%
τ_3[ns]	0.710	±0.026	3.7%
B_1	0.2766	±0.0074	2.7%
φ_1[ns]	0.455	±0.025	5.3%

C

Parameter	Value	Δ	δ
A_1[kCnts/Chnl]	1.280	±0.014	1.1%
τ_1[ns]	4.975	±0.019	0.4%
A_2[kCnts/Chnl]	3.34	±0.13	3.7%
τ_2[ns]	1.195	±0.032	2.6%
A_3[kCnts/Chnl]	5.451	±0.098	1.8%
τ_3[ns]	0.277	±0.016	5.7%
B_1	0.1862	±0.0076	4.1%
φ_1[ns]	0.725	±0.070	9.5%

Chapter III.

Development and automation of the microfluidic system.

III.1 Introduction

Working with microfluidic systems offers the benefits of miniaturization and microfluidic physics behaviors due to the impact of scaling laws.[1] Given the complexity of this format and the differences to well established assays, it is essential to understand the underlying physical governing equations, limitations, and boundary conditions. Only then is it possible to obtain the fitting instrumentation for the specific task to design the experiments accordingly.

The simplest mathematical depiction of an incompressible fluid, thus with uniform density, starts with the static description in a motionless equilibrium.[2] The fluid pressure (p) is described as a sum of the body forces per unit volume $(\vec{f})$ (Equation 3).

Equation 3: Static description of incompressible fluid. p: pressure; f: body force per unit.

$$\nabla p = \sum_i \vec{f_i}$$

In a gravitation field, these forces are given by the pressure on the static column with a density of ρ, parallel to the gravitational field (Equation 4).

Equation 4: Impact of gravitational force on an incompressible static fluid. p: pressure; ρ: density of the fluid, g: gravitational force; z: direction of gravitation.

$$p - p_0 = -\rho g z$$

The application of strain to the static liquids creates flow motion or deformation, described by the kinematics of the liquid, which is the description of the velocity field of the fluid in space and time at any point.[2] In the ideal case of an incompressible fluid, all the kinetic energy received is transformed into the motion of the liquid without loss to internal energy. Another critical factor for fluids in motion is the conservation of mass, described by the continuity equation stating that the total divergence of the velocity vector equals 0, signifying that fluid leaving the defined system must be replaced by the same amount (Equation 5).[2]

Equation 5: First Navier-Stokes equation: conservation of mass. $\vec{u}$: velocity vector.

$$\nabla \vec{u} = 0$$

The conservation of the liquid's momentum is characterized by the Navier-Stokes equation declaring that the mass momentum of a given liquid is the sum of the net stress applied to the liquid's surface and the body forces per unit volume minus the momentum leaving the control volume. For a fluid with uniform density ρ and with conservation of mass, this equation is simplified to the Cauchy momentum equation, where $\vec{u}$ is the velocity vector, $\overrightarrow{f_\iota}$ are the body forces, and $\nabla * \vec{\vec{r}}$ are the stresses applied to the control surface (Equation 6).[2]

Equation 6: Second Navier-Stokes equation: conservation of momentum: ρ: density of fluid; $\vec{u}$: velocity vector; $\overrightarrow{f_\iota}$: body forces; $\nabla * \vec{\vec{r}}$: applied stress.

$$\rho \frac{\overrightarrow{\partial u}}{\partial t} + \rho\vec{u} * \nabla\vec{u} = \nabla * \vec{\vec{r}} + \sum_i \overrightarrow{f_\iota}$$

Under these conditions, the velocity field's deformation is the direct result of the applied strain resulting in the skewing (shear strain), extension (extensional strain), or rotation (solid-body rotation strain) of the fluid. The resulting constitutive correlation between strain rate, due to the applied stress, and flow motion is the fluid's inherent viscosity. According to the Newtonian relations, the increase of shear stress results in a direct correlation of flow velocity field increase (Equation 7).[3]

Equation 7: Newtonian relation between shear stress and flow motion. $\vec{\vec{r}}_{visc}$: shear stress; μ: viscosity; $\vec{\vec{\varepsilon}}$: velocity field.

$$\vec{\vec{r}}_{visc} = 2\mu\vec{\vec{\varepsilon}}$$

Deviations of this model are called shear-thinning fluids or shear-thickening fluids and are mostly observed with larger polymers or colloidal systems. Shear-thinning fluids decrease the effective viscosities with increased strain rate, while shear-thickening behave in the opposite way and increase the effective viscosities upon increased strain rate.

The resulting fluid motion described by the Navier Stokes equation is categorized into laminar, transitional, and turbulent flow requiring analytical solutions for simpler laminar systems up to numerical ones for complex turbulent flows (Equation 6). Laminar flows are described by viscous dominated behaviours with ordered sheets of laminas, stable to external perturbations. On the other hand, turbulent flows are characterized by their inherent instability dominated by random, three-dimensional, and unpredictable flow motions, often leading to random vortices, rotations, and unsteady flow patterns. The transitional flow is in between the two other flow patterns and is mostly predictable but still affine to external perturbations.[3]

The flow pattern of the fluid is dependent on the density ρ, the characteristic length of the system L (usually the diameter), and the liquid's mean velocity $\bar{v}$ and viscosity μ which can be expressed with the dimensionless Reynold number (Re, Equation 8).

Equation 8: Reynold number. ρ: density of the fluid; u velocity of the fluid; L: Characteristic length of the system; μ: viscosity of the fluid

$$Re = \frac{\rho \bar{v} L}{\mu}$$

Re categorizes the approximate transition between the different flow regimes with laminar flows having Re < 2,300 and turbulent ones Re > 4,000. Usually, microfluidic systems have Re ranging from 0.01 to 10, meaning that the flows are strictly laminar, which must be considered for several flow characteristics and mixing.

Under laminar flow conditions, the flow in a small pipe driven by pressure is described as the Hagen-Poiseuille flow (Equation 9).[4,5]

Equation 9: Hagen-Poieuille flow in a symmetric, cylindric pipe. Q: volumetric flowrate; r: radius of the pipe; μ: viscosity of the liquid; ρ: density of the liquid.

$$Q = -\frac{\pi r^4}{8\mu}\frac{\partial \rho}{\partial z}$$

In this case, the Navier stokes equation is simplified by assuming that the steady state is reached with no convective transports of momentum. Therefore, all the flow is in the z-direction (direction of the tubing) without any acceleration, resulting in velocity gradients of 0. Furthermore, the flow is in a symmetrical cylinder with a circular cross-section and constant pressure source. The resulting flow represents a parabolic distribution of a uniform concavity in the pipe dependent on the slip length of the system. In summary, with the above-defined conditions, the volumetric flow rate Q is defined as a function of the pipes radius r, the viscosity μ and density ρ of the liquid, and the flow velocity in the z-direction u_z (Equation 10).

Equation 10: Hagen-Poieuille flow velocity distribution transversal to flow direction. u_z: Flow velocity in z-direction; μ: viscosity of the liquid; ρ: density of the liquid; r: pipe radius, a: distance to the channel center in z direction.

$$u_z = -\frac{1}{4\mu}\frac{\partial \rho}{\partial z}(r^2 - a^2)$$

In turn, the fluidic resistance R is calculated in dependence on the pressure drop across the channel Δp and the volumetric flow rate Q.

Equation 11: Fluidic resistance (R). Q: volumetric flowrate; Δp: pressure drop

$$R = \frac{\Delta p}{Q}$$

The construction and the underlying physics of the microfluidic devices lead to a specific flow condition with low Re but high Peclet number (Pe). The Pe in turn describes the importance of convection to diffusion for the mixing in flow with u being the velocity transverse to diffusion, l the characteristic length of diffusion, and D the diffusion coefficient (Equation 12).

Equation 12: Peclet number. u: velocity transverse to flow direction; L characteristic length of diffusion; D diffusion coefficient.

$$Pe = \frac{uL}{D}$$

Essentially, the flow is strictly laminar and convection-dominated, beneficial for flow patterning but strongly minimizing the mixing, which is performed by diffusion due to non-existing convection normal to the flow's direction. Diffusion itself is a random motion, owing to the thermal fluctuations in the fluid system. This leads to the distribution of heat or matter in the opposite direction to the local highest gradient. In one dimension, the diffusion is described by Fick's law for flux density, which is a good approximation for most quasi 2D microchips with lower heights compared to their width (Equation 13).[3]

Equation 13: Fick's law in single dimension. d: distance traveled by diffusion; D: diffusion constant; t: time.

$$d^2 = 2Dt$$

Consequently, the only option for enhancing the mixing in microfluidics systems without transverse convection elements is the shortening of the channel until the spatial distribution is at the length scale of the characteristic diffusion length. Therefore, to increase diffusion mediated mixing at lower length scales kinematic structures exists including Baker's transformation, stretching and folding of the liquids, and twist maps or vortices. In addition, chaotic mixing is an often-used method for mixing, which describes the exponential increase of interfacial area between two liquids with time (III.4.3.1 Chaotic advection type micromixers).

Finally, the low Re and high Pe flow conditions allow flow patterning relations, compound separation, or dilution. For example, TAD describes the convection-diffusion mediated compound dilution in a circular symmetric microchannel under Poiseuille flow with a length of L and radius of R. If the Pe is smaller than the length ratio (Equation 14), then the compounds are diluted with convection-diffusion mediated TAD (Equation 14, and Equation 15).

Equation 14: Length ratio of a system. L: length in flow direction; R: channel radius.

$$Length\,ratio = \frac{L}{R}$$

The equation in 1 D is thus a function of the average concentration $\bar{c}$, the average velocity $\bar{u}$, and the effective diffusivity D_{eff} (Equation 15).

Equation 15: TAD. $\bar{c}$: average concentration; x: distance traveled; t: time; D_{eff}: effective diffusivity.

$$\frac{\partial \bar{c}}{\partial t} + \bar{u}\frac{\partial \bar{c}}{\partial x} = D_{eff}\frac{\partial^2 \bar{c}}{\partial x^2}$$

The effective diffusivity is, in turn, a function of the diffusivity D, Pe, and A a geometry and flow boundary dependent constant (48 for Hagen-Poiseuille flow) (Equation 16).

Equation 16: Effective Diffusivity (D_{eff}). D: diffusivity; Pe: Peclet number; A: geometry dependent constant.

$$D_{eff} = D(1 + \frac{Pe^2}{A})$$

With the Navier-Stokes relations under the above-described conditions, already many types of fluid motion are modelable. In the next step, the interaction of fluids and other fluids or solids will be elucidated, due to their ubiquitous presence in microfluidics. Compared to conventional batch methods, the surface-to-volume area (SAV) is significantly larger due to the miniaturization of the channel sizes. As the SAV ratio increases in microfluidic systems, so does surface tension; therefore, its effects on the liquids adsorption to microchannels and the formation of liquid droplets in multiphase system. Physically the surface tension γ between phases 1 and 2 is defined as the Gibs free energy of the system (G) minus the free energy of the two phases and thus the energy of the interface (A) (Equation 17).[2]

Equation 17: Young Laplace equation. γ_{12}: surface tension between phase 1 and 2; G: Gibs free energy; A interfacial energy between the two phases

$$\gamma_{12} = \frac{\partial G}{\partial A}$$

Young Laplace defined several static equations based on surface tension allowing the calculations of pressure drops along curved interphase separating phase 1 and 2 with their respective radii and internal pressures (Equation 18).

Equation 18: Young Laplace description of pressure drop along curved interphases. γ_{12}: surface tension between phase 1 and 2; Δp: pressure drop; R: radius of the curved interface.

$$\Delta p = \gamma_{12}\left(\frac{1}{R_1} - \frac{1}{R_2}\right)$$

Furthermore, the equations allowed the determination of the contact angle between a liquid's drop and a solid surface as well as the equilibrium capillary height for a circular tube (Equation 19).

Equation 19: Contact angle between a liquid's drop: γ_{sg}: surface tension between solid and gas interface; γ_{sl}: surface tension between solid and liquid interface; γ_{lg}: surface tension between liquid and gas interface.

$$\cos(\theta) = \frac{\gamma_{sg} - \gamma_{sl}}{\gamma_{lg}}$$

Equation 20: Equilibrium capillary height for a circular tube: ρ: density of the fluid, g: gravitational force; d: direction of gravitation; γ_{sg}: surface tension between solid and gas interface; γ_{sl}: surface tension between solid and liquid interface.

$$H = \frac{4}{\rho g d}(\gamma_{sg} - \gamma_{sl})$$

However, as microfluidics are in constant motion, static descriptions of interfaces and contact are mostly insufficient. Therefore, the kinematic and dynamic definitions of velocity boundary conditions were introduced. The kinematic boundary describes the interaction of the normal fluid velocity to the interface and its consequent deformation. Meanwhile, the dynamic boundary condition describes the fluid motion tangent to the interface, expressed as the total velocity minus the normal one. If the interface is an unmovable solid object, such as the case for tubings, then the direct tangential velocity u_t becomes zero, described as the no-slip condition.[2]

In the ideal case, the interface is a perfectly flat, non-penetrable, noninteractive solid wall, and the molecule is reflected specularly upon hitting the wall with its normal momentum inverted and the tangential momentum reserved. However, this ideal state is never met since no surface is flat on an atomic level, resulting in reducing the average tangential momentum of the reflected atoms.[2] Moreover, dependent on the density of the medium, the atom is colliding with other atoms resulting in bouncing between the wall and medium, hence lowering the tangential momentum even further. If the characteristic length of the tubing is much larger than the atom's distance traveled until collision with another atom of the fluid (mean free path), then the tangential velocity near the wall can be approximated to 0. In the case of liquids, the order of the mean path length is 0.2 Å requiring a proper definition of the tangential velocities at solid-fluid interfaces using the slip length (b) (Equation 21), where n describes the normal coordinate to the interface. If b is 0, then no motion at the wall is observed having a no-slip condition. Meanwhile, nonzero b represents a nonzero tangential velocity at the interface between wall and liquid. In summary, the approximate velocity of the wall of the liquid can be estimated by dividing the slip length by the characteristic length of the system.[2]

Equation 21: Boundary condition of tangential velocity close to an interface. b: slip length; $\overrightarrow{u_t}$: tangential velocity; n: distance normal to solid liquid interface.

$$\overrightarrow{u_t} = b\frac{\partial u_t}{\partial n}$$

With the theoretical foundation of microfluidic systems, an automated microfluidic system was obtained fitting for the adaptation of the HBc assembly assay to flow. In this sense, several different providers were evaluated, and the various steps required for microfluidics, including flow generation, flow control, inflow mixing, inflow dilution, and inflow data measurement, were addressed with the best suiting modular devices.

III.2 Aim of work

The main objective of this chapter was the development and automation of a microfluidic screening system to reduce the time and resource requirements of the hit-to-lead cycle. The setup should be equipped with advanced flow handling modules for multiple compound measurements and an automated interface to the flow synthesis to allow the imminent measurement of compounds' activities. The task includes selecting and evaluating the most fitting modular devices with the optimal characteristics in inflow dilution, mixing, and the assay's readout. Finally, the harmonization of the microfluidic setup using standard software and the evaluation of the obtained data must be addressed. With the combination of automated workflow and data evaluation, the system should perform independent measurements of compounds for several days without human interference and obtain a higher data quality and quantity than microtiter formats.

III.3 Methods, equipment, and materials

Table 19: Materials used in chapter II.

	Materials/ equipment used	**Vendor, article number**
Chemicals	(Fluorescein isothiocyanate) FITC	CAS: 518-47-8
	5,6-Carboxyfluorescein	CAS: 72088-94-9
	50 mM Hepes buffer ph 7.4	CAS: 7365-45-9
	NaCl	CAS: 7647-14-5
	Tetradecane	CAS: 629-59-4
	$SPAN_{20}$	CAS: 1338-39-2
	FC770	CAS: 1093615-61-2
	DBT	Synthesised at Symeres Nijmegen, Netherlands. [6]
	GPA	Synthesised by Symeres Nijmegen, Netherlands. [7,8]
	BAY 41-4109	Synthesized at Bayer AG Wuppertal Germany [9]
	GLS4	Synthesized at Vandyck [10]
	CP150-BO (3 µM)	Expressed, purified and labeled at AiCuris Anti-infective Cures AG, Wuppertal, Germany
Tubings	Rotilabo®-silicone tubes OD 3 mm, ID 1 mm	Analytics Shop, Munich, Germany Catalog number: 9556.1
	Tubing, PFA, 1/16 x 1.0 mm ID	Analytics Shop, Munich, Germany SN: JR-T-4007-M3
	Tubing, PFA, 1/16 x0.75 mm ID	Analytics Shop, Munich, Germany SN: JR-T-4002-M3
	Tubing, PFA, 1/16 x0.50 mm ID	Analytics Shop, Munich, Germany SN: JR-T-4001-M3
	Tubing, PFA, 0.2 mm ID, 1.6 mm OD	Analytics Shop, Munich, Germany SN: AGG1833-65573
	Tubing, PTFE, 2.0 x 1.70 mm	Analytics Shop, Munich, Germany SN: JR-T-6801-M3
	PEEK-Tubing 1/16" OD x 0.13 mm ID	SCP Seitz Chromatographie Produkte GmbH, Weiterstadt, Germany SN: 41.159.013.01
	PEEK-Tubing 1/16" OD x 0.25 mm ID	SCP Seitz Chromatographie Produkte GmbH, Weiterstadt, Germany SN: 41.079.025.00
	Membranfilter hellrot; PVDF 0.2 µm	Klaus Trott Chromatographie-Zubehör; Kriftel, Germany SN: 082530020
Fluigent flow system	Fluigent low pressure Generator (FLPG, pressure source)	FLUIGENT, Jena, Germany item number: FLPG003
	Flow EZ^{TM} 1,000 mbar (Pumps) (X 4)	FLUIGENT, Jena, Germany, item number: LU-FEZ-1000
	Flow rate sensor L (X 3)	FLUIGENT, Jena, Germany, item number: FLU_L_D
	Flow rate sensor M (X 2)	FLUIGENT, Jena, Germany, item number: FLU_L_M
	Flow rate sensor S (X 2)	FLUIGENT, Jena, Germany, item number: FLU_L_S
	High flowrate connection kit	FLUIGENT, Jena, Germany, item number: CTQ_KIT_HQ

	Low flowrate connection kit	FLUIGENT, Jena, Germany, item number: CTQ_KIT_LQ
	Reservoirs (2x50 ml, 1x15 ml)	FLUIGENT, Jena, Germany, item number: P-CAP15_HP, P-CAP50_HP
	Rack for P-caps	FLUIGENT, Jena, Germany, item number: P-Cap_Rack
	LineUP logistic kit	FLUIGENT, Jena, Germany, item number: LU-SPK-0001
	L-Switch$^{\text{TM}}$	FLUIGENT, Jena, Germany
	Switch board, ESS Platform	FLUIGENT, Jena, Germany
	L-Switch connection kit	FLUIGENT, Jena, Germany
	Bubble traps	FLUIGENT, Jena, Germany
	5 ml pointed, high-pressure glass reservoirs	Custom made
CETONI	ROTAXYS 360 LHS	CETONI GmbH, Korbußen, Germany CETONI_ROTAXYS 360 LHS
	neMESY low-pressure syringe 100 µl	CETONI GmbH, Korbußen, Germany CETONI_ neMESY Low-Pressure
AMF technologies	OEM RVM Microfluidic Electric Rotary Valve	AMF ANDREAS MAIER GmbH & Co. KG, Fellbach, Germany SN: V-D-1-12-050-C-U
Checkvalves	Fluigent check-valve	FLUIGENT, Jena, Germany
	CV-3000 inline Cartidge check valve	IDEX Europe GmbH, Erlangen Germany
	SS-2C-KZ-1	Best Fluid Systems GmbH | Swagelok, Hamburg, Germany
Elveflow	OptoReader	Elveflow microfluidic flow control, Paris, France FDG_ELV_OPR-01 (No longer available)
Combo kit	Vici Easy-Flange Combi Kit in Plastic	FLUIGENT, Jena, Germany Case 201539, Lab Unlimited
Microfluidic chips	µ-Slide VI 0.1	ibidi GmbH, Gräfelilfing, Germany
	µ-Slide VI 0.5	ibidi GmbH, Gräfelilfing, Germany
	µ-Slide III	ibidi GmbH, Gräfelilfing, Germany
	VIM2 (droplet)	IPHT, Jena, Germany
	VIM2b (droplet)	IPHT, Jena, Germany
	WCA1b (droplet)	IPHT, Jena, Germany
	ROSAR GF-T75 (mixing)	IPHT, Jena, Germany
	HTM-ST3-1	LTF, Wasserburg, Germany
	3D-Serpentine microreactor	Microfluidic ChipShop, Jena, Germany
Software packages	QmaxElements	CETONI GmbH, Korbußen, Germany
	Microfluidic Automation tool (MAT)	FLUIGENT, Jena, Germany
	All-In-One (AIO)	FLUIGENT, Jena, Germany
	Elveflow Smart Interface (ESI)	Elveflow microfluidic flow control, Paris, France
	GraphPrism7	GraphPad Software Inc San Diego, United States
	KNIME	Cloudera, DYMATRIX, TIBCO, Vertica, Hortonworks, ChemAxon, Schrödinger
	ORIGIN	OriginLab Corporation, Northampton, Massachusetts

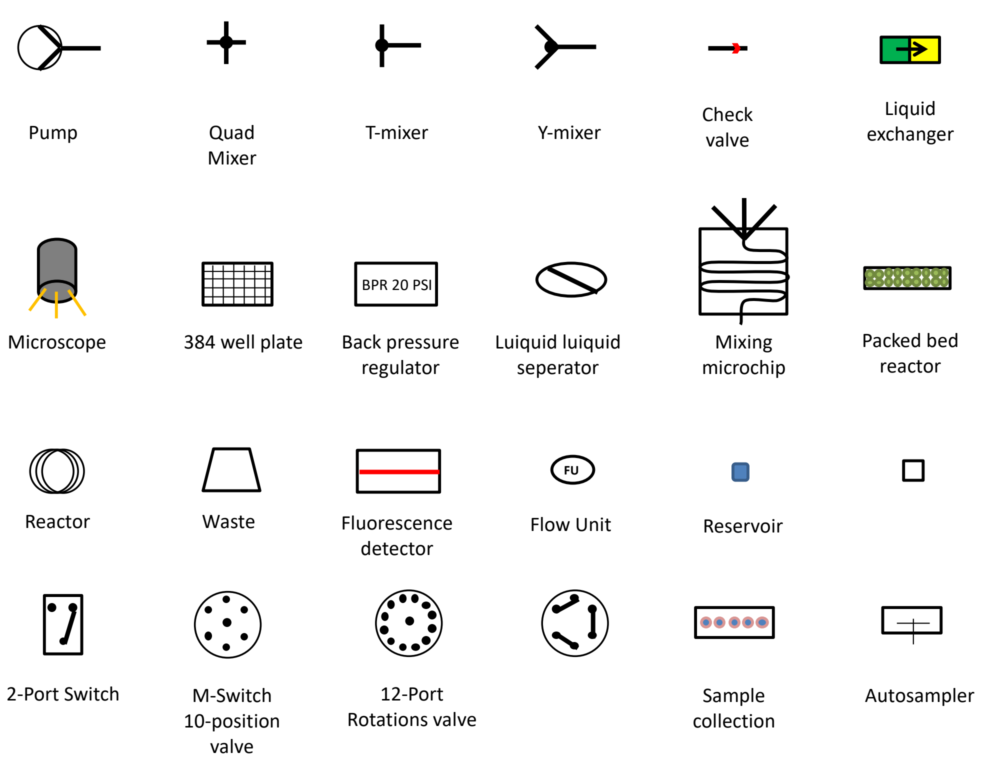

Figure 30: Pictogramms used for the depiction of the flowschemes in the here presented work.

III.4 Results and Discussion

III.4.1 Flow generation and control

Any microfluidic operation starts with the generation of a fluidic flow. Flow driving can be performed either passively without an external energy source, for example with adsorption, absorption (paper-based analytical devices), capillary and gravitation forces, or in an active manner by inducing energy into the system as it is in the case of pressure, electric or magnetic fields, mechanic pressure, centrifugation, ultrasound, piezoelectric, electroosmotic or electrowetting.[11–16]

While passive flow generators are much simpler and easier to use, they usually do not offer the precision for constant flow rates required for a biochemical assay. On the other hand, active micromixers rely on external energy and are more complex but can manipulate and hold flowrates over an extended period with high stability and precision. These active pumps, in turn, can be categorized into displacement and dynamic types based on the method the external force is introduced to the liquid.[17] Displacement pumps execute pressure forces on the fluids by one or more moving mechanical compartments, primarily leading to a pulsing flow.[18,19] For example, the mechanical parts consist of pistons (syringe pumps), aperiodic external energy, rotary or diaphragm based on drivers (piezoelectric,[20] thermopneumatic,[21] electrostatic,[22] magnetic,[23] pneumatic), valves, or chambers. Dynamic pumps continuously add energy either in the form of momentum (centrifugal) or by directly applying pressure (pressure pumps, electroosmotic, magnetohydrodynamic, acoustic, miscellaneous effects), ending in a continuous smooth flow.[17] Over the last 10 years, the most suitable and used active flow generators in organic chemistry and biochemical assay were peristaltic pumps, syringe pumps, and pressure pumps. These pump systems have distinct benefits and drawbacks; therefore, a careful evaluation is needed before the final choice for the system.[17,24,25]

Peristaltic pumps are the only standalone type offering continuous liquid handling by recycling the liquids. The fluid actuation is performed by turning a roller inside a flexible tubing within the pump, generating a vacuum due to compression. The actuation of the roller generates a pulsated flow with a triple effect. These pulses are the main drawback for the generation of laminar flow-based compound dilution (Taylor-Aris-Dispersion), wherefore, this pump category was no longer considered. Furthermore, the pumping of liquids in flexible tubing combined with mechanical stress requires higher maintenance. Other pumps based on mechanical actuation resulting in pulsed flows are solenoid pumps, made of a solenoid-driven diaphragm and two unidirectional check valves, pressure pulse, piezoelectric, and aquarium pumps.[17,26]

The currently most used pump on the market is the syringe pump operated by the rotation of a piston inside a syringe. These modules offer medium flow stability and precision, combined with a low response time (from seconds to hours). Best utilized are syringe pumps to inject smaller volumes of liquids unbeaten by any other type of microfluidic dosing system. Furthermore, the generation of high pressures up to several hundred bars is possible, allowing the flow independent of the system's fluidic resistance. Higher pressure operations are beneficial mainly for nanofluidic devices with high backpressure that would stop the flow otherwise. In synringe pumps the flow control is independent of hydrostatic pressure and fluid viscosity giving the opportunity to perform complex operations which makes syringe pumps very attractive for various applications. The main drawbacks are the mostly missing pressure control, which can lead from liquid fluctuation to the breaking of the syringe dependent on the backpressure generated by the fluid's viscosity or plugging (Figure 31, A). Furthermore, syringe pumps are limited due to maximal volume, maintenance, sample agitation or temperature control difficulties, and chemical tolerance, dependent on the piston's material. Some organic solvents (e.g. Toluene, or DCM) lead to the piston's swelling or shrinking, which can result in leaking. In addition, potent oxidizing agents and corrosive acids start the corrosion of the metal connection parts, and seldom even the glass surfaces of the syringe (Figure 31, B).

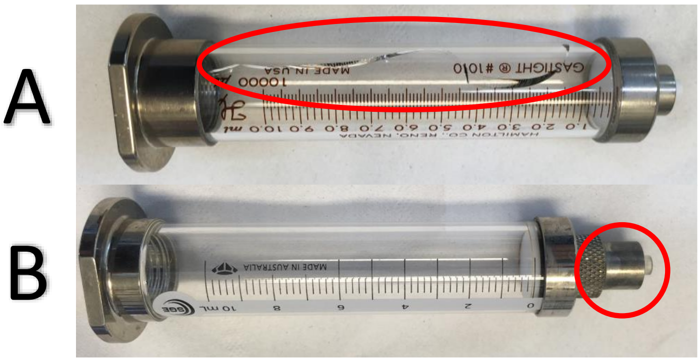

Figure 31: Two used high-precision glass syringes. The first syringe cracked (A) due to a clogging in the system. (B) Utilization of trifluoroacetic acid oxidised the headpart of the second syringe.

Pressure pumps were recently developed and marketed, providing an accurate gas pressure to the respective sealed reservoirs leading to continuous flow. Pressure pumps as standalone cannot measure or control flow rates directly like other types of pumps do, wherefore the addition of flow measuring units are required. The respective flow measure units in combination with the pressure pumps offer the best possible flow stability (pulseless), the response time (approx. 80 ms), and precision (around 0.05 %) of flow rates down to sub-nanoliter per min up today (Table 22). Moreover, the pressurized reservoirs as a liquid holder prevent the contamination of the pumps with fluids leading to facilitated maintenance, the possibility of sample agitation, higher reservoir volumes, and heating or cooling using thermal or ice baths. Especially the last point is crucial for biochemical applications with enzymes or proteins. At the same time, multiple reservoirs can be connected to a single pump, which in combination with a check valve, allows economic screening of multiple compounds using a single unit. The main drawbacks are higher errors with the injection of volumes under 100 µl, small maximum pressures of up to 8 bar, and an impact of hydrostatic pressure influence. The hydrostatic pressure can cause complications in the form of backflow if complex systems with multiple pressure pumps are used, but this issue can be easily circumvented by using different check valves.[27–29]

After careful evaluation of different providers and pumps, it was decided that response time and precision are the main drivers for the developed sytem (Table 20). The measurement of dose-response curves, EC_{50} values, and enzyme kinetics require the optimal consensus of flow rates between the channels to allow accurate stoichiometric mixing and a robust reproducibility between measurements. Therefore, a microfluidic system based on pressure pumps was designed. The maximal possible pressure of 8 bar was not a further issue since the size of the target microreactors is in the range of 40 µM to 1,000 µM resulting in manageable backpressure.

Two companies (Fluigent, and Elveflow) offered suitable equipment and expertise in comparison to other suppliers. Likewise, the pressure pumps from Fluigent (LU-FEZ-1000) and Elveflow (OB1 M3+) were compared to a high precision syringe pump of CETONI for the final evaluation (Table 21). The syringe pump performed far better at maximal pressures, and maximal flowrates. These values are not of interest for the target assay due to the low maximal planned flowrates around 1 ml/min. The two pressure pumps outperformed the syringe pump in every other aspect offering response times of 80 ms (Fluigent) and 9 ms (Elveflow), excellent flowrate stabilities, and precision. Furthermore, both companies provided identical flow measure units for several different flowrate ranges covering from 1 µl/min to 5,000 µl/min and were close in performance and price wherefore the final decision was based on logistics and better customer support (Table 22).

Table 20: Benefits and drawbacks of peristaltic, syringe and pressure pumps.

	Peristaltic pump	**Syringe pump**	**Pressure driven pump**
Flow stability	Bad	Medium	Excellent
Response time	High (10 s to 1 min)	Low (10 s-1 h)	Excellent (down to 80 ms to 1 min)
Precision	Bad (pulsation)	Medium (1 % of the flowrate)	Excellent (0.05 % of the flowrate)
Volume limitation	No	Dependent on syringe volume	Dependent on reservoir volume
Gas injection	No	No	Yes
Sample agitation and temperature control	Possible	Not possible	Possible
Flow pressure control	Yes	No	Yes
Flow rate control	Yes	Yes	No
Complex flow profile	No	Yes	Yes
Hydrostatic pressure influence	No	No	Yes

Table 21: Comparision of three different flow generators.

	FLUIGENT (LU-FEZ-1000)	**Elveflow (OB1 MK3+)**	**CETONIA (OEM neMESYS 310)**
Pressure range	0 – 1,000 mbar	0 – 2,000 mbar	Up to several hundred bars
Pressure stability	0.005 %	0.005 %	
Flowrate range	8 nl /min – 5000 µl/min (dependent on flow measure unit and tubings/backpressure)	7 nl/min – 5000 µl/min (dependent on flow measure unit and tubings/backpressure)	100 nl/min – 600 ml/min (dependent on the syringe)
Flow stability (aqueous)	Excellent (0.05 %)	Excellent 0.05 %)	Medium (around 1 %)
Response time	80 ms	9 ms	1 s- 1 min
Liquid compatibility	Any liquid type (contained in reservoirs)	Any liquid type (contained in reservoirs)	Dependent on the syringe (Incompatible with corrosive acids and organic compounds)
Operational temperature	0-55 °C	0-55 °C	0-45 °C

Table 22: Optimal area of activity of the flow measure units.

	Flow unit S	**Flow unit M**	**Flow unit L**
Sensor inner diameter	150 µM	430 µM	1 mm
Wetted materials	PEEK and quartz glass	PEEK and borosilicate glass	PEEK and borosilicate glass
Maximum pressure	200 bar	100 bar	15 bar
Flowrate range (aqueous)	0 ± 7 µl/min	0 ± 80 µl/min	0 ± 1000 µl/min
Flowrate accuracy (aqueous)	5 % mv above 0.42 µl/min	5 % mv above 2.4 µl/min	5 % mv above 40 µl/min
Flowrate repeatability (aqueous)	0.5 % mv above 0.42 µl/min	0.5 % mv above 2.4 µl/min	0.5 % mv above 40 µl/min

Since Fluigent was more promising in this regard, the initial system was purchased containing a low-pressure generator 1,000 mbar pressure pumps Flow EZ^{TM} 1,000 mbar two C-caps for 50 ml reservoirs, and one for a 15 ml reservoir, and three different types of flow measure units (Figure 32 and

Table 22). For the dosing of compounds between the microtiter well format and the 5 ml reservoirs the syringe pump neMESY low-pressure syringe was used given the better precision at injection of low volumes.

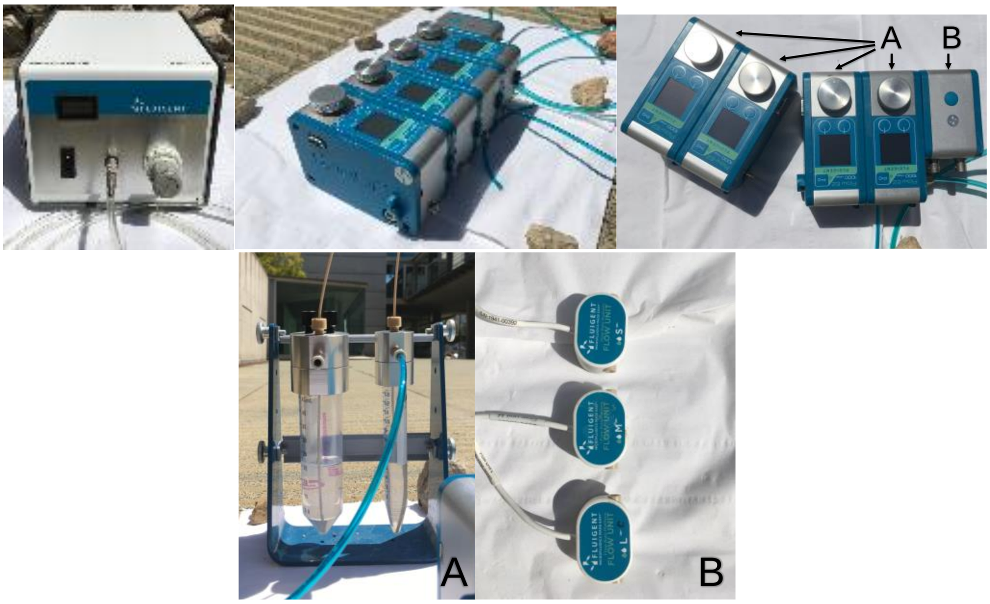

Figure 32: Microfluidic system from Fluigent used for flow generation. (Upper row) Fluigent low pressure generator (FLPG) as a pressure sorce for up to 8 pressure pumps and **(A)** Flow EZ^{TM} 1,000 mbar pressure pumps connected to each other. The LineUp logistic kit **(B)** served as an interface to the computer and the pressure source FLPG. **(Lower row): (A):** C-caps used to seal 50- and 15-ml Centrifuge tubes serving as pressure reservoirs connected with pneumatic tubings (blue) to the respective pressure pumps. **(B)** Flow measure units in three different sizes (L, M, and S) directly connected to the pressure pumps to measure and control the flow rates via a feedback loop.

The initial system was examined for flow stability, fluid leakage, and plugging with the testing of pressure-dependent flowrates using H_2O in the provided PFA tubings with an inner diameter of 0.5 mm. The generated flow was not stable, and the pressure at a given flow rate was subject to fluctuations even with the correct tightening of the connections. Besides, variations of the heights of different parts of the tubings or the simultaneous operation of two pumps in one microreactor increased the flow fluctuations, which will result in the backflow of the mixed liquids into one of the reservoirs, distorting any results. Consequently, flow fluctuations had to be prevented by upgrading the system with higher resistances for flowrate alterations. As discussed previously, the pressure drop in a pipe can be calculated according to Hagen–Poiseuille equation (Equation 22):

Equation 22: Hagen-Poiseuille's equitation: p: pressure; µ: viscosity; L: characteristic length of the system; Q: volumetric flow rate; R: characteristic radius of the system

$$\Delta p = \frac{8\mu LQ}{\pi R^4}$$

According to this formula, decreasing the radius of the capillaries would enhance the pressure difference by the power of 4. Therefore, other effects such as the length of the tubings and the gravitational impact due to differences in the tubings' height are minimized. In this regard, the pressure-flow characteristics of three peek capillaries with an inner diameter of 0.13 mm with a length of 50 cm were determined by collecting for 30 s the flowthrough and comparing it to the pressure increments for several biochemically relevant solutions (Figure 33 and Figure 35).

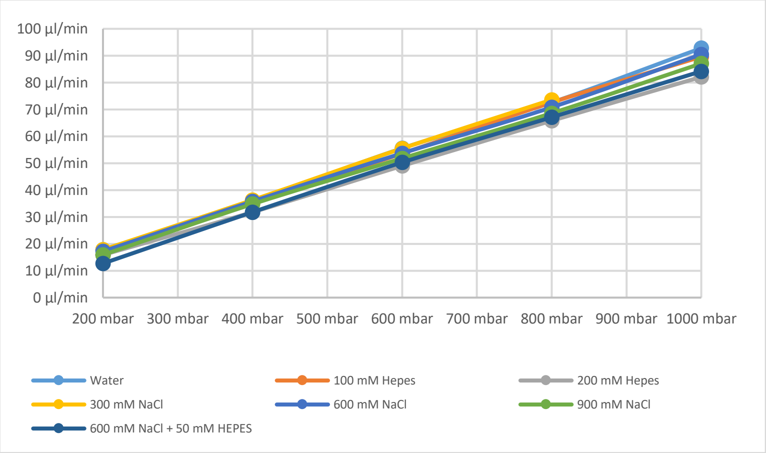

Figure 33: Measured flowthrough characteristics of several biochemically relevant solutions as a function of the pumps pressure. Measurements were repeated in three technical deviates, with the error bars behind the point markers. The absolute flowrates of the solutions at constant pressure rates differ due to slight differences in liquid viscosities (Figure 34).

Most of the solutions behaved as Newtonian solutions in the tested pressure range, and the measured values (collected flowthrough) were in perfect correlation with the flow unit displayed ones (displayed value), except for a couple carrier oils. Overall, liquids of different NaCl and HEPES concentrations had slightly different pressure flowthrough characteristics dependent on their viscosity. Still, no deviations were observed between the measured and the displayed values (Figure 34 and Figure 35). Larger variations between measured and displayed values were observed for the FC770 and tetradecane-based oil solutions requiring a correction factor for the flow measurement unit to work correctly (Figure 35). In these cases, the measured flowrates were depicted as a function of the displayed flowrates, and the resulting functions were used to adjust the displayed flowrates (Figure 36). The deviations for tetradecane were addressed easily by adjusting the viscosity difference using a linear function. On the other hand, FC770 behaved as a dilatant fluid, wherefore the resulting correction function had to be a polynomial of third-order.

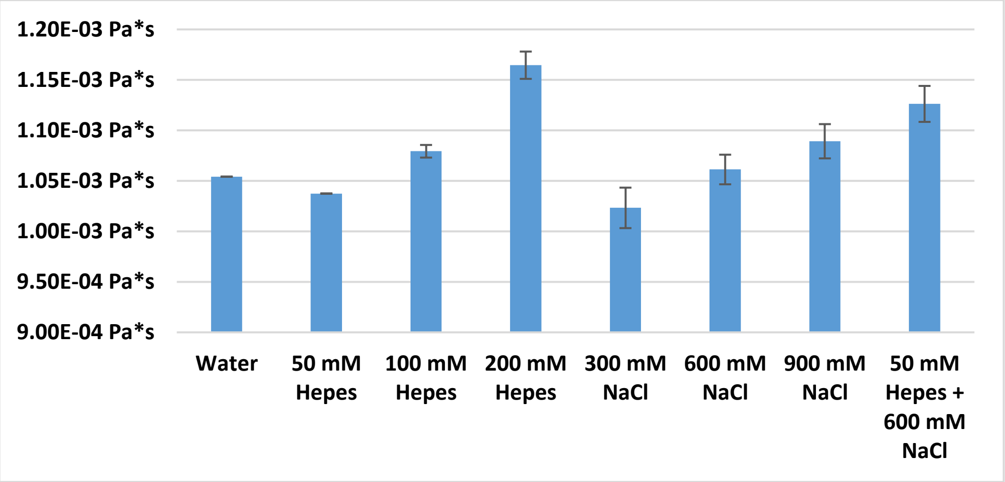

Figure 34: Viscosities of several biochemically relevant solutions determined in thin capillaries with the dimensions of L:50 cm and ID of 0.14 mm. The viscosity was calculated with the Hagen-Poiseulle’s law based on the flowthrough rates of the samples.

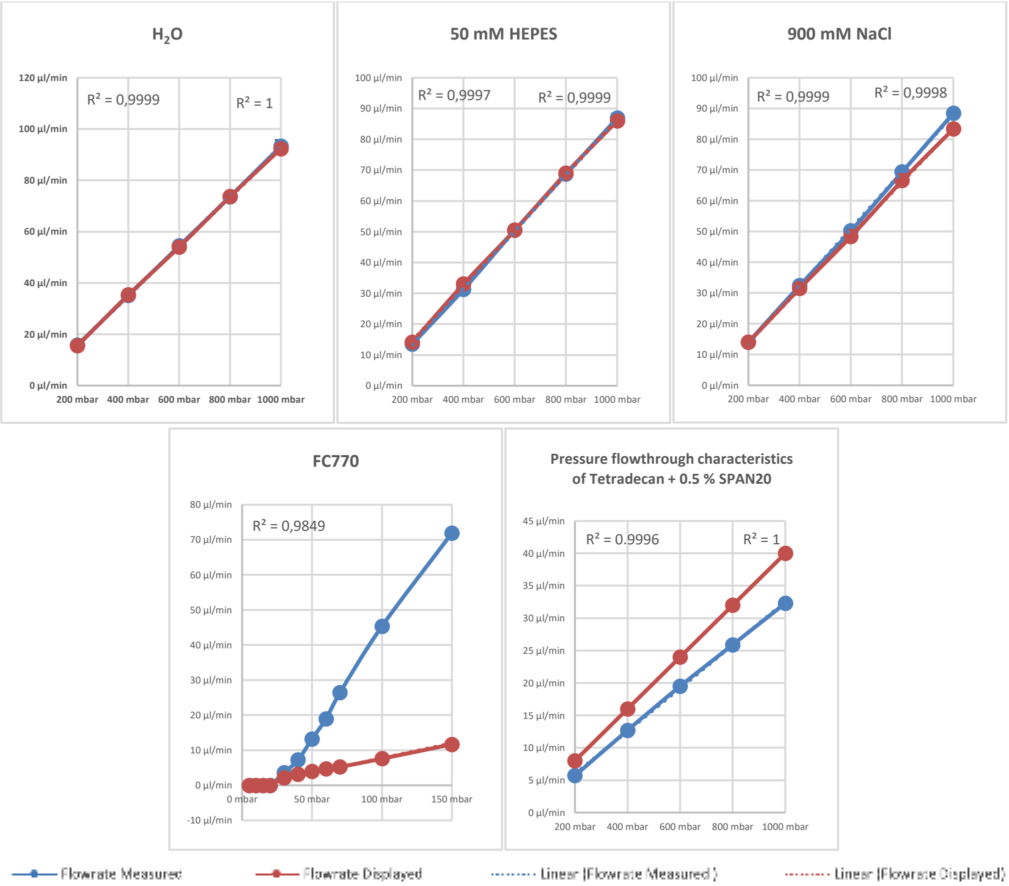

Figure 35: Pressure flowthrough characteristics of oils and other liquids which are relevant for the biochemical CP150C assembly assay. The flowrates displayed by the flow units are marked red, the measured flowthrough in blue. Each measurement was repeated three times, and the standard deviations are depicted as error bars. In addition, R^2 was calculated for the linear approximation are displayed in the top left corner for the displayed and in the top right corner for the measured values.

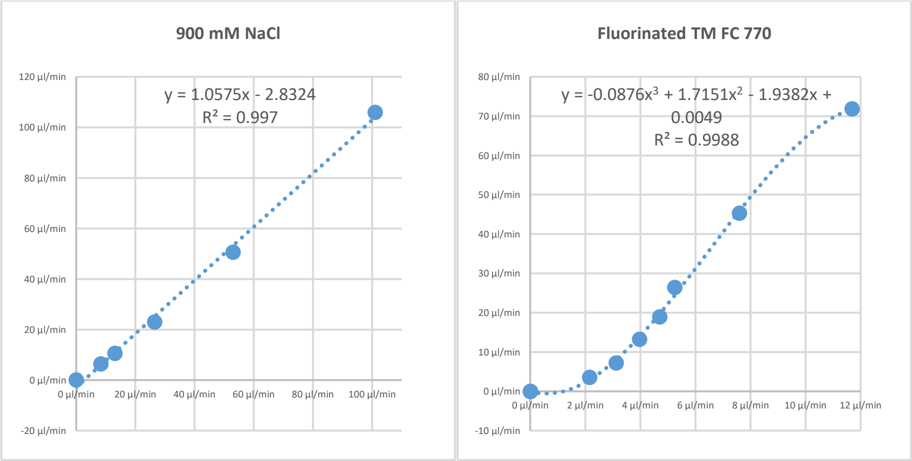

Figure 36: Correction factors used for 900 mM NaCl and fluorinated TM FC770. The measured flowrates were depicted as a function of the displayed flowrates and the obtained functions was used to adjust the flowrates in future measurements.

In systems with two or more pumps connected to a single chip, a backflow from one pump to another can occur if the backpressure is too high. Accordingly, three different check valves from Fluigent, IDEX, and Swagelok were taken into consideration to prevent flow fluctuations and backflows (Table 23).

Table 23: Technical data of the three checkvalves.

	Fluigent check-valve	**CV-3000 inline Cartidge check valve**	**SS-2C-KZ-1**
			
Supplier	Fluigent	IDEX Health and Science	Swagelok
Inner volume	49 µl	150 µl	500 µl
Material	PEEK / Perfluoroelastomer	PEEK / Perfluoroelastomer	Stainless steel
Maximal pressure	138 bar	69 bar	69 bar
Problems	Backflow can occur spontaneously if the sphere inside the valve is displaced.	Backflow can occur spontaneously if the sphere inside the valve is displaced.	High inner volume, flowrate fluctuations in the respective flow channel

The Swagelok check valve was disregarded due to the high inner volume of 0.5 ml and the fluctuations it caused in the flowrate generation. On the other hand, IDEX performed far better than the Fluigent check valves and was used as the standard check valve for the system. Major issues were the sporadic failure of the IDEX check valves to prevent backflow, which mainly occurred after air passing through a valve or if the pumps were used to generate periodic pressure jumps. The check valve were reset by following three steps:

(1) Flush the check valve with air
(2) Connect the valve backward and flush it again with air
(3) Fill the valve with a liquid and apply backflow to test the functionality

In this sense, pressure jumps or air in the system should be avoided as much as possible. The initial system with the flugient pumps produced stable, precise continuous flows with an excellent response time. Backflow and flow instabilities were prevented by using CV-3000 inline cartridge check-valves and peek tubings with a small inner diameter connected directly after the reservoirs (Figure 37). In the following steps, the system was complemented with readout and mixing units to enable first measurements of the biochemical reactions.

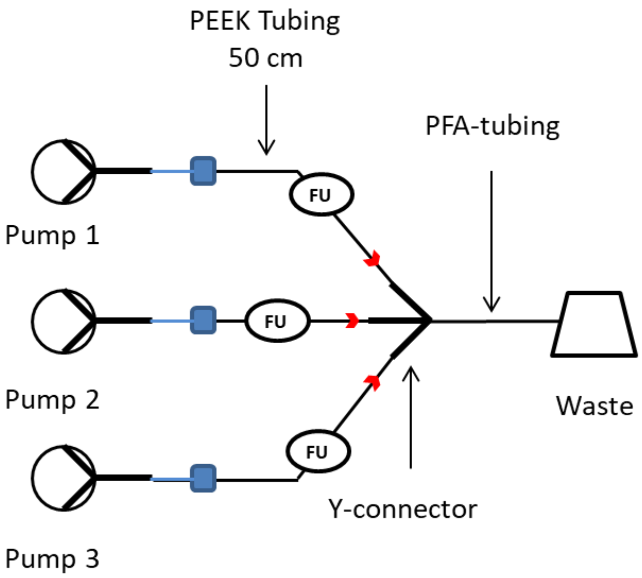

Figure 37: Flow scheme of the innitial system with pumps and checkvalves. This initial system was able to generate flowrates of three different liquids with the Fluigent pressure pumps, which were connected with a Y-mixer. Legend for the various units is depicted in Figure 30.

III.4.2 Fluorescence spectrometer-based readout

A microfluidic system provides strong miniaturization possibilities to reduce sample consumption and measurement times while enhancing the assay's specificity at the same time. In order to utilize these benefits to their full potential, the detection technology used must be sensitive enough to monitor the given entities in real-time selectively. In recent years, strong efforts were made on detection methods with increased sensitivity, reproducibility, precision, speed, automation, low power consumption, minimal sample preparation, and potential for multiplex analysis and compactness at a manageable cost.

The most used detector types in the research and industry nowadays are based on electrochemical, mechanical, or optical methods. [30–34] Electrochemical detectors use conductance, resistance, and capacitance to distinguish between the samples. These methods are widely used in point of care due to real-time detection and low-cost fabrication of mostly unlabelled samples. Even so, limitations arise due to the necessity to control the ionic concentrations before detection and the requirement for conductive materials.

Mechanical detectors allow the label-free detection of samples based on surface stress or alteration of the resonant frequency on the mechanical sensors. Major drawbacks are the long detection times of up to 30 min, limitation of liquid samples due to the damping effect, and the complex fabrication of the sensors.

Finally, optical detection methods including fluorescence, chemiluminescence, absorbance, and surface plasmon resonance are based on variations in light intensity, interference, or refractive index. These methods need minimal to moderate sample preparation, such as labeling, and require more expensive systems than electrical or mechanical methods. However, optical methods are non-invasive/ non-destructive and ubiquitous in most research groups used for quantitative proteomic analysis, infectious disease diagnostics, lab-on-a-chip devices, and conventional laboratories leading to excellent know-how.[35] Additionally, it is the best choice for the real-time detection of samples providing the highest temporal (real-time) and spatial (sensitivity and robustness) resolution for the detection of bio-analytes down to the micro and nano scales in-situ or in-line.[32]

Therefore, a fluorescence based optical detector was used in the microfluidic system. Fluorescence is a three-staged process based on (1) the excitation of the electrons of a fluorophore by absorption of photons with suitable wavelength followed by (2) a short-excited state lifetime and (3) the emission of fluorescence light. After excitation, the fluorophore undergoes conformational changes in 1-10 ns and releases energy in the form of vibration due to collision and interaction with other molecules (internal conversion) until the first relaxed singlet excitation state is reached. Finally, fluorophores relax to the ground state by the emission of a photon of a longer wavelength than the one initially used. The difference in wavelength of the exciting and released photon is called Stokes's shift resulting in a deviation of the band maximas for the absorption and emission spectra. Using different fluorophores with optimal size and quantum yield to label several biological samples allows the selective multiplex analysis with exquisite sensitivity and selectivity at real-time.[36] However, sample dependent problems can arise from photodecomposition, inner filter effects, collisional quenching, fluorescence resonance energy transfer (FRET), Rayleigh and Raman scattering, and intersystem crossing. Many of these complications (FRET, Scattering, inner filter effects) are strongly dependent on the fluorophore concentration and lead to subtractive or additive interferences. As a result, the miniaturization of the microfluidic systems and readout chambers further improves the already strong sensitivity of the method by reducing most of these unwanted effects.[34] Of course, the adequate choice of labeling dyes is an essential factor, as it is correlating with quantum yield, reflection, absorption and even FRET if Stoke's shift is not large enough.[36]

Equally important is the well-considered choice of the fluorescence readout device, as it has a notable impact on the quality of the obtained data. It starts with selecting the light source with a more elevated focus on the lamp's intensity, lifetime, and wavelength characteristics. At the time, three types of light sources are employed: broadband sources such as mercury-arc and tungsten-halogen lamps, laser sources with a well-defined peak over a few nanometers, and high-output light-emitting diodes (LEDs) with the intrinsic low cost, energy consumption, and a long lifetime.[37] Selective excitation of the fluorophores with a wavelength close to their absorption maximum is usually striven to increase the method's selectivity. Laser light sources excel in precisely this, while LEDs have a broader spectrum requiring a bandpass excitation filter that only transmits a narrow range of the wavelengths. Aside from the excitation filters, emission filters and lenses are build into the complex optical pathway to focus the emitted light since it is up to three orders of magnitude lower than the excitation using fluorescence readouts. The detection can also be challenging, leading to the development of CCD cameras or photon counting modules. Furthermore, the detector is usually equipped with a photomultiplier tube to further enhance the light signal.[32,35,38]

Finally, the fluorescence spectrometer used in microfluidic applications must have a strong light focus since most of the microreactors used had parameters of 1 mm height and channel sizes of 40 µm width and 300 µm. With these factors in mind, several commercially available fluorescence spectometers were compared and evaluated.

One of the major challenges initially recognized was the absence of suitable spectrometers for microfluidics offered by most companies, such as Edinburgh

Instruments, Thermo Fischer Scientific, Shimadzu, Horiba Instruments, DeNovix, Agilent Technologies, Lumex instruments, which were specifically manufactured for the use of standard cuvette or microtiter plate formats. On the other hand some companies, such as Ocean Insights and Avantes, offered possible fluorescence spectrometer adaptations for microfluidic systems, however, these were more extensive and optimized for higher volume analysis of at least 62 µl, making the high-resolution detection of smaller samples an impossible task. Subsequently, the only available instrumentations were offered by the microfluidic system providers. However, even here only two companies offered fluorescence-based readout systems. The first device was an inverted fluorescence video microscope from LabSmith, the second a fluorescence spectrometer from Elveflow (Figure 38).

Figure 38: Optical readout devices provided by microfluidic companies. On the left: OptoReader from Elveflow connected to the 3D alignment platform with a duplex optical fiber cable. On the right, SCM340 from LabSmith.

The reserved fluorescence video microscope SCM340 is equipped with an extensive filter, camera, illumination (up to 4-channel synchronous), objectives (10 x DIN), and a motorized reverse and focus system that allows real-time data acquisition in high resolution. The crucial benefits of SCM340 are the all-image resolution over the whole microfluidic chip length enabling the observation of the development of fluorescence reactions over the full kinetic spectrum. However, a significant drawback is the large amount of image data generated, resulting in complications with the storage and evaluation. The primary function of the microfluidic system is the continuous screening of multiple compounds over several days up to weeks which would generate terabytes of data. Hence, using a fluorescence spectrometer with the adjustable acquisition was much more promising.[39]

The compact (35 cm^2 x 25 cm^2 x 12 cm^2) fluorescence spectrometer "OptoReader" from Elveflow offered several benefits as a readout device. Vital strengths were the fast acquisition of data points up to 100 kHz, high sensitivity with the possibility to detect down to 1 nm FITC, and the compact duplex optical fiber (50 µM) based alignment allowing the real-time processing of the fluorescence data. With the provided alignment platform and the small fiber core diameter of 50 µM, a robust 3D focus was achieved in the microreactor, enabling the detection of fluorescence in a 35 µM spot. As a light source, a blue diode with a maximal excitation wavelength of 470 nm was used. To detect BODIPY labeled proteins, a FITC fluorescence filter set was installed, permitting excitation of the fluorophores at 475 nm and detection of the resulting fluorescence at 530 nm. More information is noted on the homepage of sources for those who are interested in further specifications and details.[40]

Following the readout's establishment different microfluidic chips were evaluated as optical detection cells focusing on transparency, scattering, and light absorption properties as well as biocompatibility. The CP150-BO dimer signal was measured compared to the background of the chip (50 mM HEPES (S/ B_1)) and of 5 M NaCl assembled CP150-BO capsid ratios (S/ B_2). During the experiments, the laser diode power and the gain were standardized to 1 % and 3.6 %, respectively, to allow comparative results.

The initial glass microreactors obtained from LTF were proven unsuitable for optical detection, given that the dimer signal was barely distinguishable from the HEPES signal. In search of other more suitable solutions, ibidi microchips were purchased and evaluated. These units are specialized for fluorescence microscopy and spectroscopy, and in agreement with this, the tested chips (µ-slide VI 0.1 and µ-slide VI 0.5) showed the best-observed signal to HEPES ratio and a reliable S/ C ratio. Other microreactors used in later experiments such as the Active Droplet Manchip 2, WCA1ab, VIM2, and VIM2b from Dr. Henkel (IPHT) showed a solid signal to dimer to the background and good dimer to capsid ratios (S/ B_1: 20, S/ B_2: 4.8) but were not reaching the optical properties of the ibidi slides (Figure 39).

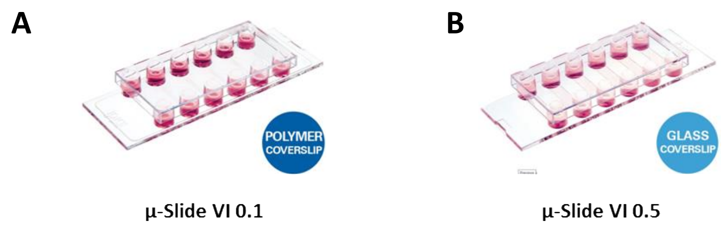

Dimer / HEPES: 49
Dimer / Capsid: 8.54 (1.5 µM CP150c + 2.5 M NaCl)

Dimer / HEPES: 7.25
Dimer / Capsid: 6.25 (1.5 µM CP150c + 2.5 M NaCl)

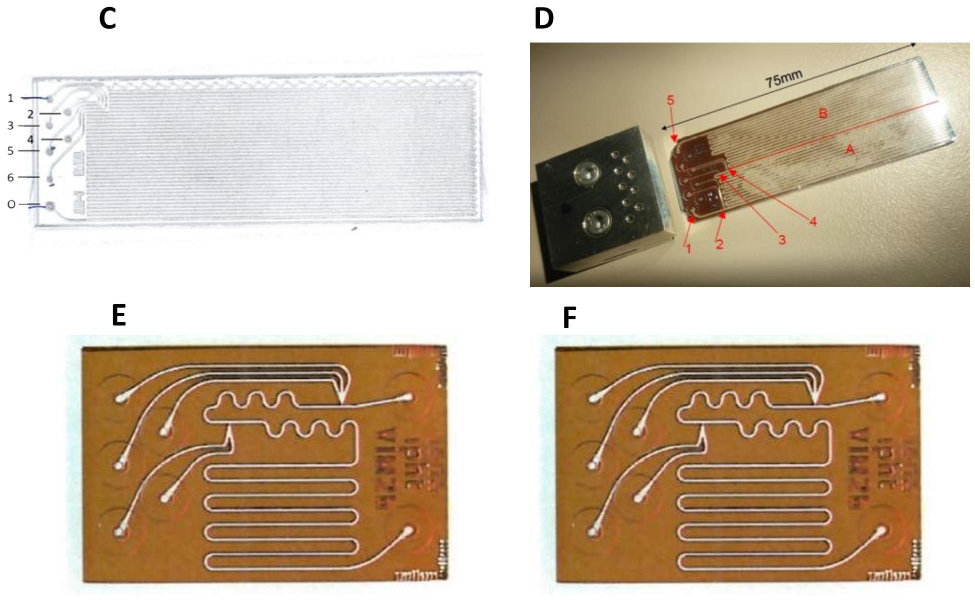

Dimer / HEPES: 20 (1.5 µM CP150c)
Dimer / Capsid: 4.8 (1.5 µM CP150c + 2.5 M NaCl)

Figure 39: Main microfluidic chips evaluated for optical readout properties. The signal ratio of a labeled CP150-BO dimer (Dimer) is calculated against 50 mM HEPES as a background, or against the 2.5 M NaCl assembled labeled CP150-BO capsid. The best performance was obtained by the µ-Slides from ibidi (A) and (B). Several microfluidic chips provided by IPHT (C-F) possessed good optical properties.

However, the ibidi chips were unpractical in later experiments due to the large connecting volume of 1 ml leading to high amounts of compound waste as well as limiting the utilization of inflow dilutions with TAD (IV.4.1 Experimental screening of volume normalized capillaries to determine the optimal capillary parameters for unilateral TAD measurements). Therefore, the VIM2 and VIM2b type glass microreactors were utilized for further studies.

After evaluating the microreactors the advanced settings of the OptoReader were evaluated using dilution curves of FITC. The main objective was to obtain optimal gain and light source power settings to produce data with the best dimer to capsid (D/C), to background (D/B), and to noise (D/N) ratios. Furthermore, to prevent subtractive effects such as fluorescence quenching, which would falsify the calculated EC_{50}-values, the linear detection range of the system and the boundary to the dynamic detection range were investigated. Finally, to determine the minimal detection concentrations, the limit of detection (LOD) and the limit of quantification (LOQ) were determined. The mathematical definition was defined as three times the standard deviation of the blank (k=3) added to the mean of the blank. LOQ is the smallest concentration that can be quantitatively detected with a stated accuracy. According to Currie's definition, the limit of detection can be defined as the signal to noise multiplied by 10 (k=10) (Equation 23). [41]

Equation 23: Calculation of the LOD and LOQ. C: Analyte concentration; B: Mean blank value; k: numerical factor chosen according to the confidence level. In the case of LOD, k equals 3, for LOQ k is 10; sB standard deviation of the blank value.

$$C = B + k * sB$$

The experiment was conducted using dilution steps of FITC from 3.2 nM to 32 µM covering 5 logarithmic ranges. The relative fluorescence (RFU) of FITC was measured as a function of the diode's laser power and the gain settings in three independent experiments, respectively (Figure 71 to Figure 73). The background was subtracted from the arithmetic middle value of the fluorescence values and depicted with the standard deviation between the measurements (Figure 74 to Figure 76). With the obtained data, the signal to background (H_2O) and the signal to noise (arithmetic middle value of 30 data points over 3 s) were calculated (Figure 79). Analyzing the data following observations were made: First, Increasing the gain reduces the noise of the measurement drastically for lower concentrated fluorophores. Secondly, increasing the diode power until the limit of detection increases the S/N ratio, exceptionally for higher concentrated fluorophores, but decreases the S/B ratio especially for higher concentrated fluorophores (Figure 77 and Figure 78). Naturally, higher gain settings and diode powers lead to the detector's faster saturation, impairing it for higher dye concentrations. Overall, the benefits of the increased signal-to-noise ratio were quantitatively more substantial than the decrease of signal to background, wherefore increasing the diode power to the limit of the linear detection range is essential to get the best possible results. For every compound concentration, this region was determined by calculating the linear regression of the RFU plotted against the diode power and only until R^2 stayed above 0.999 (Figure 74 to Figure 76)

In conclusion, there is no universal setting optimal to every fluorescence dye, quantum yield, or concentration. Instead, it must be determined specifically for the required application. In the case of FITC, which will be used more excessively in the course of this work, the optimal detection ranges are listed in the table with a limit of detection was 3.2 nm using a gain of at least 3.6 (Table 24). With these parameters, three different calibration curves were generated, allowing the determination of FITC concentrations over 5 logarithmic ranges (Figure 40).

Table 24: Optimal regions for detecting low to high concentrations of sodium fluorescein in dependency of the gain and diode power of the OptoReader.

	Low concentrations	**Middle concentrations**	**High concentrations**
Diode power	4.8 %	3.2 %	3.1 %
Gain	10	3.6	1
Range of detection	0.0032-0.106 µM	0.032-3.2 µM	0.32-32 µM

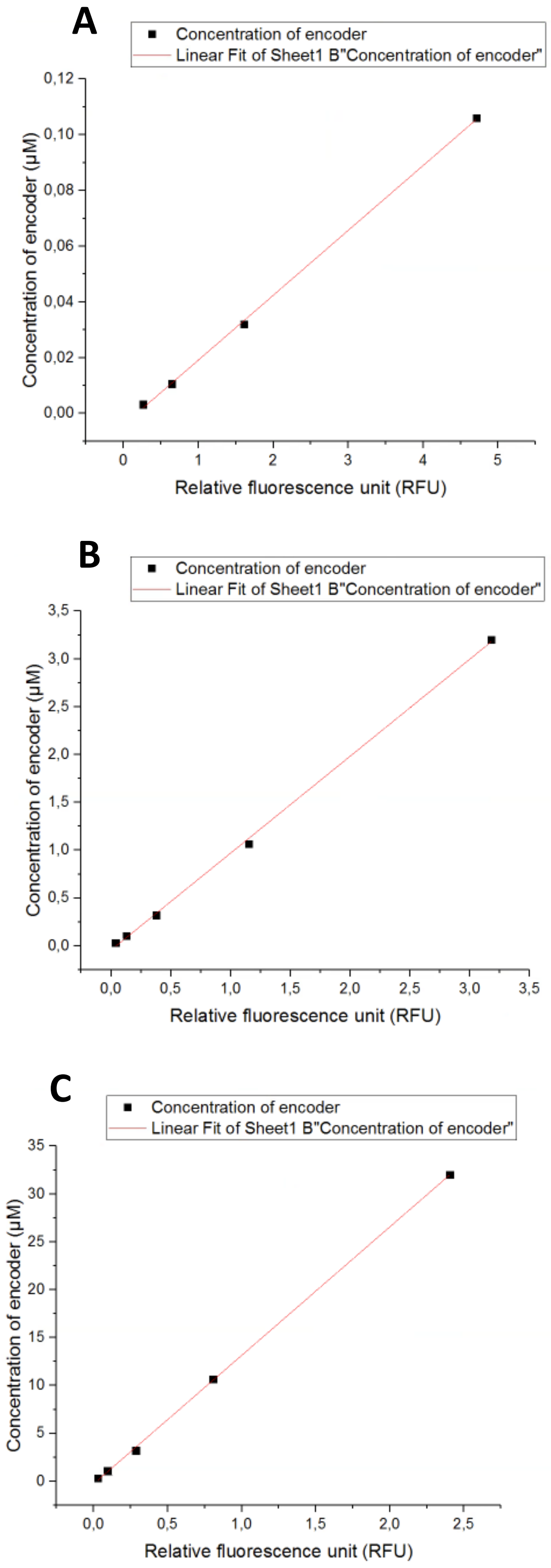

Figure 40: Three calibration curves for low, middle and high concentrations of FITC. With the here presented correlation curves the concentration of FITC could be calculated from single digit naomolar concentrations up to 32 µM based on the RFU displayed by the opto-reader. Linear fit of the linear regressions is depicted in red with an R2 above 0.999 for every linear regression.

Finally, the linear detection range of CP150-BO dimers in 50 mM HEPES buffer was determined (Figure 41). Given the higher cost of CP150-BO fewever values were evaluated to determine the linear detection limit. In this case measurements up to 3 µM CP150-BO concentrations were possible.

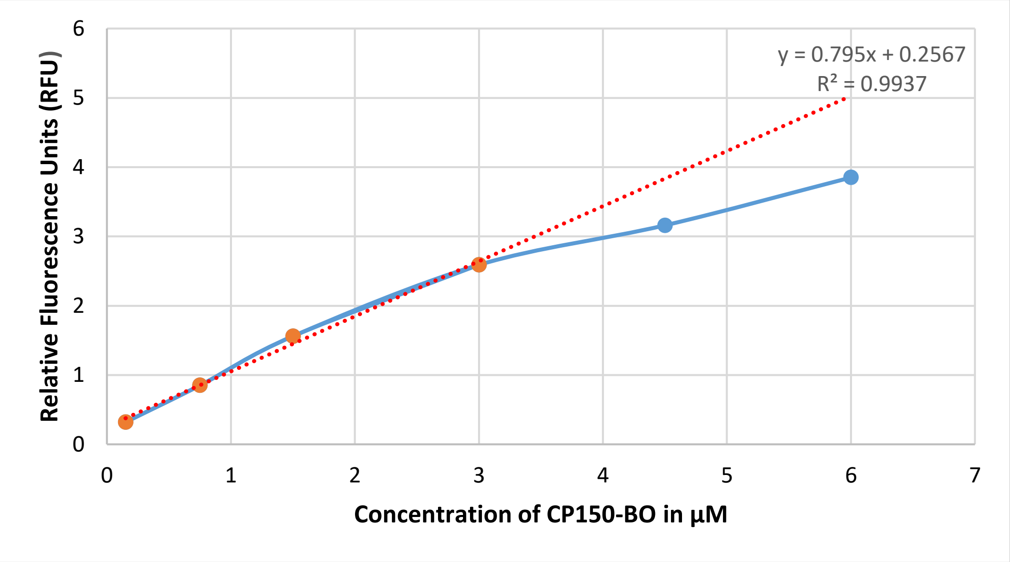

Figure 41: Fluorescence intensity as a function of the labelled CP150-BO dimers' concentration. A linear regression was fitted through the first four data points (orange), the formula and standard deviation are depicted on the right upper corner.

The linear detection range is given until an approximate concentration of 3 µM CP150-BO. Higher concentrations resulted in a deviation from the linear fluorescence signal/concentration correlation (dynamic detection range). Therefore, EC_{50} measurements should be conducted with a maximal CP150-BO concentration of 3 µM or below.

In conclusion, OptoReader was obtained and evaluated as the fluorescence spectrometer for the microfluidic system offering high data acquisition (10 kHz), compact form, real-time evaluation, and highest sensitivity. Different microreactors were evaluated regarding their suitability for optical properties, such as transparency, S/N, and S/B using the OptoReader.

As for the chips, ibidi chips performed with the best in optical transparency and absorption but were unsuitable due to higher inner volumes. IPHT chips performed well with dimer to capsid rations of around 5 and dimer to the background of around 20. Therefore, the IPHT microreactor WC1ab was utilized to evaluate optimal gain and diode power configurations to achieve optimal S/N, S/B, and linear detection range with various concentrations of fluorescein and CP150-BO. With these optimizations, the initial system was equipped with pressure pumps for the flow generation and the OptoReader as a fluorescence readout system already allowing one-dimensional reactions (Figure 42). In order to measure reactions directly combined inflow, the implementation of a mixing technology to the system was investigated.

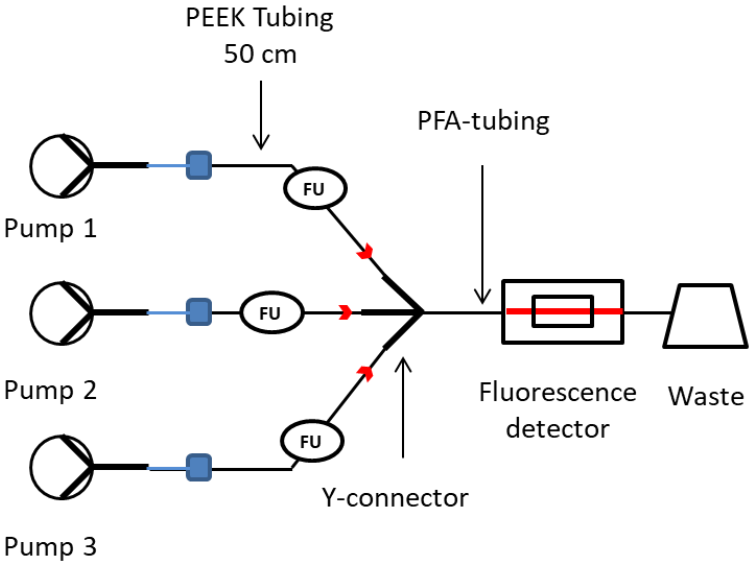

Figure 42: Flowscheme of the microfluidic setup equipped with fluorescence spectrometer-based readout. This initial system was able to generate flowrates of three different liquids with the Fluigent pressure pumps, which were connected with a Y-mixer. The subsequent fluorescence readout was sufficient to obtain initial in-flow CP150-BO assembly values. Legend for the various units is depicted in Figure 30.

III.4.3 Mixing in flow under laminar flow conditions

Since most biochemical reactions start with physical mixing of two or more reactants a robust and homogeneous mixing inflow is essential for a reproducible, efficient, and sensitive biochemical assay. Moreover, mixing has to be time scales faster than the reaction the study of its kinetics. The same concept applies to microfluidic systems, which require special attention regarding the mixing of the components. As described in the introduction, the scaling laws in microfluidic systems change drastically due to miniaturization.[2,42] Therefore, microfluidic mixing under laminar flow conditions is either achieved by external turbulences or unique structures and obstacles creating secondary flow patterns, or transversal flows, or through enhanced diffusion due to substantial surface to volume ratios.[13,16,43]

In this sense, it is essential to understand the underlying biophysical factors attributing to the mixing efficiency such as the mixing time (residence time), Re, microreactor geometry, asymmetrical or symmetrical mixing.[44–47] Furtheremore the fabrication complexity and material costs of the newly designed microreactors has to be considered.[2,46] By using the most applicable parameters, one will obtain a high degree of mixing with a superior SAV ratio, heat control, and safety due to the sealed handling of hazardous substances and better control of runaway reactions.[48] As a result, many applications with fast kinetics, crystallization of nanoparticles, polymer synthesis, multiphase reactions, polymerase chain reaction (PCR) benefit from the utilization of microfluidic mixers.[44,49–54]

Since the first conceptualization of total microfluidic analytical systems, substential development was achieved in micromixing.[55] Most of the micromixers are categorized according to the energy source used for the mixing. If the mixing is performed only relying on the pumping energy, therefore the intrinsic kinetic energy of the liquid flowing through the system, then the type of mixing is nominated as a passive one.[45] Under laminar flow conditions, the flow layers do not mix, hence in this case the primary source of mixing is diffusion, which passive micromixers address by enhancing the SAV ratios and increasing heat and mass transfer efficiency.[13,16,43] Alternatively, obstacles can disrupt the laminar flow layers leading to secondary flow structure mediated mixing. Dependent on their way of achieving this, passive micromixers are categorized into T-/Y-shaped micromixers,[56,57] parallel or sequential lamination micromixers,[4,44,58,59] focusing enhanced micromixers,[60] chaotic advection micromixers,[61–63] and droplet micromixers.[64,65]

Active micromixers add external energy to the system and thereby lead to an increase of the fluid contact area or inducing chaotic structures. Based on the external force mixers are cathegorized as sound field,[66,67] electrokinetics and dynamics,[68,69] thermal fields,[70,71] dielectrophoretic disturbance,[72,73] electrowetting,[74,75] or magneto-hydrodynamics.[76,77] Active micromixers do not rely on the pumping force and flow rates and can function as an independent mixing opportunity if needed.[45] However, the design and operation of such mixers are by far more complicated and expensive, limiting their use only to systems where it is absolutely required.[45,46] To choose the right micromixer type for the microfluidic system, the basic guidline of microfluidics was considered: The simpler, the better. Therefore, many microreactors evaluated for the system were all passive types with various methods of mixing. During the evaluation of the microreactors, one of the vital impact factors was the mixing efficiency which is usually calculated in literature as the mixing index (MI) (Equation 24).[46]

Equation 24: Mixing index (MI): N is the number of sampling points, C_i is the point concentration, C_m is the mean concentration.

$$MI = \sqrt{\frac{1}{N}\sum_{i=1}^{N}(c_i - c_m)^2}$$

The exact mathematical determination of the MI requires the experimental acquisition of several independent point concentrations in the microfluidic system. This, however, was not possible with the previously described fluorescence spectrometer OptoReader. Therefore, the mixing efficiency of the reactors was based on published values. In an initial test, the 1.5 µM CP150-BO dimers mixed with 5 M NaCl were measured at residence times of 60 s. These values were used as a reference for the testing of further microreactors by comparing the EC_{50} values of premixed dimers with the EC_{50} obtained inflow. It has to be mentioned that the absolute assembly values were varying dependent on the protein charge and the location of the experiment (AiCuris / ICIQ), presumably due to different ambient temperature and humidity, but the relative values were constant. Hence the reference was repeated for each microreactor separately. For other systems mixing efficiency was determined by using colored reactions with ultra-short kinetics.

III.4.3.1 Chaotic advection type micromixers

The passive chaotic advection type micromixers allow mixing by introducing obstacles and unique 2D or 3D structures, such as grooves asymmetric structures, recirculations, solid curves and corners, and constrictions. These architecture results in secondary flows, transverse flow components, and vortices causing an exponential growth of the interfacial area.[61–63] Dependent on the type of secondary flow, chaotic mixers are categorized into slanted-groove micromixers, staggered herringbone mixers, connected-groove mixers, circulation-disturbance mixers, 2D serpentine micromixers, Coanda mixers, convergence-divergence based mixers, spiral based micromixers, unbalanced collision mixers, and topological mixers.[45,46] The secondary flows generated mainly depend on the chip structure and strongly on the Re of the system, mostly requiring higher flow rates than other micromixers.[62]

At the time of testing, the flow rates of the system were not fixed. Therefore two chaotic advection type microreactors were tested as possible mixing units: The 3D-Serpentine mixer (Figure 44) from Chip-Shop and the HTM-ST3-1 mixing unit (Figure 43) from the Little Things Factory.[62]

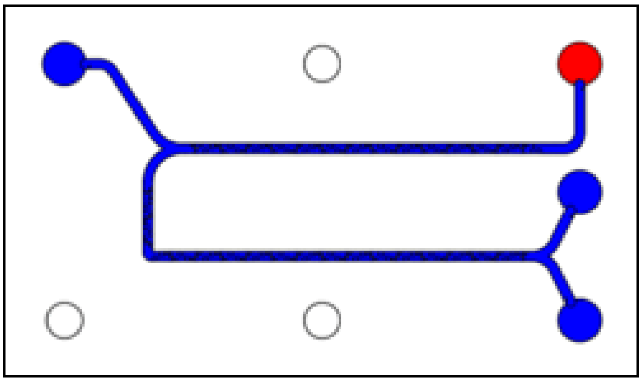

Figure 43: Chaotic advection based HTM-ST-3-1 micromixer with throughput connection and heat exchanger obtained form LTF.

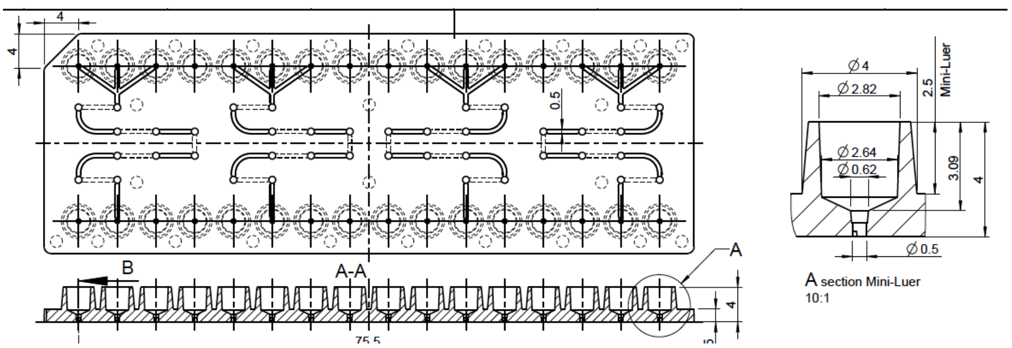

Figure 44: Layout of the 3D-Serpentine microreactor provided by microfluidic ChipShop. Mini-Luer connection to the chip is depicted in the right half of the figure.

The HTM-ST3-1 mixing unit exhibiting an inner volume of 60 µl was constructed for higher flow rates up to 40 ml. Furthermore, the glass surface of the chip led to a substantial absolute fluorescence signal reduction of CP150-BO solutions, which turned out to be the result of protein adsorption to the reactor's surface. Pretreating the microreactor with BSA indeed reduced the fluorescence reduction, further affirming that the fluorescence signal reduction was due to protein adsorption. Due to these negative impacts on the experiment, the HTM-ST3-1 and other mixing units from the little things factory were disregarded from further experiments.

The 3D-Serpentine microreactor initially showed promising results. Due to the mini-Luer connection technology and the small inner surface, it had an inner surface of only 15 µl. The chip was constructed using the thermoplastics PC and Zeonor, both providing excellent biochemical, optical, and chemical properties. Furthermore, thermoplastic components prevent protein adsorption and the uptake of small molecules as well. At this time point, the flow rates of the system were set to overall maximal values of 40 µl/min. Initial results showed that 32 µM BAY 41-4109 and 5 M NaCl led to an 80 % assembly 1 min after mixing.

However, in later experiments, the flow rate had to be restricted to a maximal 16 µl/min per channel due to the dilution method, resulting in a Re of maximal 2.28. Literature research suggested that to reach adequate mixing of around 80 % with this serpentine mixer, at least a Re of 35 is required, which was not achievable given that the high flowrates would interfere with the TAD of the compounds.[62] Additionally, the mixing was analyzed experimentally by comparing the GLS4 mediated assembly of the 3D-Serpentine mixer with the microtiter format, resulting in a shift of the EC_{50} value from 0.7 (microtiter plate) to 1.9 (mixed inflow after 1 min) (Figure 45).

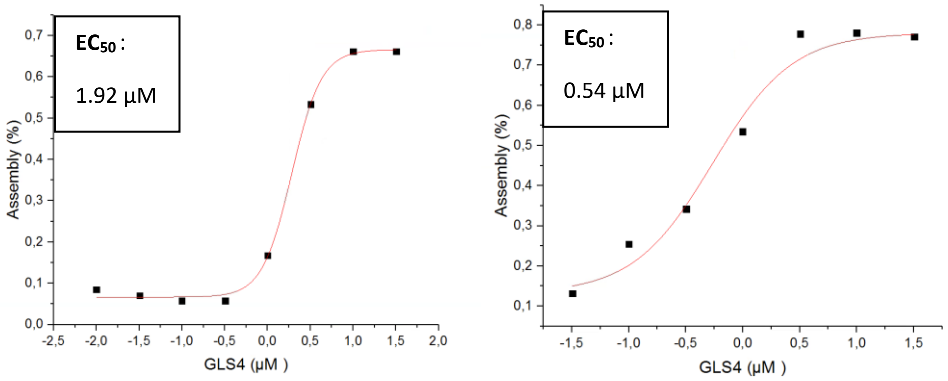

Figure 45: EC_{50} measurement of GLS4 60 s post inflow mixing with CP150-BO and 300 mM NaCl (left figure), or in microtiter well format 5 min post mixing with CP150-BO and 300 mM NaCl (right figure).

These last findings conclude that neither the 3D-Serpentine mixer nor most of the chaotic advection mixers are suited for the here presented microfluidic system due to the low Re numbers.

III.4.3.2 Hydrodynamic flow focusing

Any mixing processes between two laminar co-flows in the radial direction is purely diffusion driven. Since diffusion scales quadratically with time, miniaturization, and hence thinning (focusing) of the inner flow laminar allows diffusion-controlled reactions to be accelerated.[60] In a 2D setup using steady laminar flows, a constant channel height, and Newtonian fluids with the same density, the width of the inner flow can be calculated as a function of the respective flow rates (Equation 25).

Equation 25: Volume distribution in a 2D hydrodynamic focusing flow with a constant height of Newtonian liquids with the same viscosity. W_f Width of the liquid with the volumetric flowrate Q, W_o: Width of all the liquids (channel width), Q_1, Q_2, Q_3 Volumetric flowrates of the respective liquids.

$$\frac{W_f}{W_o} = \frac{Q_2}{Q_1 + Q_2 + Q_3}$$

Thus, the thinner the inner flow lamellae, the faster the mixing, which was investigated by visualizing the mixing of two flows with pH-indicators. For this experiment the thermoplastic microreactor μ-slide III from ibidi was used. The chip was sufficient for initial testings, but due to the 1 ml connections, the inner volume was too high for the biochemical assay. During the experiments, two side channels were connected to either 200 mM acetic acid pH 4.0 (Figure 46) or 20 mM sodium phosphate buffer pH 8.0, while the inner channel was connected to bromophenol blue. A different thickness of the laminar flows was achieved by varying the flow rates with different pressure settings of the pumps. Bromophenol blue is a color-based pH indicator changing from blue to yellow under acidic conditions with pH under 4. Decoloration of bromophenol blue represented the diffusional mediated mixing and was best observed for in the second experiment in condition A (Figure 46).

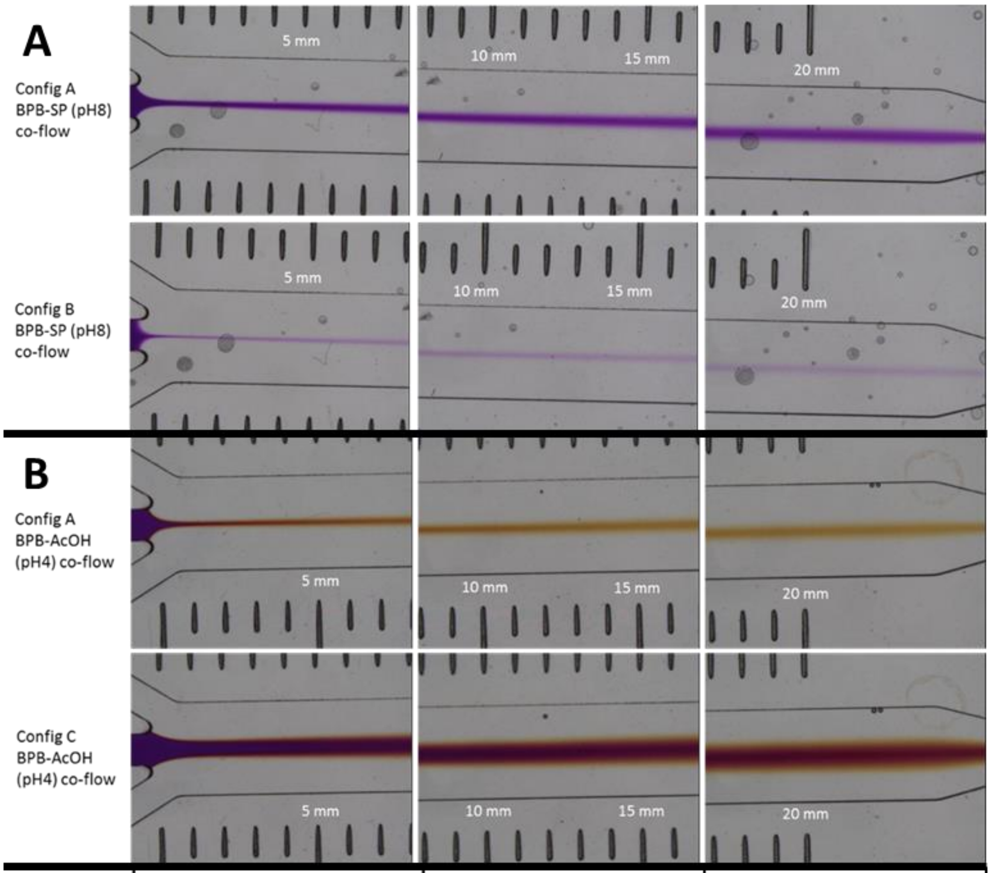

C

Pump (Condition A)	**Pressure in mBar**	**Flowrate in µl/s**
1	500	42
2 (Bromphenol blue pH 8)	39	8
3	500	42
Pump (Condition B)	**Pressure in mBar**	**Flowrate in µl/s**
1	500	42
2 (Bromphenol blue pH 8)	4	3.3
3	500	42
Pump (Condition C)	**Pressure in mBar**	**Flowrate in µl/min**
1	500	42
2 (Bromphenol blue pH 8)	200	28
3	500	42

Figure 46: Laminar co-flow between bromophenol blue (BPB) and sodium phosphate buffer (pH8) (A), or acetic acid pH4 (B) (SP) in a µ-slide III. Diffusion of Bromophenol blue (BPB) was observed over the 2 cm chip. The three flow configurations used for the lamella generations are depicted in tabelle C with Pump 1 and 3 connected to 20 mM sodium phosphate (A) or mM acetic acid pH 4.0 (B). Pump 2 was connected to bromophenol blue pH 8.0.

The mixing time requirement was calculated for conditions A, and B with the overall flow rates, microreactor dimensions, and distance traveled until complete conversion. While in condition A, the mixing was achieved after a residence time of 1.65 s, in condition C, this did not happen even after 12.85 s (20 mm distance). Therefore, the thinner the inner channel, the higher the mixing rate of the compounds. In the biochemical assay, however, all three components (protein, buffer, compounds) must be mixed in equal volume portions, which is best conducted with equal flow rates and laminar widths. Consequently, the only way to reduce the laminaes' width and enhance the mixing is by reducing the overall flow rate or by unique structures increasing the surface between the lamellae. One way of accomplishing this is by splitting and recombining already existing lamellae introduced in the following chapter.

III.4.3.3 Sequantial lamination

3D sequential lamination is performed by split and recombination (SAR) of the initial two lamellae in n iterations leading to an increase in a 2^n co-flows, thus exponentially reducing the thickness of the liquids. The resulting growth in surface area leads to an excellent mixing with an MI of 90 % even at the lowest Re numbers.[4,58,78] Furtheremore, the Rotate Split and Recombine micromixer (ROSAR) GF-T75 also rotates the fluids after splitting thereby adding a slight chaotic advection mixing character before recombination (Figure 47).

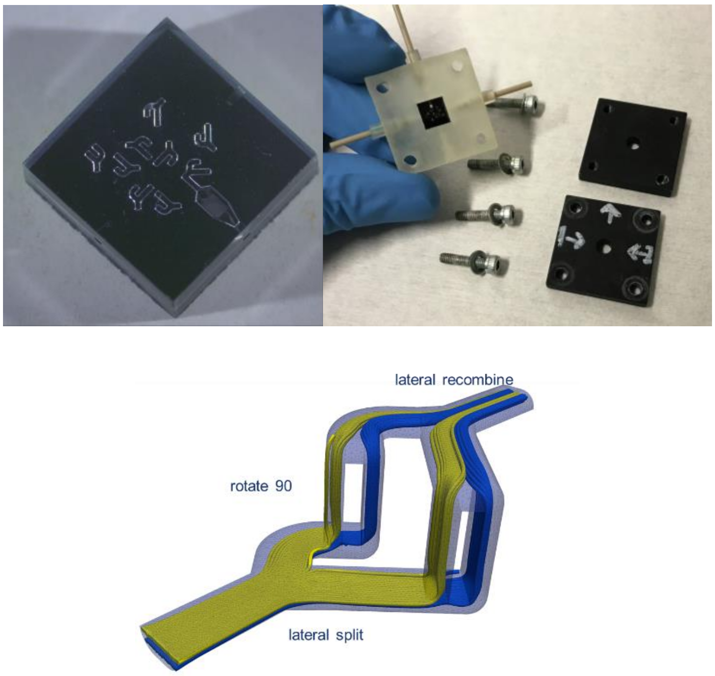

Figure 47: Design and structure of the ROSAR GF-TF75 microreactor in the polymeric chip holder, kindly provided by Dr. Thomas Henkel from IPHT (upper figure). Mixing mechanism of the chip with two fluids including splitting, rotation and recombination of the fluids. This step was repeated 7 times sequentially within the microreactor leading to ultra-thin co-flows.

The GF-T75 micromixer exhibits an insignificant inner volume (under 1 µl) in which it performs 7 iterations of rotate, split, and recombine actions leading to ultra-thin co-flows and mixing within ms.[79] The microreactor displayed perfect theoretical and practical values and was incorporated into the system as the mixing unit. However, after a couple of experiments clogging occurred due to the small inner diameters of the reactor, and the cleaning in flow with the 4 % Alconox detergence and H_2O was no longer possible. The first problems were solved by removing and washing the chip submerged in 15 % HCl under ultrasonication at 40 °C for 2 h, followed by the same procedure but submerged into H_2O. This way, most of the NaCl crystals and proteins were removed and the microreactor was again usable for a short period. However, the initial polymer-based bracket supplied and used in the first experiments was shedding, leading to the chip's unrepairable clogging, wherefore, the ROSAR GF-T75 was disregarded for a longer period. After optimizations, a metal bracket was constructed by IPTH, which allowed the operation of the microreactor without further problems.

Initially ROSAR GF-T75 mixing properties were evaluated with an ibidi chip as an optical readout. Prior to mixing measurements, samples of preincubated (1 h) BAY 41-4109 solutions were taken and measured in microtiter format using CLARIOSTAR before and after the flow measurement and compared to the inflow measured values (Table 25).

Table 25: Assembly rates of CP150-BO preincubated with different dilutions of BAY 41-4109 and NaCL measured inflow, as well as before and after flow in microtiter plate format.

Solution	**Assembly before flow measurement**	**Assembly during flow measurement**	**Assembly after flow measurement**
Dimers	0 %	0 %	0 %
2.5 M NaCl assembled capsids	96 %	96 %	95 %
Dimers + 300 mM NaCL	29 %	15 %	35 %
Dimers + 300 mM NaCL+ HAP (0.01 µM)	26 %	20 %	29 %
Dimers + 300 mM NaCL + HAP (0.32 µM)	56 %	35 %	50 %

The obtained EC_{50} was nearly identical with a single deviation at 0.32 µM BAY 41-4109 concentration representing the EC_{50} point of this compound. This deviation is acceptable due to the steepness of BAY 41-4109's hillslope. Artifacts, such as in the case of LTF's glass microreactors, due to protein adsorption and fluorophore bleaching were no longer observed as the prior and post flow measurement data. Consequently, the inflow mixed BAY 41-4109 solutions with 1.5 µM CP150-BO were measured at approximately 15 s showing substantial overlap with the data obtained from preincubated solution (Figure 48). These findings validate the ROSAR GF-T75 mixing efficiency and demonstrate that the BAY 41-4109 mediated CP150-BO assembly occurs already within 15 s at room temperature.

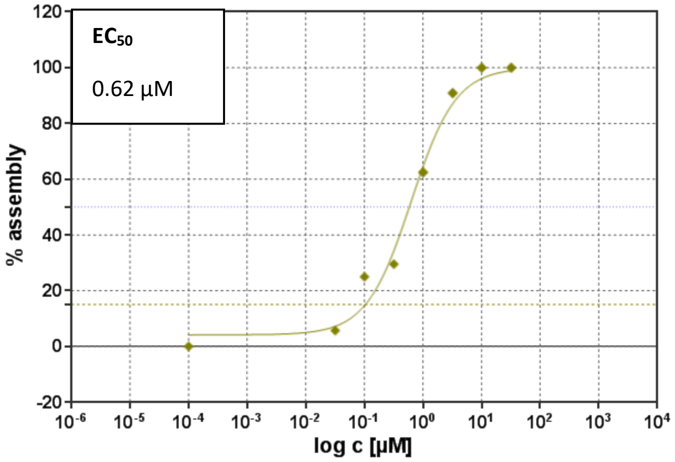

Figure 48: EC_{50} measurement of inflow mixed CP150-BO with different dilution steps of BAY 41-4109 with a reaction time of 15 s.

In later experiments, the mixing of ROSAR GF-T75 was re-evaluated by mixing several dilution steps of GLS4 inflow and measuring the resulting values at 60 s post mixing at room temperature. The acquired EC_{50} of 0.54 value was again in good agreement with the microtiter obtained ones 0.71 (Figure 49).

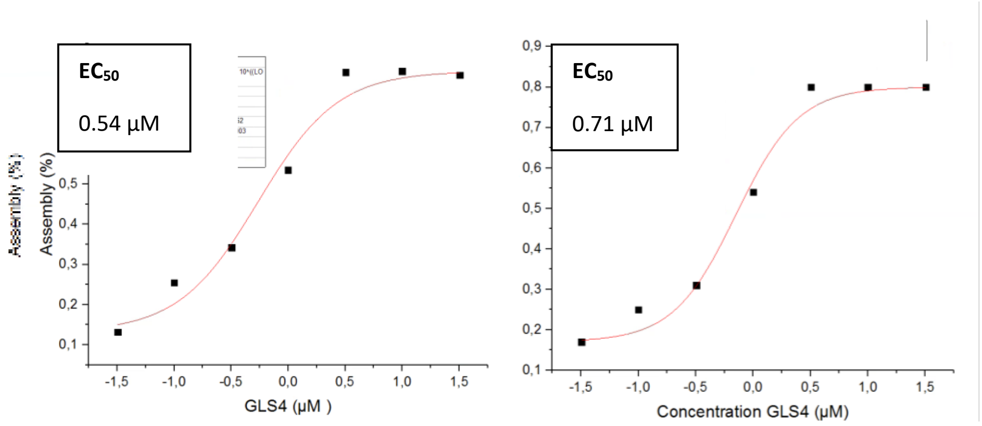

Figure 49: EC$_{50}$ values of inflow mixed CP150-BO with different dilution steps of GLS4 with a reaction time of 60 s (left figure) and EC$_{50}$ values obtained from GLS4 mixed CP150-BO in microtiter format at 5 min.

In conclusion, several passive-type micromixers were evaluated with different mixing mechanisms. The initial acquired chaotic advection type micromixers HTM-ST3-1 and the 3D serpentine micromixers needed high Re numbers above 35 to achieve mixing above 85 %. Unfortunately, this was not the case for the microfluidic system only having an Re around 5. Hydrodynamic flow-focusing using the µ-slide III could achieve fast mixing for the inner laminary under 2 s, but it relied on the asymmetrical high flow rates of the two surrounding luminaries. Finally, sequential lamination using the ROSAR GF-T75 microreactor showed excellent mixing in ms under low Re numbers. Initial problems regarding plugging of the chip were overcome by using sufficient chip bracket holders and cleaning procedures. The final system containing pressure pumps, optical readout, and the adequate mixing unit allowed initial EC$_{50}$ determinations of CP150-BO inflow using several dilution curves of BAY 41-4109 (Figure 50).

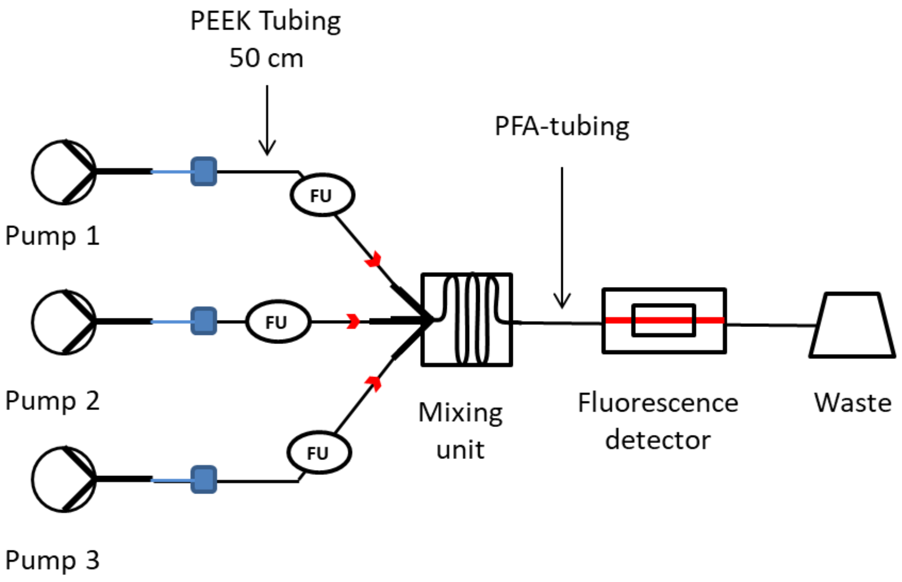

Figure 50: Flow scheme of the microfluidic setup equipped with Fluigent flow pumps, a mixing unit, and the OptoReader as a fluorescence spectrometer. The microfluidic setup was used for the inflow mixing of CP150-BO with CAMs and assay buffers with subsequent fluorescence spectrometer-based readout. Legend for the various flow units is depicted in Figure 30.

III.4.4 Advanced operations using Liquid handling systems and valves

At this point the microfluidic system was able to generate a stable flow, mix compounds in ms, and evaluate the obtained data with a highly sensitive fluorescence spectrometer. In addition, the system allowed the automated measurement of multiple technical replicates but was limited to a single compound concentration. A screening platform must be able to measure multiple compound concentrations and several compounds simultaneously.[80–84] Therefore, advanced liquid handling operations have to be introduced to solve these challenges adequately.

III.4.4.1 Generation of dilution curves

The most straightforward option for inflow dilution was the respective flow rates' variation, which was evaluated with a specific device configuration. The compound of interest, diluted in 50 mM Hepes and 600 mM NaCl, was first mixed with 600 mM NaCl using a Y-mixer. Different dilutions were generated by varying the flow rate between the compound and the NaCl, but the overall flow rate was kept constant. These compound dilutions were then mixed 1:1 with the CP150-BO using the ROSAR GF-T75 chip, mixing all three compounds in ms, and the assembly reaction was measured on the µ-III chip with the OptoReader (Figure 51).[79]

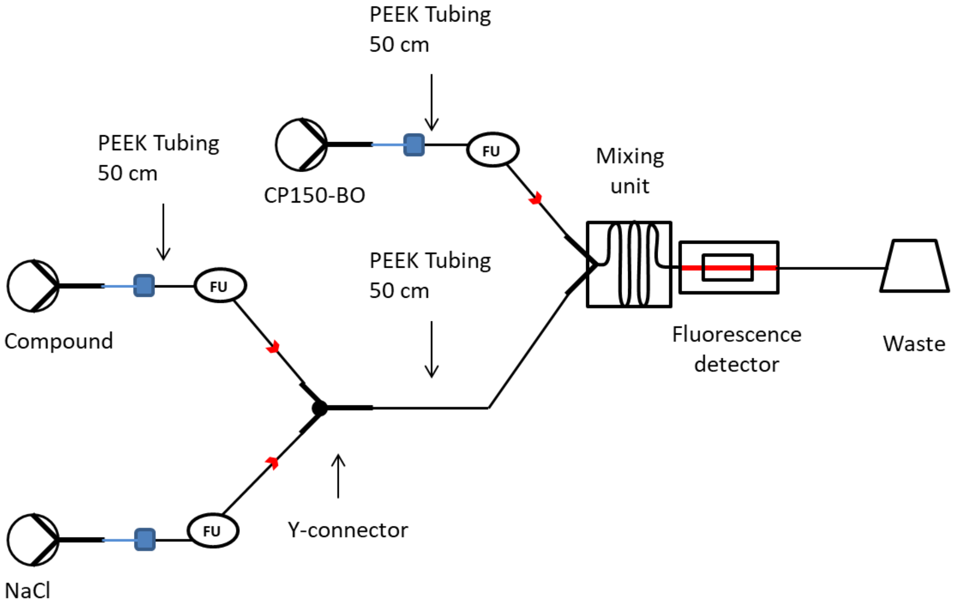

Figure 51: Scheme of the flow system utilizing the ROSAR-GF-T75 micro reactor for mixing and µ-slide VI 0.5 for the optical readout. Variation between the flowrates for the compound and the 600 mM NaCl led to different dilution steps of the compound in flow. Legend for the various units is depicted in Figure 30.

The main restriction for mixing by flow rate variations was the maximal difference of 1:32 between the two channels (Figure 52). Furthermore, the consumption of this methodology was exceptionally high, and hence more sophisticated methods were evaluated.

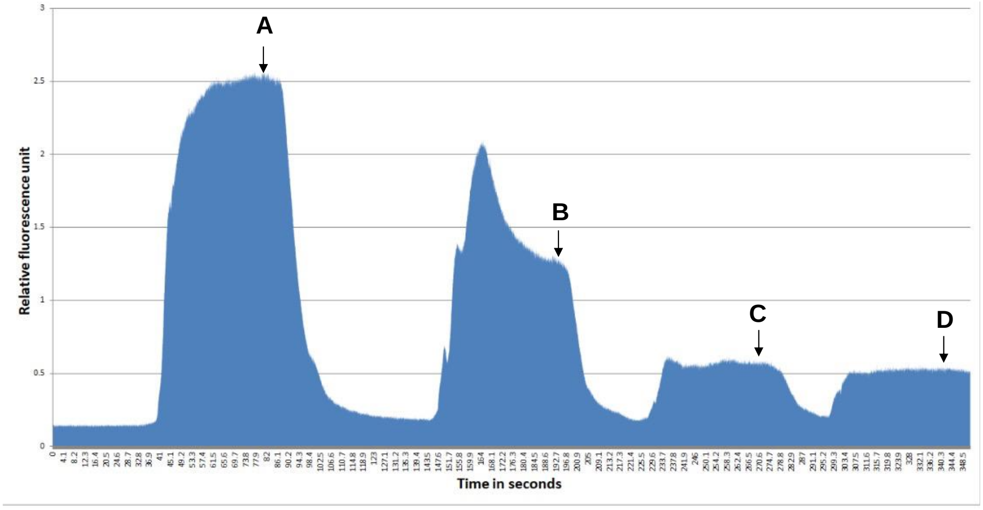

Figure 52: Automated mixing of CP150-BO with 1 (A), 3.2 (B), 10 (C), 32 (D) µM of BAY 41-4109 in flow using the ROSAR-GF-T75 micro reactor. The dilution steps of HAP were generated by variations in flowrates between the stock solution of HAP and a 600 mM NaCl solution.

An alternative to generate dilutions was the integration of specific mixing microreactors. The requirement for these chips was relatively high givent the automated inflow generation of a dose-response curve prerequisite the dilution of the compounds in at least 3 logarithmic ranges followed by the sequential transfer of the dilutions to the mixing unit starting from the lowest to the highest concentration. In addition, these had to be achieved while taking the pressure pump's hydraulic pressure into account. Passive types of dilution chips can use the system's hydraulic pressure by having structures with different inner diameters leading to variations in the flow rate according to the Hagen-Poiselleu law. In this way, complex systems with multiple junctions are calculated according to Kirchhoff's circuit laws (Equation 26).

Equation 26: Kirchoffs current law: n is the total number of branches with liquids flowing in or out of them, I represents the current.

$$\sum_{k=1}^{n} I_k = 0$$

Alternatively, active mechanisms, such as a valve-driven circulatory dilution based on sequential mixing, digital microfluidics or programmed 2-dimensional arrays with pneumatically actuated microvalves, can be employed to generate a dilution ladder.[85–87] However, most of these chips had a complicated design and operation resulting in costs around 20,000 €. Furthermore, most of these microreactors also showed lower compatibility with the already established microfluidic system.

In contrast to these cumbersome devices, another physical transport phenomenon was found and further evaluated for inflow generation of compound dilutions using only the inherent flowrates and inexpensive capillaries. TAD was used in previously described µ-TAS systems to dilute compounds in a logarithmic manner generating an unparalleled high amount of dilution points.[82,84,88–90] TAD is an absolute physical description of the motion (convection) and diffusion-driven compound dispersion in cylindrical tubing at low laminar flow conditions.[91–93] The most fundamental forces for TAD are the flow rate-dependent axial convection and the molar mass-dependent radial and axial diffusion of compounds. Pure axial convection leads to a parabolic distribution of the dilute inflow direction caused by the velocity distribution of the fluid along the radial cross-section of the channel. While the axial diffusion increases the band broadening, the radial diffusion of the compound decreases the convection-mediated dilution by slowing down the leading interface and accelerating the trailing interface of the dilute. The technical requirement for the utilization of TAD is an initial sharp compound concentration margin and a capillary for the dilution. For the generation of the sharp compound concentration, the utilization of different valves was considered. While many companies offered automated and hand-driven versions, the highest compatibility regarding both hardware and software was offered by the L-Switch™. The L-Switch™ is a 6 port/ 2-position bi-directional valve with the vital benefits of high chemical, biochemical and biological compatibility, instantaneous control with live monitoring, and a compact size (Figure 53). This module allowed the highly reproducible production of dilution curves by first equilibrating it with the compound of interest, generating a sharp margin, then injecting this solution into the capillary and diluting the compounds with TAD before entering the mixing unit (Figure 53).

Figure 53: L-Switch^{TM} switch with depicted interface. The 6 port/ bidirectional valve allowed the automated switch between independent flows.

The module's functionality was proven by the dilution of BAY 41-4109 performed in a PEEK tubing using TAD as a first experiment. The flow system was equilibrated by mixing 50 mM HEPES buffer with CP150-BO until a stable signal was reached. After equilibration, the L-switch was switched to enable the flow-through of BAY41-4109, which was diluted in the PEEK tubing and mixed in the LyseV1-HSG-IMIT chip with CP150-BO (Figure 54).

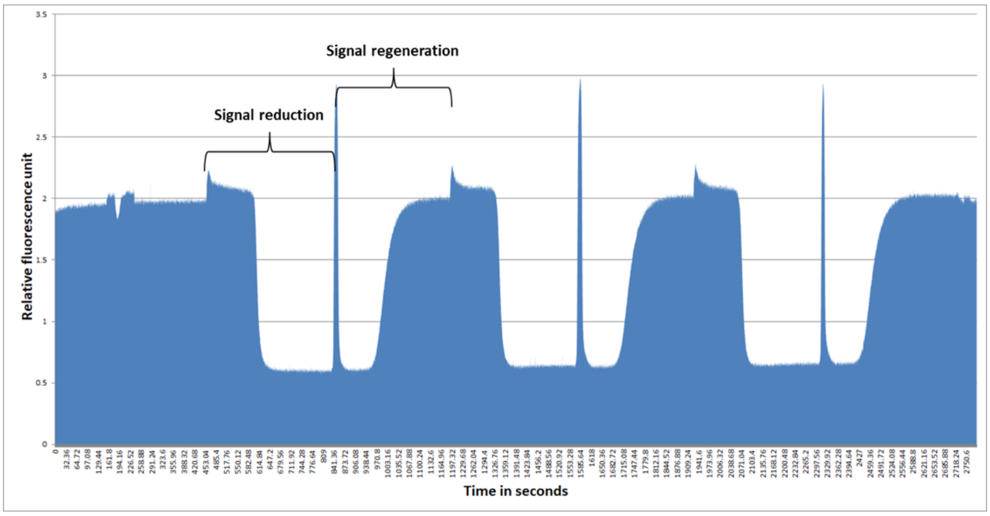

Figure 54: Automated TAD of 10 µM BAY 41-4109 follwed by mixing with CP150c in flow. The reaction was repeated in three signal reduction and regeneration cycles.

With this method, the possible dilution of the compounds with a great granularity was successfully shown. As the last step, the automated sequential screening of multiple compounds was evaluated.

III.4.4.2 Automated screening of multiple compounds

A valve module, reservoirs, and a connection from the sealed reservoirs to a micropump were needed for the automated sequential screening of multiple compounds inflow. Initially, the unidirectional rotary valve M-Switch™ with 11 ports was considered, coming with the same benefits as the L-Switch™.[94] The module was designed to screen up to 10 compounds and provide bio- and chemical compatibility, compact design, very low dead volume, and a rapid switch. Despite the promising data, initial experiments showed a leaking intrinsic to the machine, therefore a different switch was utilized: the AMF valve (Figure 55).

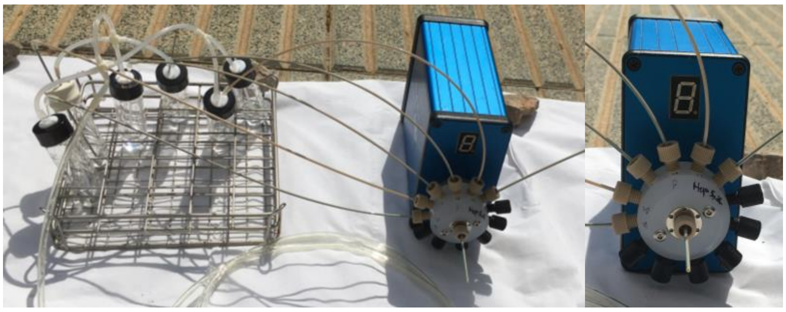

Figure 55: AMF unidirectional 12-port valve connected to six 5 ml pressurized glassreservoirs. The glass reservoirs in turn are connected with a single transparent pneumatic tubing to a pressure pump.

This valve is a unidirectional rotary valve equipped with 12 inlets and one outlet, allowing the screening of up to 12 compounds sequentially.[95] Furthermore, it was optimized for biochemical applications with an ultra-low internal volume and limited contamination between the injections and compact size. The valve was integrated into the Microfluidic automatization tool and was connected to 8 glass reservoirs with a tapered bottom, 5 ml inner volume, and pressurizable sealed caps. The reservoirs, in turn, were connected to a single Flow EZ™ 1,000 mbar (Pumps) using several manifolds combined with the pneumatic tubing (Figure 56).

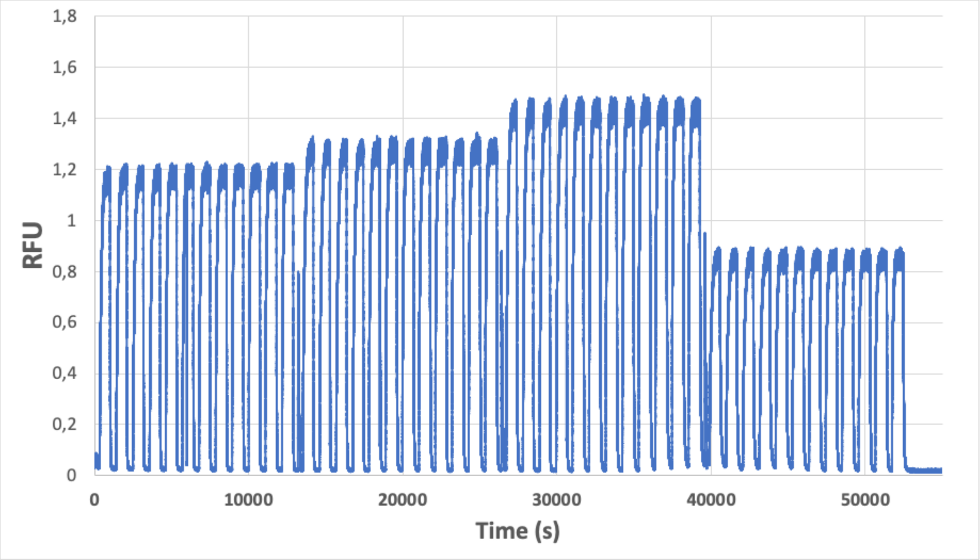

Figure 56: Automated measurement of four different BODIPY compound dilutions in flow. Each compound was measured at three different flowrates and three technical replicates, respectively.

Overall, the microfluidic system was able to measure up to 8 compounds in several technical replicates, combined with the inflow dilution, mixing, and optical readout. With this model already several experiments were completed described in later chapters. As a final upgrade, the maximal number of compounds was increased and an interface to the synthesis was established.

III.4.4.3 Interface to 96 microtiter well-format

Recent developments of µ-TAS and MEMs analysis systems were directly combined with flow chemistry to allow an automated, seamless synthesis-screening cycle.[82,96] As a result, the synthesized molecules were evaluated by the telescoped assay directly, collecting information on compound efficacy supported by artificial intelligence. These feedback loops lead to faster throughput by shortening the synthesis analysis cycle and accelerating the hit-to-lead development.[97,98] In this sense a future integration of the microfluidic platform to chemical synthesis was striven for and several possible interfaces were evaluated for a 96 microtiter well format. The best options were the liquid handling system (LHS) of PALSystems, AMPLIFY of NovoLAB, and the RotAxys360 from CETONI. PALSystem offered a 3D robot handling with ultrafast injections (100 ms), automatic process (detection of missing vials), and large sample capacity of up to 648 of 2 ml storable vials. DeNovo's AMPLIFY was able to perform dilutions starting from larger sample volumes. In the end RotAxys360 system was fitting the required profile the best due to economic reasons and the direct integration to microtiter well plates as an interface. It offered a liquid handling arm which could operate in 3D freely, allowing the transfer of compounds from up to 6 different 96 microtiter plates to the pressurized reservoir of interest. The liquid handling arm was equipped with a neMESY low-pressure syringe opted for 100 µl allowing the transfer of liquids from a 96-well-plate to the respective 5 ml pressure glass reservoirs sealed with septa (Figure 57).

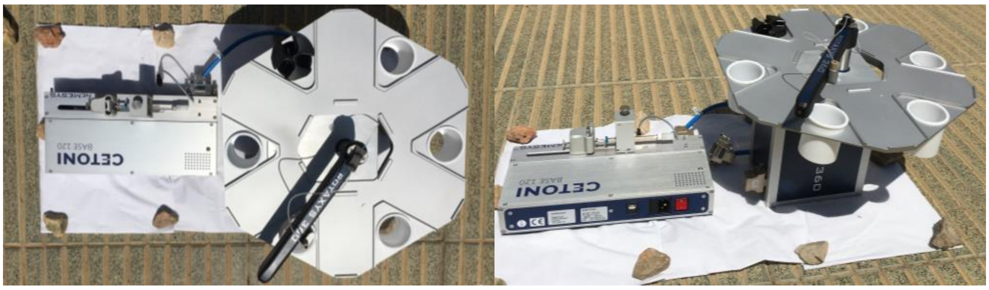

Figure 57: ROTAXYS 360 LHS equipped with a base module 120 and a neMESY low-pressure syringe opted for 100 µl max volume.

In conclusion, the final microfluidic system offered an interface to the 96-microtiter well format allowing sequential measurement of up to 576 compounds with technical replicates, respectively. Furthermore, the generation of high-resolution dilution curves using L-Switch^{TM} followed by the inflow mixing with the target protein in the ROSAR microreactor, and finally the evaluation using the fluorescence spectroscope OptoReader was feasable. The individual components excelled in their fields, leading to a robust microfluidic hardware setup for multiple different assay formats (Figure 58).

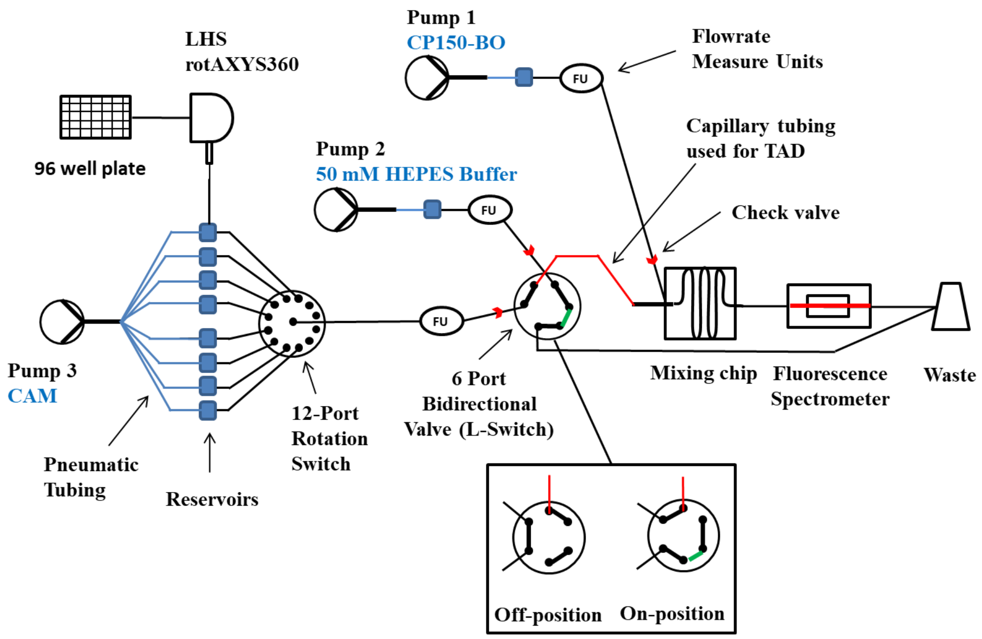

Figure 58: Schematic representation of the microfluidic system used for the screening and characterization of novel HBV CAMs. The compounds were transferred from a 96 well plate to the pressurized reservoirs (blue squares) with the LHS rotAXYS360. Afterward, the system was equilibrated by first loading the first compound until the L-Switch, which was set to the Off-position to remove compound excess into the waste. Simultaneously, Pump 2 and Pump 3 were running with identical flowrates allowing the mixing of 50 mM HEPES with CP150-BO in the mixing chip and thereby generating the baseline. Following the initiation, pump 3 was set to the same flowrate as pump 1, and the L-Switch turned to the On-position, allowing the TAD of the CAM's compound margin in the designated (red) capillary and its subsequent mixing with the CP150-BO protein. After the measurement, the system was cleaned with H_2O using pump 3 switched to the respective reservoir and 50 mM HEPES using pump 2. Legend for the various units is depicted in Figure 30.

III.4.5 Automation of the microfluidic system

The previous chapter described the selection and setup of the microfluidic system, primarily comparing different modular components according to their economic value and performance. Since the system was assembled from individual devices, a universal platform for the combined control had to be established first. Regarding this task following software interfaces were at the disposal: Microfluidic Automation Tool (MAT), All-In-One (AIO), QmixElements (Qm), and Elveflow Smart Interface (ESI) (Table 19).

The first step in the operation of the microfluidic system was the cleaning of the devices followed by the transfer of the compounds from a 96-well reservoir to the 8 pressure reservoirs, which was performed with the Qm interface. The transfer was accomplished by the automated operation of the RotAxys360 needle's movement and the compounds' loading and unloading with the neMESY low-pressure syringe (Figure 59).

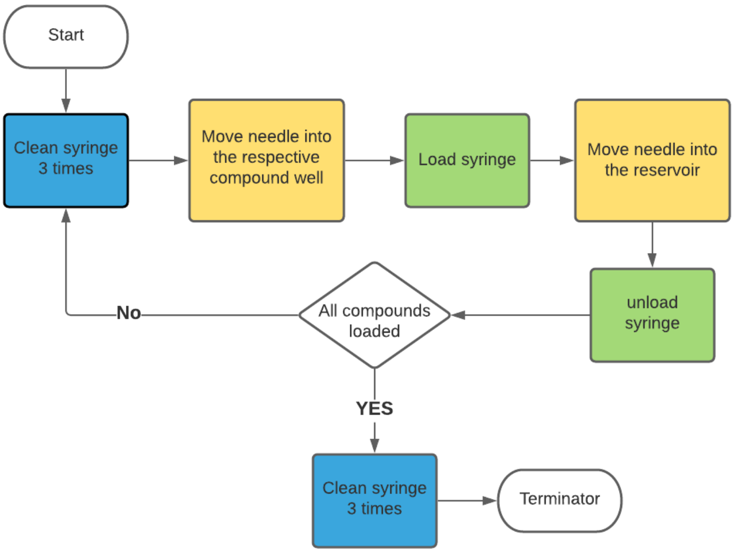

Figure 59: Annotated flowchart of the compounds' loading from the 96 well-microtiter plates to the 5 ml reservoirs using CETONI's RotAxys360 equipped with a syringe pump as an interface. In the flowchart, operations are written in squares, decision markers in transparent rhombuses, and start and termination of the process in transparent ovals. The process started with cleaning the syringe 3 times before and after the transfer with H_2O (blue square). After the purification, the needle moved into the respective well (first yellow square), loaded the compound (first green square), and transferred it into one of the pressurized 5 ml reservoirs (yellow). The process was repeated until all the compounds were measured (rhombus as decision marker), after which the system was cleaned again (second blue square).

The OptoReaders fluorescence and reflection data were recorded using the ESI software interface, which was later trimmed and used to calculate the CAM mediated HBc EC_{50} values, the Z' factor, LoD, and LoQ, with the open-source software KNIME 4.0.2 (III.4.5.2 Evaluation of the obtained assay data using KNIME). Subsequently, all the other modules (pumps and valves) were coordinated using MAT, which was used to write the automated protocols for the HBc assays (III.4.5.1 Utilization of the MAT for the generation of CAM mediated HBc assembly kinetics and dose-response curves).

III.4.5.1 Utilization of the MAT for the generation of CAM mediated HBc assembly kinetics and dose-response curves

Aside from the operation of the microfluidic tools, MAT used logical operators such as loops, repeat loops, if loops, and waiting modules. With these basic operations, three major types of protocols were written in MAT that can be categorized in cleaning and air removal, Dose-response (up to 50 protocols), and kinetic (up to 20 protocols) operations (not shown).

The measurement of the capsid assembly's kinetics induced by different CAMs required a relatively simple protocol. The different time points for the HBc were generated by varying the overall flow rates starting from high to low, resulting in short to long residence times. For the kinetic measurements, three pumps equipped with respective M-flow units and valves were utilized:

- Pump 1 was operated for HBc protein.
- Pump 2 was applied for the CAMs diluted in assay buffer with 600 mM NaCl.
- Pump 3 was utilized for cleaning the system between measurements using H_2O.

The AMF allowed the sequential measurement of up to 7 compounds before refilling the vials using the RotAxys360 (Figure 60).

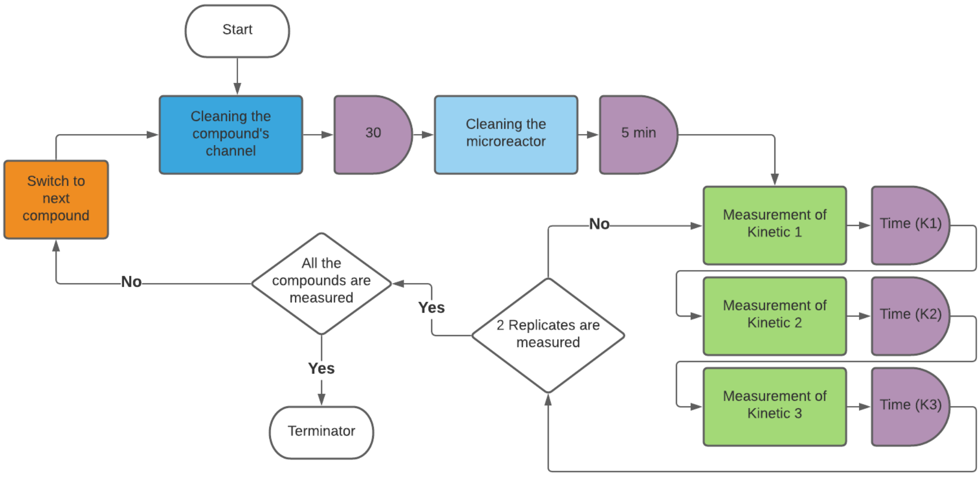

Figure 60: Annotated flowchart of the compounds' kinetic measurement at three different time points and two replicates. In the flow, operations are written in squares, operation times in purple half circles, decision markers in transparent rhombuses, and start and termination of the process in transparent ovals. The process started with cleaning the compound's channel 3 times for 30 s with H_2O (blue square), followed by the cleaning of the microreactor for 5 min (light blue square). After the initiation, several HBc assembly kinetics were measured sequentially (green squares) with their respective residence times (purple half-circles), and the process was repeated until all the replicates were obtained (rhombus). Next, the AMF valve switched to the following compound if it was available; otherwise, the program terminated.

During the dose-response measurement, four pumps were used:

- Pump 1 was used for NaCl.
- Pump 2 was utilized for the CAM compounds and their dilution.
- Pump 3 was taken for cleaning with H_2O.
- Pump 4 was operated for the HBc protein.

The MAT protocol was based on the previously introduced system (Figure 58) with the above-mentioned pump configuration and was able to generate CAMs induced HBc assembly high-resolution curves for up to 7 compounds in sequential order. The first step in the generation of dose-response curves for the HBc assembly assay was the TAD dilution of the CAMs performed in a capillary by the L-Switch creating a dilution of three logarithmic scales. This step was very sensitive to backflow, air bubbles, or traces of previous compounds requiring the optimizations described in (Figure 61). Afterward, the diluted compounds were directly mixed with assay buffer, NaCl, and HBc, and the capsid assembly was measured. Notably, rigorous cleaning was performed between measurements to remove traces from previous compounds down to single-digit nanomolar concentrations (Figure 61).

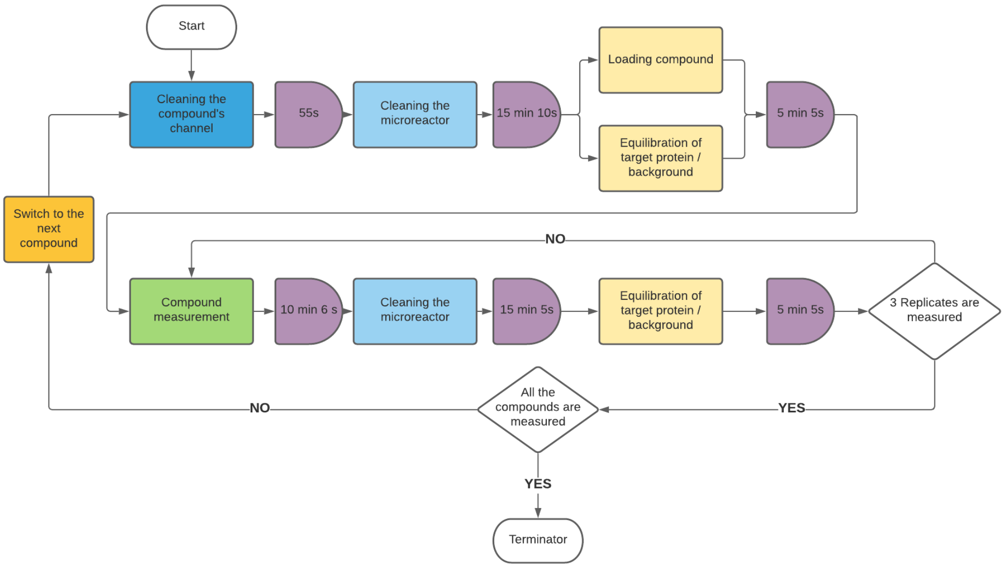

Figure 61: Annotated flowchart of multiple compounds' high-resolution dose-response measurements in three replicates, respectively. In the flowchart, operations are written in squares, operation times in purple half circles, decision markers in transparent rhombuses, and the start and termination of the process in transparent ovals. The reaction starts with cleaning the compounds channel for 55 s (blue square) followed by the 15 min cleaning off the microreactor (light blue square). Next, the 3 µM protein was mixed 1:1 with 50 mM Hepes buffer to create the background signal (yellow squares). Simultaneously the compound was loaded up until the L-switch to generate a sharp margin necessary for the TAD (second yellow square). Finally, the measurement was initiated by rotating the L-switch resulting in the compound's dilution in the capillary before mixing with the target protein in a 1:1 ratio (Green square, second line). After the measurement, the reactor was cleaned again (blue square, second line), and the protein was reinjected as described above (yellow square, second line). These steps were repeated three times to produce the replicates required for the assay (first rhombus). Finally, the AMF valve switched to the following compound, and the process was repeated until 7 compounds were measured (second rhombus).

The above-described protocol was repeated with FITC instead of the CAMs and without the protein to determine the compound's concentration at given time points. During the evaluation of the EC_{50} values, introduced in (III.4.5.2 Evaluation of the obtained assay data using KNIME), the two data sets were superimposed, allowing the generation of high-resolution dose-response curves. All the protocols have been deposited in their original form in the attached folders for those interested in more details.

III.4.5.2 Evaluation of the obtained assay data using KNIME

KNIME is an open-source analytics platform operating on JavaScript and logical nodes arranged to generate workflows. Using this software, various individual tasks, meta nodes, variables, and operations were written to analyze the obtained fluorescence data. In the following, the utilization of KNIME for the calculation of the CAMs EC_{50} values is elucidated (Figure 62).

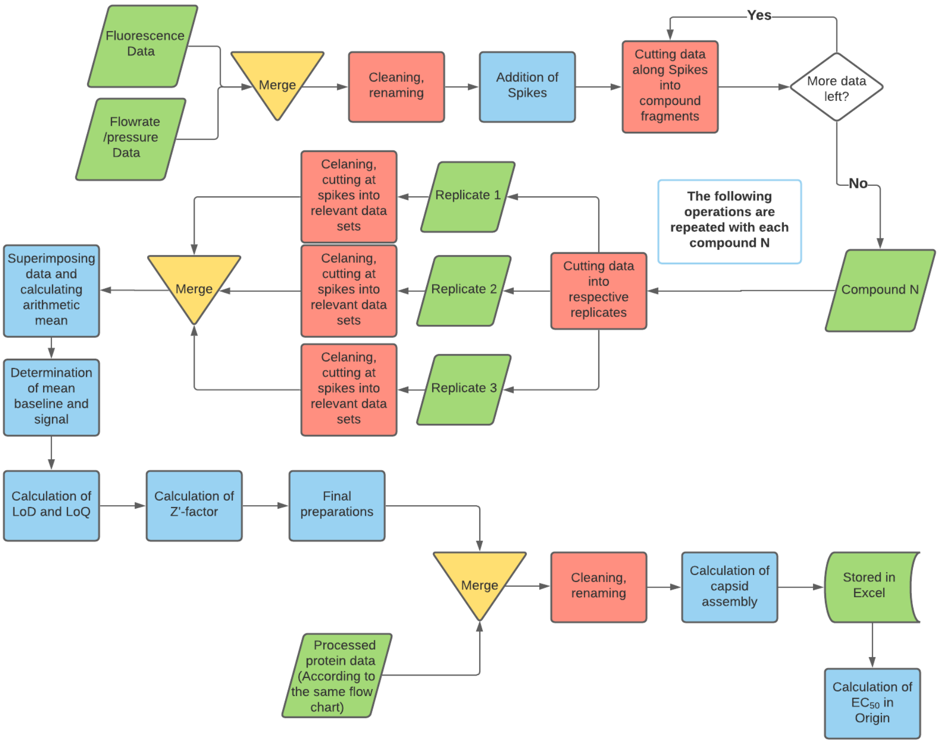

Figure 62: Annotated flow scheme of the total KNIME workflow for the fully automated measurement of EC_{50} values from the dose-response curves of several different test compounds on the HBV assembly. In the flowchart, data operations are written in blue squares, data sets in green parallelograms, data trimming and cutting of irrelevant data between measurements (cleaning) in red squares, data mergings in yellow triangles, and decision markers in transparent rhombuses. First, the excel and text data containing the fluorescence and reflection values at given time points are merged with the data from the pressure pumps and flow units. Then, after the data cleaning (first red square) and the addition of spikes which marked the beginning of each reaction (first blue square), the complete data set was split into separate compounds (second red square) until completion (white rhombus). At this point, each compound was evaluated separately (third greed parallelogram), including cutting the data into replicates followed by the cleaning and finally superimposing the three replicates (second yellow triangle). The complete set was then used to calculate the arithmetic mean and standard deviation of the maximal and minimal values and, based on these data, the Lod, LoQ, and Z'factor (five blue squares after the second triangle). The same processes have been repeated with the data obtained from fluorescein's dilution, which served as an encoder for the CAMs'concentration (last green parallelogram). Finally, the two data sets were merged (third triangle), and the data was used to calculate the capsid assembly and the EC_{50} values (last two squares).

For the calculation of the EC_{50} values, the concentration of the CAMs as well as the CAM-mediated HBc assembly had to be determined at each time point (every 0.1 s) during the reaction. The measurement was challenging since the OptoReader did not offer multiplex measurements, requiring first the measurement of the CAM-mediated HBc assembly followed by the dilution of FITC under the same conditions. FITC was used as a concentration marker which was possible due to the high reproducibility of the compound dilution profiles without deviations between compounds using convectional dominated TAD (IV.4.1 Experimental screening of volume normalized capillaries to determine the optimal capillary parameters for unilateral TAD measurements). For simplicity, only the final KNIME protocol used for EC_{50} values with a residence time of 51 s and two separate channels with flowrates of 12 µl/min was described.

The initial text files contained fluorescence and reflection data every 0.1 s and flowrate and pressure values every 1 s. The first step was uploading the data to the Knime workflow performed by simple data readers for text and excel files. This data was then formatted, including removing unnecessary columns, renaming the other ones vital for further handling, and generating a counter with an increment of 0.1. The counter generation was used in many steps of the workflow, with the primary function as a time marker to allow the data's joining and handling at the correct time points. The start of each reaction was marked with "Spikes" by using the math node to add 10 RFU to the fluorescence data, which exceeded the maximal measured RFU and henced became global maxima (Figure 63).

Following the initial formatting, the data was divided into individual compounds packages, each containing three to four replicates using the combination of several different meta nodes into a c meta node. The data separation was executed with the Rule Engine module by cutting the data at the respective compound spike points (Figure 63 to Figure 65).

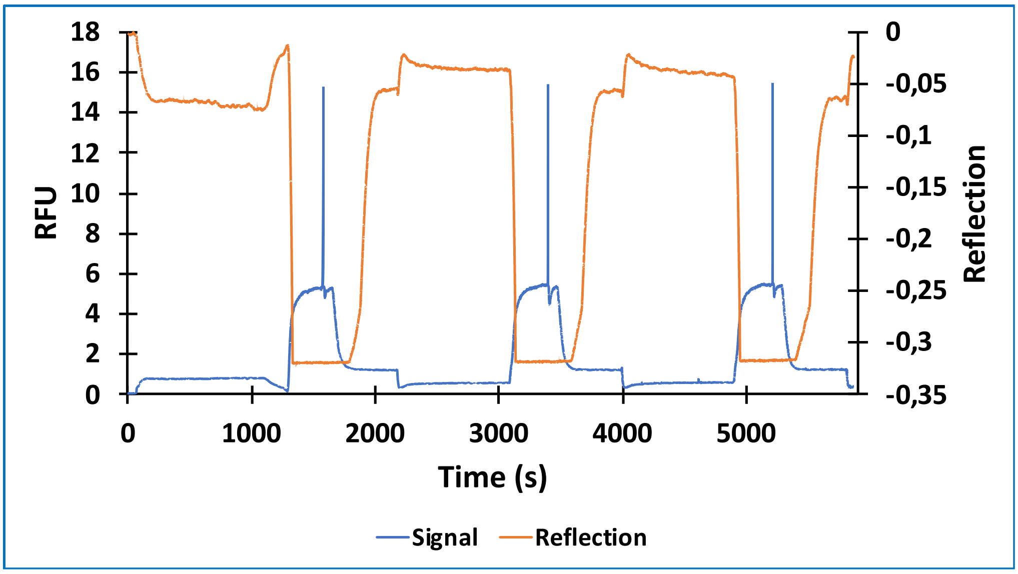

Figure 63: Singal (blue) and reflection (orange) data of capsid assembly reaction induced by BAY 41-4109 in three replicates. The reaction consisted of cleaning, signal saturation (CP150-BO mixed with 50 mM HEPES), and assembly reaction marked with the high blue peaks. During the assembly, the CP150-BO was mixed with the TAD-generated dilution gradient of the BAY 41-4109, resulting in the asymptotic quenching of the fluorescence signal.

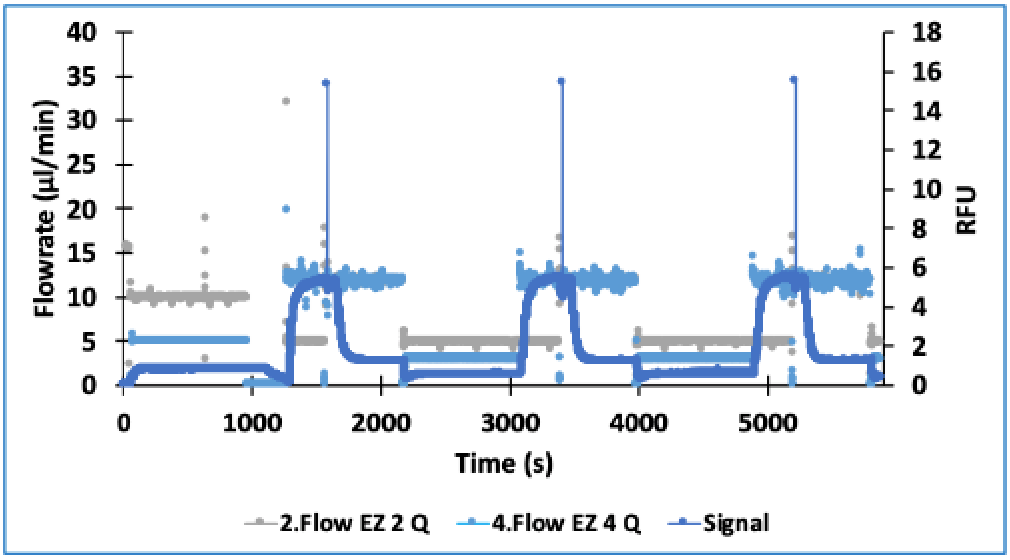

Figure 64: RFU signal (blue graph) of BAY41-4109 with three replicates and the flowrates of CP150-BO (4) and BAY41-4109 (2). The reaction consisted of cleaning, signal saturation (CP150-BO mixed with 50 mM HEPES), and assembly reaction marked with the high blue peaks. During the assembly, the CP150-BO was mixed with the TAD-generated dilution gradient of the BAY 41-4109, resulting in the asymptotic quenching of the fluorescence signal. The flowrates were constant and reproducible during the whole reaction. In this graph, only the two relevant ones were displayed for the purpose of clarity.

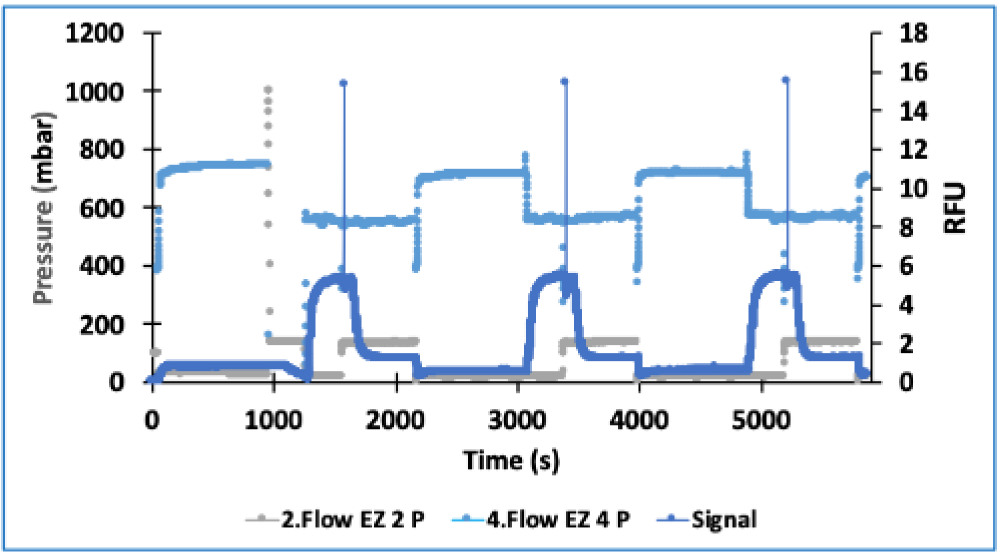

Figure 65: RFU signal of BAY41-4109 with three replicates and the pressures of the pumps used of CP150-BO (4) and BAY41-4109 (2). The reaction consisted of cleaning, signal saturation (CP150-BO mixed with 50 mM HEPES), and assembly reaction marked with the high blue peaks. During the assembly, the CP150-BO was mixed with the TAD-generated dilution gradient of the BAY 41-4109, resulting in the asymptotic quenching of the fluorescence signal. The pump pressures were constant and reproducible during the whole reaction. In this graph, only the two relevant ones were displayed for the purpose of clarity.

The fluorescence data of each compound was split into the respective technical replicates using partitioning nodes set to the individual percentual parts. Next, the data were trimmed by cutting unnecessary parts before the measurement's starting point, marked by a Spike, and the completion of the reaction. Finally, the technical replicates were combined to a single file in the joiner meta node (Figure 62, second yellow triangle).

The arithmetic means and standard deviations of the fluorescence and the reflection data were calculated in the "standard deviation" meta node with the combined file. Minimal and maximal values were determined based on the HBc's fluorescence values with and without the respective CAMs. Next, the mean value and the baseline's standard deviation were determined and used to calculate the LoD and LoQ according to the definition of Currie.[41] Finally, with a Rule Engine module, the results were categorized into non-detectable, above LoD, and above LoQ. Eventually, all the obtained data were joined in a single file, and the assay's Z'-factor was calculated using an equation with the baseline being CP150-BOs' RFU and the signal being the assembled CP150-BOs' RFU values, according to Zhang et al. (Figure 62, 2-6 blue squares).[99] The evaluated data was saved in an excel sheet and was depicted as a Line Plot (Figure 66).

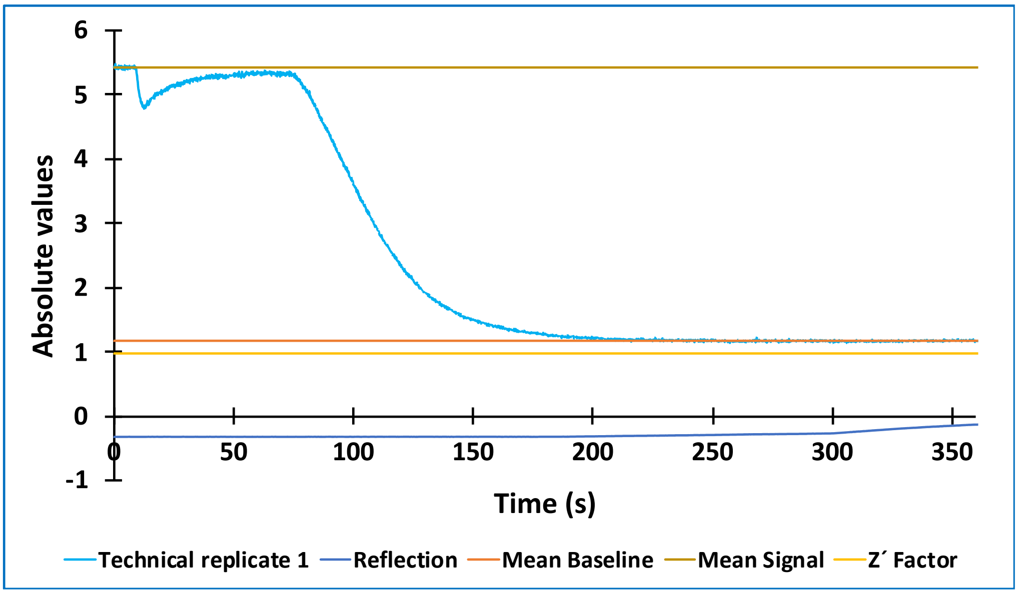

Figure 66: High-resolution dose response curve of BAY41-4109 mediated CP150-BO assembly, including the fluorescence and reflection data, and the calculated maximal (Mean Signal), minimal signals (Mean Baseline), and the Z'-factor. The here displayed curves were generated as the arithmetic mean of three independent measurements with a SD under 5%. Values were recorded every 0.1 s from 350 s up to 3500 s which were used to calculate the EC_{50} values.

The capsid assembly was calculated based on the CP150-BO fluorescence signal (Equation 27). Meanwhile, the encoder containing the time-dependent concentration distribution of the compound was loaded from an excel file or directly connected from the evaluated text data. Finally, the data was processed, and the CAM-mediated HBc assembly curve was joined with the encoder's dilution (Figure 62 third yellow triangle). Both data sets were superimposed, allowing the calculation of a high-resolution dose-response curve with individual data points at every 0.1 s. The data was saved with an excel writer, and the EC_{50} values were evaluated (Figure 67 and Figure 68).

Equation 27: Calculation of the capsid assembly in the EC_{50} methanode.

$$1 - (\$Technical\ replicate\ 1\$/\$Mean\ Signal\$)$$

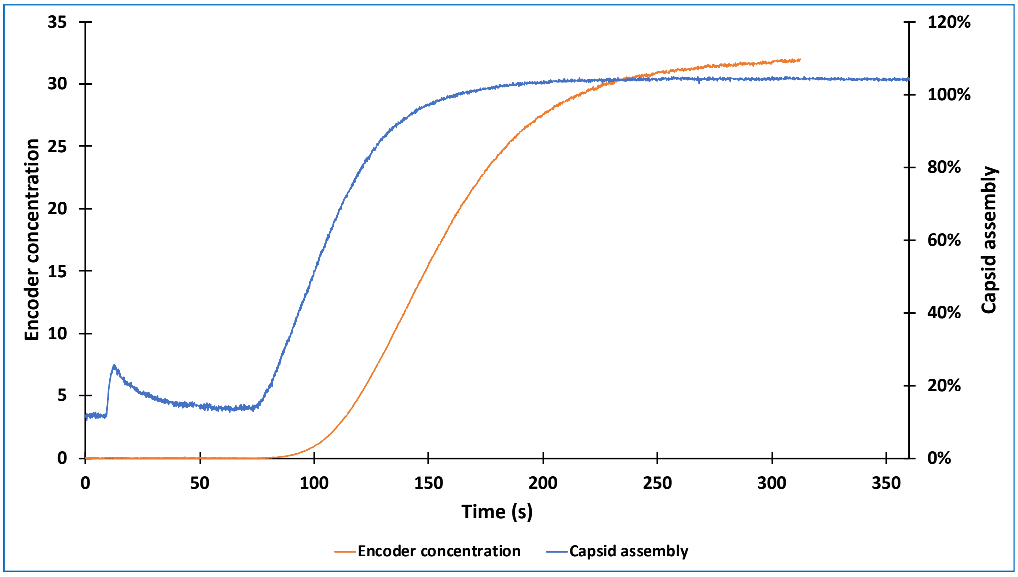

Figure 67: Concentration of the compound depicted by the encoder (orange) joined with the capsid assembly data (blue). The fluorescence quenching of CAM mediated CP150-BO assembly was used to calculate the assembly at each time point with a precision down to 0.1 s. The data was superimposed with the positive control, where FITC was used to mark the compound's concentration. The high-resolution dose-response curves were calculated using the percentual assembly at each time point as a function of the encoder's concentration.

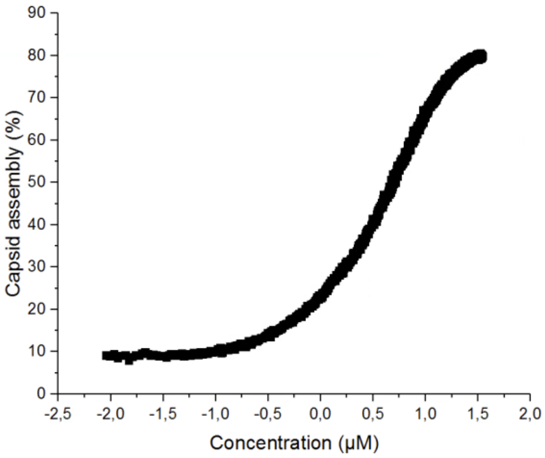

Figure 68: High resolution dose-response curve of a BAY41-4109 by depicting the capsid assembly concentration as a function of the encoder's concentration. The here displayed curves were calculated with data obtained in 5 minutes consisting of over 3000 independent data points.

III.5 Conclusion

In this chapter, the development and automation of the microfluidic system was described, from the evaluation of the individual items of equipment to the harmonization of the microfluidic system, including automation and the handling of problems. The first step was the generation and control of flow, for which three major types of active micropumps were compared: syringe pump, peristaltic pump, and pressure pumps.[17–19,24,25] In the end, pressure pumps with adequate flow measure units were chosen for the main system due to their superior response time, precision, and flow stability compared to the alternatives.[27–29] With these pumps, the flowthrough characteristics of several relevant solutions were measured, evaluated, and, if necessary, adjusted so that the measured and displayed flow rates were in close correlation. After combining multiple pumps, the stable flow was maintained by generating higher backpressure using PEEK tubings with a narrow ID of (0.13 mm) directly connected to the reservoirs, that was succeeded by PFA tubings with higher ID. The combination of the two tubings prevented backflow and flow fluctuations resulting from the system's height differences. Additionally, three different check valves were evaluated. The CV-3000 inline Cartridge outperformed the other two due to its reduced inner volume and compound adsorption properties, even though problems occurred due to the displacement of the active sphere by air bubbles.

After establishing stable flows, several different readout methods, including electrochemical,[30] mechanical,[31] and optical,[32–34] were considered, of which fluorescence spectrometry was chosen due to the benefits of non-invasive ubiquitous readout with real-time detection and highest temporal and spatial resolution of bio-analytes down to the nanoscale.[32,35] A more extensive search was necessary to find the ideal fluorescence spectrometer because of the limited equipment availability. The OptoReader spectrometer was ultimately selected, providing high acquisitions rates of up to 100 kHz, high sensitivity with detection down to 1 nm FITC and compact duplex optical fiber. The OptoReader was evaluated extensively with several different microreactors and FITC dilutions from 32 µM down to 3.2 nM. In this way, optimal diode power and gain conditions were evaluated to determine range of detection, S/N, and S/B ratios (Figure 77 to Figure 79).

In the next step, mixing under laminar flow conditions was assessed. Several passive micromixers were evaluated among those the chaotic advection type 3D-serpentine mixer,[61–63] the hydrodynamic flow focusing µ-slide III,[60] and the sequential lamination based ROSAR GF-T75.[4,58,78] ROSAR GF-T75 outperformed all the other mixers at the low Re numbers (max 6), showing excellent mixing times of a couple of ms combined with a low inner volume of under 1 µl. Despite the immense benefits, the initial use of the chip was overshadowed by complex maintenance issues, which were only solved later in the work by changing the chips adapter.

Afterwards, inflow dilution, multiple compound screening, and flexible flow pathing were addressed. Several different options were evaluated, including flowrate variations, valve-driven circulatory dilution based on sequential mixing,[85] digital microfluidics[86] or programmed 2-dimensional arrays with pneumatically actuated microvalves,[87] and finally TAD. The TAD was chosen as the best option given the low material requirement, ease of use, and the quality and quantity of data points generated.[82,84,88–90] The initial sharp compound margin required for TAD was generated by the 6-port bidirectional L-Switch™ and a short capillary with a higher inner diameter (IV.4.1.1 The impact of capillaries' ID on the convection dominated TAD). Subsequently multiple compound measurements were possible using first the 12 port AMF unidirectional valve coupled to up to 8 reservoirs. Finally, problems were adressed and different troubleshooting guides were developed for the most common errors in the system, including flow fluctuations, deviations in TAD dilution, and problems with the biochemical assay (Figure 69).

Microfluidic processes are often combined with automation to reduce the redundant lab work and increase the assays reproducibility and precision.[100] Automation is heavily used in the drug discovery process, mainly within the hit to lead development cycle.[101] The automation of the microfluidic system and the harmonization of the microfluidic setup into a single software interface was performed using MAT. The various workflows permitted the measurement of CAMs mediated HBc assembly kinetics (Figure 60) and high-resolution dose-response curves in three technical replicates, including three basic steps:

washing, signal regeneration, and measurement (Figure 56, Figure 61, and Figure 63).
Furthermore, to facilitate the usage of the system workflows were written in the open-source software KNIME (version 4.9) (KNIME AG, Zurich, Switzerland) for the evaluation of fluorescent and reflection data. With the protocol, the kinetic measurements and the EC_{50} values were calculated for each compound. The limit of detection and quantification were determined according to Currie's definition,[41] and the Z'-factor[99] was recorded in excel sheets for each measurement individually. Furthermore, the final protocols are easily adjustable, thus allowing a simple adaptation to novel requirements or system expansions at near zero additional costs.

The last part of this work focused on the interface between synthesis and subsequent screening of compounds which greatly reduces the time and handling requirement of a hit-to-lead and lead optimization processes as previously demostrated.[82,102–104] A simple initial solution was the employment of an LHS equipped with a robotic arm. With the RotAxys360 equipeed with a small syringe pump the transfer of up to 5x96 compounds from the microtiter plate to the reservoirs was performed. A syringe pump was better suited for sample dosing than pressure pumps given its more reliable handling of injection at lower volumes.[27–29] While the robotic LHS is a feasible choice as an interface, more sophicticated solutions are possible. The direct integration of the chemical synthesis to the biochemical evaluation would reduce the handling time and sample exposure even further.[82] However, a fully automated synthesis and screening platform requires further optimization mainly the compound purification, the exchange of solvents, and the accurate determination of final compound concentrations. In the future, the microfluidic assay presented here could be telescoped to a synthesis platform in this way. This upgrade is highly feasible given the modularity of the setup permitting an easy exchange of hardware. Furthermore, all protocols (automation and evaluation) were written such that additional modules could be easily included at a future timepoint.

In order to demonstrate the flexibility and performance of the system, the HBc assembly assay was adapted to the flow format. The capsid assembly assay was a good initial choice given that this is a largely unexplored reaction in flow with fast assembly rates which could provide unique results in the microfluidic format.[105]

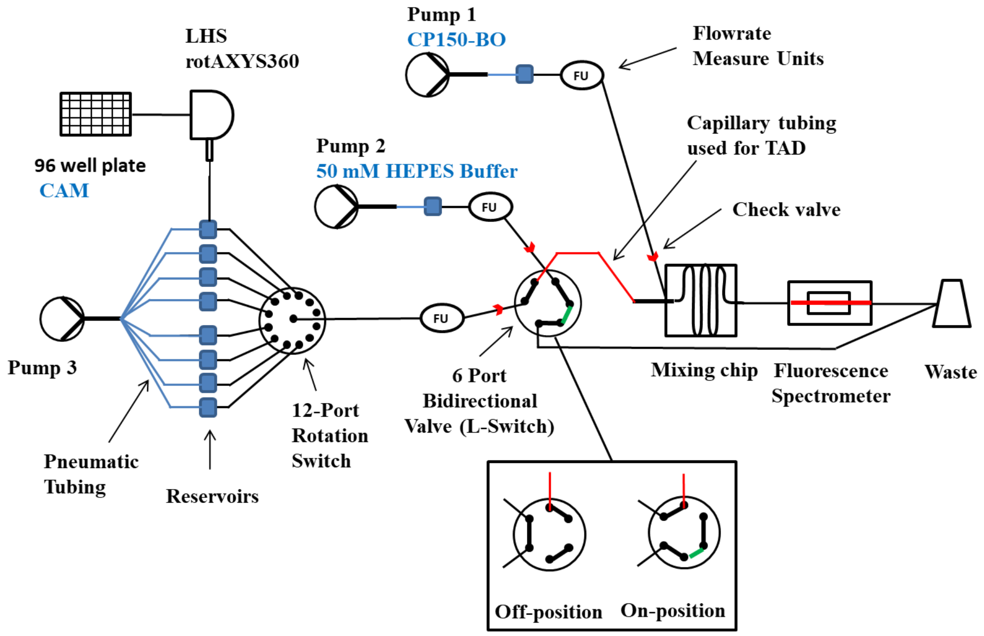

Figure 69: Schematic representation of the microfluidic system used for the screening and characterization of novel HBV CAMs. The compounds were transferred from a 96 well plate to the pressurized reservoirs (blue squares) with the LHS rotAXYS360. Afterward, the system was equilibrated by first loading the first compound until the L-Switch, which was set to the Off-position to remove compound excess into the waste. Simultaneously, Pump 2 and Pump 3 were running with identical flowrates allowing the mixing of 50 mM HEPES with CP150-BO in the mixing chip and thereby generating the baseline. Following the initiation, pump 3 was set to the same flowrate as pump 1, and the L-Switch turned to the On-position, allowing the TAD of the CAM's compound margin in the designated (red) capillary and its subsequent mixing with the CP150-BO protein. After the measurement, the system was cleaned with H_2O using pump 3 switched to the respective reservoir and 50 mM HEPES using pump 2. Legend for the various units is depicted in Figure 30.

III.6 References

1. Whitesides, G. M. The origins and the future of microfluidics. *Nature* **442**, 368–373 (2006).
2. Kirby, B. J. *Micro- and Nanoscale Fluid Mechanics*. (CAMBRIDGE UNIVERSITY PRESS, 2010).
3. Wiley, J. Transport Laws 3.1. **1**, (2020).
4. Hardt, S., Pennemann, H. & Schönfeld, F. Theoretical and experimental characterization of a low-Reynolds number split-and-recombine mixer. *Microfluid. Nanofluidics* **2**, 237–248 (2006).
5. Resistance, H. Channel Flow 2.1. (2020).
6. Turner, J. et al. United States Patent; Patent No.: US 10 , 183 , 936 B2. (2019).
7. Corcuera, A. *et al.* Novel non-heteroarylpyrimidine (HAP) capsid assembly modifiers have a different mode of action from HAPs in vitro GPA, PT, DBT. *Antiviral Res.* **158**, 135–142 (2018).
8. VANDYCK, Koen; HACHE, Geerwin; Yvonne, Paul; Stefaan, Julien;David, Craig;ROMBOUTS, Geert; VERSCHUEREN, Wim, Gaston; RABOISSON, Pierre, Jean-Marie, B. WO 2014/184350 A1. vol. 5 (2014).
9. Karl Deres, H. R.-W. Inhibition of Hepatitis B Virus Replication by Drug-Induced Depletion of Nucleocapsids. *Science (80-.).* **303**, 1829 (2003).
10. Wang, X. Y. *et al.* In vitro inhibition of HBV replication by a novel compound, GLS4, and its efficacy against adefovirdipivoxil-resistant HBV mutations. *Antivir. Ther.* **17**, 793–803 (2012).
11. Li, X., Ballerini, D. R. & Shen, W. A perspective on paper-based microfluidics: Current status and future trends. *Biomicrofluidics* **6**, (2012).
12. Prins, M. W. J., Welters, W. J. J. & Weekamp, J. W. Fluid control in multichannel structures by electrocapillary pressure. *Science (80-.).* **291**, 277–280 (2001).
13. Weigl, B. H., Bardell, R. L., Kesler, N. & Morris, C. J. Lab-on-a-chip sample preparation using laminar fluid diffusion interfaces computational fluid dynamics model results and fluidic verification experiments. *Anal. Bioanal. Chem.* **371**, 97–105 (2001).
14. Teo, A. J. T. *et al.* Negative Pressure Induced Droplet Generation in a Microfluidic Flow-Focusing Device. *Anal. Chem.* **89**, 4387–4391 (2017).
15. Li, B. *et al.* A smartphone controlled handheld microfluidic liquid handling system. *Lab Chip* **14**, 4085–4092 (2014).
16. Weigl, B. H., Bardell, R. L. & Cabrera, C. R. Lab-on-a-chip for drug development. *Adv. Drug Deliv. Rev.* **55**, 349–377 (2003).
17. Forouzandeh, F., Arevalo, A., Alfadhel, A. & Borkholder, D. A. A review of peristaltic micropumps. *Sensors Actuators, A Phys.* **326**, 112602 (2021).
18. Iverson, B. D. & Garimella, S. V. Recent advances in microscale pumping technologies: A review and evaluation. *Microfluid. Nanofluidics* **5**, 145–174 (2008).
19. Nisar, A., Afzulpurkar, N., Mahaisavariya, B. & Tuantranont, A. MEMS-based micropumps in drug delivery and biomedical applications. *Sensors Actuators, B Chem.* **130**, 917–942 (2008).
20. Cui, Q., Liu, C. & Zha, X. F. Study on a piezoelectric micropump for the controlled drug delivery system. *Microfluid. Nanofluidics* **3**, 377–390 (2007).
21. Bodén, R. *et al.* A polymeric paraffin actuated high-pressure micropump. *Sensors Actuators, A Phys.* **127**, 88–93 (2006).
22. MacHauf, A., Nemirovsky, Y. & Dinnar, U. A membrane micropump electrostatically actuated across the working fluid. *J. Micromechanics Microengineering* **15**, 2309–2316 (2005).
23. Nagel, J. J., Mikhail, G., Noh, H. & Koo, J. Magnetically actuated micropumps using an Fe-PDMS composite membrane. *Smart Struct. Mater. 2006 Smart Electron. MEMS, BioMEMS, Nanotechnol.* **6172**, 617213 (2006).

24. Laser, D. J. & Santiago, J. G. A review of micropumps. *J. Micromechanics Microengineering* **14**, (2004).

25. Boyd-Moss, M., Baratchi, S., Di Venere, M. & Khoshmanesh, K. Self-contained microfluidic systems: A review. *Lab Chip* **16**, 3177–3192 (2016).

26. González, P., Knochen, M., Sasaki, M. K. & Zagatto, E. A. G. Pulsed flows in flow analysis: Potentialities, limitations and applications. *Talanta* **143**, 419–430 (2015).

27. Peristaltic, syringe and pressure microfluidic pumps comparison | Fluigent. https://www.fluigent.com/resources/microfluidic-expertise/advantages-of-pressure-based-microfluidic/system-comparison-for-microfluidic-applications-2/.

28. Flow control in microfluidics device - Elveflow. https://www.elveflow.com/microfluidic-reviews/microfluidic-flow-control/flow-control-in-microfluidics-device/.

29. Flow Control in Microfluidics– Darwin Microfluidics. https://darwin-microfluidics.com/pages/flow-control-in-microfluidics.

30. Wongkaew, N., He, P., Kurth, V., Surareungchai, W. & Baeumner, A. J. Multi-channel PMMA microfluidic biosensor with integrated IDUAs for electrochemical detection. *Anal. Bioanal. Chem.* **405**, 5965–5974 (2013).

31. Ferrari, M. Cancer nanotechnology: Opportunities and challenges. *Nat. Rev. Cancer* **5**, 161–171 (2005).

32. Măriuța, D. *et al.* Miniaturization of fluorescence sensing in optofluidic devices. *Microfluidics and Nanofluidics* vol. 24 (2020).

33. Kuswandi, B., Nuriman, Huskens, J. & Verboom, W. Optical sensing systems for microfluidic devices: A review. *Anal. Chim. Acta* **601**, 141–155 (2007).

34. Dittrich, P. S. & Manz, A. Single-molecule fluorescence detection in microfluidic channels-the Holy Grail in µtAS? *Anal. Bioanal. Chem.* **382**, 1771–1782 (2005).

35. Pires, N. M. M., Dong, T., Hanke, U. & Hoivik, N. Recent developments in optical detection technologies in lab-on-a-chip devices for biosensing applications. *Sensors (Switzerland)* **14**, 15458–15479 (2014).

36. Guilbault, G. G. *Practical fluorescence*. (2020).

37. B Valeur, J. B. *New trends in fluorescence spectroscopy: applications to chemical and life sciences*. (2012).

38. Wei, L., Yan, W. & Ho, D. Recent advances in fluorescence lifetime analytical microsystems: Contact optics and CMOS time-resolved electronics. *Sensors (Switzerland)* **17**, (2017).

39. SVM340 Synchronized Video Microscope - LabSmith. https://products.labsmith.com/svm340-synchronized-video-microscope/?_ga=2.159278458.1764283324.1623145246-205680780.1607953706&_gac=1.162596686.1623145246.CjwKCAjwqvyFBhB7EiwAER786Z3H6hrDesuDmoyOE6G-YZpKuql6jB-pcaKIq25PMXAd0b3Z6vixlBoC29gQAvD_BwE#.YL87KOuxVhE.

40. Fiber optic sensor - Elveflow. https://www.elveflow.com/microfluidic-applications/setup-microfluidic-flow-control/fiber-optic-ph-sensor-based-fluorescent-molecules/.

41. Currie, L. A. Limits for Qualitative Detection and Quantitative Determination: Application to Radiochemistry. *Anal. Chem.* **40**, 586–593 (1968).

42. Brody, J. P., Yager, P., Goldstein, R. E. & Austin, R. H. Biotechnology at low Reynolds numbers. *Biophys. J.* **71**, 3430–3441 (1996).

43. Beebe, D. J., Mensing, G. A. & Walker, G. M. Physics and applications of microfluidics in biology. *Annu. Rev. Biomed. Eng.* **4**, 261–286 (2002).

44. Wörz, O., Jäckel, K. P., Richter, T. & Wolf, A. Microreactors, a new efficient tool for optimum reactor design. *Chem. Eng. Sci.* **56**, 1029–1033 (2001).

45. Lorenzo Capretto, Wei Cheng, Martyn Hill, X. Z. & Deming, T. J. Micromixing Within Microfluidic Devices. *Springer-Verlag Berlin* **310**, 1–26 (2011).

46. Cai, G., Xue, L., Zhang, H. & Lin, J. A review on micromixers. *Micromachines* **8**, (2017).

47. Naher, S., Orpen, D., Brabazon, D. & Morshed, M. M. An overview of microfluidic mixing application. *Adv. Mater. Res.* **83**–**86**, 931–939 (2010).

48. Haswell, S. J. & Skelton, V. Chemical and biochemical microreactors. *TrAC - Trends Anal. Chem.* **19**, 389–395 (2000).

49. Michelle R. Bringer, Cory J. Gerdts, Helen Song, J. D. T. and R. F. I. Microfluidic systems for chemical kinetics. *Phil. Trans. R. Soc. Lond. A* 1087–1104 (2004).

50. Schwarzer, H. C., Schwertfirm, F., Manhart, M., Schmid, H. J. & Peukert, W. Predictive simulation of nanoparticle precipitation based on the population balance equation. *Chem. Eng. Sci.* **61**, 167–181 (2006).

51. Ståhl, M., Åslund, B. L. & Rasmuson, Å. C. Reaction crystallization kinetics of benzoic acid. *AIChE J.* **47**, 1544–1560 (2001).

52. Wilms, D., Klos, J. & Frey, H. Microstructured reactors for polymer synthesis: A renaissance of continuous flow processes for tailor-made macromolecules? *Macromol. Chem. Phys.* **209**, 343–356 (2008).

53. Doku, G. N., Verboom, W., Reinhoudt, D. N. & Van Den Berg, A. On-microchip multiphase chemistry - A review of microreactor design principles and reagent contacting modes. *Tetrahedron* **61**, 2733–2742 (2005).

54. Zhang, C., Xing, D. & Li, Y. Micropumps, microvalves, and micromixers within PCR microfluidic chips: Advances and trends. *Biotechnol. Adv.* **25**, 483–514 (2007).

55. Manz, A., Graber, N. & Widmer, H. M. Miniaturized total chemical analysis systems: A novel concept for chemical sensing. *Sensors Actuators B. Chem.* **1**, 244–248 (1990).

56. Gobby, D., Angeli, P. & Gavriilidis, A. Mixing characteristics of T-type microfluidic mixers. 6–13 (2001).

57. Li, X., He, L., He, Y., Gu, H. & Liu, M. Numerical study of droplet formation in the ordinary and modified T-junctions. *Phys. Fluids* **31**, (2019).

58. Branebjerg, J., Gravesen, P., Krog, J. P. & Nielsen, C. R. Fast mixing by lamination. *Proc. IEEE Micro Electro Mech. Syst.* 441–446 (1996).

59. Lee, S. W., Kim, D. S., Lee, S. S. & Kwon, T. H. A split and recombination micromixer fabricated in a PDMS three-dimensional structure. *J. Micromechanics Microengineering* **16**, 1067–1072 (2006).

60. Knight, J. B., Vishwanath, A., Brody, J. P. & Austin, R. H. Hydrodynamic Focusing on a Silicon Chip: Mixing Nanoliters in Microseconds James. 1–4 (1998).

61. Stroock, A. D. *et al.* Chaotic mixer for microchannels. *Science (80-.).* **295**, 647–651 (2002).

62. Liu, R. H. *et al.* Passive mixing in a three-dimensional serpentine microchannel. *J. Microelectromechanical Syst.* **9**, 190–197 (2000).

63. JM Ottino. *The kinematics of mixing: stretching, chaos, and transport*. (1898).

64. Tung, K. Y., Li, C. C. & Yang, J. T. Mixing and hydrodynamic analysis of a droplet in a planar serpentine micromixer. *Microfluid. Nanofluidics* **7**, 545–557 (2009).

65. Helen Song, Joshua D. Tice, and R. F. I. A Microfluidic System for Controlling Reaction Networks in Time**. *Angew. CHem. Int..* **42**, 767 (2003).

66. Moroney, R. M., White, R. M. & Howe, R. T. Ultrasonically induced microtransport. *Proceedings. IEEE Micro Electro Mech. Syst.* 277–282 (1991).

67. Phan, H. Van *et al.* Vibrating membrane with discontinuities for rapid and efficient microfluidic mixing. *Lab Chip* **15**, 4206–4216 (2015).

68. Eribol, P. & Uguz, A. K. Experimental investigation of electrohydrodynamic instabilities in micro channels. *Eur. Phys. J. Spec. Top.* **224**, 425–434 (2015).

69. Posner, J. D., Pérez, C. L. & Santiago, J. G. Electric fields yield chaos in microflows. *Proc. Natl. Acad. Sci. U. S. A.* **109**, 14353–14356 (2012).

70. Dog, X., Zhang, L. & Fu, J. Laser-induced thermal bubble-mixing on a microfluidic platform

for lab-on-a-chip applications. *Adv. Mater. Res.* **557**–**559**, 2197–2201 (2012).

71. Zhang, F., Chen, H., Chen, B. & Wu, J. Alternating current electrothermal micromixer with thin film resistive heaters. *Adv. Mech. Eng.* **8**, 1–10 (2016).

72. Deval, J., Tabeling, P. & Ho, C. M. A dielectrophoretic chaotic mixer. *Proc. IEEE Micro Electro Mech. Syst.* 36–39 (2002).

73. Lee, H. Y. & Voldman, J. Optimizing micromixer design for enhancing dielectrophoretic microconcentrator performance. *Anal. Chem.* **79**, 1833–1839 (2007).

74. Paik, P., Pamula, V. K., Pollack, M. G. & Fair, R. B. Electrowetting-based droplet mixers for microfluidic systems. *Lab Chip* **3**, 28–33 (2003).

75. Paik, P., Pamula, V. K. & Fair, R. B. Rapid droplet mixers for digital microfluidic systems. *Lab Chip* **3**, 253–259 (2003).

76. Eickenberg, B. *et al.* Continuous-flow particle guiding based on dipolar coupled magnetic superstructures in rotating magnetic fields. *Lab Chip* **13**, 920–927 (2013).

77. Cao, Q., Han, X. & Li, L. An active microfluidic mixer utilizing a hybrid gradient magnetic field. *Int. J. Appl. Electromagn. Mech.* **47**, 583–592 (2015).

78. He, M., Li, W., Zhang, M. Q. & Zhang, J. Numerical investigation on the efficient mixing of overbridged split-and-recombine micromixer at low Reynolds number. *Microsyst. Technol.* **25**, 3447–3461 (2019).

79. Thiele, M. *et al.* High-Throughput Synthesis of Uniform Silver Seed Particles by a Continuous Microfluidic Synthesis Platform. *Chem. Eng. Technol.* **38**, 1131–1137 (2015).

80. Chován, T. & Guttman, A. Microfabricated devices in biotechnology and biochemical processing. *Trends Biotechnol.* **20**, 116–122 (2002).

81. Dittrich, P. S., Tachikawa, K. & Manz, A. Micro total analysis systems. Latest advancements and trends. *Anal. Chem.* **78**, 3887–3907 (2006).

82. Werner, M. *et al.* Seamless integration of dose-response screening and flow chemistry: Efficient generation of structure-activity relationship data of β-secretase (BACE1) inhibitors. *Angew. Chemie - Int. Ed.* **53**, 1704–1708 (2014).

83. Baccouche, A. *et al.* Massively parallel and multiparameter titration of biochemical assays with droplet microfluidics. *Nat. Protoc.* **12**, 1912–1932 (2017).

84. Miller, O. J. *et al.* High-resolution dose-response screening using droplet-based microfluidics. *Proc. Natl. Acad. Sci. U. S. A.* **109**, 378–383 (2012).

85. Ahrar, S., Hwang, M., Duncan, P. N. & Hui, E. E. Microfluidic serial dilution ladder. *Analyst* **139**, 187–190 (2014).

86. Roy, S., Bhattacharya, B. B. & Chakrabarty, K. Optimization of dilution and mixing of biochemical samples using digital microfluidic biochips. *IEEE Trans. Comput. Des. Integr. Circuits Syst.* **29**, 1696–1708 (2010).

87. Jensen, E. C. *et al.* Digitally programmable microfluidic automaton for multiscale combinatorial mixing and sample processing. *Lab Chip* **13**, 288–296 (2013).

88. Bello, M. S., Rezzonico, R. & Righetti, P. G. Use of Taylor-Aris dispersion for measurement of a solute diffusion coefficient in thin capillaries. *Science (80-.).* **266**, 773–776 (1994).

89. Wei, Y., Zhu, Y. & Fang, Q. Nanoliter Quantitative High-Throughput Screening with Large-Scale Tunable Gradients Based on a Microfluidic Droplet Robot under Unilateral Dispersion Mode. *Anal. Chem.* **91**, 4995–5003 (2019).

90. Solit, D. B. & Jänne, P. A. Primed for resistance. *Nature* **483**, 44–45 (2012).

91. Taylor, G. I. Diffusion by continuous movements. *Proc. London Math. Soc.* **s2-20**, 196–212 (1922).

92. Vedel, S., Hovad, E. & Bruus, H. Time-dependent Taylor-Aris dispersion of an initial point concentration. *J. Fluid Mech.* **752**, 107–122 (2014).

93. Ananthakrishnan, V., Gill, W. N. & Barduhn, A. J. Laminar dispersion in capillaries. *A.I.Ch. E.*

J. **11**, 1063–1072 (1965).

94. ESS^{TM} M-switch^{TM} 10-way microfluidic valve for sequential injections | Fluigent. https://www.fluigent.com/product/microfluidic-components-3/m-switch/.

95. OEM RVM Microfluidic Electric Rotary Valve - Advanced Microfluidics. https://amf.ch/product/oem-rotary-valve/.

96. Miller, O. J. *et al.* High-resolution dose-response screening using droplet-based microfluidics.

97. Schneider, G. Automating Drug Discovery. **17**, (2018).

98. Fleming, G. S. & Beeler, A. B. Integrated Drug Discovery in Continuous Flow. *J. Flow Chem.* **7**, 124–128 (2017).

99. Ji-Hu ZHANG, T. D. Y. C. K. R. O. A Simple Statistical Parameter for Use in Evaluation and Valiation of High Thorughput Screening Assays. (1999).

100. Schneider, G. Automating drug discovery. *Nat. Rev. Drug Discov.* **17**, 97–113 (2018).

101. Parry, D. M. Closing the Loop: Developing an Integrated Design, Make, and Test Platform for Discovery. *ACS Med. Chem. Lett.* **10**, 848–856 (2019).

102. Eduati, F. *et al.* A microfluidics platform for combinatorial drug screening on cancer biopsies. *Nat. Commun.* **9**, (2018).

103. Lauschke, V. M., Hendriks, D. F. G., Bell, C. C., Andersson, T. B. & Ingelman-Sundberg, M. Novel 3D Culture Systems for Studies of Human Liver Function and Assessments of the Hepatotoxicity of Drugs and Drug Candidates. *Chem. Res. Toxicol.* **29**, 1936–1955 (2016).

104. Desai, B. *et al.* Rapid discovery of a novel series of Abl kinase inhibitors by application of an integrated microfluidic synthesis and screening platform. *J. Med. Chem.* **56**, 3033–3047 (2013).

105. Zhou, J. *et al.* Characterization of Virus Capsids and Their Assembly Intermediates by Multicycle Resistive-Pulse Sensing with Four Pores in Series. *Anal. Chem.* **90**, 7267–7274 (2018).

III.7 Appendix

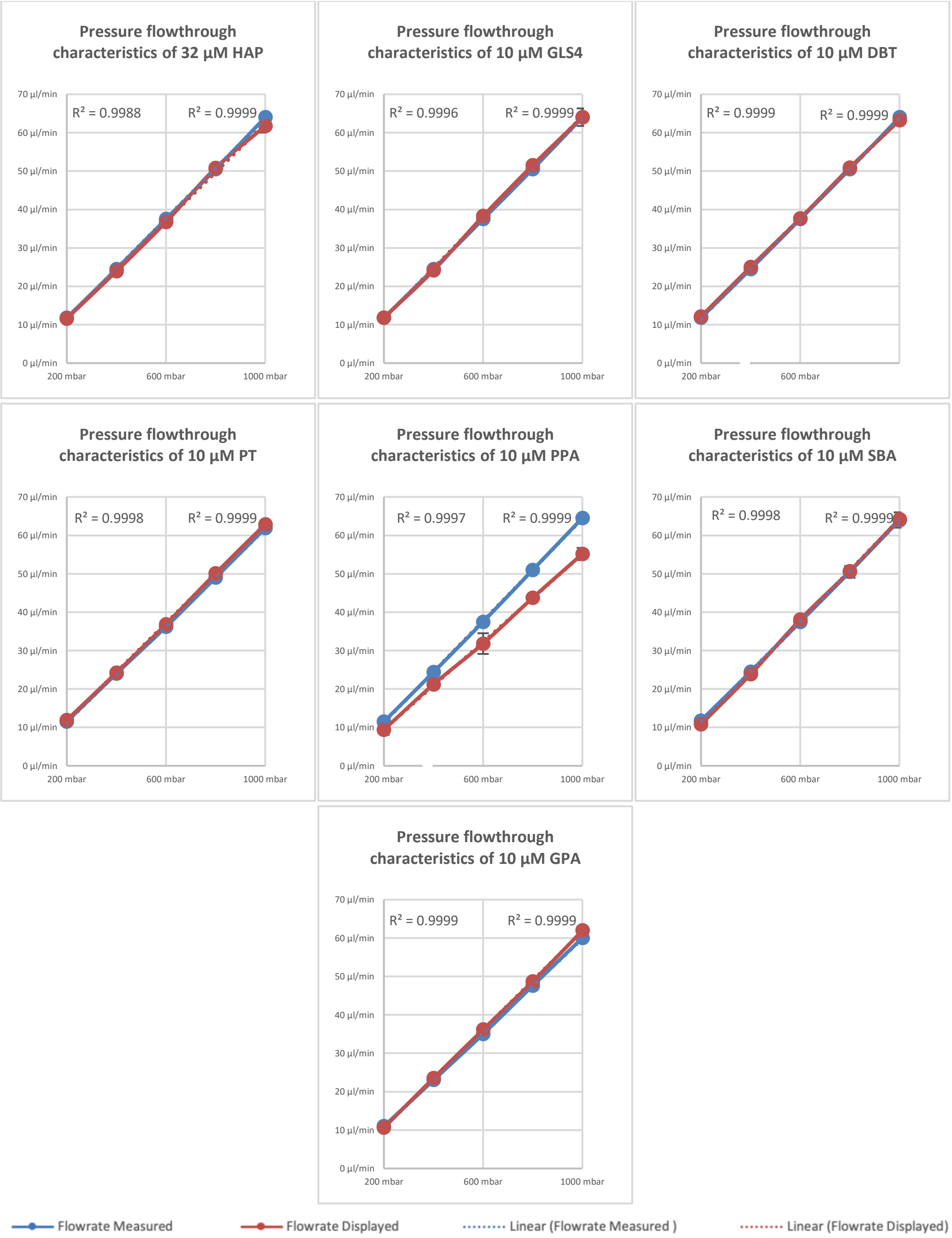

Figure 70: Pressure flowthrough characteristics of several CAM solutions relevant for the CP150c assay. The flowrates displayed by the flow units are marked red, the measured flowthrough in blue. Each measurement was repeated three times, and the standard deviations are depicted as error bars. In addition, R^2 was calculated for the linear approximation are displayed in the top left corner for the displayed and in the top right corner for the measured values.

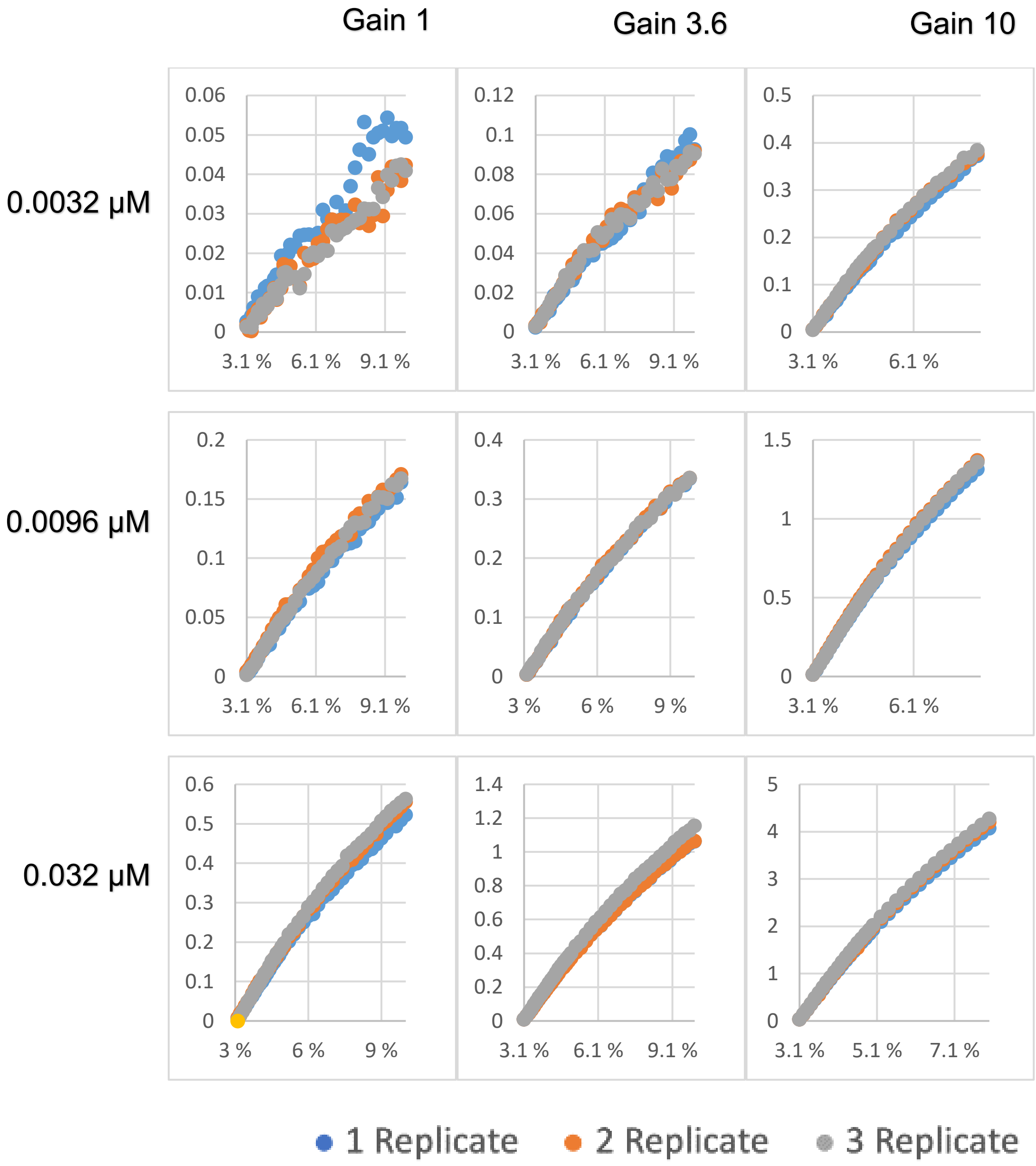

Figure 71: RFU of various fluorescein concentrations as a function of the laser power (x-axis) and the gain (three major columns) of the OptoReader. The experiments were repeated in three independent measurements.

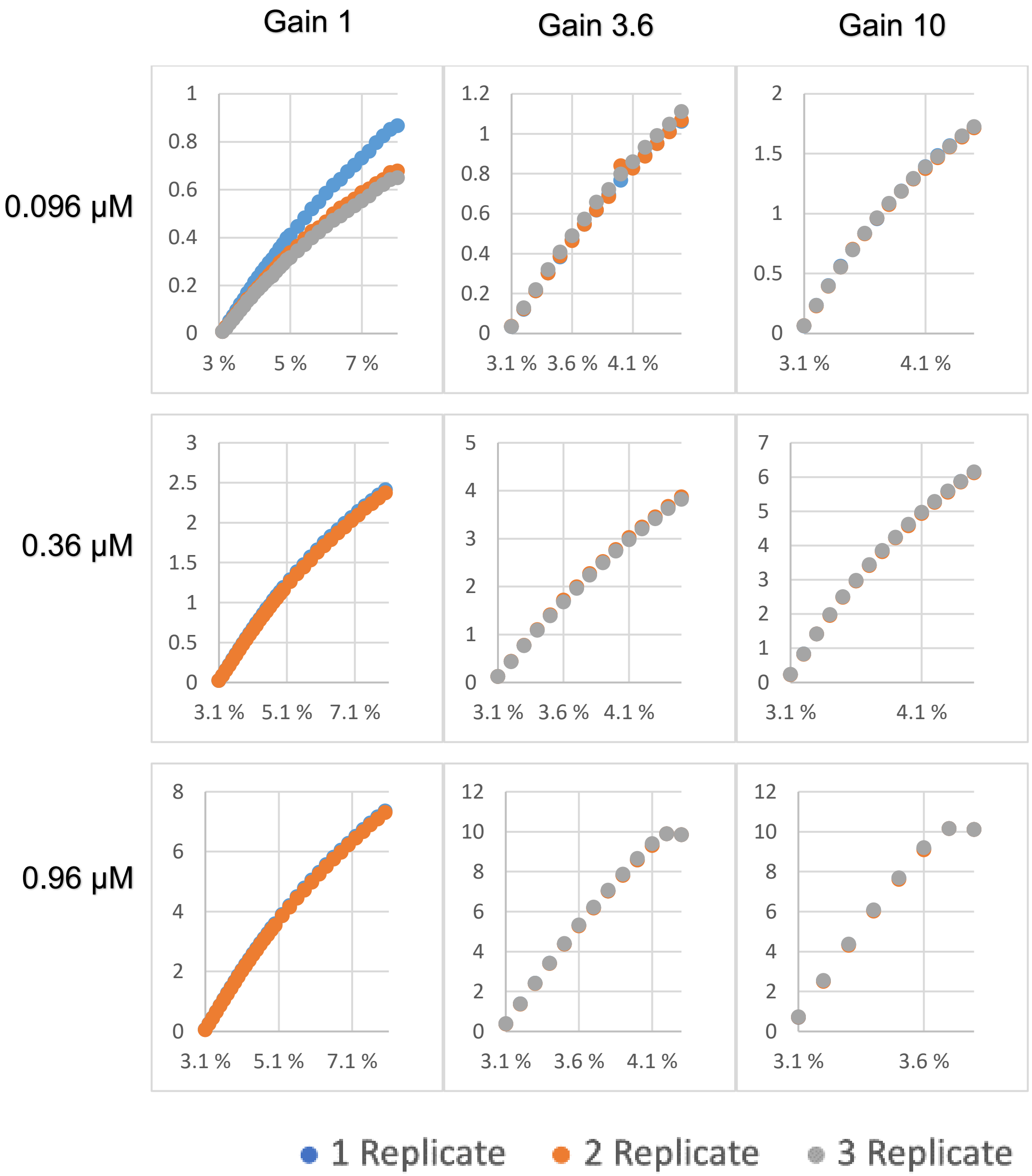

Figure 72: RFU of various fluorescein concentrations as a function of the laser power (x-axis) and the gain (three major columns) of the OptoReader. The experiments were repeated in three independent measurements.

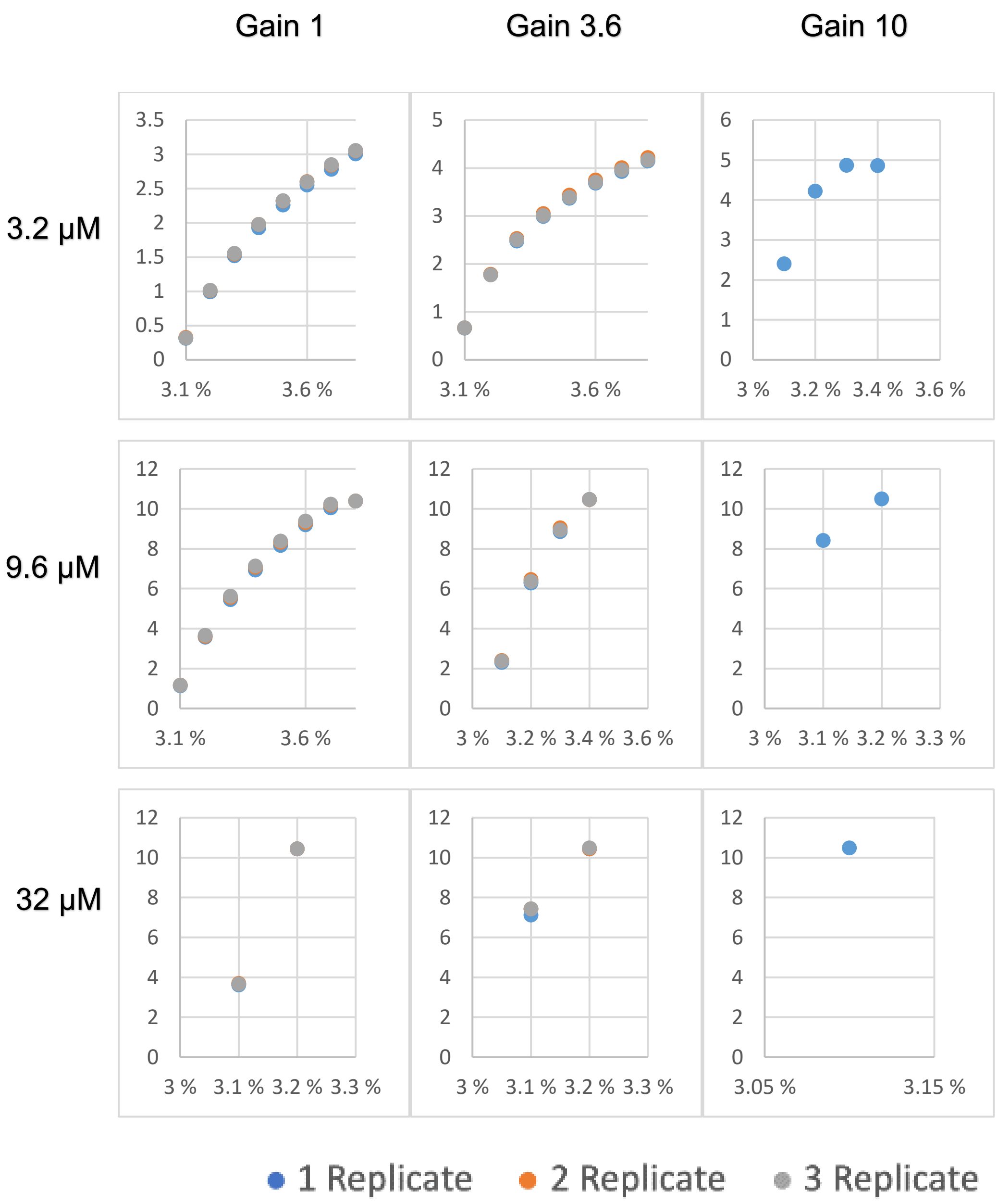

Figure 73: RFU of various fluorescein concentrations as a function of the laser power (x-axis) and the gain (three major columns) of the OptoReader. The experiments were repeated in three independent measurements.

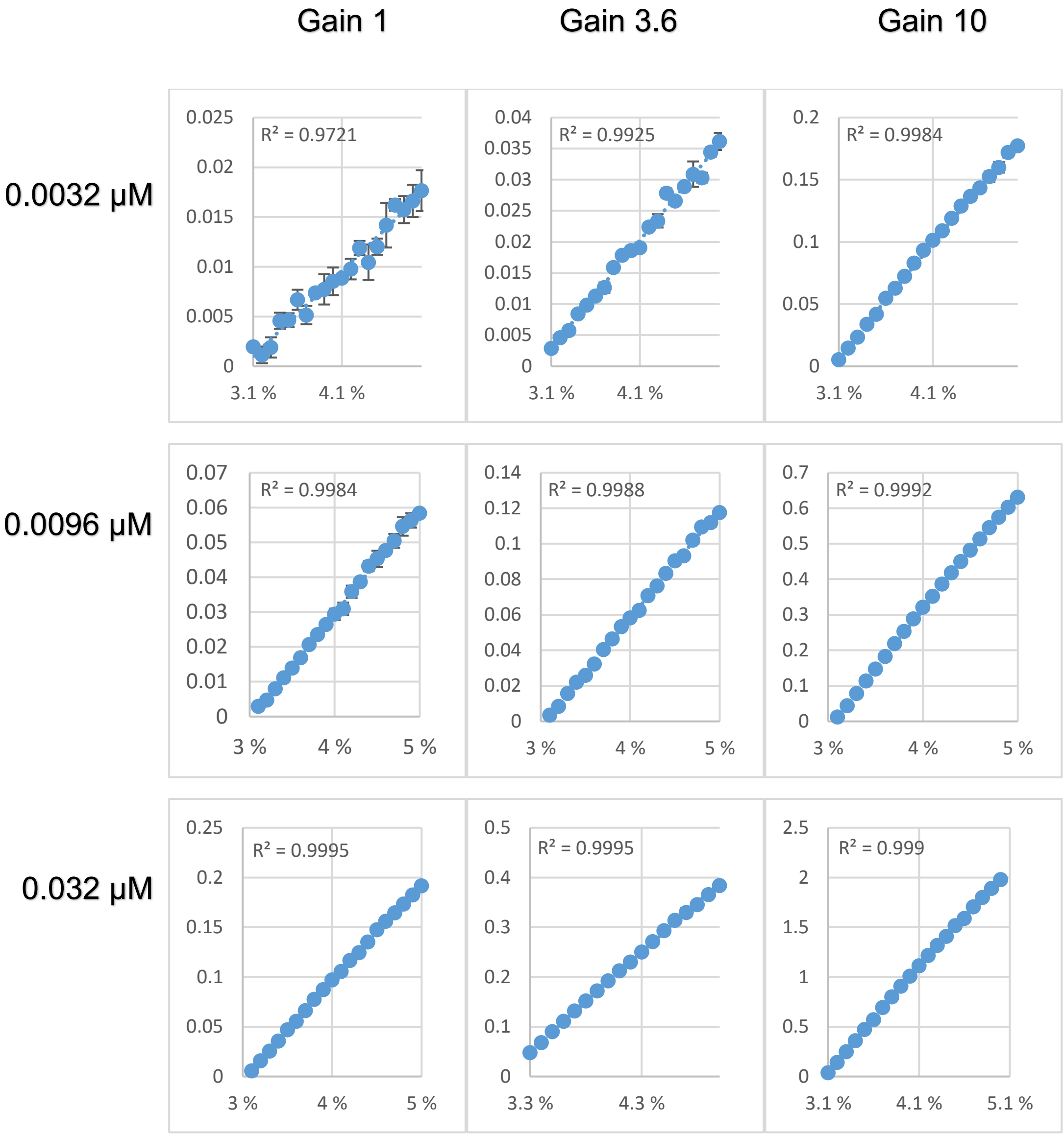

Figure 74: Arithmetic mean of three independent RFU of several fluorescein concentrations as a function of the laser power (x-axis) and the gain (three major columns) of the OptoReader. Values were depicted until the end of the linear detection range by fitting a linear regression with an R2 of at least 0.999 through the data points.

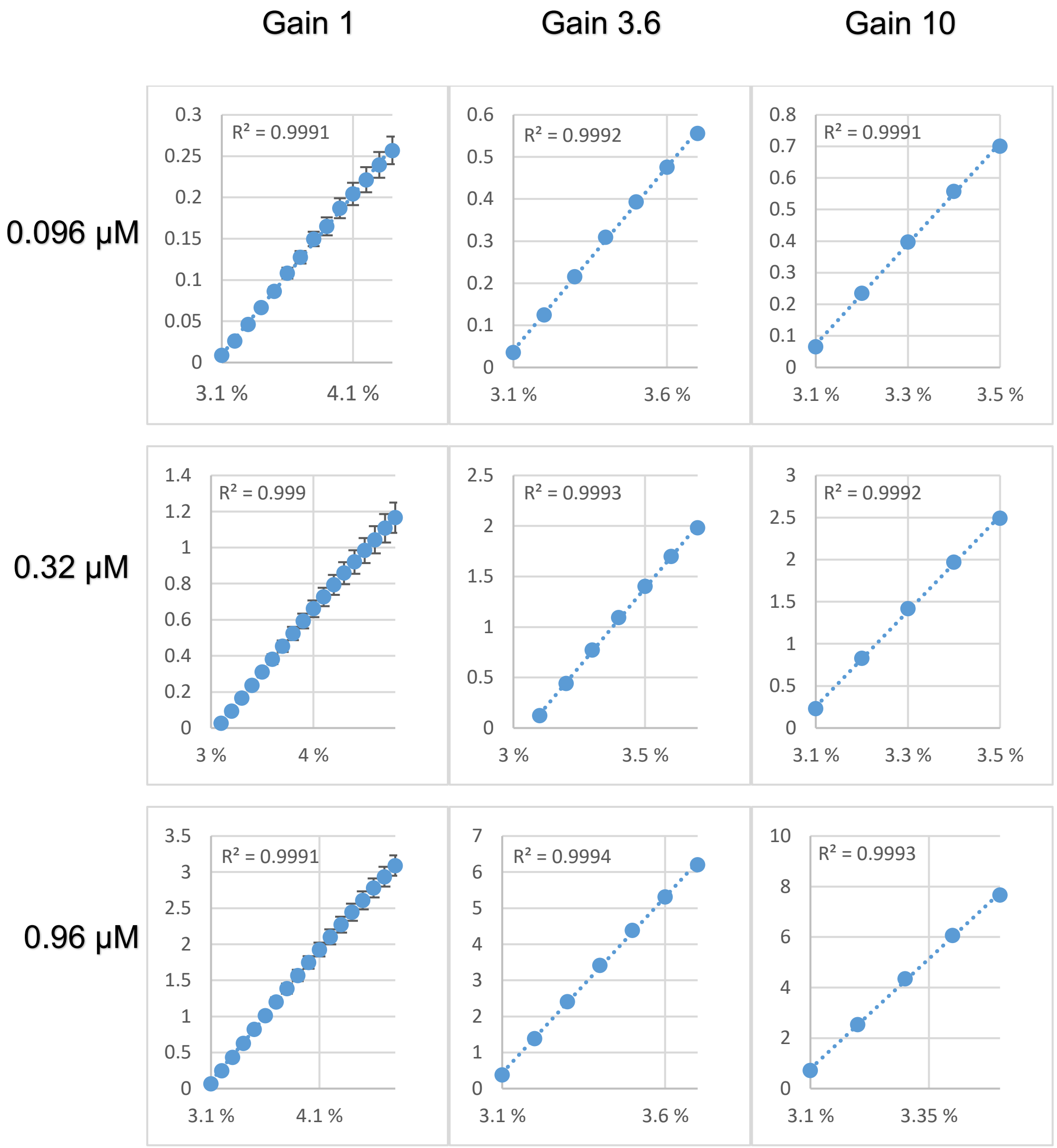

Figure 75: Arithmetic mean of three independent RFU of several fluorescein concentrations as a function of the laser power (x-axis) and the gain (three major columns) of the OptoReader. Values were depicted until the end of the linear detection range by fitting a linear regression with an R2 of at least 0.999 through the data points.

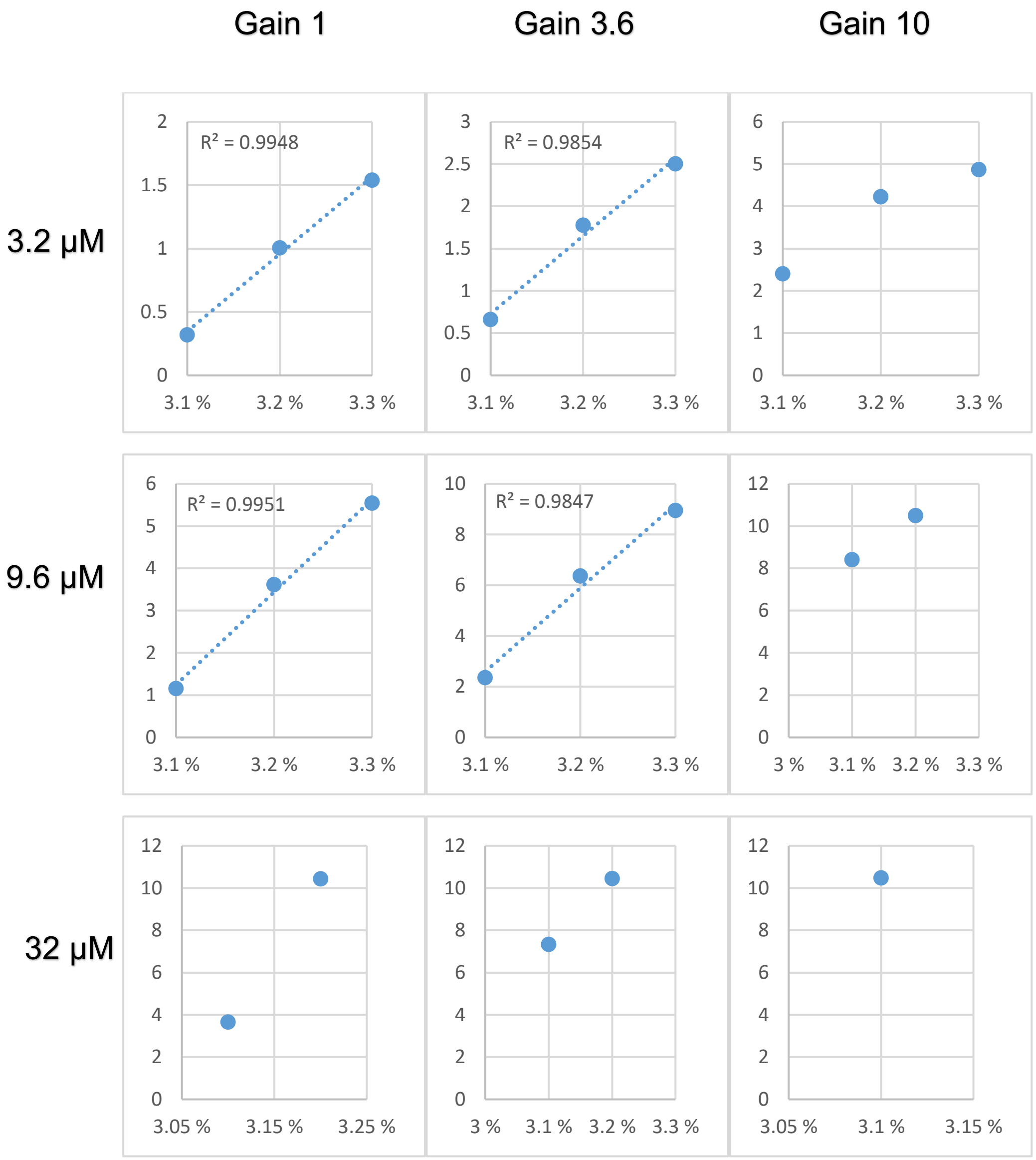

Figure 76: Arithmetic mean of three independent RFU of several fluorescein concentrations as a function of the laser power (x-axis) and the gain (three major columns) of the OptoReader. Values were depicted until the end of the linear detection range by fitting a linear regression with an R2 of at least 0.999 through the data points. Starting from FITC concentrations above 3.2 µM values were slightly out of the linear detection range.

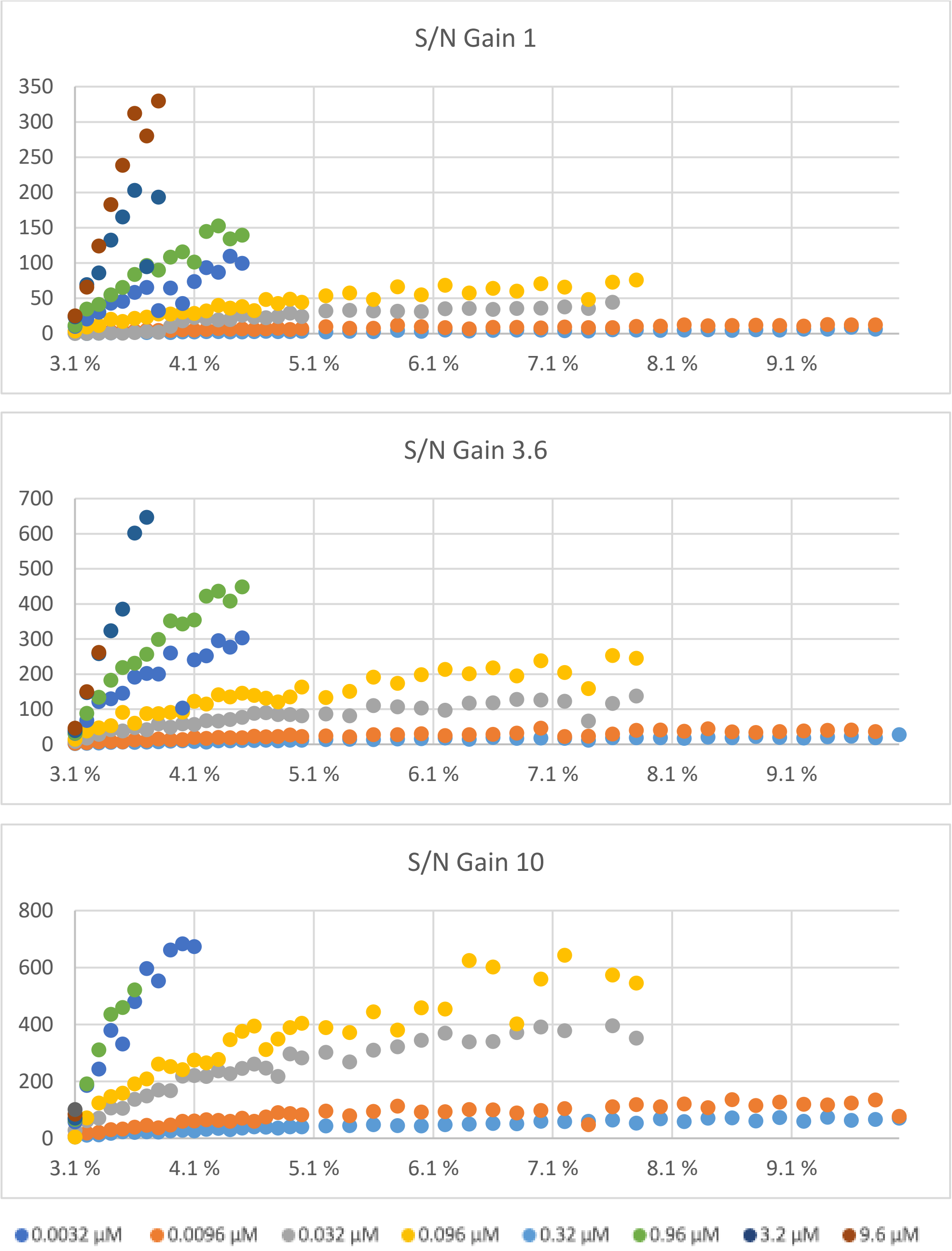

Figure 77: S/N ratios of FITC concentrations ranging from 3.2 nm to 9.6 µM as a function of the diode power (x-axis) and the gain. The signal is the arithmetic mean of three independent fluorescence measurements with substracted background, and noise represents the variations of these signals over 3 s by measuring 30 independent time points. Increased gain increased the S/N ratio by enhancing the signal while maintaining a constant noise level, especially for lower FITC concentrations. This effect was no longer observed at higher concentrations due to the signal saturation of the fluorescence spectrometer.

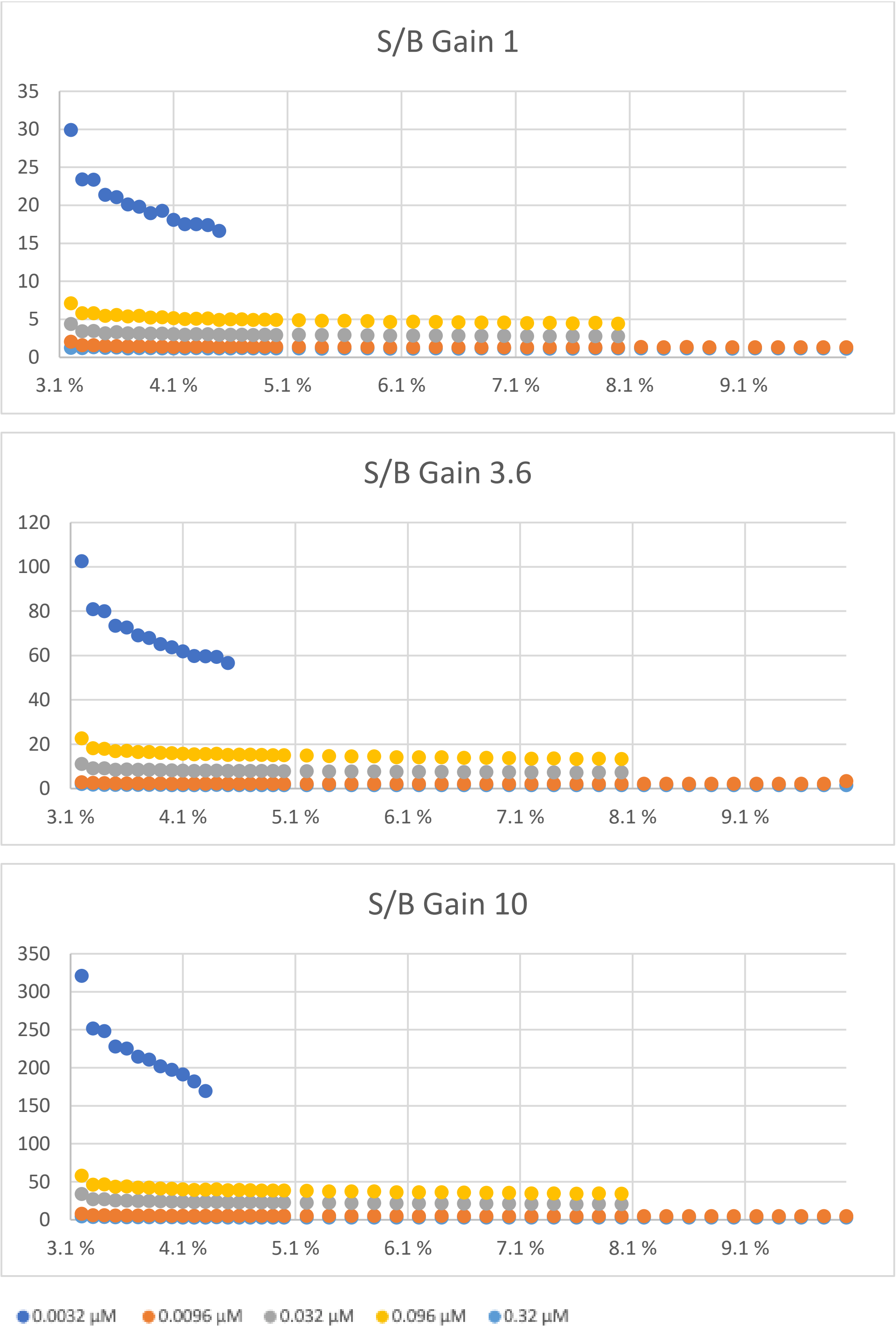

Figure 78: S/B ratios of FITC concentrations ranging from 3.2 nm to 0.32 µM as a function of the diode power (x-axis) and the gain. The signal is the arithmetic mean of three independent fluorescence measurements with substracted background, and the background represents the measurement of the microreactor filled with H_2O. Increased gain increased the S/B ratio by enhancing to signal strongly while slightly increasing the background. FITC concentrations above 0.32 µM are no longer depicted due to the exceptionally large values of up to 12,000.

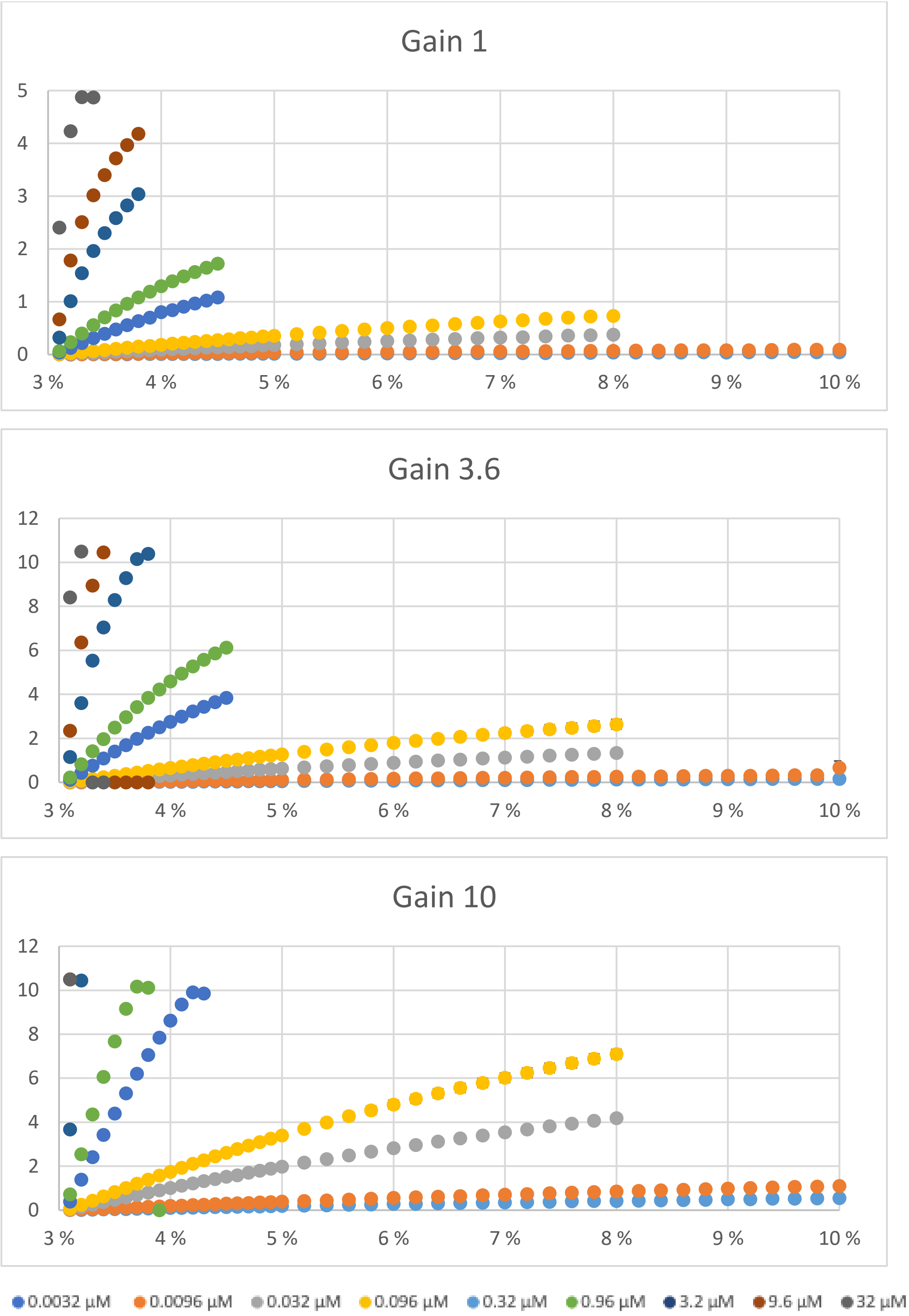

Figure 79: Arithmetic mean of three independent RFU of several fluorescein concentrations from 3.2 nm to 32 µM as a function of the laser power (x-axis) and the gain of the OptoReader. Error bars are depicted behind the dots marking the RFU values.

III.7.1 Correct operation and troubleshooting of the microfluidic system

The previous chapter describes the physical background and boundary conditions, as well as the purchase of the several indepent devices. In the here present section, a short but comprehensive instruction manual for the device's correct operation is given.

III.7.2 Instruction manual for the microfluidic system

Safety measurements

The microfluidic system provides an enclosed environment under low pressure, facilitating the handling of dangerous substances and reducing contamination risks. The devices themselves, especially the OptoReader fluorescence spectrometer, should never be touched with gloves due to the risk of contamination and to prevent static discharges.

After each measurement, the devices have to be cleaned adequately with H_2O using high flow rates for 5 min followed by isopropanol for other 5 min. In case of longer breaks between the measurement, the liquids should be removed from the system by flushing them with air.

III.7.3 Possible problems and troubleshooting guide

During the three years of use, several problems relating to the microfluidic systems were identified and corrected. In the following subchapter, the most prevalent obstacles are discussed, and the possible solutions are offered.

III.7.3.1 Unstable flow/ flow fluctuations

The variations in flow rate can be the result of several independent causalities. The accurate utilization of the equipment is a requisite to have a stable flow rate, wherefore L-flow measure units were used only for flowrates higher than 9 µl/min and the M-flow units above 1 µl/min. The pressure pumps' constant and stable pressure supply, the correct connections to reservoirs, and non-damaged tubings are needed to prevent high pressures without reaching the required flow rates (Figure 80).

Damaged capillaries can also lead to the flow's blocking and fluctuation and must be evaluated one by one until the problematic connection is found. Air droplets are easily recognized due to the periodic pressure jumps they can cause (Figure 81). However, air removal is not always trivial since they mostly stick inside rotational valves and are not visible to the eye. The installation of bubble traps prevented the dilemma, but these were only suitable for water-based solutions. Furthermore, the bubble traps were never used for the compound channel due to the possibility of contamination. A reliable method was flushing the system with isopropanol or by high-pressure fluctuations of the liquids. If non of these options help, then the system must be set on air again, followed by slow refilling with isopropanol. Lastly, several chips and devices' plugging can decrease the flow rate until a complete stop if not attended. The primary source of this problem was the ROSAR-GFT75 microreactor with narrow inner channels. If the frequent cleaning of the system is not sufficient, then the microreactor has to be removed and cleaned for 2 h in 30 % HCl under ultrasonication. Moreover, the chip has to be operated with the metal housing instead of the polymer ones since the latter often led to shedding and hence plugging.

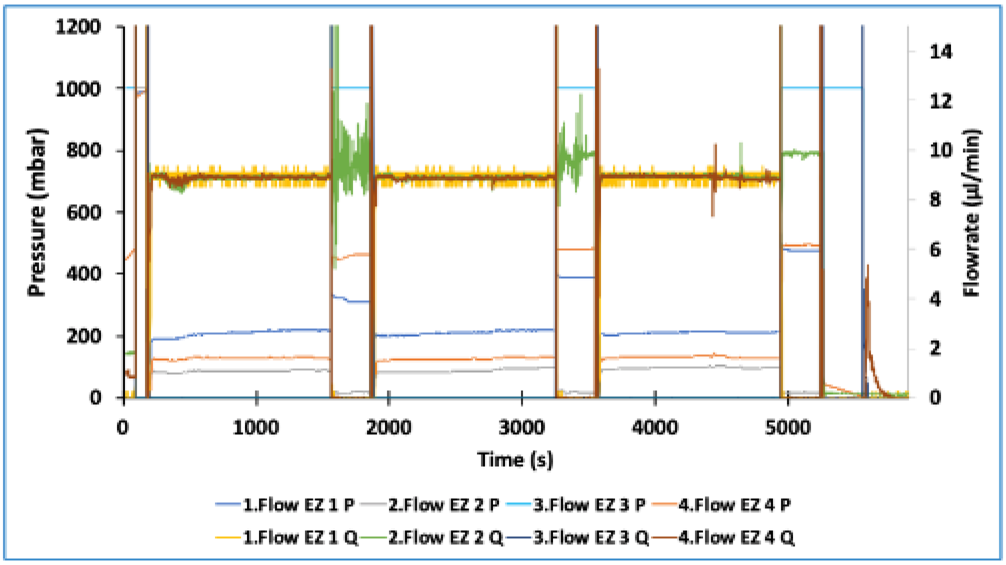

Figure 80: Pressure and flow rate depiction of a compound measurement with three replicates. Aside from small fluctuations of channel 1, the flow rates and pressures were stable. During a high-resolution dose-response measurement, four pumps were used for the cleaning of the system (1), cleaning of the microreactor and puffers (3), the target protein (2), and the analyzed compound (4). Pressures are marked with P, while volumetric flowrates are displayed with Q. During the measurement, channels 2, 3, and 4 were set o 9 µl/min to allow stochiometric mixing. The cleaning stage was performed with flowrates of 150 µl/min with pump 1, which is not displayed for the purpose of clarity.

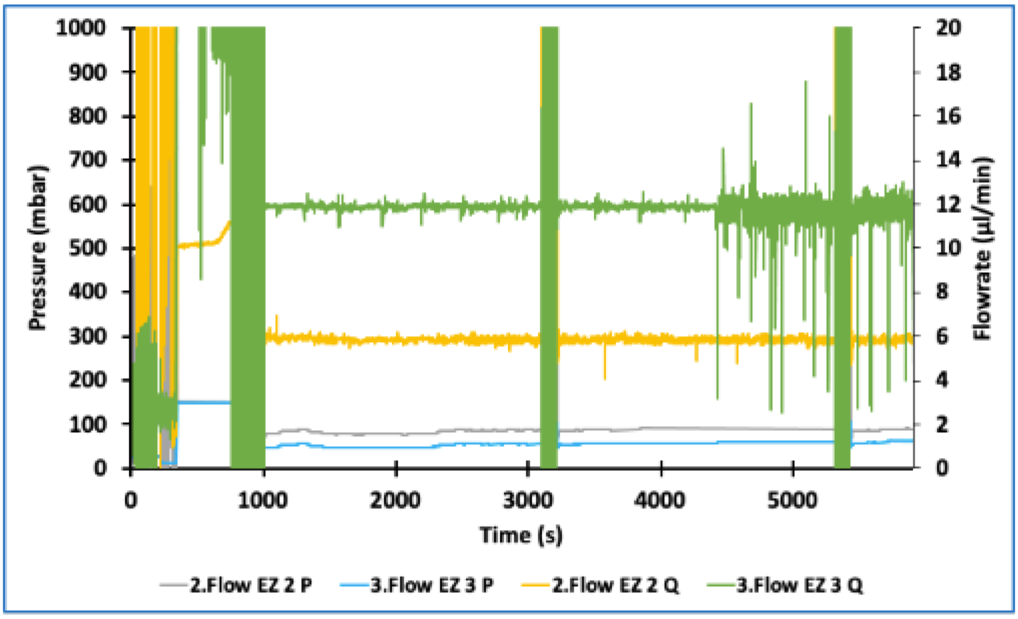

Figure 81: Pressure and flow rate depiction of a compound measurement with three replicates. Higher flowfluctuations occurred in channel three after 4,500 s due to air bubbles in the system. During a high-resolution dose-response measurement, four pumps were used for the cleaning of the system (1), cleaning of the microreactor and puffers (3), the target protein (2), and the analyzed compound (4). Volumetric flowrates are displayed with Q. During the measurement, channels 2, 3, and 4 were set o 9 µl/min to allow stochiometric mixing. The cleaning stage was performed with flowrates of 150 µl/min with pump 1, which is not displayed for the purpose of clarity. At the end of the reaction, higher fluctuations were observed in channel 3, which also had an impact on 2. The reaction's stoichiometry was impaired, and the results had to be disregarded.

III.7.3.2 Increase of fluorescence between the replicates and deviations from previously defined values

The fluorescence value was measured in each chip after the equilibration of the detector on the chip using the 3D platform. The most common reason for variations of the maximal signal is the moving of the chip out of focus which can be the result of insufficient or the weakening of the adhesive strip by fluid leakage. If the equilibration time of the mixture is not suitable, then the initial measurement might have a lower maximal fluorescence signal than the following ones. Another problem is the uncomplete dilution of compounds with slowly increasing concentration in the liquid phase. A rather unusual phenomenon of maximal signal increasing over the three replicates was observed for some measurements which were ascribed to damaged capillaries (Figure 82). The exact mechanism to the casualization between the observed effect and the capillary is not clear but likely linked to increased absorption of compounds in the resulting cavities, which in turn leaked to the following experiments.

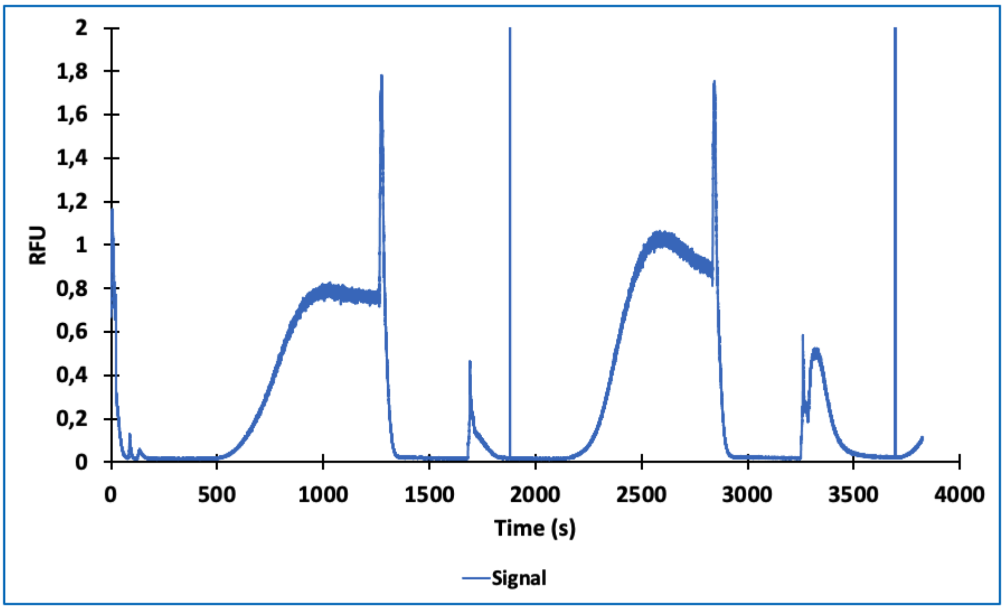

Figure 82: TAD dilution of fluorescein in two replicates. The reaction consisted of cleaning, signal saturation, and assembly reaction marked with the high blue peaks. During the assembly, the CP150-BO was mixed with the TAD-generated dilution gradient of the fluorescein (as concentration encoder), resulting in the asymptotic quenching of the fluorescence signal. Maximal signals were not stable, and a high peek prior to the measurement indicated backflow of fluorescein in other channels.

III.7.3.3 The fluorescence signal of CP150-BO was not reached after the first compound measurements.

In some cases a significantly lower maximal fluorescence signals after the first measurement was observed (Figure 83). After evaluating several possibilities, the problem was narrowed down to the backflow of the compounds into other channels. In every protocol, the flow rates were adjusted by an initial pressure jump equivalent to the pressure required to generate the flow to prevent the backflow.

However, these solutions were not sufficient, and the only possible way of preventing backflow was the utilization of functioning check-valves. Aside from the sporadic backflow, compounds also adsorbed to the inner surface of the CV-3000 inline cartridge check valves, as it was shown with FITC requiring 15 min cleaning with a flowrate of 100 µl/min. Therefore, the check valves were removed from the compound channel since a small backflow of protein or salt had no significant impact. All the other channels were equipped with check valves.

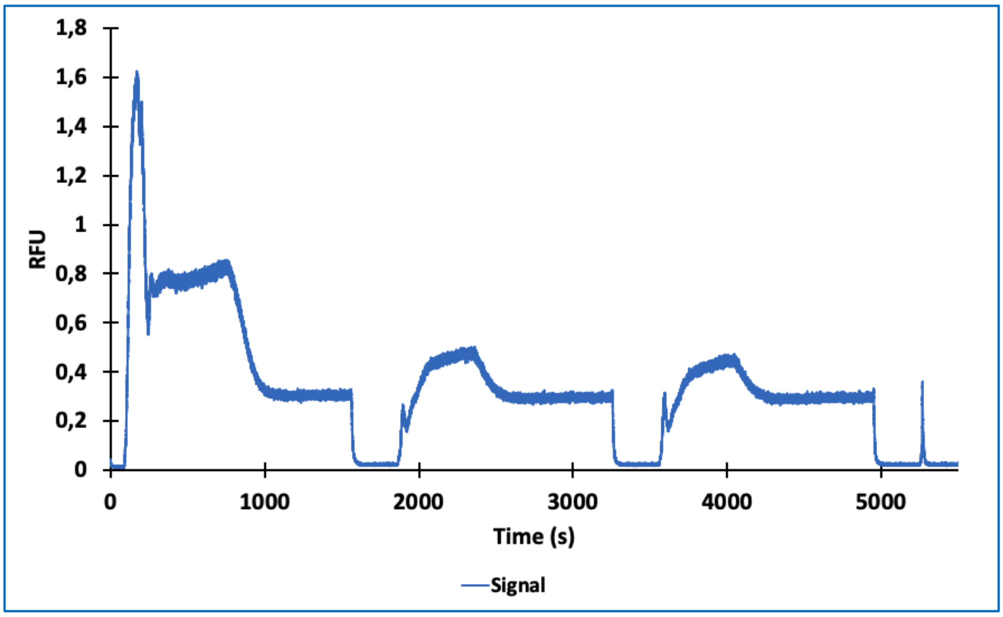

Figure 83: Innitial measurement of GLS4 meadiated CP150-BO assembly. The reaction consisted of cleaning, signal saturation (CP150-BO mixed with 50 mM HEPES), and assembly reaction marked with the high blue peaks. During the assembly, the CP150-BO was mixed with the TAD-generated dilution gradient of the BAY 41-4109, resulting in the asymptotic quenching of the fluorescence signal. In this reaction, the background signal could not be regenerated after the first measurement. This indicated that the compound was leaking back to the protein channel, leading to an assembly prior to measurement.

III.7.3.4 Deviations in the TAD mediated dilution of compounds or replicates

As it was introduced at the beginning of the chapter, the TAD of compounds depends on the microfluidic systems convection and the diffusion of the compounds in the transverse direction. In chapter IV, specific conditions are evaluated at which the TAD was convection-dominated, allowing the molar mass-independent dilution of compounds (IV.4.1 Experimental screening of volume normalized capillaries to determine the optimal capillary parameters for unilateral TAD measurements). The strict control of the physical flow conditions is a prerequisite to prevent deviations due to molar mass or non-uniformities of the channels. Aside from the capillary dimensions, any damage dealt to the capillaries, the existence of cavities or surface irregularities, and leakages all interfere with the robust reproduction compound dilution. In many experiments, the presence of air bubbles led to significant deviations between the different compounds. Aside from the system errors, unsoluble compounds also had substantial deviations in their dilution pattern, likely due to enhanced surface adsorptions. Furthermore, the representative fluorescent dye serving as an encoder for the compounds had to have the suitable quantum yield, absorption, excitation limits and be measured in the linear detection range of the OptoReader. Finally, the software operating the OptoReader had to be restarted before each measurement; otherwise, the time counting was off by a couple of seconds.

The measurement of the TAD dilution curves was the most sensitive part of the present Ph.D. project, since deviations in the range of seconds was enough to shift the EC_{50} value by several magnitudes. Therefore, these measurements were performed under the highest meticulousness preventing all possible compound, device, or software-induced deviations.

Chapter IV.

Adaptation of the CAM-induced HBc assembly assay to microfluidic format.

IV.1 Introduction

Microfluidic systems are one of the major trends in improving drug discovery processes, especially in the hit-to-lead process. This assay format is performed in small enclosed platforms, providing the decisive benefits of miniaturization, such as reduced sample consumption and higher throughput.[1] Furthermore, the resulting increased surface-to-volume ratios allow more precise control over physical variables, such as temperature, pressure, mass transfer, and evaporation, leading to readouts with higher selectivity, increased data resolution, and better reproducibility.[1–5] These advantages result in higher analytical reliability, and thus, better prediction of drug profiles. Furthermore the continuous operation of microfluidics promotes facile automation, with improved reproducibility thereby reducing the necessity of redundant lab work.[6] Finally, the lower detection volume allows improved fluorescence-based readouts, resulting in high volume-to-background ratios similar to confocal setups.[7,8] These listed advantages led to the integration of microfluidics into all the different drug discovery stages, from target discovery to drug screening and synthesis.[9] In particular, in the hit-to-lead development, multiple enzymatic assays have been successfully integrated.[1] Nonetheless, there is still much room for improvement, especially in integrating other druggable viral or microbial non-enzymatic targets.

The development of a microfluidic system has its own challenges regarding flow control, inflow mixing, readout, and compound dilution (III.5 Conclusion). An interesting technique used for the inflow dilution of compounds was TAD. In most microfluidic systems, the Reynold number does not exceed values beyond 10, leading to laminar flow conditions suitable for TAD compound dilution. As described in Chapter III, TAD is an absolute physical description of the motion (convection) and diffusion-driven compound dispersion in cylindrical tubing at laminar flow conditions. The most fundamental forces for TAD are the flow rate-dependent axial convection and the molar mass-dependent radial and axial diffusion of compounds. Pure axial convection leads to a parabolic distribution of the dilute inflow direction caused by the velocity distribution of the fluid in a cylindric tubing along the radial cross-section of the channel (Figure 84). At the same time, two diffusion effects take place: the axial diffusion increases the band broadening, while the radial diffusion of the compound decreases the convection-mediated dilution by slowing down the leading interface and accelerating the trailing interface of the dilute (Figure 85).[10] Therefore, by increasing the advective transport rate and decreasing the radial diffusion components, dilution curves with longer hillslopes and reduced deviations between compounds with varying molar mass are generated.[11–13] At the same time, TAD usually results in the generation of a high number of data points (up to 10,000) which allows the calculation of a high-resolution dose-response curve and the detection of complex dose-response relationships.[14] Lastly, in contrast to expensive and complicated micro reactor-based solutions (III.4.4.1 Generation of dilution curves), the only physical requirement for TAD is a thin capillary making this technique a complicated but very favorable tool for continuous flow systems.

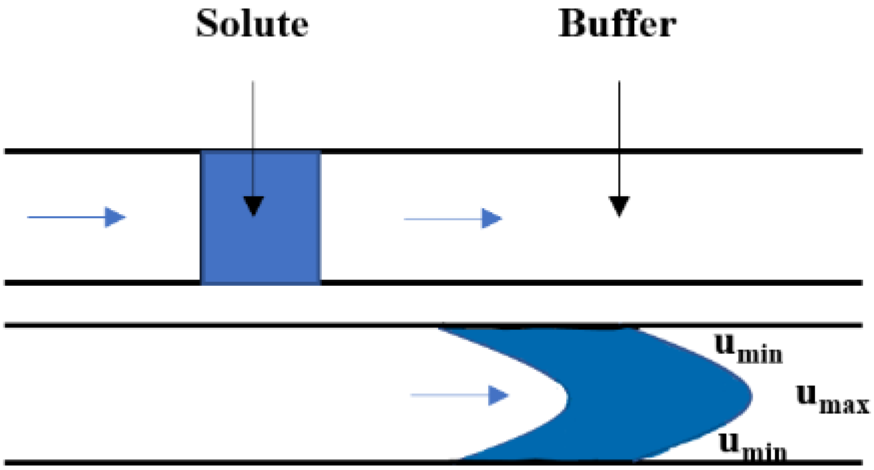

Figure 84: Convectional distribution of the solute in a thin capillary under laminar flow conditions. Solutes (blue) are being dispersed in buffer systems (transparent) along the depicted movement vectors (blue arrow). U_{max} and U_{min} are the maximal and the minimal flow rates respectively.

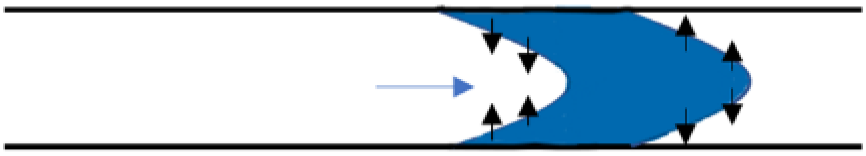

Figure 85: Axial diffusion of the solute in a thin capillary under laminar flow conditions. Solutes (blue) are being dispersed in buffer systems (transparent) along the depicted movement vectors (blue arrow) while radial diffusion (black arrows orthogonal to blue arrow) decreases the initial dilutions.

IV.2 Aim of the work

This chapter's main objective was to adapt the CP150-BO (II.3.5 High-Throughput Screening using 384 microtiter well format) assay to the microfluidic format (III.5 Conclusion). With this assay, the system's functionality and novelty were evaluated by determining the CAMs dose-response measurements, kinetics, and mode of action. To generate an inflow dilution of compounds required to generate the dose-response curves, the convection-dominated TAD is extensively evaluated in the following. By mixing the diluted compounds with the target protein, high-resolution dose-response curves can be generated which in turn could be used to calculate the EC_{50} values. Finally, the concentration-dependent kinetics of the CAMs could be measured at early time points given the inherent benefits of microfluidics.

IV.3 Methods

Table 26: Chemicals, microfluidic equipment, and software packages used in chapter IV.

Material Class	Materials/ equipment used	Industry, article number, preparation
Chemicals	FITC	Merck, Buchs, Switzerland CAS: 518-47-8
	Na_3PO_4 pH 8.0	Merck, Buchs, Switzerland CAS: 10101-89-0
	Ethanol	Merck, Buchs, Switzerland CAS: 64-17-5
	DMSO	Merck, Buchs, Switzerland CAS: 67-68-5
	Spee Color (Detergent with Lipase)	IPHT, Jena, Germany
	5,6-Carboxyfluorescein	CAS: 72088-94-9
	Albumin-FITC	ThermoFischer SCIENTIFIC GmbH, Darmstadt, Germany
	Fluorescein-Dextran	ThermoFischer SCIENTIFIC GmbH, Darmstadt, Germany CAS: 60842-46-8
	50 mM HEPES buffer ph 7.4	Merck, Buchs, Switzerland CAS: 7365-45-9
	NaCl	Merck, Buchs, Switzerland CAS: 7647-14-5
	Tetradecane	Merck, Buchs, Switzerland CAS: 629-59-4
	DBT	Synthesized as described in Corcuera et al.[15] patented by Turner Jr. et al.[16]
	Selvita-1399-025	Synthesized as described in Corcuera et al.[15]
	AT130	Synthesized as described in Corcuera et al.[15]
	NVR-3-778	Synthesized as shown in Vandyck[17,18]
	JNJ 56136379	Patented by Vandyck[18]
	BAY 41-4109	Synthesized at Bayer AG Wuppertal Germany
	GLS4	Synthesized Wang et al.[19]
	JAKL11-034-2	AiCuris Anti-infective Cures AG, Wuppertal, Germany
	JAKL11-076-1	AiCuris Anti-infective Cures AG, Wuppertal, Germany
	MABR13-005	AiCuris Anti-infective Cures AG, Wuppertal, Germany
	BODIPY-derivates, as listed in Table 27	Synthesized at Merchachem, Nijmegen, Netherlands
	CP150-BO (3 μM)	Expressed, purified, and labeled at AiCuris Anti-infective Cures AG, Wuppertal, Germany
Tubings	Rotilabo®-silicone tubes OD 3 mm, ID 1 mm	Analytics Shop, Munich, Germany Catalog number: 9556.1
	Tubing, PFA, 1/16 x 1.0 mm ID	Analytics Shop, Munich, Germany SN: JR-T-4007-M3
	Tubing, PFA, 1/16 x0.75 mm ID	Analytics Shop, Munich, Germany SN: JR-T-4002-M3
	Tubing, PFA, 1/16 x0.50 mm ID	Analytics Shop, Munich, Germany SN: JR-T-4001-M3

	Tubing, PFA, 0.2 mm ID,1.6 mm od	Analytics Shop, Munich, Germany SN: AGG1833-65573
	Tubing, PTFE, 2.0 x 1.70 mm	Analytics Shop, Munich, Germany SN: JR-T-6801-M3
	PEEK-Tubing 1/16" OD x 0.13 mm ID	SCP Seitz Chromatographie Produkte GmbH, Weiterstadt, Germany SN: 41.159.013.01
	PEEK-Tubing 1/16" OD x 0.25 mm ID	SCP Seitz Chromatographie Produkte GmbH, Weiterstadt, Germany SN: 41.079.025.00
	Membranfilter hellrot; PVDF 0.2 µm	Klaus Trott Chromatographie-Zubehör; Kriftel, Germany SN: 082530020
Fluigent flow system	Fluigent low-pressure Generator (FLPG, pressure source)	FLUIGENT, Jena, Germany item number: FLPG003
	Flow EZ^{TM} 1,000 mbar (Pumps) (X 4)	FLUIGENT, Jena, Germany, item number: LU-FEZ-1000
	Flow rate sensor L (X 3)	FLUIGENT, Jena, Germany, item number: FLU_L_D
	Flow rate sensor M (X 2)	FLUIGENT, Jena, Germany, item number: FLU_L_M
	Flow rate sensor S (X 2)	FLUIGENT, Jena, Germany, item number: FLU_L_S
	High flowrate connection kit	FLUIGENT, Jena, Germany, item number: CTQ_KIT_HQ
	Low flowrate connection kit	FLUIGENT, Jena, Germany, item number: CTQ_KIT_LQ
	Reservoirs (2x50 ml, 1x15 ml)	FLUIGENT, Jena, Germany, item number: P-CAP15_HP, P-CAP50_HP
	Rack for P-caps	FLUIGENT, Jena, Germany, item number: P-Cap_Rack
	LineUP logistic kit	FLUIGENT, Jena, Germany, item number: LU-SPK-0001
	L-Switch^{TM}	FLUIGENT, Jena, Germany
	Switch board, ESS Platform	FLUIGENT, Jena, Germany
	L-Switch connection kit	FLUIGENT, Jena, Germany
	Bubble traps	FLUIGENT, Jena, Germany
	5 ml pointed, high-pressure glass reservoirs	Custom made
CETONI	ROTAXYS 360 LHS	CETONI GmbH, Korbußen, Germany CETONI_ROTAXYS 360 LHS
	neMESY low-pressure syringe 100 µl	CETONI GmbH, Korbußen, Germany CETONI_ neMESY Low-Pressure
AMF technologies	OEM RVM Microfluidic Electric Rotary Valve	AMF ANDREAS MAIER GmbH & Co. KG, Fellbach, Germany SN: V-D-1-12-050-C-U
Check valves	Fluigent check-valve	FLUIGENT, Jena, Germany
	CV-3000 inline Cartridge check valve	IDEX Europe GmbH, Erlangen Germany
	Swagelok Checkvalve	Best Fluid Systems GmbH | Swagelok, Hamburg, Germany
Elveflow	OptoReader	Elveflow microfluidic flow control, Paris, France FDG_ELV_OPR-01 (No longer available)

Combo kit	Vici Easy-Flange Combi Kit in Plastic	FLUIGENT, Jena, Germany Case 201539, Lab Unlimited
Microfluidic chips	µ-Slide VI 0.1	ibidi GmbH, Gräfelilfing, Germany
	µ-Slide VI 0.5	ibidi GmbH, Gräfelilfing, Germany
	µ-Slide III	ibidi GmbH, Gräfelilfing, Germany
	VIM2 (droplet)	IPHT, Jena, Germany
	VIM2b (droplet)	IPHT, Jena, Germany
	WCA1b (droplet)	IPHT, Jena, Germany
	ROSAR GF-T75 (mixing)	IPHT, Jena, Germany
	HTM-ST3-1	LTF, Wasserburg, Germany
	3D-Serpentine microreactor	Microfluidic ChipShop, Jena, Germany
Software packages	QmaxElements	CETONI GmbH, Korbußen, Germany
	Microfluidic Automation tool (MAT)	FLUIGENT, Jena, Germany
	All-In-One (AIO)	FLUIGENT, Jena, Germany
	Elveflow Smart Interface (ESI)	Elveflow microfluidic flow control, Paris, France
	GraphPrism7	GraphPad Software Inc San Diego, United States
	KNIME	Cloudera, DYMATRIX, TIBCO, Vertica, Hortonworks, ChemAxon, Schrödinger
	ORIGIN	OriginLab Corporation, Northampton, Massachusetts

IV.3.1 Reference compounds

All compounds used in this study were synthesized at Merchachem (Nijmegen, Netherlands) (now Symeres) and had purities of >95 %. CAMs used in this study (Fig. 2) had >95 % purity. BAY 41-4109 was synthesized at Bayer AG (Wuppertal, Germany).[20] The other CAMs were synthesized at Mercachem (now Symeres) as shown in Vandyck[17,18] for NVR Patent, Corcuera et al.[15] for Compound 917 Patent, Wang et al.[19]for GLS4, Vandyck[18] for JNJ Patent, Turner Jr. et al.[16] for ABI patent. Compounds A and B were obtained through in-house research of novel substance classes with thus far undisclosed structures.

The seven BODIPY derivates were synthesized at Mercachem and diluted in isopropanol prior to measurements (Table 27).

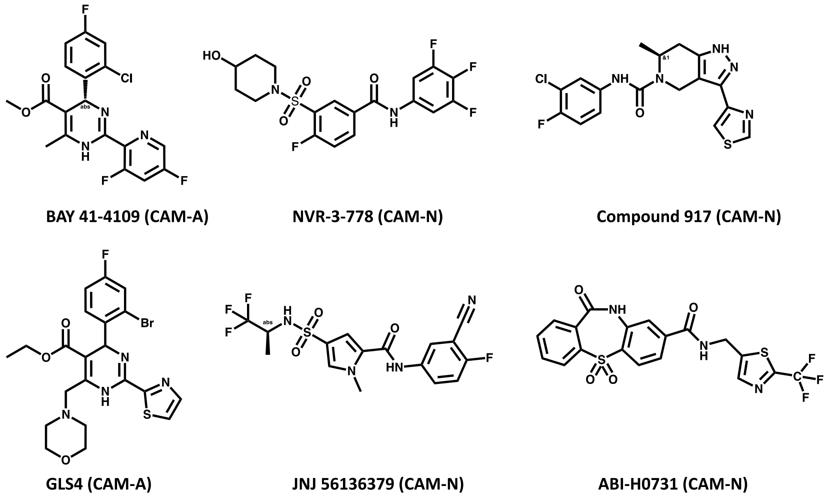

BAY 41-4109 (CAM-A) **NVR-3-778 (CAM-N)** **Compound 917 (CAM-N)**

GLS4 (CAM-A) **JNJ 56136379 (CAM-N)** **ABI-H0731 (CAM-N)**

Figure 86: Chemical structures of the CAMs along with their known mechanism of action (CAM-A and CAM-N).

Table 27: BODIPY derivatives with increasing molar mass used for the characterization of convection-dominated TAD.

Compound names	-R	Molar mass (g/mol)
B-01	H	291.16
B-02	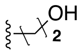	335.19
B-03	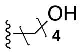	363.23
B-04	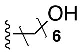	391.27
B-05	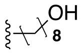	419.31
B-06	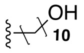	447.35
B-07	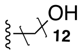	475.39

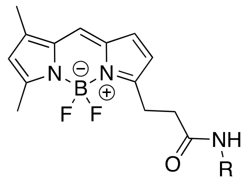

IV.3.2 Expression, purification, and labeling of CP150C

The truncated Cp assembly domain CP150C was expressed in *E. coli* Rosetta2 (DE3) according to Chapter II.[15,21] After extraction using the Qproteome Bacterial Protein Prep Kit the proteins were precipitated with ammonium sulfate to 40 % saturation and dissolved in 100 mM Tris, pH 7.5, 100 mM NaCl, 2 mM DTT.

The purification of CP150C by serial affinity and size-exclusion chromatography steps and the labeling with BODIPY-FL maleimide was performed as described in II.3.3 Purification of CAM selective CP150C proteins using a series of size exclusion- and affinity columns.

IV.3.3 Unilateral TAD measurements in volume normalized measurements

The experiments were conducted according to the flow schema with a dilution protocol as described in IV.4.1.1 The impact of capillaries' ID on the convection dominated TAD (Figure 87). PFA capillaries with varying lengths and inner diameter (ID) but the constant inner volume of 471 µl were used (Table 28). Before the first measurement, the system was filled with 50 mM HEPES buffer, and the OptoReader was equilibrated. During the measurement, FITC, 5.6-Carboxyfluorescein, and Protein-A FITC were diluted in three technical replicates and on two independent days to showcase the molar mass-dependent deviation between compounds. The reaction started with 3 µM of the fluorophoric compounds diluted in the capillary with a volumetric flow rate of 9, 6, or 4 µl/min. The OptoReader recorded the fluorescence signal at gain 1, laser power at 4.1 %, and acquisition of 2. Finally, the text files generated by the OptoReader were evaluated according to III.4.2 Fluorescence spectrometer-based readout.

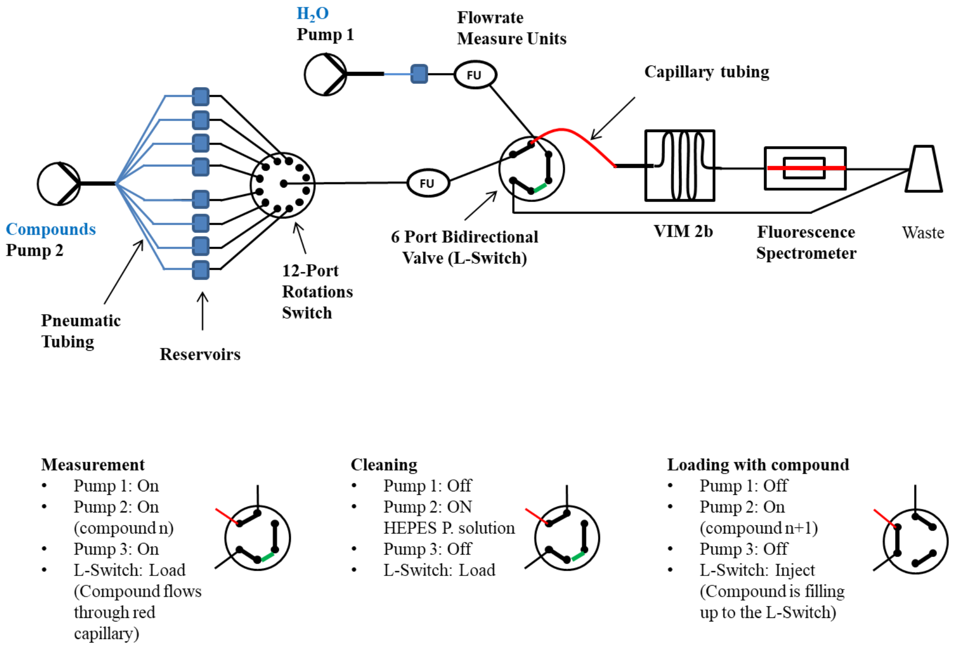

Figure 87: Scheme of the microfluidic system used for the evaluation of the convectional TAD dilution. The capillary utilized for TAD is marked red. VIM 2b and Active droplet Manchip 2 were utilized as a readout chip. Legend for the various units is depicted in Figure 30.

Table 28: Different capillaries used for the convectional mediated TAD dispersion of compounds. The capillaries were all volume normalized to 471 µl.

ID of the capillary in mm	Length of the capillary in cm
0.25 (PEEK capillary)	240
0.5	60
0.75	26
1	15
1.4	7.61

IV.3.4 Bilateral TAD measurements in volume normalized measurements

The experiments were conducted according to (IV.3.3 Unilateral TAD measurements in volume normalized measurements) with the exception of 5 cm PFA loops installed on the L-Switch before the capillary used for the TAD. The loop was filled with the compound of interest before the measurement which was then injected into the TAD capillary by a constant flow of 50 mM HEPES.

Table 29: Different capillaries used as loops prior to the TAD dispersion of compounds. The capillaries were all PFA tubings with a length of 5 cm and varying inner diameters and volumes.

ID of the capillary in mm	Volume of the loop in µl
0.25 (PEEK capillary)	9.8
0.5	39.3
0.75	88.3
1	157

IV.3.5 Final volume normalized unilateral measurements

The BODIPY-derivates (Table 27) were diluted to 0.32 µM concentration in isopropanol for the TAD-mediated dilution curves as described in System operation and hardware setup. From the capillaries analyzed for the TAD-dilution (Table 30), a 2.5 cm PFA capillary with an ID of 1 mm, followed by a 1.5 cm tubing with an ID of 0.75 mm, was used for the dispersion of BODIPY-FL derivatives. The experiment was repeated at three flow rates: 9, 13, and 17 µl/min. Using the conditions described above, the dilution curves of FITC, 5(6)-carboxyfluorescein, albumin-FITC, and fluorescein-dextran were generated in a water medium.

Table 30: PFA tubings used for the characterization of convection-dominated TAD-mediated compound dilution. The tubing with the ideal settings with regards to reaction time and domination of convection mediated dilutions was marked yellow.

Tubing specification	ID (mm)	Length (cm)	Volume (µl)	L/R ratio	Peclet number (D based on FITC)	Distance traveled until mixing by diffusion (cm)
PTFE, 2.0 x 1.70 mm/ JR-T-6801-M3 / Analytic Shop	1.70	4.86	117.00	27.80	273.44	46.5
PFA, 1/16 x 1.0 mm ID; JR-T-4007-M3 / Analytic Shop	1.00	14.90	117.00	148.97	156.25	15.6
PFA, 1/16 x 1.0 mm ID; JR-T-4007-M3 / Analytic Shop	1.00	10.00	78.54	100.00	156.25	15.6
PFA, 1/16 x 1.0 mm ID; JR-T-4007-M3 / Analytic Shop	1.00	5.00	39.27	50.00	156.25	15.6
PFA, 1/16 x 1.0 mm ID; JR-T-4007-M3 / Analytic Shop	1.00	2.50	19.63	25.00	156.25	15.6
PFA, 1/16 x0.75 mm ID; JR-T-4002-M3 / Analytic Shop	0.75	26.48	117.00	353.11	117.19	8.8
PFA, 1/16 x0.50 mm ID; JR-T-4001-M3 / Analytic Shop	0.50	59.59	117.00	1191.75	78.13	3.9
PEEK-Tubing 1/16" OD x 0.25 mm ID	0.25	238.35	117.00	9534.02	39.06	1.0
PFA, 0.2 mm ID. 1.6 mm od; AGG1833-65573 / Analytic Shop	0.20	372.42	117.00	18621.13	31.25	0.6
PEEK-Tubing 1/16" OD x 0.13 mm ID; SCP 41.159.013.01	0.13	881.47	117.00	67805.66	20.31	0.3

IV.3.6 High-resolution EC_{50} measurements

The microfluidic system was built from several independent modules (Figure 88), all operated by protocols written in the Microfluidic Automation Tool 2019 (MAT), version 19.0.0.1, from Fluigent (Jena, Germany) (III.5 Conclusion). Before the measurements, all the glass microreactors were purified using haste purification followed by repel silane coating to prevent nonspecific protein and compound binding to the channel walls. The glass microreactors were submerged for 25 min in freshly prepared haste solution (HCl, H_2O_2, and H_2O mixed 1:1:1) to remove the old coating and contaminants, followed by thorough cleansing first in H_2O than in ethanol. Next, the microreactor was dried at 60 °C for 3 . The microreactor's coating was performed with PlusOneRepelSilan solution injected into the glass channels, which was incubated for 15 min at room temperature, followed again by cleansing with H_2O than in ethanol.

Measuring multiple compounds was achieved using RotAxys360 positioning system from CETONI (Korbussen, Germany) equipped with a neMESYS low pressure 1 syringe and a needle as an interface allowing the transfer of liquids from a 96-well-plate to the respective 5 ml pressure glass reservoirs (Fluigent, Jena, Germany) sealed with septa. Initiating the flow was conducted using Flow EZ^{TM} 1,000 mbar pressure pumps (Fluigent, Jena, Germany), and the flow rates were controlled using the respective flow rate sensor L, M, or S. The logarithmic dilution of the compounds was conducted by generating a sharp compound margin using the L-Switch, a 6-port bidirectional valve (Fluigent, Jena, Germany) followed by the injection into a PFA capillary (length 2.5 cm, ID 1 mm, JR-T-4007-M3; ANALYTICS SHOP, Munich, Germany) to create convection-dominated TAD dilution curves. Following dispersion in the capillary, each smoothed pulse passes to the rotate-split-and-recombine-based microfluidic mixer (ROSAR GF-T75) from IPHT (Jena, Germany)[22], where it is combined with the target protein and the required buffers. This passive micromixer is based on sequential multi-lamination, allowing optimal mixing conditions even at the low Reynold numbers of the system (Fig. S2)[22]. Finally, the solutions were passed onto a long glass chip WC1AB (IPHT, Jena, Germany), in which the fluorescence and reflection were measured using the fluorescence spectrometer OptoReader, equipped with a FITC filter set (excitation of 480 nm and an emission of 520 nm) (Elveflow, Paris, France). With the provided alignment platform and through the miniaturization-mediated reduction of sample volume, a strong 3D focus was achieved in the microreactor.

In the final assay, two pumps were used with a flow rate of 12 µl/min. One pump was dedicated to the CP150-BO (3 µM in 50 mM HEPES), and the other one was dedicated to the compound (64 µM diluted in 50 mM HEPES with 600 mM NaCl), resulting in the final assay conditions of 1.5 µM CP150-BO, 300 mM NaCl and 32 µM compound. Each experiment consisted of 5 min for equilibration, 10 min for measurement, and 15 min for cleaning, resulting in a total run time of 30 min. Percentage assembly values are normalized to CP150-BO (1.5 µM) dimers in 50 mM HEPES as the negative control, and 2 M NaCl-assembled CP150-BO (1.5 µM) capsids at a residence time of 120 s as the positive control.

(1): Calculation of CAM mediated percentual CP150-BO assembly based on P150-BO mixed with 50 mM HEPES as negative, and BO mixed with 2 M NaCl as the positive control at 2 min post mixing.

$$Percentual\ Assembly = 100 * \frac{(1 - \left(\frac{RFU\ (CP150 - BO\ mixed\ with\ CAM)}{RFU\ (CP150 - BO\ mixed\ with\ 50\ mM\ HEPES)}\right))}{(1 - \left(\frac{RFU\ (CP150 - BO\ mixed\ with\ 2M\ NaCl)}{RFU\ (CP150 - BO\ mixed\ with\ 50\ mM\ HEPES}\right)}$$

As an internal standard, the dilution curves of sodium fluorescein were measured under assay conditions in three replicates. Using three independent measurements with different laser and gain settings of the fluorescence reader, the encoder's high-resolution dilution curve was generated, covering compound concentrations from 3.2 nM up to 32 µM (Figure 97). The dilution curve was fitted against the capsid assembly curves of the reference compounds, generating the high-resolution dose-response curves.

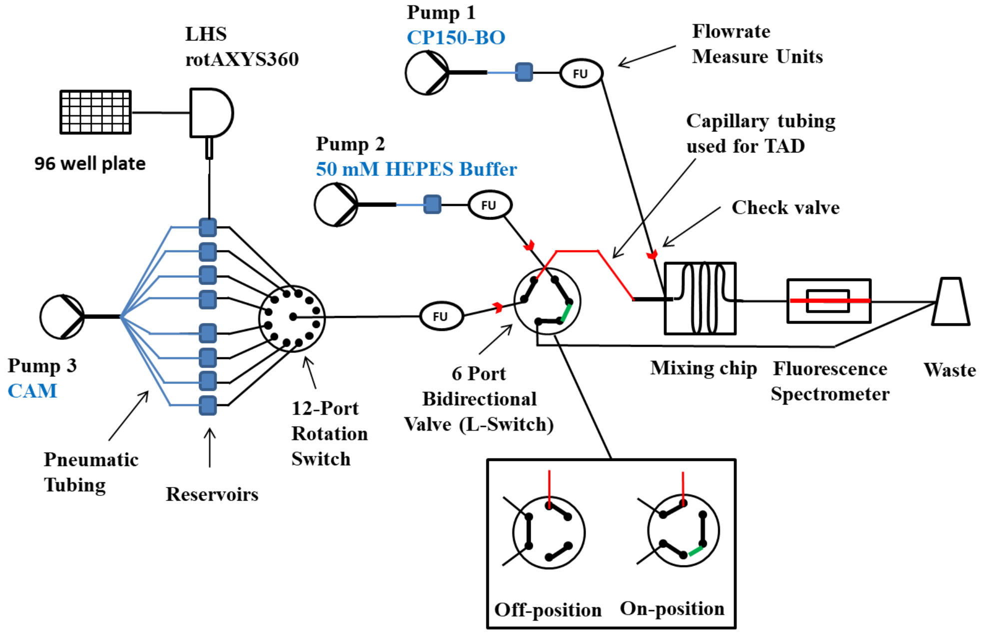

Figure 88: Schematic representation of the microfluidic system used for the screening and characterization of novel HBV CAMs. The compounds were transferred from a 96 well plate to the pressurized reservoirs (blue squares) with the LHS rotAXYS360. Afterward, the system was equilibrated by first loading the first compound until the L-Switch, which was set to the Off-position to remove compound excess into the waste. Simultaneously, Pump 2 and Pump 3 were running with identical flowrates allowing the mixing of 50 mM HEPES with CP150-BO in the mixing chip and thereby generating the baseline. Following the initiation, pump 3 was set to the same flowrate as pump 1, and the L-Switch turned to the On-position, allowing the TAD of the CAM's compound margin in the designated (red) capillary and its subsequent mixing with the CP150-BO protein. After the measurement, the system was cleaned with H_2O using pump 3 switched to the respective reservoir and 50 mM HEPES using pump 2. Legend for the various units is depicted in Figure 30.

IV.3.7 Assembly kinetic measurements

The above-described microfluidic system was used for the evaluation of CAM-mediated CP150-BO assembly kinetics (Figure 88). The reaction was mixed in the ROSAR GF-T75 microreactor 1:1:1 with 4.5 µM CP150-BO, 900 mM NaCl, and the CAMs with a concentration equal to 10-fold EC_{50} values in microtiter format and a DMSO concentration of 0.5 %. Percentage assembly values are normalized to CP150-BO (1.5 µM) dimers in 50 mM HEPES as the negative control, and 2 M NaCl-assembled CP150-BO (1.5 µM) capsids at a residence time of 120 s as the positive control. Prior to each measurement, the system was equilibrated using a volume equal to three residence times. The kinetic points were produced by the variation of the flow rates of all the channels simultaneously.

IV.3.8 Analytical size exclusion chromatography (SEC)

Analytical size exclusion chromatography (SEC) was performed as described previously[15] to differentiate between capsid and core protein dimer species in a sample,. Briefly, 5 µM CP150-BO was incubated with either 10 µM BAY 41-4109, 32 µM Compound A, or 32 µM Compound B in 60 mM BES, pH 6.8, 150 mM NaCl and 1 % DMSO at 25 °C for 2 h. Afterward, samples were separated on a Superose6 Increase 10/300 size-exclusion column mounted on an ÄKTA Pure 25 using the same buffer. Sample peaks were monitored at 280 nm.

IV.3.9 Immunofluorescence staining

The HepG2.117 cell line, a doxycycline-inducible HepG2 cell line stably transfected with an HBV genome, was obtained from Prof. Michael Nassal (University Hospital Freiburg, Germany).[23] Cells were maintained in DMEM supplemented with 10 % fetal bovine serum (FBS), 1 % L-glutamine, 1 % MEM NEAA, 1 % sodium pyruvate, 200 µg/mL G 418, and 80 µg/mL hygromycin B. To suppress HBV replication, 1 µg/mL doxycycline was added.

To determine the effect of NVR-3-778, BAY 41-4109, Compound A, and Compound B on the localization of HBV capsids and core protein (HBcAg), 3 x 10^4 HepG2.117 cells were seeded onto sterile coverslips in 12-well plates. For 6 days, cells were cultured without doxycycline and treated with 50-fold EC_{50} of the compounds. Afterward, the cells were fixed with 4 % paraformaldehyde in phosphate-buffered saline (PBS) and permeabilized with 0.2 % Triton X-100 in PBS. The cells were then blocked with 5 % FBS in PBS. HBcAg was detected with an anti-HBc primary antibody (Abcam ab115992) and an anti-rabbit-Alexa 488 secondary antibody (Invitrogen A-11034). The nuclei were then counterstained with DAPI (Sigma D9542). Samples were mounted onto glass slides with VECTASHIELD antifade medium (Vector Laboratories) and viewed under an inverted fluorescence microscope (Leitz DMRB). Images were taken with the pco.panda 4.2 camera (Visitron Systems) and the VisiView software (Visitron Systems, ver. 4.5.0.5). Images were analyzed using ImageJ (National Institutes of Health, ver. 1.53 g).

IV.4 Results and Discussion

IV.4.1 Experimental screening of volume normalized capillaries to determine the optimal capillary parameters for unilateral TAD measurements

The first step in the measurement of high-resolution dose response curves is the generation of a compound dilution for which TAD was utilized. The ideal TAD distribution leads to a high resolution of the compound's concentration observed in the increased length of the dispersing zone. Increasing the ID of a volume normalized capillary enhances the dispersion of the compounds and, at the same time, reduces the molar mass-mediated difference in the compound's dilution profiles. Therefore, an increased radius of the volume normalized capillary increases the time scale for the radial diffusion, subsequently reducing the radial mass transfer and leading to a higher compound concentration distribution. Moreover, decreasing diffusion-mediated effects compared to convection-mediated dilutions diminishes differences based on the compounds' molecular weight during the dilution process, ultimately leading to a higher overlap between the dilution curves.[12]

IV.4.1.1 The impact of capillaries' ID on the convection dominated TAD

After studying TAD, the first unilateral TAD dilution curves were measured. The primary focus of this experiment was to analyze the effects of the capillary's diameters in volume normalized capillaries on the TAD-mediated dilutions of the fluorophore compounds. Furthermore, the MW'‘s impact of the on TAD were analyzed by comparing the FITC's, 5,6-Carboxyfluorescein's, and protein-A's dilution curves.

During the measurements, five-volume normalized capillaries with varying ID were evaluated. The experiments showed a high reproducibility except for a few replicates impaired by air bubbles in the system. As expected, the best performance was obtained from the PEEK capillary with the highest ID. However, the PEEK tubing was fragile at this ID, which often led to breakings and creaks, resulting in significant deviations in EC_{50} values between the compounds (III.7.3.4 Deviations in the TAD mediated dilution of compounds or replicates). Hence, the PFA capillary with an ID of 1 mm and a length of 15 cm was chosen due to the best characteristics regarding compound dilution and deviations between compounds (Figure 89). During a single measurement of 25 min, the respective compound was dispersed over 14.2 min. The dilution profile for FITC and Protein-A was highly overlapping, indicating that the effect of radial diffusion in this capillary is minimal (Figure 90).

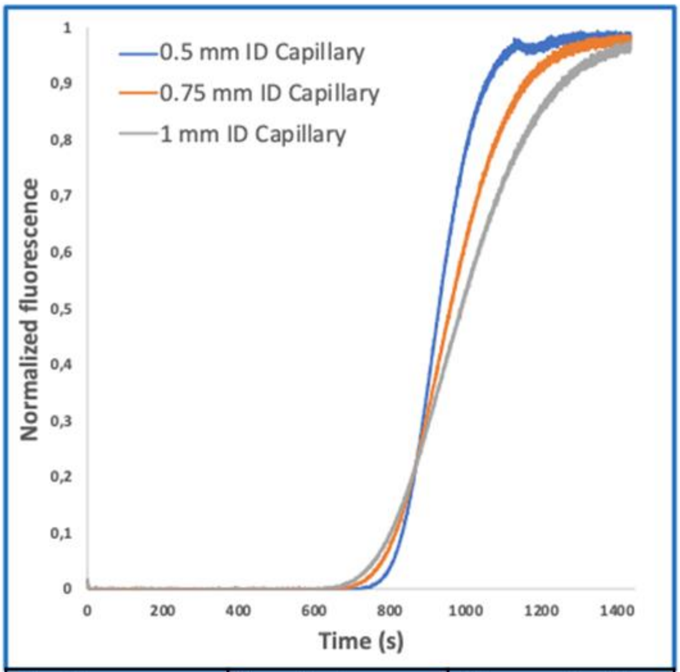

Capillary parameters	Length of dispersion zone in min	Time required for a single replicate in min
PEEK; ID:0.25 mm/ L:240 cm	5	Ca. 25
PFA; ID:0.5 mm/ L:60 cm	5.8	Ca. 25
PFA; ID:0.75 mm / L:26 cm	8.3	Ca. 25
PFA; ID:1 mm /L:15 cm	14.2	Ca. 25
PEEK; (ID:1.4 mm/ L: 7.61 cm)	15	Ca. 25

Figure 89: TAD-mediated dispersion of FITC in volume-normalized PFA tubing with an ID of 0.5 mm (blue), 0.75 mm (orange), and 1 mm (grey), respectively. Each measurement was repeated in three replicates at a flow rate of 9 µl/min. Increasing the ID while retraining the volume of the capillaries led to a reduction of the axial dispersion, increasing the dispersion of FITC. The evaluated capillaries are listed in the table below, with the optimal capillary for data reproducibility and the dispersion zone marked yellow.

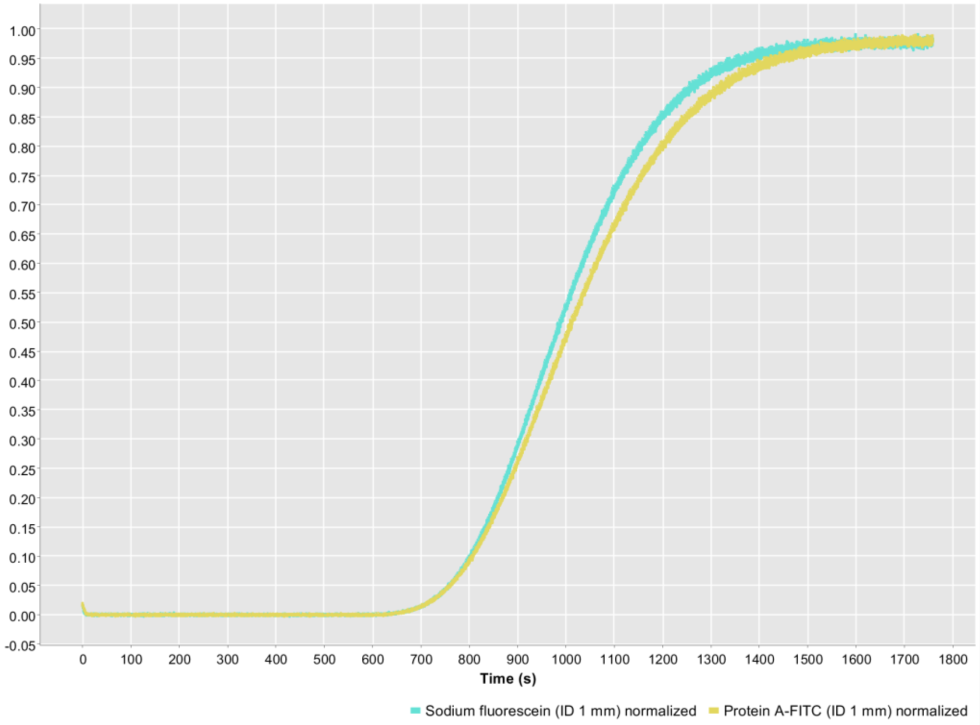

Figure 90: TAD of FITC and protein A – FITC in a 1 mm ID, 15 cm L PFA tubing. The two dilution curves were highly overlapping, indicating intense convection domination of the dilution process.

IV.4.1.2 The flowrates' impact on the convection dominated TAD

The impact of flowrates on convection-dominated TAD was estimated by measuring three different flowrates: 4, 6, and 9 µl/min in the PEEK (ID 1.4 mm/ L:7.61 cm) and PFA (ID 1 mm/ L:15 cm) capillaries. A faster flow rate decreases the time required for the convection-mediated dilution in the axial direction at a constant radial diffusion. The resulting increased Peclet number showcases that the so achieved dilution curves are more dominated by convection, thereby further decreasing the molar mass deviated differences in compound dilutions.

Decreasing the flow rates was unfavorable due to the increased measurement times and reduction of the convection-dominated effects, which in turn led to a higher deviation between compounds of varying molar masses. This was most evident by matching the dilution curves of fluorescein with Albumin-FITC. Furthermore, the dispersion zones decreased in comparison to the measurement time (Relative dispersion zone) even if the dispersion zones themselves increased (Absolute dispersion zone) (Figure 91)

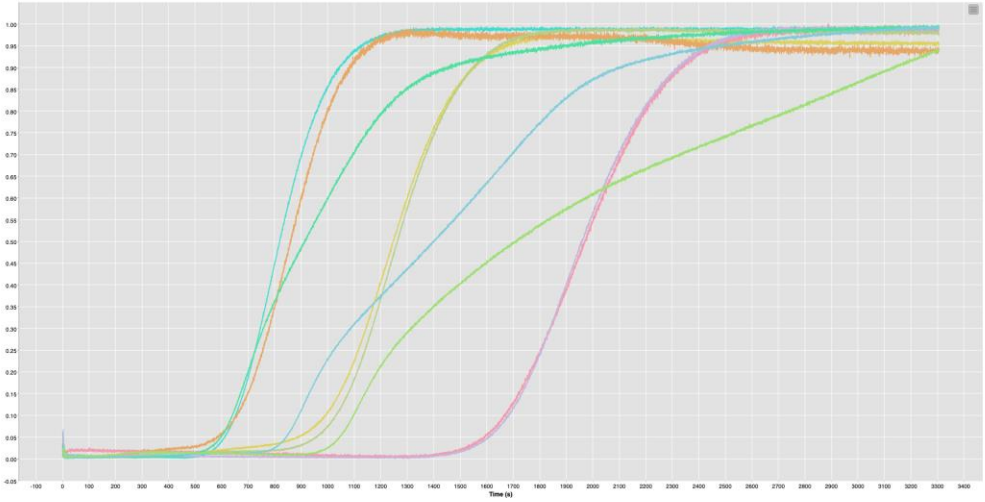

Figure 91: TAD mediated dispersion of fluorescein, 5(6) Carboxyfluorescein, and Albumin-FITC in a PEEK capillary (1.4 mm ID and 7.61 cm L) with flow rates of 9, 6, and 4 µl/min respectively (Figure 91). Each compound represents the middle value of three technical replicates.

Table 31: Impact of various flowrates on the convectional dominated TAD of fluorescence compounds regarding radial diffusion, measurement times, and absolute/relative dispersion. The PFA (1 mm ID and 15 cm length) and PEEK capillary (1.4 mm ID and 15 cm L) were evaluated with flow rates of 9, 6, and 4 µl/min, respectively (Figure 91). The deviation of the dispersion profile between different compounds was ranked from – to +++ according to the deviation of albumin-FITC from fluorescein and 5(6)-carboxyfluorescein. The overall length of dispersion and the time requirements were listed for the measurements. The best condition for future experiments was marked yellow.

Capillary parameters	**Flowrates in µl/min**	**Radial diffusion (based on the deviation of Albumin-FITC from fluorescein)**	**Absolute dispersion in min (based on fluorescein)**	**Measurement time of a single replicate in min (based on fluorescein)**	**Relative dispersion in % (based on fluorescein)**
PFA tubing (1 mm ID; 15 cm L)	9	-	9	25	36
PFA tubing (1 mm ID; 15 cm L)	4	+	18	54	33
PEEK tubing (1.4 mm ID; 7.61 cm L)	9	+	11	25	44
PEEK tubing (1.4 mm ID; 7.61 cm L)	6	++	14	33	42
PEEK tubing (1.4 mm ID; 7.61 cm L)	4	++	19	48	40

In the end, even though the dilution curves of Albumin-FITC had a notable deviation compared to the other two compounds, the dilution curves of fluorescein and 5(6)-Carboxyfluorescein were nearly identical even at flow rates of 4 µl/min. Therefore, it is safe to assume these flow rates can be used without significant difference between compound dilution profiles if the molecular masses are in a similar range (100-700 g/mol).

IV.4.1.3 Utilization of bilateral TAD measurements

In the previous chapter, the unilateral TAD dilution was implemented, which is only depends on the leading interface of the dilute. However, to gain a higher resolution, the trailing interface of the dilute can be used.[24] The challenge with this technique is the interaction of the trailing interface with the channel walls, increasing adsorption and absorption which leads to differences in the dilution profile between compounds.

In this sense, a system was set up as described previously (IV.3.4 Bilateral TAD measurements in volume normalized measurements). The only difference was that a loop was installed into the L-Switch module, which was loaded with the compound of interest. In total, four different 5 cm PFA capillaries with various ID were tested as possible loops (0.25 mm, 0.5 mm, 0.75 mm, and 1 mm ID). The compound with the defined volume was then loaded from the loop into a short 3 cm capillary with an ID of 1 mm to generate the convection-dominated TAD.

The objective was to find the minimal injection volume that is still sufficient to reach the maximal compound concentration. Hence the unilateral TAD. The best conditions were achieved by the 5 cm, 0.5 mm ID capillary with a volume of 39.2 µl after evaluating the data obtained from the five loops (Figure 92).

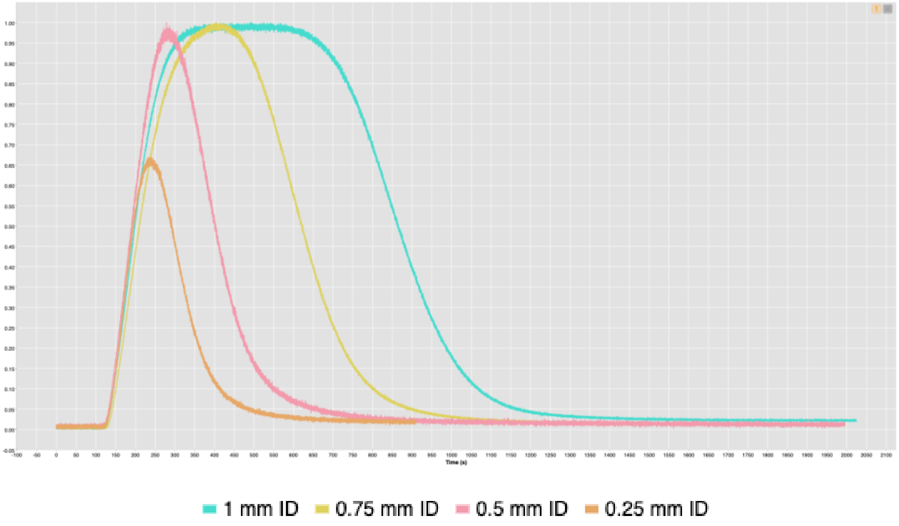

Figure 92: Bilateral TAD mediated dispersion of fluorescein by injecting the compound from four different loops with a length of 5 cm and a varying ID into a PFA capillary (1 mm ID and 2.5 cm L) with a flow rate of 9 µl/min respectively. The displayed RFU values are normalized to the maximal value obtained from the unilateral measurements under the same conditions. The four loops, 0.25 mm (brown), 0.5 mm (red), 0.75 mm (yellow), and 1 mm (cyan) ID, is represented by the middle value of three technical replicates.

In the next step, the reproducibility of the method was evaluated between different compounds. Consequently, the dilution of FITC and 5,6-Carboxyfluorescein were measured injected from the 0.5 mm ID loop at three different flow rates: 9, 13, and 17 µl/min. Even though the compounds showed a robust reproducibility between the replicates, this was no longer the case between the dilution of FITC and 5,6-Carboxyfluorescein (Figure 93).

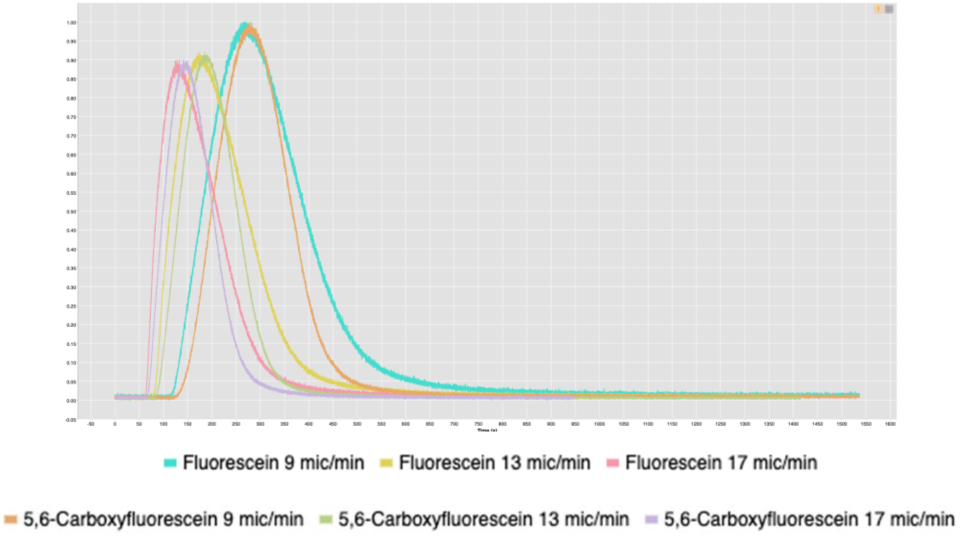

Figure 93 Bilateral TAD mediated dispersion of fluorescein and 5,6-Carboxyfluorescein in a PFA capillary (1 mm ID and 2.5 cm L) with a flow rate of 9 µl/min respectively. Compounds were injected from 5 cm PFA loops with an ID of 0.5 mm at three different flow rates: 9, 13, and 17 µl/min. Each compound represents the middle value of three technical replicates.

Repeated experiments led to the same results, confirming that the bilateral injection of compounds in this system is not reproducible. The main reason for this behavior is the previously noted interaction between the compounds and the microchips of the system. Therefore, glass chips were freshly coated with Plus-One-Repel silane, which indeed reduced the deviations. However, the compounds were still not sufficiently overlapping to use the bilateral TAD for the compound's dilutions. Therefore, instead of the bilateral TAD, the unilateral compound dispersion was utilized since the overlap between the compound's dilution curve is an absolute prerequisite for determining the compound's concentration in the high-resolution measurements.

IV.4.1.4 The impact of the system's length scale on the connection dominated TAD

As described in (IV.4.1.2 The flowrates' impact on the convection dominated TAD), a faster flowrate favors convection dominated TAD by decreasing the time scale available for radial diffusion effects compared to the axial convection. In addition, similar effects are obtained by reducing the length ratio of the system (IV.3.5 Final volume normalized unilateral measurements). The capillary for the unilateral convection-dominated TAD of the compounds was evaluated both mathematically and experimentally.

Mathematically, the convection-mediated dilution can be described in circular tubing with Reynold numbers below 10 which were generated in collaboration with Dr. Thomas Henkel (IPHT, Germany, Jena). Under laminar flow conditions, the pressure drop in the tubing is expressed with the Hagen Poiseuille equation, where Δp equals the pressure difference between inlet and outlet, L the length of the tubing, Q the volumetric flow rate, μ the dynamic viscosity, and R the radius of the tubing (Equation 2).

Equation 2 is converted to Equation 2.1 by substituting Q with Equation 3.

$$\Delta p = -\frac{8LQ\mu}{\pi R^4} \tag{2}$$

$$p = -\frac{8L\mu v_{mean}}{R^2} \tag{2.1}$$

$$Q = v_{mean}\pi R^2 \tag{3}$$

The radial velocity distribution v_Z under laminar flow in the cylindric channel is described by Equation 4, with r as the radial distance from the tube center orthogonally to the flow direction and p as the respective pressures.

$$v_Z = \frac{pr^2 - R^2 p}{4L\mu} \tag{4}$$

Solving Equation 2.1 and substituting it into Equation 4 results in Equation 4.1 describing the radial velocity distribution dependent on the difference to the tubing center.

$$v_Z = \frac{(2r^2 - 2R^2)v_{mean}}{R^2} \tag{4.1}$$

A stepwise transition between a fluid phase S (sample) and fluid phase B (pure buffer) is created by the variation of time. Regarding the composition of the mixture, this means that the fluid fraction α_s varies between a percental ratio between 0 and 1 (Equation 5).

$$\alpha_s = \frac{Q_s}{Q_s + Q_B} \tag{5}$$

The derivation of convection-dominated TAD was started with the velocity distribution, which yields a particular velocity Z of the fluid at a distance r from the channel center. Please note the differences between flowrates dependent on the radial distance of the center $v_Z(r)$ and the mean flowrates v_{mean}. Since $v_Z(r)$ is uniform, $v_Z(r)/dz=0$. Therefore, $v_Z(r)$ is substituted by $v_Z(r) = z/t$ and the equation is solved for r^2:

$$\frac{Z}{t} = \frac{(2r^2 - 2R^2)v_{mean}}{R^2} \tag{4.2}$$

$$r^2 = -\frac{R^2 z - 2R^2 t v_{mean}}{2t v_{mean}} \tag{4.3}$$

R^2 describes the square radius r^2 of the interphase between the two phases at the position z for a given time t. This can be used to calculate the cross-sectional area A_S of the sample fluid lamella inside the channel. The total cross-sectional area of the channel is given by $A_T = \pi * R^2$. The phase fraction alpha is calculated from the two cross-sectional areas.

$$\alpha_s = \frac{A_s}{A_T} \tag{5.1}$$

After simplification, the final model for the pure Taylor Dispersion without Diffusion terms is obtained.

$$a_s = 1 - \frac{z}{2t v_{mean}} \tag{6}$$

During the simplification, the geometrical parameters are completely lost in the equation. Hence, the model is highly generic and depends only on the average fluid velocity, which can be easily calculated for a given channel from the flow rate and the channel cross-sectional area. The model yields negative values for $2*t * v_{mean} < z$, which can be substituted by zero.

In most microfluidic setups, the capillary of interest is connected to other capillaries or microreactors with varying inner diameters, leading to a further dispersion of compounds. Equation 6 can be modified by substituting v_{mean} for Q/A (Equation 3) to account for the total TAD-mediated dispersion. The final equation was simplified to 6.1, and the hereby calculated values were compared to the experimental values.

$$a_s = 1 - \frac{\sum_{i=1}^{n} A_i z_i}{2tQ} \tag{6.1}$$

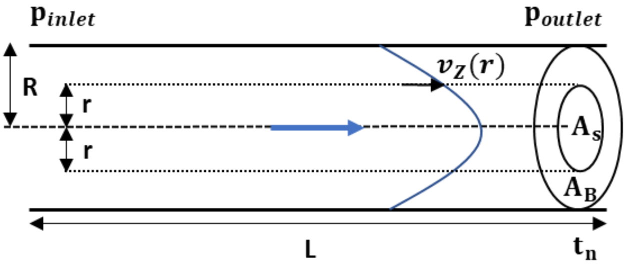

Figure 94: Schematic representation of convection mediated TAD in a tubing with length L and radius R. The parabolic distribution of the flow profile results from variations of flowrates ($v_Z(r)$) orthogonal to flow direction (r). With the flowrate distribution the cross-sectional area of the sample fluid (A_s) and the buffer (A_b) At can be calculated at given time t_n.

To analyze the new shortened capillaries experimentally, seven BODIPY derivatives with molar masses ranging from 291-475 g/mol were diluted in isopropanol and dispersed in the PFA tubing with 1.0 mm ID and a length of 2.5 cm at three different flow rates. As shown in (Figure 95), the experimental values were not only in high consensus with each other, and they also showed a solid approximation to the theoretical value calculated from equation 6.1 (Figure 95, brown graph). Furthermore, even the dilution curve of compounds with high molar masses, such as fluorescein-dextran (20,000 g/mol) and albumin-FITC (~ 62,0000 g/mol) dispersed in water, showed a strong alignment with FITC, especially at higher flow rates (Figure 96).

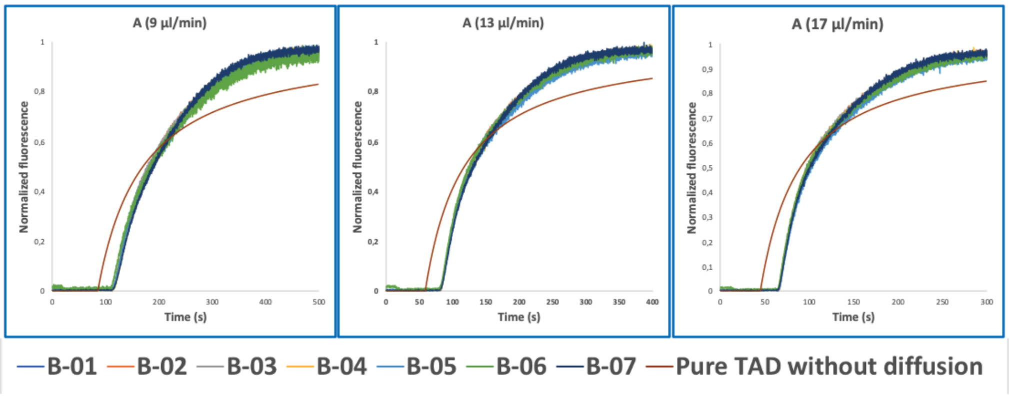

Figure 95: Normalized fluorescence spectra (y-axis) of the convection-dominated TAD in isopropanol of the BODIPY derivatives B-01 to B-07 (legend) in a 2.5 cm tubing with an ID of 1 mm followed by a 1.5 cm tubing with an ID of 0.75 mm as a function of time in s (x-axis). The dilution curves of all seven compounds aligned perfectly at the three different flow rates evaluated: 9 µl/min (A), 13 µl/min, and (C) 17 µl/min. TAD without diffusion was calculated using Equation 5.1 for the two short capillaries (ID 1 mm, L 2.5 cm; ID 0.75 mm, L 1.5 cm) and the microfluidic channel of the chip (ID 0.04 mm, L 3 cm). Measurements for each compound were repeated in three technical replicates.

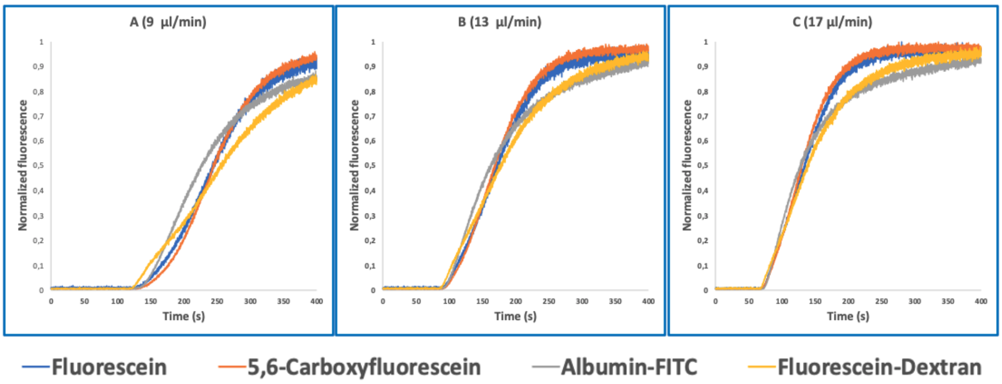

Figure 96: Normalized fluorescence spectra (y-axis) of the convection-dominated TAD in the water of fluorescein (blue), 5,6-carboxyfluorescein (red), albumin-FITC (green), and fluorescein-dextran (purple) in a 2.5 cm tubing with an ID 1 mm followed by a 1.5 cm tubing with an ID of 0.75 mm as a function of time in s (x-axis). The dilution curves of all seven compounds showed an increasing alignment at the higher flow rates: 9 µl/min (A), 13 µl/min, and 17 µl/min. Measurements for each compound were repeated in three technical replicates.

These results concluded that the compounds are diluted with convection-mediated TAD in the optimized system (PFA capillary with 2.5 cm and 1 mm ID at a compound flowrate of 13 µl/min), proposing that the dilution of compounds with a molar mass between 200 g/mol and 600 g/mol follows the same dilution profile FITC.

IV.4.2 Generation of high-resolution dose-response curves of the CAM mediated CP150-BO assembly inflow

With the established optimal conditions for convection-dominated TAD, the dilution curve of fluorescein was measured from single-digit nanomolar to 32 µM concentrations using the OptoReaders configurations (Figure 97) (III.4.2 Fluorescence spectrometer-based readout). FITC was diluted in the PFA capillary (L 2.5 cm, ID 1 mm), and the dilution curve was recorded at the same position in the microreactor in three different measurements with different gain and laser power settings, each in three replicates. The partial dilution curves covering different FITC concentrations were then complemented with each other resulting in the final high-resolution dilution curve (Figure 97) that served as the concentration marker for future high-resolution dose-response measurements.

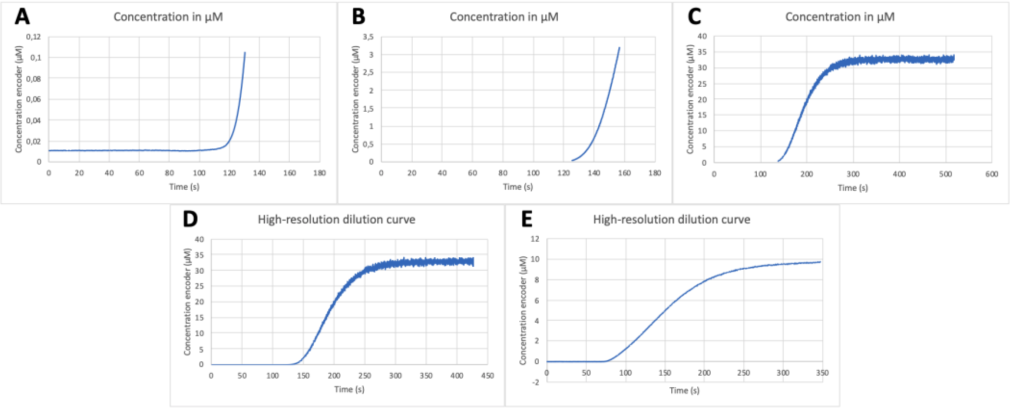

Figure 97: Generation of the high-resolution encoder curves at residence times of 3 min (D) and 51 s (E) using 32 µM sodium fluorescein solution. A single high-resolution curve is composed of three independent ones with three technical replicates, representing low (A), middle (B), and high concentrations (C), respectively. With the known concentration of FITC and the RFU obtained, the calibration curves were generated.

Despite the previous optimizations, the measurement of the dose-response curves has proven quite complicated due to the sensitivity of the TAD mediated compound dilution to air bubbles, backflow of compounds, damage of capillaries or leaking, adsorption to chips, or solubility of the compounds. Therefore, rigorous optimizations had to be performed to allow the absolute control of flow variables, pressures, and other parameters (III.7.1 Correct operation and troubleshooting of the microfluidic system).

After troubleshooting, the generation of high-resolution dose-response curves in a reproducible manner was successful, as presented here for BAY 41-4109. Hence, the resolution curves for the six reference compounds with known compounds (Figure 86) and the two in-house compounds (A, B) were measured at approximately 51 s post-mixing. At maximal compound concentrations of 32 µM, only the CAM-A compounds BAY 41-4109 and GLS4 reached an assembly of 100 %, while the other CAMs yielded lower assembly, ranging from 91 % (Compound B) to 58 % (ABI-H0731) (Figure 99 and Figure 100). The resulting EC_{50} values were higher than those derived from microtiter plates, mainly due to the shorter measurement times and the different assay formats (Figure 100). Compounds with slower assembly kinetics showed significantly higher EC_{50} values due to the incomplete assembly reaction at this time point compared to the longer incubation times in the microtiter plate format. This was visualized by comparing the resulting dose-response curves, which show an exponential increase instead of a sigmoidal curve. Measuring accurate EC_{50} values for “slower” CAMs could be performed at later time points, but the inhibition of further dilution due to TAD has to be prevented for comparative results.

In summary, the assay presented here measured the EC_{50} values of 8 CAMs at early timepoints (51 s) in an automated and reproducible manner. In addition, information about the mode of action of the compounds was provided based on their assembly kinetics and is further elucidated in the following section.

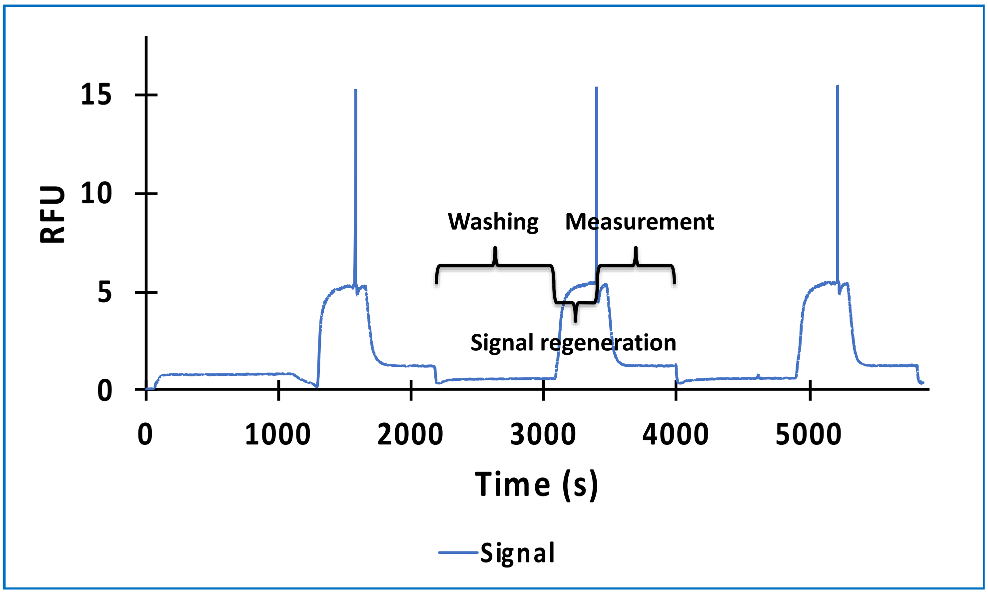

Figure 98: Measurement of 32 µM BAY 41-4109-mediated CP150C assembly at 51 s post-mixing. The reaction consisted of cleaning, signal saturation (CP150-BO mixed with 50 mM HEPES), and assembly reaction marked with the high blue peaks. During the assembly, the CP150-BO was mixed with the TAD-generated dilution gradient of the BAY 41-4109, resulting in the asymptotic quenching of the fluorescence signal.

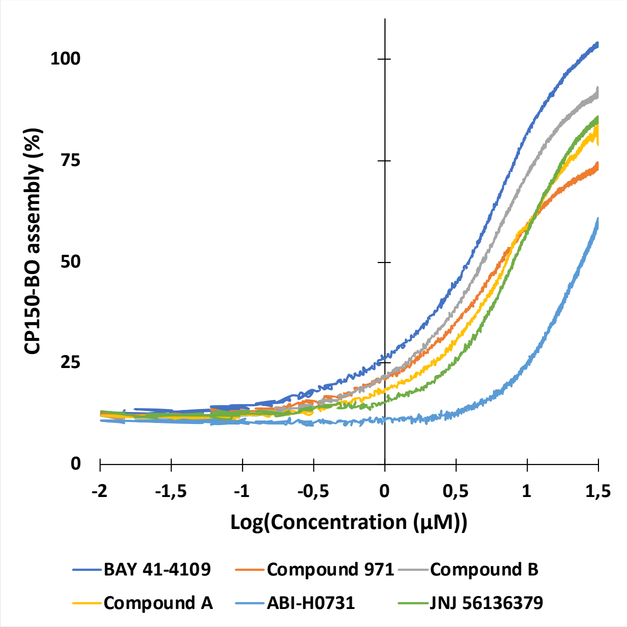

Figure 99: High-resolution dose-response curves for the six CAMs at 51 s post-mixing inflow. Compounds were diluted using TAD-mediated dispersion and mixed inflow as described in the Experimental section. CAM-N compounds had mostly incomplete CP150-BO assembly at 51 s, resulting in higher EC_{50} values. This was mainly evident for ABI-H0731, which yielded a non-sigmoidal assembly curve due to the incomplete reaction. GLS4 and NVR-3-778 were measured at 10 µM maximal concentration due to solubility issues, and so, were not displayed in this graph.

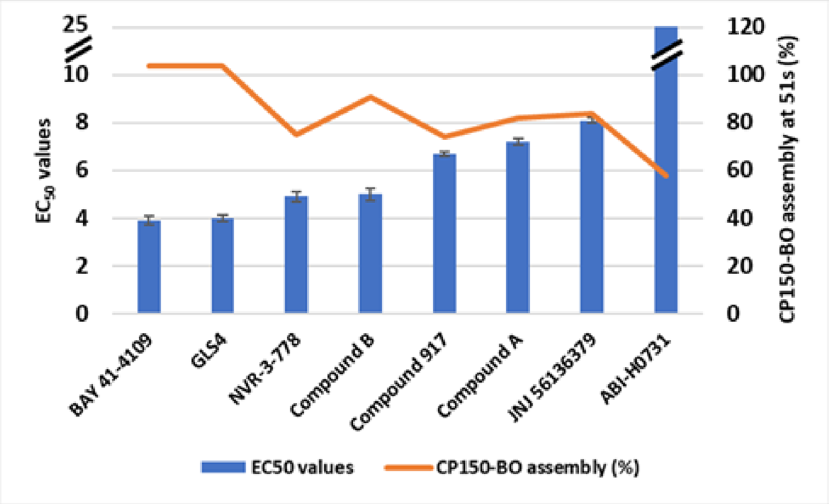

Figure 100: EC$_{50}$ values of the six reference CAMs and the two in-house compounds inflow after 51 s. Each compound was tested at least two times. Interestingly, only the heteroaryldihydropyrimidine (HAP) compounds BAY 41-4109 and GLS4 reached 100 % assembly, while the in-between CAM, Compound B, resulted in a maximum assembly of 91 %. Compounds with maximal CP150-BO assembly under 60 % resulted in relatively higher EC$_{50}$ values due to the incomplete reaction.

IV.4.3 CP150-BO assembly kinetics as an indicator of the mode of action of CAMs

Capsid assembly is dependent on the buried hydrophobic interface between dimers, which regulates the strength of the interaction and, consequently, the assembly rate. Zhou et al. showed that HAPs could alter the buried interface between dimers, thereby strengthening the assembly reaction. In addition, HAPs could also change the probability of contact to spike domain type of binding, increasing the probability of aberrant structure formation.[25] The fast assembly reaction due to high association energies, and rapid nucleation, in turn, leads to the formation of kinetically trapped intermediates due to the depletion of free core proteins.[26]

Therefore, to distinguish between the modes of action of CAMs in this study, the differences in CAM-mediated CP150-BO assembly kinetics were used instead of the morphology of the capsids and aggregates. Microfluidic systems fit these requirements perfectly since they allow measurements after just a few seconds post-mixing, giving new insights into the reaction.

Hence using the microfluidic platform, the assembly kinetics of six well-characterized reference inhibitors, two of which were categorized into CAM-A and four into CAM-N, as well as the two in-house compounds with unknown mode of action were screened. The goal was to observe apparent differences between the assembly kinetics of the known CAM-As compared to the CAM-Ns, and based on this data, to categorize the two in-house compounds. The reaction was conducted in three replicates at 10-fold EC_{50} concentrations, obtained in microtiter plates, and at several time points, ranging from 5 s up to 336 s (Fig. 7). Both CAM-A compounds led to a rapid assembly (GLS4: 99 % assembly; Bay 41-4109: 82 %) completed at 10 s post-mixing. On the other hand, CAM-N compounds showed variations in their respective kinetics and were categorized into two groups. "Slow" CAM-N led to an assembly of 6-18 % at 7.5 s, while "fast" CAM-N compounds, such as Compound B, NVR-3-778, and Compound 917, were able to achieve assembly values between 44 % to 61 %. At the endpoint of 336 s, all the compounds reached an assembly of at least 88 %, with the highest values obtained by GLS4 (109 %), BAY 41-4109 (100 %), Compound B (98 %), JNJ 56136379 (92 %) and Compound A (94 %). These tendencies showed that compounds with a CAM-A mode of action indeed have faster assembly kinetics, reaching slightly higher endpoint values inflow (Figure 101).

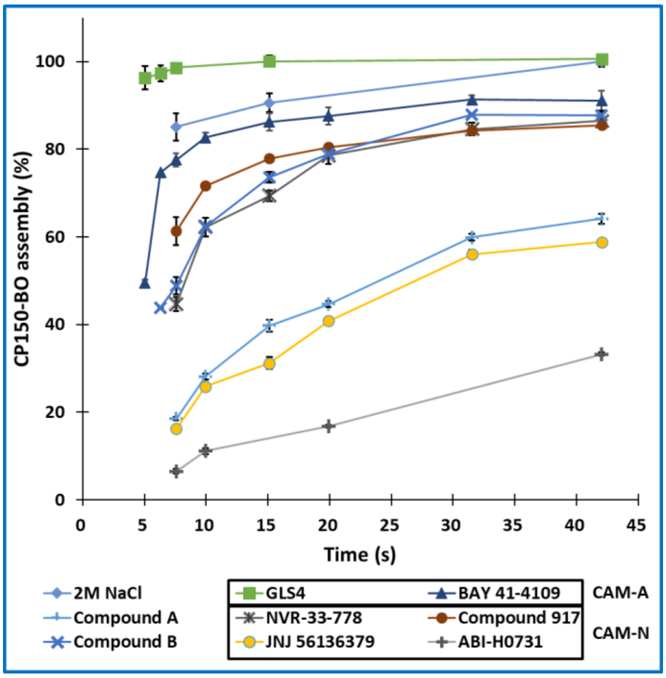

Figure 101: Kinetic development of the CP150-BO assembly reaction at various time points using the six references and the two inhouse compounds at 10-fold EC_{50} concentrations. The reactions were tested three times.

To further study the impact of CAM concentration on capsid assembly kinetics and to facilitate the characterization of the mode of action of the two in-house compounds, measurements were conducted with 1, 10, and 100 µM CAMs. Using **1 µM** CAM and a residence time of 2 min, CAM-A compounds and Compound B reached approximately 40 % assembly, while other compounds reached only around 29 %. Increasing the concentration to **10 µM** while maintaining the same residence time of 2 min, led to a nearly complete assembly of approximately 95 % for the CAM-As and 77 % for Compound B. Contrarily, the other compounds only reached maximal values ranging from 58 % to 37 %. Interestingly, significant differences in assembly between CAM-A (BAY 41-4109: 75 %, GLS4: 89 %) and the other compounds (31 % to 2 %) could be observed by reducing the residence time to 7.7 s, while maintaining a 10 µM concentration. Among the other compounds, Compound B, NVR-3-778, and Compound 917 achieved the highest assembly with approximately 27 %. Finally, the CAM concentration was further increased to **100 µM** with a residence time of 2 min, at which all the compounds reached an assembly of at least 75 %. CAM-As again yielded the highest assembly rates at around 100 %, followed by Compound B at around 91 %, and JNJ 56136379 at 87 %. Measurement of the effect of 100 µM CAM at a shorter residence time of 7.7 s again displayed the difference between CAM-A (BAY 41-4109: 98 %, GLS4: 92 %) and CAM-N (around 65 %) (Figure 102).

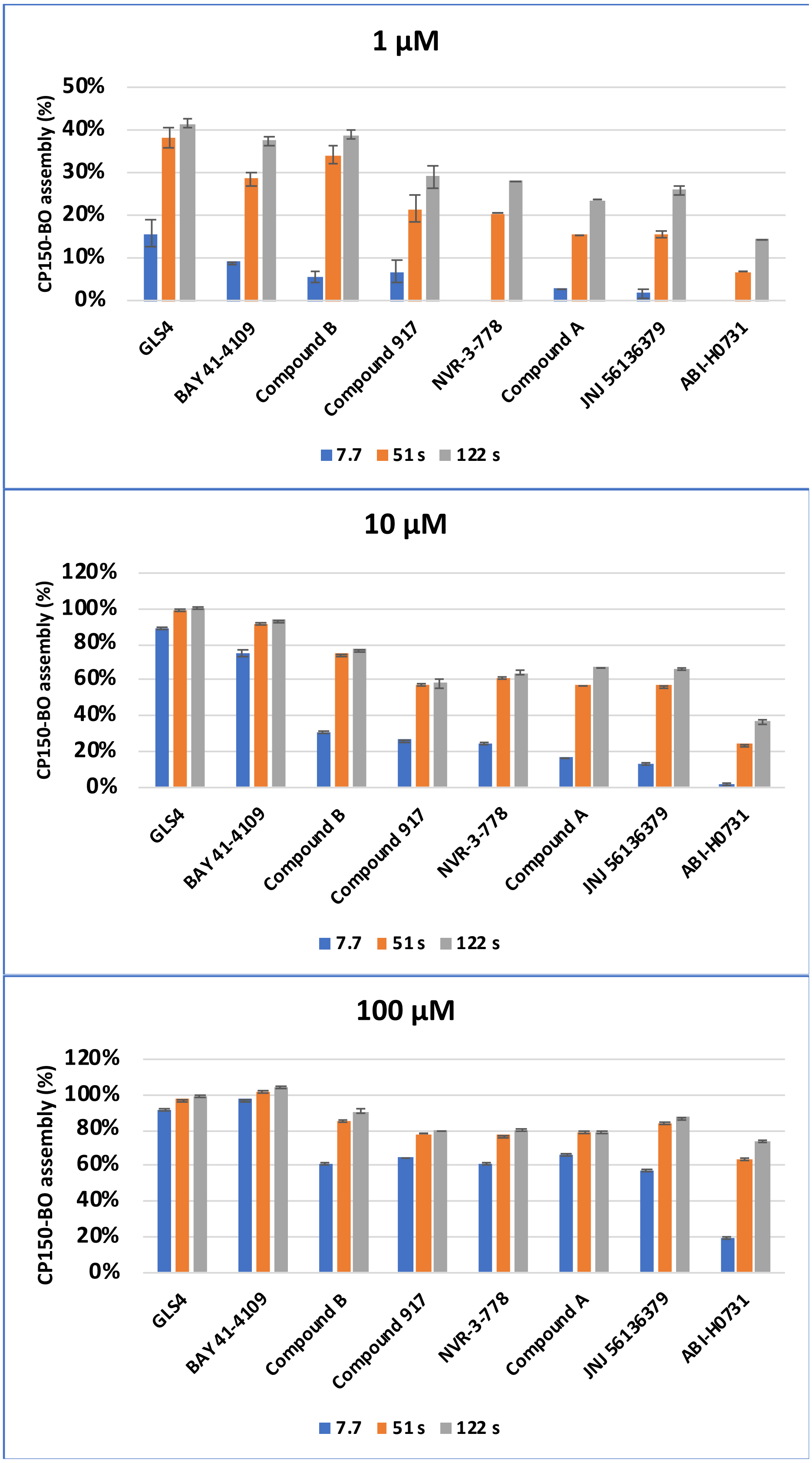

Figure 102: CP150C assembly mediated by different CAMs at three incubation time points (7.7 s, 51.1 s and 122.7 s) and in three concentrations (1 µM, 10 µM, 100 µM). For each compound, the reaction was performed in duplicate.

In summary, the reactions with 10 µM (or 32 µM as used in the EC_{50} measurements) CAMs were most appropriate to elucidate the difference between the two compound classes by eliminating oversaturation and, at the same time, maintaining an excellent signal to background ratios. Therefore, to accurately distinguish the mode of action, a 10 µM solution of the respective CAMs with 7.7 and 51 s as residence times have to be used, which led to the most apparent differentiation of the CAM's mode of action. At 7.7 s, CAM-A reached assembly values around 50 % higher than CAM-N, and at 51 s, the assembly reaction for CAM-A was mostly completed contrary to CAM-N.

Interestingly, while Compound A behaved more like a classical "fast" CAM-N compound, Compound B showed an in-between kinetic behavior at 1 µM and 10 µM concentrations, making a precise classification for this compound challenging. The difference of compound B to CAM-N was especially eye-catching at a concentration of 10 µM and 51 s at which both the other fast CAM-Ns compound 917 and NRV-33-778 showed a lower CP150-BO assembly rate.

Therefores size exclusion chromatography and immunofluorescence assays were performed by Dr. Andreas research group (AiCuris, Germany, Wuppertal) verifying the above determined CAMs’ mode of actions (IV.7.1 Analytical size exclusion chromatography and immunofluorescence-based determination of CAMs’ mode of action kindly provided by Dr. Andreas Urbans research group).

IV.5 Conclusion

The focus of this chapter was the adaptation of the CAM mediated HBc assembly assay to the fully automated microfluidic system. The first step was the evaluation of convection-mediated, unilateral TAD as a possible method for the inflow dilution of CAMs prior to mixing with HBc. While TAD has been utilized in previous flow formats to generate high-resolution dilution curves, it was often used in thin capillaries resulting in a complicated evaluation based on axial convection and radial diffusion of compounds.[24,27–29] Contrary to the general convection-diffusion dominated TAD, the convection dominated TAD only depends on the system's flowrate and is independent of the compounds' radial diffusion. Therefore, the optimal conditions were evaluated experimentally to generate convection-dominated TAD, including, various capillary geometries, flow rates, and the difference in unilateral and bilateral dilutions. Best conditions were obtained at unilateral dilutions with high Pe compared to the system's length ratio achieved by increasing the capillary radius of the tubings while simultaneously decreasing its length. These findings were experimentally proven in the excellent overlap of seven different BODIPY-derivates' dilution curves in a PFA tubing with 2.5 cm and 1 mm ID at a compound flowrate of 13 µl/min. Furthermore, the experimental values were very close to the mathematically predicted dilution curves for convectional dominated TAD. Based on these results, it can be reasoned that under conditions presented here, each compound's dilution curve in the range from 250-600 g/mol follows the same dilution as from FITC.

The convection dominated TAD was utilized to dilute the CAMs before mixing with HBc. The resulting dilution curves were used to generate high-resolution dose response curves for the HBc capsid assembly assay at 51 s post-mixing for six references and the two in-house compounds. The dose response curves in turn were used for the calculation of the respective EC_{50} inflow. In this microfluidic assay, the in-flow measured values were higher than those measured in microtiter format with EC_{50} around 3-4 µM. This variation is attributed to the lower residence time (51 s compared to

5 min in microtiter plate assay), and general differences in the assay format.

The microfluidic format gave the possibility to measure at short residence times, contrary to the microtiter plate format. Therefore, the capsid assembly's kinetic was recorded at residence times of down to 5 s for the first time with six well-characterized reference CAMs and two in-house compounds in the early drug discovery research stage. At concentrations of 10-fold EC_{50} value, both CAM-A compounds BAY 41-4109 and GLS4 displayed a rapid assembly unmatched by the other CAMs. Furthermore, at higher residence times, these compounds led to a higher overall CP150-BO assembly of 100 % compared to CAM-N compounds with maximal assemblies around 60-84 % inflow.

The concentration-dependent kinetics were measured in a second experiment using three different stock concentrations (1 µM, 10 µM, and 100 µM). CAM-A were significantly faster than CAM-N at all three concentrations, with especially profound differences at the lower residence times of 7.7 s. Interestingly, the in-house compound B showed a faster and higher maximal assembly rates, particularly at a concentration of 10 µM and residence times of 7.7 and 51 s compared to the other CAM-Ns but did not quite reached the levels of the other CAM-As. This compound showcased similar in-between behavior in the immunofluorescence assay and SEC as well. Therefore, it can be concluded that, aside from the morphology of the assembled products, the aggressive assembly displayed by CAM-A compounds is a possible identification factor for the mode of action of different CAMs. This result is especially interesting considering the measurement times and experimental efforts of the other methodologies.[30] To-date, the techniques available for differentiation of the CAM's mediated HBc assembly products include dynamic light scattering,[31] size exclusion chromatography, and immunofluorescence assays,[15,32] small-angle X-ray scattering,[33] time-of-flight mass spectrometry[34], and fluorescence correlation spectroscopy.[35] All of these require at least 1 h sample preparation and measuremt time. In contrast the system presented here can obtain the required data within 4 min (measurement at 3 residence times).

The evaluation of HBc capsids' frequency with different NaCl concentrations was reported in literature using a microfluidics-based on resistive-pulse analysis. Nonetheless, since the mixing was performed off-platform in these assays, the first results were obtained after 10 min and last after overnight incubation, which therefore does not provide information about the early kinetics of HBc assembly.[36–39]

In conclusion, the microfluidic system offers a valuable opportunity to rapidly screen for novel CAMs. It simultaneously provides information about the activity and the kinetics of compounds, therefore also giving a first hint regarding the mode of action of novel CAMs. Furthermore, with the evaluation of the kinetic data at three independent time points (7.7, 51, and 122 s), the differentiation of mode of action per compound is possible within 4 min, as opposed to the analytical size exclusion chromatography requiring at least 3 h for sample preparation and evaluation. Finally, the possibility of measuring reactions at a couple of seconds provides an excellent opportunity to study capsid kinetics and further novel drug targets.

IV.6 References

1. Pereira, S. A. P., Dyson, P. J. & Saraiva, M. L. M. F. S. Miniaturized technologies for high-throughput drug screening enzymatic assays and diagnostics – A review. *TrAC - Trends Anal. Chem.* **126**, 115862 (2020).

2. Reyes, D. R., Iossifidis, D., Auroux, P. & Manz, A. Micro Total Analysis Systems . 1 . Introduction , Theory , and Technology. **74**, 2623–2636 (2002).

3. Lee, S. J. & Lee, S. Y. Micro total analysis system (μ-TAS) in biotechnology. *Appl. Microbiol. Biotechnol.* **64**, 289–299 (2004).

4. Manz, A., Graber, N. & Widmer, H. M. Miniaturized total chemical analysis systems: A novel concept for chemical sensing. *Sensors Actuators B. Chem.* **1**, 244–248 (1990).

5. Dittrich, P. S., Tachikawa, K. & Manz, A. Micro total analysis systems. Latest advancements and trends. *Anal. Chem.* **78**, 3887–3907 (2006).

6. Whitesides, G. M. The origins and the future of microfluidics. *Nature* **442**, 368–373 (2006).

7. Măriuţa, D. *et al.* Miniaturization of fluorescence sensing in optofluidic devices. *Microfluidics and Nanofluidics* vol. 24 (2020).

8. Dittrich, P. S. & Manz, A. Single-molecule fluorescence detection in microfluidic channels-the Holy Grail in μtAS? *Anal. Bioanal. Chem.* **382**, 1771–1782 (2005).

9. Nys, G. & Fillet, M. Microfluidics contribution to pharmaceutical sciences: From drug discovery to post marketing product management. *J. Pharm. Biomed. Anal.* **159**, 348–362 (2018).

10. Ananthakrishnan, V., Gill, W. N. & Barduhn, A. J. Laminar dispersion in capillaries. *A.I.Ch. E. J.* **11**, 1063–1072 (1965).

11. Vedel, S., Hovad, E. & Bruus, H. Time-dependent Taylor-Aris dispersion of an initial point concentration. *J. Fluid Mech.* **752**, 107–122 (2014).

12. Kirby, B. J. *Micro- and Nanoscale Fluid Mechanics*. (CAMBRIDGE UNIVERSITY PRESS, 2010).

13. Vedel, S. & Bruus, H. Transient Taylor-Aris dispersion for time-dependent flows in straight channels. *J. Fluid Mech.* **691**, 95–122 (2012).

14. Agresti, J. J. *et al.* Ultrahigh-throughput screening in drop-based microfluidics for directed evolution. *Proc. Natl. Acad. Sci. U. S. A.* **107**, 4004–4009 (2010).

15. Corcuera, A. *et al.* Novel non-heteroarylpyrimidine (HAP) capsid assembly modifiers have a different mode of action from HAPs in vitro GPA, PT, DBT. *Antiviral Res.* **158**, 135–142 (2018).

16. Turner, J. et al. United States Patent; Patent No.: US 10 , 183 , 936 B2. (2019).

17. Vandyck, K. *et al.* Synthesis and Evaluation of N-Phenyl-3-sulfamoyl-benzamide Derivatives as Capsid Assembly Modulators Inhibiting Hepatitis B Virus (HBV). *J. Med. Chem.* **61**, 6247–6260 (2018).

18. VANDYCK, Koen; HACHE, Geerwin; Yvonne, Paul; Stefaan, Julien;David, Craig;ROMBOUTS, Geert; VERSCHUEREN, Wim, Gaston; RABOISSON, Pierre, Jean-Marie, B. WO 2014/184350 A1. vol. 5 (2014).

19. Wang, X. Y. *et al.* In vitro inhibition of HBV replication by a novel compound, GLS4, and its efficacy against adefovirdipivoxil-resistant HBV mutations. *Antivir. Ther.* **17**, 793–803 (2012).

20. Karl Deres, H. R.-W. Inhibition of Hepatitis B Virus Replication by Drug-Induced Depletion of Nucleocapsids. *Science (80-.).* **303**, 1829 (2003).

21. Zlotnick, A. *et al.* In vitro screening for molecules that affect virus capsid assembly (and other protein association reactions). *Nat. Protoc.* **2**, 490–498 (2007).

22. Thiele, M. *et al.* High-Throughput Synthesis of Uniform Silver Seed Particles by a Continuous Microfluidic Synthesis Platform. *Chem. Eng. Technol.* **38**, 1131–1137 (2015).

23. Sun, D. & Nassal, M. Stable HepG2- and Huh7-based human hepatoma cell lines for efficient regulated expression of infectious hepatitis B virus. *J. Hepatol.* **45**, 636–645 (2006).

24. Miller, O. J. *et al.* High-resolution dose-response screening using droplet-based microfluidics.

25. Zhou, Z. *et al.* Heteroaryldihydropyrimidine (HAP) and Sulfamoylbenzamide (SBA) Inhibit Hepatitis B Virus Replication by Different Molecular Mechanisms. *Sci. Rep.* **7**, 1–12 (2017).

26. Zlotnick, A., Johnson, J. M., Wingfield, P. W., Stahl, S. J. & Endres, D. A theoretical model successfully identifies features of hepatitis B virus capsid assembly. *Biochemistry* **38**, 14644–14652 (1999).

27. Werner, M. *et al.* Seamless integration of dose-response screening and flow chemistry: Efficient generation of structure-activity relationship data of β-secretase (BACE1) inhibitors. *Angew. Chemie - Int. Ed.* **53**, 1704–1708 (2014).

28. Terekhov, S. S. *et al.* Microfluidic droplet platform for ultrahigh-throughput single-cell screening of biodiversity. *Proc. Natl. Acad. Sci. U. S. A.* **114**, 2550–2555 (2017).

29. Cai, L. F., Zhu, Y., Du, G. S. & Fang, Q. Droplet-based microfluidic flow injection system with large-scale concentration gradient by a single nanoliter-scale injection for enzyme inhibition assay. *Anal. Chem.* **84**, 446–452 (2012).

30. Newman, M., Suk, F.-M., Cajimat, M., Chua, P. K. & Shih, C. Stability and Morphology Comparisons of Self-AssembledVirus-Like Particles from Wild-Type and Mutant Human Hepatitis B VirusCapsidProteins. *J. Virol.* **77**, 12950–12960 (2003).

31. Zlotnick, A., Aldrich, R., Johnson, J. M., Ceres, P. & Young, M. J. Mechanism of capsid assembly for an icosahedral plant virus. *Virology* **277**, 450–456 (2000).

32. Sauviller, S. *et al.* Development of a cellular high-content, immunofluorescent HBV core assay to identify novel capsid assembly modulators that induce the formation of aberrant HBV core structures. *J. Virol. Methods* **293**, 114150 (2021).

33. Tresset, G. *et al.* Norovirus capsid proteins self-assemble through biphasic kinetics via long-lived stave-like intermediates. *J. Am. Chem. Soc.* **135**, 15373–15381 (2013).

34. Uetrecht, C., Barbu, I. M., Shoemaker, G. K., Van Duijn, E. & Heck, A. J. R. Interrogating viral capsid assembly with ion mobility-mass spectrometry. *Nat. Chem.* **3**, 126–132 (2011).

35. Borodavka, A., Tuma, R. & Stockley, P. G. Evidence that viral RNAs have evolved for efficient, two-stage packaging. *Proc. Natl. Acad. Sci. U. S. A.* **109**, 15769–15774 (2012).

36. Zhou, J. *et al.* Characterization of Virus Capsids and Their Assembly Intermediates by Multicycle Resistive-Pulse Sensing with Four Pores in Series. *Anal. Chem.* **90**, 7267–7274 (2018).

37. Harms, Z. D., Selzer, L., Zlotnick, A. & Jacobson, S. C. Monitoring Assembly of Virus Capsids with Nanofluidic Devices. *ACS Nano* **9**, 9087–9096 (2015).

38. Kondylis, P. *et al.* Nanofluidic Devices with 8 Pores in Series for Real-Time, Resistive-Pulse Analysis of Hepatitis B Virus Capsid Assembly. *Anal. Chem.* **89**, 4855–4862 (2017).

39. Kondylis, P. *et al.* Competition between Normative and Drug-Induced Virus Self-Assembly Observed with Single-Particle Methods. *J. Am. Chem. Soc.* **141**, 1251–1260 (2019).

40. Zlotnick, A. & Katen, S. The thermodynamics of virus capsid assembly. *Methods Enzymol.* **6879**, 1–19 (2009).

IV.7 Appendix

IV.7.1 Analytical size exclusion chromatography and immunofluorescence-based determination of CAMs' mode of action kindly provided by Dr. Andreas Urbans research group

CAMs were reported to induce either the formation of morphologically intact but empty HBV capsids (CAM-N) or larger aberrant structures (CAM-A). Analytical size-exclusion chromatography is a well-established method of demonstrating CAM activity and differentiating between the two different modes of action.[15,40] Consequently, Compound A and Compound B were incubated with CP150C for 2 h prior to separation on a Superose6 Increase column (Fig. 9). As expected, two absorbance peaks, one corresponding to the capsid and the other to the core protein dimer, were observed. In the DMSO control, the equilibrium between capsid and core protein dimer was shifted to the core protein dimer. On the other hand, as observed in previous studies, the incubation with the CAM-A reference BAY 41-4109 caused a shift of the capsid peak towards a lower retention volume, indicating the formation of larger structures. Comparing the SEC profiles obtained after incubation with Compound A or B showed that Compound B induced a shift of the capsid peak towards larger structures, similar to BAY 41-4109, whereas Compound A did not.

In addition to the biochemical analysis, the mode of action of Compound A and B were analyzed in an antiviral assay using the immunostaining of HBcAg as a readout. In the HepG2.117 cell line, the expression of HBV is regulated by a tetracycline responsive minimal CMV promoter. As shown in Fig. 10, HBV replication was repressed in doxycycline-treated cells, whereas in DMSO-treated cells, HBcAg was detected in both the nucleus and the cytoplasm. As previously described, the HBcAg staining in cells treated with the CAM-N reference NVR-3-778 was almost exclusively found in the cytoplasm, whereas BAY 41-4109 is known to follow the CAM-A mode of action, induced punctuated aggregates in or near the nucleus.[15] In line with the observation from the SEC, treatment with compound A-induced a CAM-N phenotype, whereas treatment with compound B had the tendency to induce aggregated dot-like structures exclusively seen after CAM-A treatment. However, the number and size of these aggregates were significantly lower than in BAY 41-4109-treated cells. From these results, the classification of Compound A as having a classical CAM-N mode of action. On the other hand, this study showed evidence that Compound B induces a CAM-A phenotype in all three experiments — kinetics analysis using the microfluidic system, SEC, and immunostaining of HBcAg in HepG2.117 cells.

Therefore, the aggressive assembly displayed by CAM-A compounds is a possible identification factor for the mode of action of different CAMs. Thus, the microfluidics platform offers an excellent opportunity for further study of capsid kinetics and the differentiation of the modes of action of CAMs in a rapid and reliable manner.

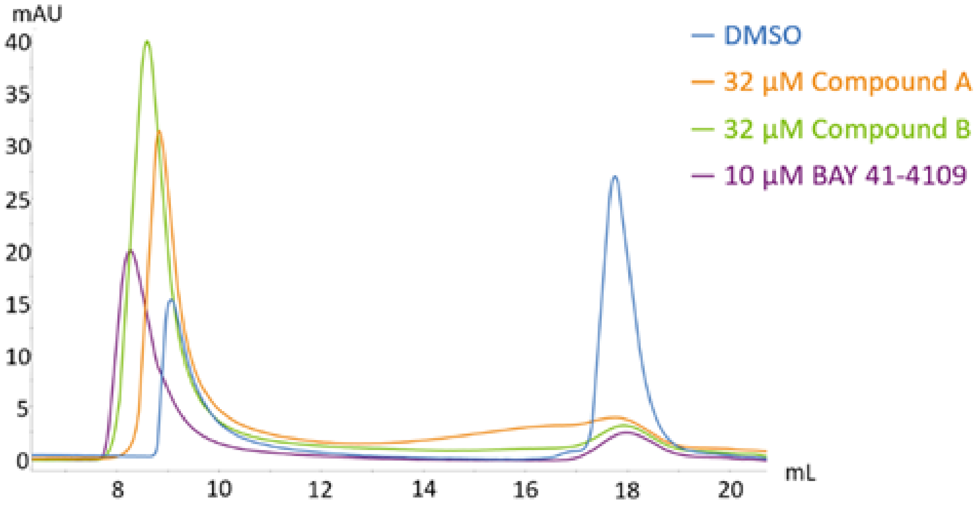

Figure 103: Analytical size exclusion chromatography of HBV capsid and core protein dimer after exposure to different CAMs. Core protein CP150 was incubated in 60 mM BES, pH 6.8 with 150 mM NaCl and 10 or 32 µM CAM at 25 °C for two h prior to separation on a Superose6 Increase column. Two distinct peaks were observed, with the capsid peak (approximately 9 ml) eluting before the core protein dimer peak (approximately 18 ml).

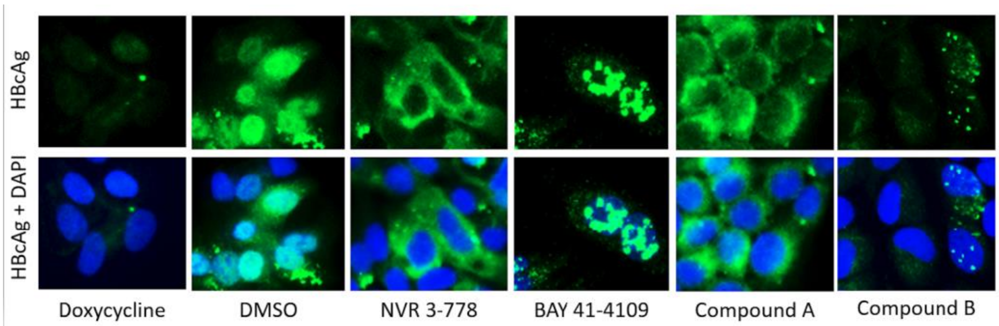

Figure 104: Immunofluorescence staining of HBcAg in HepG2.117 cells after treatment with different CAMs. Cells were cultured without doxycycline to induce HBV expression and treated with either DMSO, 50-fold EC_{50} of NVR-3-778, BAY 41-4109, Compound A, or Compound B for 6 days. HBcAg was visualized via indirect immunofluorescence staining using an anti-HBcAg antibody (green). In the lower panels, nuclei were counterstained with DAPI (blue), and the images of both stains were merged. In doxycycline-treated cells, HBV replication was repressed.

Chapter V.

Droplet-based microfluidics as suitable assay format for CAM mediated HBc assembly.

V.1 Introduction

In chapter IV, the HBc capsid assembly assay was successfully adapted to the continuous flow format, which allowed the rapid screening of CAMs'kinetics, mode of action, and the generation of high-resolution dose-response curves at residence times of around 1 min post mixing. However, some of the CAM-Ns did not lead to a complete HBc assembly under 1 min. Unfortunately, at later residence times, the TAD mediated dilution between compounds was no longer synchronous due to radial diffusion mediated deviations. In order to prevent the diffusion-mediated differences between CAMs, the compartmentalization of the reaction mixtures directly after the mixing was attempted in this chapter using droplet microfluidics. As described in the introduction, the main benefits of droplet generation are the clearly distinguishable vesicles generating truly independent data points, a reduced sample consumption, and the termination of unwanted secondary flow effects post mixing.[1,2] For reproducible results, the generation of droplets of similar size (monodispersity) is imperative. Monodispersity, in turn, is determined by the microreactors' design and surface properties and the physical properties of the carrier oil, surfactants, and additives used in the reaction.

V.1.1 Different microreactor designs considered for droplet generation

During droplet generation, one liquid is dispersed into a continuous phase resulting in independent droplets with a defined surface. The system's energy state after mixing is higher due to an increase in surface tension (III.1 Introduction). Therefore, energy must be introduced to form an unstable saddle point from which the metastable droplet flow is generated by spontaneous decay. This can be achieved by using an exogenous energy supply such as electrowetting on dielectric effects, dielectrophoresis, ferrofluids in a magnetic field, local temperature gradients, and simple mechanical methods utilizing hydraulic or pneumatic elements.[3,4] While these techniques are quite sophisticated, their cost and complexity during droplet generation usually exceed the benefits provided, wherefore many papers decided to use passive droplet generation methods. In brief, the main driving force for passive droplet generation is the shear stress, which induces fluctuations at the liquid interface, finally leading to a pinch-off of defined droplets.[4]

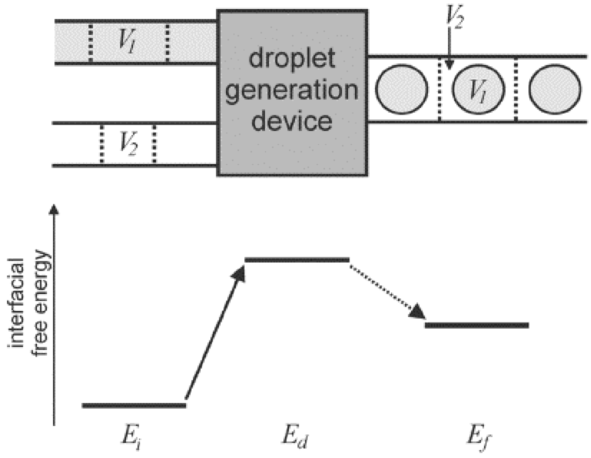

Figure 105: Schematic representation of the energy levels during droplet formation. The initial surface energy (Ei) of the two liquids is increased to a high saddle point upon mixing the two liquids (Ed). From this site, the system relaxes into a metastable position by spontaneous decay into droplets.[7]

The most frequently used designs for passive droplet generation are cross-flow, co-flow, flow-focusing, and step-wise emulsification devices made either from polymers or glass.[3]

Step-wise emulsification offers the highest homogeneity in droplet sizes coupled to very high dispersed volume ratios of up to 96 %.[5] The droplet generation frequency can be varied two orders before significant changes in droplet size occur. However, the design of these devices requires very delicate fabrication, especially regarding the height-wide ratios.

Co-flow and mainly flow-focusing devices generate droplets with great monodispersity at high to ultra-high frequencies.[3] Lastly, cross-flow devices utilize a T-junction geometry with the DP protruding into the main channel. Droplet sizes generated with T-junction are strongly dependent on the design, and to obtain smaller droplets, one has to downscale the setup leading to higher

---

[7] Reprinted by permission from [IOP Publishing, Ltd]: [Reports on Progress in Physics] [e-Journal] [Droplet based microfluidics, Seemann, Ralf Brinkmann, Martin Pfohl, Thomas Herminghaus et al.], [Order License ID: 1152419-1] (2011)[4]

hydraulic resistance in the system.[3] The possible droplet production frequencies are lower than other geometries, but the fabrication is the most straightforward among droplet microreactors. Finally, this design offers the highest resistance to external physical noise given the microreactor's opposite solid sidewall participating in the droplet generation.[6] After comparing the different geometries, cross-flow devices were used for the droplet generation given their availability and lower-cost production. Furthermore, since proteins and compounds were mixed with a defined concentration, minor variations in droplet sizes did not impact the assay in a significant manner. Moreover, the higher resistance to physical variations enables similar droplet sizes at different temperatures that are beneficial during kinetic measurements, which might require a temperature change.

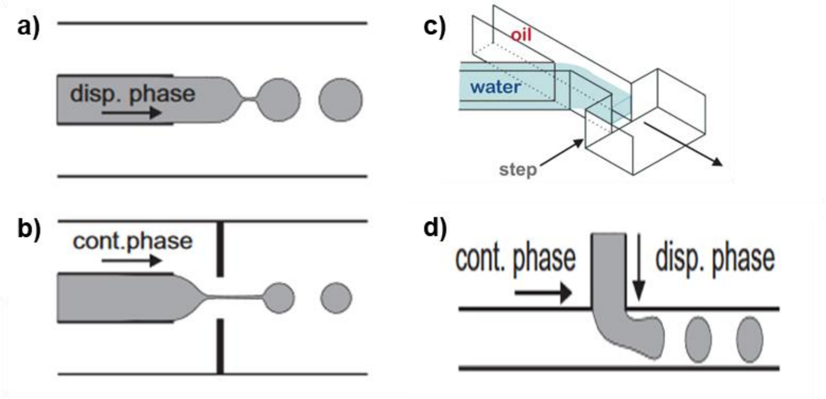

Figure 106: Schematic representation of the most used passive droplet microreactors. A) Co-flow geometry, B) Flow-focusing geometry, C) Step-wise emulsification geometry, D) Cross-flow geometry.[8]

V.1.2 Flow regimes in a cross-flow device

It is crucial to operate the microreactor in the correct droplet generation regime (squeezing, dripping, and jetting) to achieve the best performance regarding droplet size, homogeneity, and generation frequency.[6–8] The main impact factor on the flow regimes is the interaction between shear stress produced by the CP

---

[8] Adapted by permission from [IOP Publishing, Ltd]: [Reports on Progress in Physics] [e-Journal] [Droplet based microfluidics, Seemann, Ralf Brinkmann, Martin Pfohl, Thomas Herminghaus et al.], [Order License ID: 1152419-1] (2011).[4]

and surface tension between the two phases influenced by the variation of flow rates, fluid viscosities, surfactants channel geometry, and wall wettability.

If other physical parameters are constant, then the flow rates' impact on the droplet generation regime can be examined. The squeezing regime is obtained by starting with low flow rates in which the DP enters into the CP's channel, leading to a constant pressure buildup until it blocks the channel completely. At this point, the CP's pressure dominates over the surface tension leading to a pinch-off of the droplet. Thus, the droplet size is nearly independent of other physical properties (Equation 28).

$$\frac{V}{D^3} = 1 + a * \frac{Qd}{Qc}$$

Equation 28: Droplet volume (V) dependency of channel diameter (D) and the flow rates of the dispersed phase (Qd) and continuous phase (Qc) in the dripping regime.

The dripping regime is achieved by further increasing the CP's flow rate compared to DP, thereby increasing viscous drag forces on the droplets. The saddle point is described by the competition of the viscous shear stress and the interfacial tension. During this process, the droplet size depends mainly on the liquids' viscosity ratio, allowing higher variations in the DP's flow rates without strong fluctuations in droplet size.

By further increasing both flow rates, the DP is dragged into the channel leading to a co-flow between the two phases until the breakup into smaller droplets due to the Plateau–Rayleigh instability. This operation mode of the T-Junction microchip is called the jetting regime and results in the lowest droplet monodispersity compared to the other droplet generation formats.[4]

Hence, it is favorable to operate the microreactor in the squeezing or dripping regime.

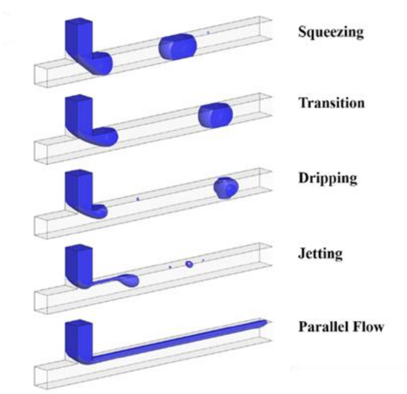

Figure 107:Different flow regimes in a T-junction device. The simulation represents the transition from squeezing, dripping, jetting, and parallel flow. [9]

V.1.3 Impact of surfactants and oils on the droplet generation

The liquids' surface tension is reduced by adding surfactants to the carrier oil, leading to an easier pinch-off at constant shear stress values. If the surface tension between the two liquids is higher than between the DP and the microreactor's hydrophobic wall, then the DP will stick to the channel walls, and a droplet flow will not be generated. Reducing the surface tension too much will lead to viscous forces' domination over the interfacial forces during the droplet generation. Instead of the monodisperse droplet formation at the chip's T-junction, the CP will be pulled into the microreactor, resulting in droplets' formation in the jetting regime. By further reducing the surface tension, a continuous co-flow of two immiscible liquids is created. Therefore, the right concentration and physical properties of the surfactants and the carrier oil are crucial for the system's operation, allowing the correct droplet generation and stabilizing the emulsion by reducing droplet coalescence due to Marangoni forces (Equation 29).

$$\boldsymbol{Ca} \sim \frac{(\boldsymbol{U} * \mu)}{\gamma}$$

Equation 29: Capillary number representing the ratio of viscous stresses to interfacial stresses. U: characteristic velocity, μ: viscosity, γ: interfacial tension

---

[9] Reprinted by permission from AIP Publishing [Physics of Fluids)] [Numerical study of droplet formation in the ordinary and modified T-junctions, Xinlong Li, Liqun He, Yi He, et al], [COPYRIGHT: 5162900878759] (2019).[6]

Fluorinated oils have emerged as an optimal continuous phase for most biochemical applications in droplet format due to their lipo- and hydrophobic properties.[9] The oils' physical properties lead to the reduced solubility of the compounds in the carrier phase, thereby decreasing unwanted droplet cross-talk and compound loss.[10,11] Furthermore, the non lipo- and hydrophobic properties of the droplet surfaces prevent the adsorption of most proteins, increasing the biocompatibility of the assays. Finally, fluorinated oils have higher compatibility with regularly used polymers such as polydimethylsiloxane (PDMS) and an increased permeability for many gases, which is crucial for the encapsulation of aerobic cells.[12]

It is desirable to achieve a substantial population of surfactants at the interface for the maximal interfacial tension reduction and the prevention of other molecules' adsorption to the droplet surface. This can be achieved by changing the relative molecular weight of the surfactants or their morphology. One of the well-known perfluorinated polyether (PFPE) based surfactant PFPE-PEG-PFPE focused on the adaptation to triblock morphology and the relative size of the PFPE unit between 1,500 and 10,000 g/mol.[12] A larger PFPE unit is increasing the anchoring of the surfactant in the fluorinated oil and hence the stability of the emulsion. However, it reduces the mobility of the surfactant, which is crucial for the fast adsorption during droplet generation.[13,14] The PEG head moiety has to be large enough to enable the surfactant's anchoring in the droplet layer. Adsorption of proteins to the surface can also be prevented by choosing the right head for the surfactants. While ionic head structures, alcohols, and carboxylic acids promote the binding of proteins to the surface, neutral ones such as polyethylene glycols and linear polyglycerols reduce it.[9]

Finally, it is necessary to take the critical micelle concentration (CMC) of a surfactant into account. If the CMC is reached, the surfactants will automatically assemble to the micelles, which will retard their ability to bind to the interface. Furthermore, micelles can also transport particles between the water phases through the oil phase leading to increased cross-talk in the system.[11,15]

V.2 Aim of the work

This study aimed to adapt the CAM-mediated HBc capsid assembly assay described in chapter IV to the microfluidic droplet format to terminate unwanted dilution effects after the initial mixing. The implementation of droplet technology required the careful choice and evaluation of several new microreactors (VIM, VIM2b, WCA1b, and Active Droplet Manchip 2) concerning droplet generation, throughput, monodispersity, consumption, reproducibility, and mixing. Comparing the above listed factors the optimal droplet size was found to be the smallest drop that completely fills the canal (SDCC). Furthermore, various fluorinated oils and surfactants were evaluated to find the optimal carrier phase regarding droplet generation, biocompatibility, and stability in the presence of biochemically relevant additives. After defining optimal conditions, the reproducibility of TAD dilutions in droplets was confirmed, and initial tests have been performed with CAM-mediated HBc assembly.

V.3 Methods

Table 32: Overview of materials used in chapter V.

	Chemicals/ equipment	**CAS number, industry, article number**
Chemicals	FITC	Merck, Buchs, Switzerland CAS: 518-47-8
	Na_3PO_4 pH 8.0	Merck, Buchs, Switzerland CAS: 10101-89-0
	Ethanol	Merck, Buchs, Switzerland CAS: 64-17-5
	DMSO	Merck, Buchs, Switzerland CAS: 67-68-5
	Detergent with Lipase	IPHT, Jena, Germany Spee Color, Henkel
	5,6-Carboxyfluorescein	CAS: 72088-94-9
	Albumin-FITC	ThermoFischer SCIENTIFIC GmbH, Darmstadt, Germany
	Fluorescein-Dextran	Merck, Buchs, Switzerland CAS:60842-46-8
	50 mM HEPES buffer ph 7.4	Merck, Buchs, Switzerland CAS: 7365-45-9
	NaCl	Merck, Buchs, Switzerland CAS: 7647-14-5
	Tetradecane	Merck, Buchs, Switzerland CAS: 629-59-4
	Span 20	Merck, Buchs, Switzerland CAS: 1338-39-2
	FC770	Merck, Buchs, Switzerland CAS: 86508-42-1
	PFPE-PEG-PFPE	CYTONIX, Belstville, USA
	FluoroN	CYTONIX, Belstville, USA
	Rose bengal	Merck, Buchs, Switzerland CAS: 4159-77-7
	Selvita-1399-025	Synthesized as described in Corcuera et al.[16]
	AT130	Synthesized as described in Corcuera et al.[16]
	NVR-3-778	Synthesized as described in Corcuera et al.[16]
	JNJ 56136379	Merchachem, Nijmegen, Netherland. [16,17]
	BAY 41-4109	Synthesized at Bayer AG Wuppertal Germany [18]
	GLS4	Synthesized at Vandyck [19]
	JAKL11-034-2	AiCuris Anti-infective Cures AG, Wuppertal, Germany
	JAKL11-076-1	AiCuris Anti-infective Cures AG, Wuppertal, Germany
	MABR13-005	AiCuris Anti-infective Cures AG, Wuppertal, Germany
	CP150-BO (3 μM)	Expressed, purified, and labeled at AiCuris Anti-infective Cures AG, Wuppertal, Germany
Tubings	Rotilabo®-silicone tubes OD 3 mm, ID 1 mm	Analytics Shop, Munich, Germany Catalog number: 9556.1
	Tubing, PFA, 1/16 x 1.0 mm ID	Analytics Shop, Munich, Germany SN: JR-T-4007-M3
	Tubing, PFA, 1/16 x0.75 mm ID	Analytics Shop, Munich, Germany SN: JR-T-4002-M3

	Tubing, PFA, 1/16 x0.50 mm ID	Analytics Shop, Munich, Germany SN: JR-T-4001-M3
	Tubing, PFA, 0.2 mm ID, 1.6 mm od	Analytics Shop, Munich, Germany SN: AGG1833-65573
	Tubing, PTFE, 2.0 x 1.70 mm	Analytics Shop, Munich, Germany SN: JR-T-6801-M3
	PEEK-Tubing 1/16” OD x 0.13 mm ID	SCP Seitz Chromatographie Produkte GmbH, Weiterstadt, Germany SN: 41.159.013.01
	PEEK-Tubing 1/16” OD x 0.25 mm ID	SCP Seitz Chromatographie Produkte GmbH, Weiterstadt, Germany SN: 41.079.025.00
	PEEK-Tubing 1/16” OD x 1.4 mm ID	Klaus Trott Chromatographie-Zubehör; Kriftel, Germany SN: 082530020
	Membranfilter hellrot; PVDF 0.2 µm	Analytics Shop, Munich, Germany Catalog number: 9556.1
Fluigent flow system	Fluigent low-pressure Generator (FLPG, pressure source)	FLUIGENT, Jena, Germany item number: FLPG003
	Flow EZ$^{\text{TM}}$ 1,000 mbar (Pumps) (X 4)	FLUIGENT, Jena, Germany, item number: LU-FEZ-1000
	Flow rate sensor L (X 3)	FLUIGENT, Jena, Germany, item number: FLU_L_D
	Flow rate sensor M (X 2)	FLUIGENT, Jena, Germany, item number: FLU_L_M
	Flow rate sensor S (X 2)	FLUIGENT, Jena, Germany, item number: FLU_L_S
	High flowrate connection kit	FLUIGENT, Jena, Germany, item number: CTQ_KIT_HQ
	Low flowrate connection kit	FLUIGENT, Jena, Germany, item number: CTQ_KIT_LQ
	Reservoirs (2x50 ml, 1x15 ml)	FLUIGENT, Jena, Germany, item number: P-CAP15_HP, P-CAP50_HP
	Rack for P-caps	FLUIGENT, Jena, Germany, item number: P-Cap_Rack
	LineUP logistic kit	FLUIGENT, Jena, Germany, item number: LU-SPK-0001
	L-Switch$^{\text{TM}}$	FLUIGENT, Jena, Germany
	Switch board, ESS Platform	FLUIGENT, Jena, Germany
	L-Switch connection kit	FLUIGENT, Jena, Germany
	Bubble traps	FLUIGENT, Jena, Germany
	5 ml pointed, high-pressure glass reservoirs	Custom made
CETONI	ROTAX 360 LHS	CETONI GmbH, Korbußen, Germany CETONI_ROTAXYS 360 LHS
	neMESY low-pressure syringe 100 µl	CETONI GmbH, Korbußen, Germany CETONI_ neMESY Low-Pressure
AMF technologies	OEM RVM Microfluidic Electric Rotary Valve	AMF ANDREAS MAIER GmbH & Co. KG, Fellbach, Germany SN: V-D-1-12-050-C-U
Check valves	Fluigent check-valve	FLUIGENT, Jena, Germany
	CV-3000 inline Cartridge check valve	IDEX Europe GmbH, Erlangen Germany

	Swagelok Checkvalve	Best Fluid Systems GmbH | Swagelok, Hamburg, Germany
Elveflow	OptoReader	Elveflow microfluidic flow control, Paris, France FDG_ELV_OPR-01 (No longer available)
Combo kit	Vici Easy-Flange Combi Kit in Plastic	FLUIGENT, Jena, Germany Case 201539, Lab Unlimited
Optical readout	Dolphin F145C	Allied Vision Technologies, Stadtroda, Germany SN:06/00-00425990 AN: 20050413
	acA 1920-40 µm	Basler AG, Ahrensburg, Germany ID 106909 S/N 22308043
Microfluidic chips	µ-Slide VI 0.1	ibidi GmbH, Gräfelilfing, Germany
	µ-Slide VI 0.5	ibidi GmbH, Gräfelilfing, Germany
	Active Droplet Manchip 2	ibidi GmbH, Gräfelilfing, Germany
	VIM2 (droplet)	IPHT, Jena, Germany
	VIM2b (droplet)	IPHT, Jena, Germany
	WCA1b (droplet)	IPHT, Jena, Germany
	ROSAR GF-T75 (mixing)	IPHT, Jena, Germany
	HTM-ST3-1	LTF, Wasserburg, Germany
	3D-Serpentine microreactor	Microfluidic ChipShop, Jena, Germany

The HBc expression, purification, and labeling was executed as described in II.3 Methods while compounds were obtained as noted in IV.3.1 Reference compounds. Finally, the microfluidic system was setup as described in III.4 Results and Discussion except for the droplet flow microreactors.

V.3.1 Equilibration of the microreactor and system setup

One end of the PTFE Teflon tubes (OD 1/16 "ID 0.5 mm) was sleeked and possible pollutions were removed by using a 4-bar air pressure pistol. The microreactor was mounted into the holder, evenly connecting the chip's inlets to the Teflon tubes. PEEK tubes from the respective reservoirs were connected to the PTFE Teflon tubes using a short silicon tube with an inner diameter of 0.5 mm. Next, the air was removed from the chip to prevent pulsation and irregular droplet formation by filling it with the continuous phase. Needles were used to close the respective outlets as soon as they were filled with liquids. Following the initial equilibration, the disperse phase (DP) flow was started.

Three pressure pumps were connected to the respective reservoirs with PEEK tubing with a length of 0.5 m and an inner diameter of 0.13 mm or 0.25 mm. PFA tubing with an inner diameter of 0.5 mm was used for all the rest of the connections. To prevent backflow of the liquids into different reservoirs, corresponding check valves were installed into the system. Pictures and videos were taken using a PCE-MM200 Microscope or Iphone5SE (slow motion), and fluorescence spectra were recorded using the OptoReader (Figure 108).

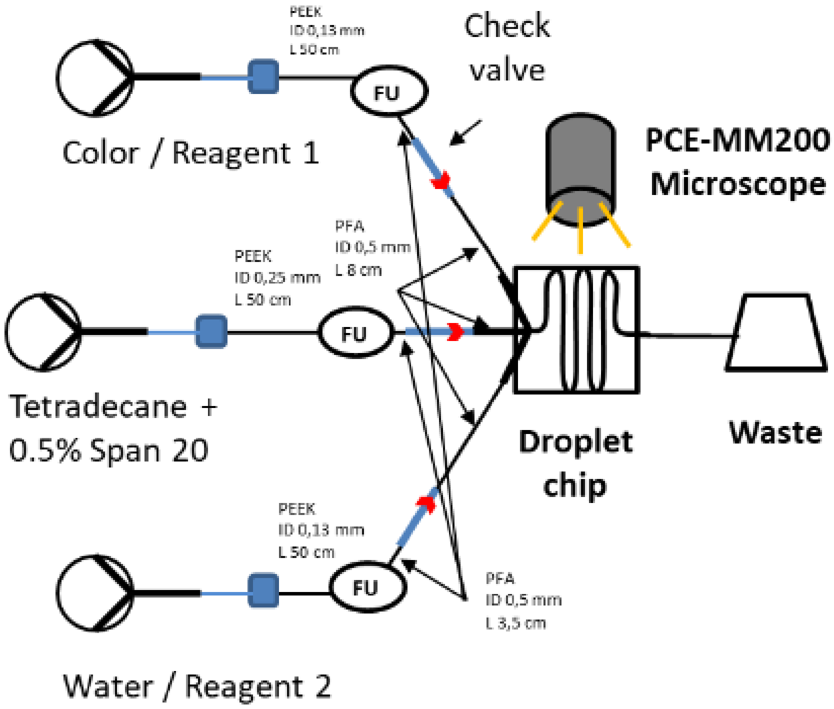

Figure 108: Scheme of the flow system for droplet generation. Pump 1 and 3 were utilized for DP, which contained the reagents and water-based liquids, while pump 2 generated the flow for the CF (Teradecane +0.5 % Span 20 or FC770 +2.4 % PFPE-PEG-PFPE) needed for the compartmentalization of the DP. Check valves (red arrows) were installed after the flow units to prevent the backflow of the liquids. VIM2 and VIM2b (figure 19) were utilized as droplet microreactors. Data was captured with a PCE-MM200 microscope. Legend for the various units is depicted in Figure 30.

V.3.2 Equilibration of the CF flowrates

Since the generation of a droplet flow from two immiscible liquids results in higher backpressure, the adequate pressure generated by the pumps must be regulated during the generation of droplets by the respective flow units. Therefore, the reactions have to be controlled over the measured flow rates instead of just applying a general pressure. For the calibration of the flow units H_2O or isopropyl alcohol can be used since these fluids generally cover most of the liquid viscosities used in biochemical systems. The flow rates of different liquids were collected and measured to verify that there is no substantial deviation between displayed and measured flow rates. The solvents used in the biochemical assay and the tetradecane with 0.5 % SPAN 20 needed for droplet generation had a high correlation between the measured and displayed values and did not require further corrections. This was only necessary for the fluorinated oil FC770, which had a linear correlation between the true volumes and sensor volume outputs for higher flow rates but a polynomial correlation at lower flow rates (III.4.1 Flow generation and control).

V.3.3 Salts and additives used in droplet microfluidics

The droplet stability and monodispersity were evaluated in the presence of biochemical relevant additives and NaCl in a FC770 + 2.4 % PEG-PFPE-PEG carrier phase (Table 33).

Table 33: Different oils, surfactants, and additives tested evaluated for the droplet generation.

Oil	**Surfactant**	**Additions to disperse phase**
Tetradecane	0.005 % Span 20	H_2O
	0.05 % Span 20	H_2O
	0.5 % Span 20	H_2O
		H_2O + 150 mM NaCl
		H_2O + 300 mM NaCl
Fluorinert™ FC-770	0.28 % PFPE-PEG-PFPE PFPE 5K, PEG 900, PFPE 5K	H_2O
		H_2O + 150 mM NaCl
		H_2O + 300 mM NaCl
	0.6 % PFPE-PEG-PFPE PFPE 5K, PEG 900, PFPE 5K	H_2O
	1.2 % PFPE-PEG-PFPE PFPE 5K, PEG 900, PFPE 5K	H_2O
		H_2O + 600 mM NaCl + 0.5 % FluoroN
	2.4 % PFPE-PEG-PFPE PFPE 5K, PEG 900, PFPE 5K	H_2O
		H_2O + 600 mM NaCl
		H_2O + 0.5 % FluoroN
		H_2O + 600 mM NaCl + 0.5 % FluoroN
	3.4 % PFPE-PEG-PFPE PFPE 5K, PEG 900, PFPE 5K	H_2O
		H_2O + 600 mM NaCl

V.4 Results and Discussion

V.4.1 Evaluation of droplet generation in different microreactors

V.4.1.1 Impact of Chip design on the droplet's size

The design and materials of the microreactors are of utmost importance, as they have an impact on the droplet's size and generation, which in turn influences the assays throughput, dynamic range, accuracy, mixing, and the reagents consumption.[4,20] Furthermore, the quality and cost of a microreactor were considered, which depends on its manufacturing, such as glass micromachining, polymer-based molding replication, modular assembly, and 3D printing.[3] In this chapter, three different chip materials were compared: Glass, Polycarbonate, and Cyclic olefin copolymer. While polymer chips from polycarbonate are cheaper than glass ones, they usually have lower optical transparency combined with higher fragility; wherefore, this material was disregarded after early attempts. On the other hand, cyclic olefin-based polymers showed high durability compared to polycarbonate and had a simple production leading to economic benefits (Figure 109).

Figure 109: Active Droplet Manchip 2 Assay chip with respective inlets and outlet. The chip has an overall length of 2.28 m and a dual-channel spacing of 600 µm

For the final experiments, glass microreactors were utilized given their superior transparency leading to the highest S/N and S/B ratios. The original VIM2 and VIM2b microreactors had a short channel. Therefore, flow rates had to be reduced to enable an adequate residence time above 30 s for the biochemical assay. This issue was later circumvented using WC1Ab having a residence time of 10 min even at higher flow rates. All the above-described microreactors utilize T-junctions for droplet generation. Hence the droplet size is mainly dependent on the size of the junction itself (Figure 110).[21]

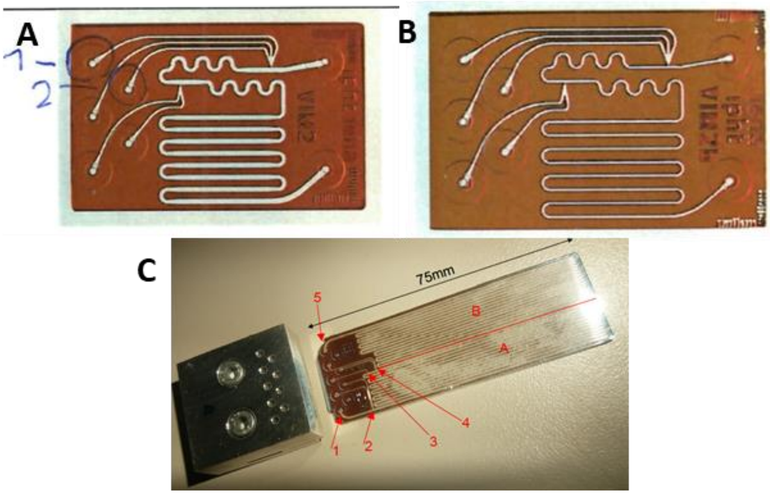

	VIM 2	VIM 2b	WCA1b
Microreactor lengths from droplet generation until exit	119.5 mm	119.5 mm	2553 mm
Channel width	0.3 mm	0.04 mm	0.04 mm
Channel depth	0.26 mm	0.26 mm	0.26 mm
Volume	7.6 µl	7.6 µl	162 µl
Specific features	Serpentine structure for mixing Two dosing nozzles	Serpentine structure for mixing Two dosing nozzles	Two dosing nozzles Elongated channel
Approximate maximal residence time at a flow rate of 24 µl/min	19 s	40 s	405 s

Figure 110: Glass microreactors used to generate a droplet flow. VIM 2 (**A**) had an overall size of 16 x 25 mm and a channel size of 300 x 150 µm. VIM 2b (**B**) was tighter than CIM2 with an overall size of 16 x 25 mm and a channel size of 40 x 150 µm. Finally, WCA1b (**C**) had a similar channel size as VIM2b but with a larger inner volume allowing measurements of later kinetics.

In order to evaluate the optimal droplet size and droplet generation as a function of the microreactors parameters, various experiments were conducted using tetradecane + 0.5 % Span 20 as CF. The DP was stained using bromophenol blue to visualize the process. Initial observations highlighted the importance of the system's equilibration prior to measurements considering the distance between the droplets changed until the whole reservoir was filled. The droplet frequency decreased during the equilibration process resulting from an increase in Laplace pressure built up with each droplet (Figure 111).[4]

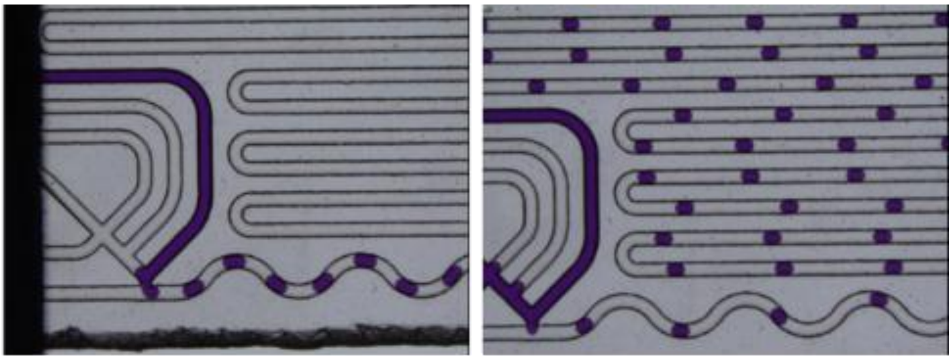

Non equilibrated system

Equilibrated system

Figure 111: Equilibration of Active Droplet Manchip 2 by injecting the colored DP to the CF (Tetradecan + 0.5 % Span 20). Pumps were set to condition A (Compare to Figure 135).

Depending on the flow conditions, different-sized droplets were formed. Hence, the faster the DP flow was compared to the continuous phase, the bigger the droplet sizes were. On the other hand, increasing the flow rate of both phases with the exact multiples resulted in identical droplet size with increased overall flow speed (Figure 111 and Figure 135). In the next experiments, the droplet generation in the jetting regime was defined in the VIM 2 microreactor. A linear correlation is measured between the DP's flow rates and the resulting droplet size at a constant CP's flow rates. However, the droplet generation showed variations between measurements, especially at higher flow rates, due to the droplet generation in the jetting regime of the VIM 2 reactor (Figure 112 and Figure 113).

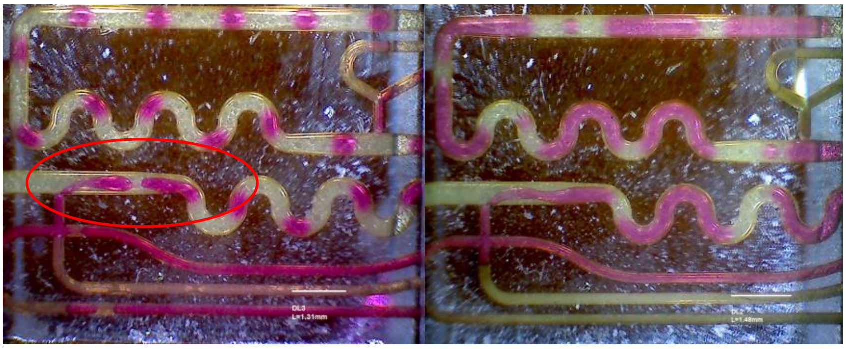

Figure 112: Generation of droplets during the first (left picture) and second (right picture) experiment. Droplet generation occurred in the jetting region (red marked area).

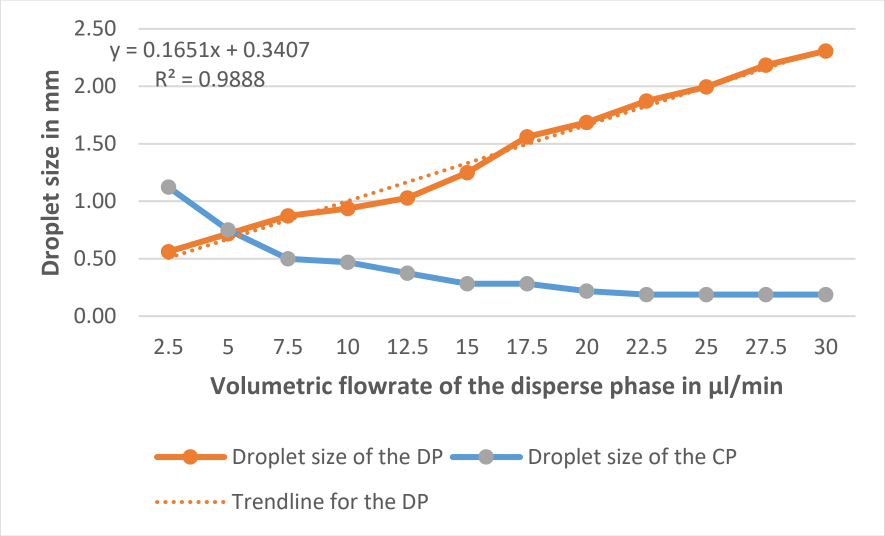

Figure 113: Correlation between droplet size and flow rate of the DP. Tetradecane with 0.5 % Span 20 was used as CP with a 10 ml/min constant flow rate. The flow rate of the DP (Bengal red water solution) was increased in increments of 2.5 µl/min. The sizes of the DP (Series2) and CP are depicted on the y-axis.

The microreactors must be operated in the dripping region to generate monodisperse and reproducible droplet sizes. Therefore, different CP and DP flow rates were screened to define the droplet generation region within the dripping zone. The state diagram (Figure 114) depicts the measured transition line from dripping to jetting for the VIM2 microreactor.

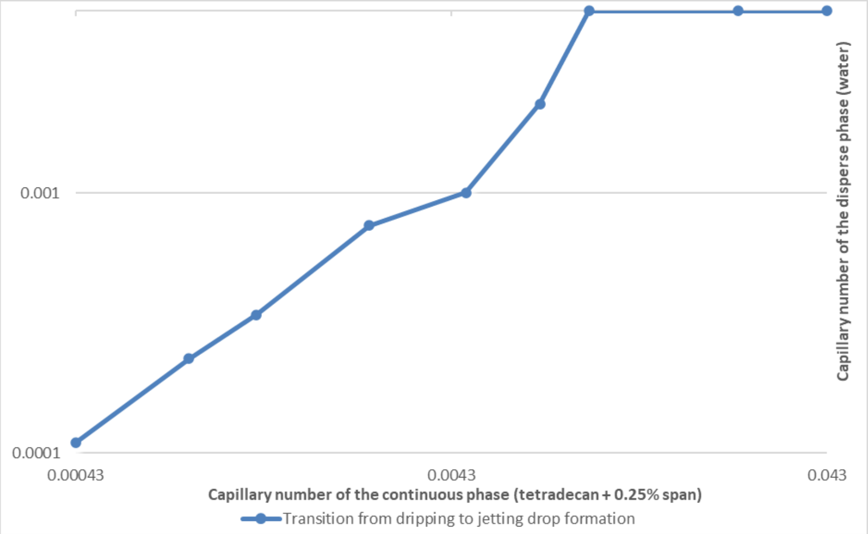

Figure 114: State diagram of the dripping to jetting transition in the VIM2 microreactor as a function of the capillary number of the CP (Tetradecane + 0.5 % Span 20) and the DP (water). Blue dots mark the last point in the dripping region for the given system. Increasing the flow rate above this curve leads to jetting and polydispersity.

In the ripping regime, the reproducibility of droplet sizes was evaluated as a function of the flow rates on three independent days, which showed a high reproducibility at higher CP flow rates (24 µl/min and higher). However, especially at lower flowrates, a substantial reduction in the droplets' sizes was observed during day three due to a change in the chips' surface characteristics. The hydrophobic layer was damaged over time, leading to the attachment of droplets to the wall. Therefore, the coating with PlusOne Repel-silane had to be repeated weekly (Figure 115). Finally, the droplet generation frequency and actual residence times were determined (Figure 136).

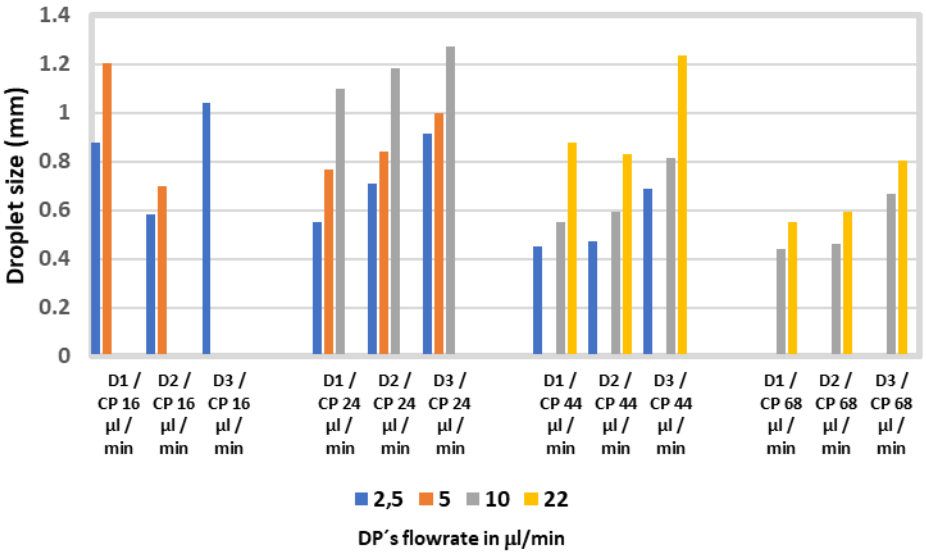

Figure 115: Reproducibility of the droplet sizes in the VIM2 microreactor. Three independent measurements of the CP's flow rates are grouped on the x-axis, respectively. The legend represents the DP's flow rate in µl/min. On the Y-axis, the droplet's size is depicted as the arithmetic mean of 10 droplets in mm.

After the extensive screening of the VIM2 microreactor, the droplet chip VIM2b was evaluated. This unit had a much lower mash width of 40 µm compared to VIM2 with 300 µm. The narrower channel design allows the DP to reach the opposing channel wall faster during droplet generation, resulting in a pinch-off of the droplets at smaller droplet volumes. As with VIM2, the droplet size was evaluated as a function of the flow rates on three independent days. In contrast to the VIM 2 reactor, VIM 2b's droplet generation was performed most of the time in the squeezing instead of the dripping regime. As a result, the droplet generation in the VIM 2b showed a significantly higher droplet monodispersity, especially at higher flow rates compared to the VIM2 microreactor (Figure 116).

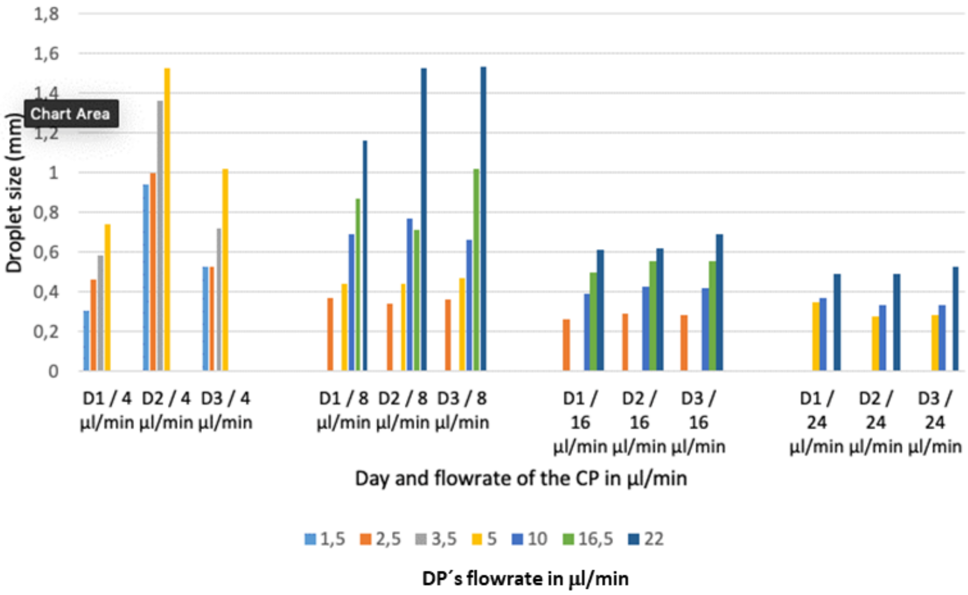

Figure 116: Reproducibility of the droplet sizes in the VIM2b microreactor. Three independent measurements of the CP's flow rates are grouped on the x-axis, respectively. The legend represents the DP's flow rate in µl/min. On the Y-axis, the droplet's size is depicted as the arithmetic mean of 10 droplets in mm.

In conclusion, in both microreactors, a direct correlation was observed between the droplet size and the flow rates in a reproducible manner. VIM2b outperformed VIM in droplet monodispersity, but had a lower inner volume and, therefore, a limited dwell time. The best results were obtained with WCA1b, which had the same droplet reproducibility as VIM2b but an overall microreactor length of around 2,553 mm, allowing the measurements of reactions with residence times up to 10 min.

V.4.1.2 Impact of different surfactants on droplet size

For the HBc assembly assay, it is crucial to prevent CP150-BO dimers' adsorption to the droplet interface, which would impair a regular capsid assembly. Therefore, aside from the initially used tetradecane + Span 20 system, alternative carrier fluids based on fluorinated oils and surfactants were evaluated. The most promising solution was the fluorinated oil FC770, which mixed with different concentrations of PFPE-PEG-PFPE showed high biocompatibility in literature.[12,22,23] As for the ideal PFPE-PEG-PFPE concentration for droplet generation, various values between 1.8 and 2.2 %(wt/wt) were described previously.[24] At the same time, the CMC concentration for PFPE-PEG-PFPE surfactant was around 0.05 %.[22] This value should not exceed too much to prevent the aggregation of the surfactants in micelles which would deplete the active surfactant concentration during the compartmentalization.

In the microfluidic setup using the VIM2 microreactor, the lowest concentration of PFPE-PEG-PFPE needed for a stable droplet generation was 2.4 % (Table 34). Therefore, in future experiments, the fluorinated oil FC770 was used with 2.4 % PFPE-PEG-PFPE for optimal droplet monodispersity and biocompatibility.

Table 34: Droplet generation in the VIM 2 microreactor as a function of the PFPE-PEG-PFPE concentration.

Surfactant concentration	**Droplet generation**
FC 770 + 0.3 % PFPE-PEG-PFPE	Droplets were not stable
FC 770 + 0.6 % PFPE-PEG-PFPE	Droplets generation in the jetting regime
FC 770 + 1.2 % PFPE-PEG-PFPE	Droplet generation in the jetting regime
FC 770 + 2.4 % PFPE-PEG-PFPE	Droplet generation in the dripping regime at lower flowrates
FC 770 + 3.4 % PFPE-PEG-PFPE	Droplet generation in the dripping regime.
FC 770 + 3.4 % PFPE-PEG-PFPE / 600 mM NaCl	Droplet generation in early jetting regime.

V.4.1.3 Impact of further additives on the droplet dispersity and size

In the next step, the addition of assay-relevant buffers and salts were evaluated to measure their impact on the droplet size, generation, and monodispersity (Table 33).

The effects of inorganic ions on the surface tension, droplet generation, and droplet stability are complicated and had to be evaluated before the assay implementation. In the initial tetradecane Span 20 system, the optimal surfactant concentration was around 0.5 % Span 20. Reducing the concentration of the surfactant any further leads to unstable droplets adsorbing to the channel walls. As expected, the addition of 300 mM NaCl to the DP at a surfactant concentration of 0.5 % decreased the surface tension leading to the generation of polydisperse droplets in the jetting regime. This experiment showed that the Tetradecane + 0.5 % Span system cannot tolerate increased NaCl concentrations and is not suitable for the biochemical assay (Figure 117).

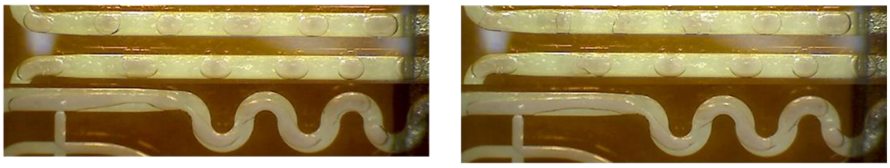
A) Tetradecane + 0.05 % Span20 / H_2O

B) Tetradecane + 0.05 % Span20 / H_2O (4 seconds after stopping flow

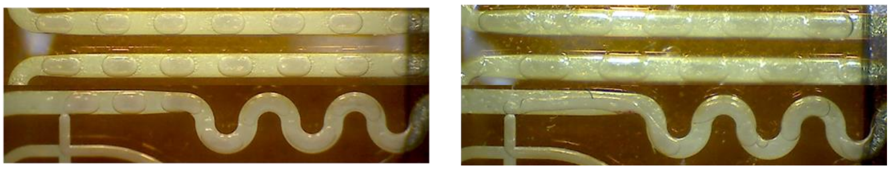
C) Tetradecane + 0.5 % Span20 / H_2O

D) Tetradecane + 0.5 % Span20 / H_2O + 300 mM NaCL

Figure 117: Droplet generation in the VIM2 microreactor using tetradecane with different concentrations of Span 20 and NaCl. Flowrates during measurement were: CP: 12 µl/min, DP: 18 µl/min. A) Tetradecane + 0.05 % Span 20/ H_2O; droplet generation in the jetting regime with a high variation in droplet sizes. **B)** Tetradecane + 0.05 % Span 20/ H_2O 4 s after stopping the flow; Droplets were not stable and adsorbed to the channel wall. **C)** Tetradecane + 0.05 % Span 20/ H_2O; Droplet generation in the dripping regime, monodisperse droplets. **D)** Tetradecane + 0.05 % Span 20/ H_2O + 300 mM NaCl; Droplet generation in the jetting regime, variation between droplet sizes.

Likewise, the fluorinated oil FC 770 was tested with different surfactant concentrations PFPE-PEG-PFPE to find the optimal conditions for droplet generation. Besides PFPE-PEG-PFPE, a one-tailed surfactant, 0.5 % FluoroN 2900, was evaluated with the FC770 as well. A surfactant with reduced molecular weight could populate the droplet interface faster during droplet generation, thereby preventing the HBc's potential absorption to the surface. However, FluoroN 2900 alone was not sufficient to generate droplets. Furthermore, the addition of 0.5 % FluoroN to the mixture FC770 with 2.4 % PFPE-PEG-PFPE led to decreased surface tension shown by the spontaneous coalescence of droplets after stopping the flow. The reduced surface stability could facilitate droplet-droplet coalescence and thereby the postponed addition of further reagents in a secondary inlet (Figure 118).

A) FC 770 / H_2O + 0.5% FluoroN

B) FC 770 + 1.2% PFPE-PEG-PFPE / H_2O + 0.5% FluoroN + 600 mM NaCl

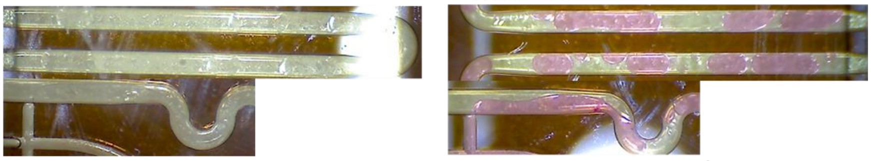

C) FC 770 + 2.4% PFPE-PEG-PFPE / H_2O + 0.5% FluoroN

D) FC 770 + 2.4% PFPE-PEG-PFPE / H_2O + 0.5% FluoroN + 600 mM NaCl

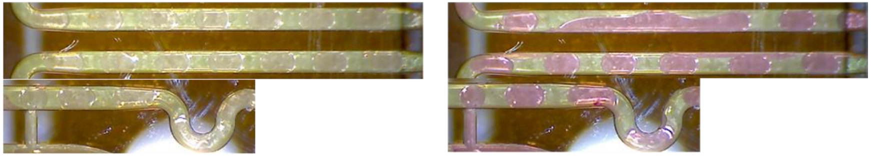

E) FC 770 + 3.4% PFPE-PEG-PFPE / H_2O + 0.5% FluoroN

F) FC 770 + 3.4% PFPE-PEG-PFPE / H_2O + 0.5% FluoroN + 600 mM NaCl

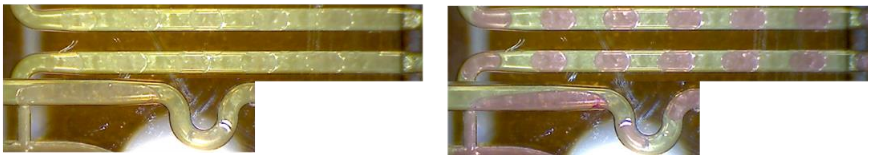

Figure 118: Droplet generation in the VIM2 microreactor using FC770 with different concentrations of PFPE-PEG-PFPE, NaCl and FluoroN. Flowrates during measurement were CP: 12 µl/min, DP: 12 µl/min. A) FC770/ H_2O + 0.5 % FluoroN; Droplets were not formed. **B)** FC770 + 1.2 % PFPE-PEG-PFPE / H_2O + 0.5 % FluoroN; Droplet formation in the jetting regime with high variation in droplet sizes. **C)** FC770 + 2.4 % PFPE-PEG-PFPE/ H_2O + 0.5 % FluoroN and **D)** FC770 + 2.4 % PFPE-PEG-PFPE/ H_2O + 600 mM NaCl +0.5 % FluoroN; Droplet formation in the dripping regime leading to highly monodisperse droplets. Droplets spontaneously coalescence after stopping the flow. **E)** 3.4 % PFPE-PEG-PFPE/ H_2O + 600 mM NaCl +0.5 % FluoroN **F)** FC770 + 3.4 % PFPE-PEG-PFPE/ H_2O + 600 mM NaCl; Droplet generation in an early jetting regime with monodisperse droplets.

Using the original 2.4 % PFPE-PEG-PFPE system, even concentrations of up to 600 mM NaCl were tolerated regarding the droplet generation (Figure 119 and Figure 120). Therefore, the FC770 carrier oil was utilized with 2.4 % PFPE-PEG-PFPE for the droplet generation due to its resistance to high NaCl concentrations.

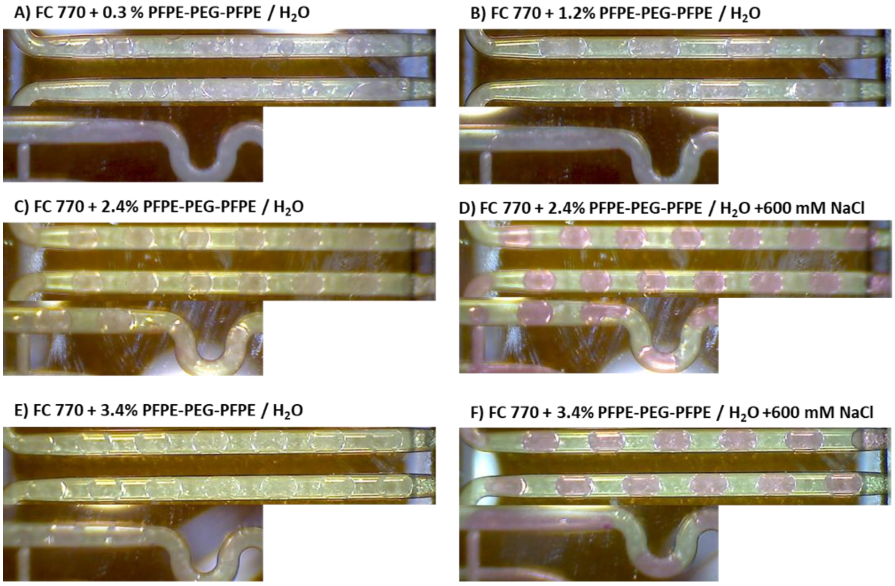

Figure 119: Droplet generation in the VIM2 microreactor using FC770 with different concentrations of PFPE-PEG-PFPE and NaCl. Flowrates during measurement were: CP: 12 µl/min, DP: 12 µl/min. **A)** FC770 + 0.3 % PFPE-PEG-PFPE/ H_2O; Droplets were not formed. **B)** FC770 + 1.2 % PFPE-PEG-PFPE/ H_2O; Droplet formation in the jetting regime with variation in droplet sizes. **C)** FC770 + 2.4 % PFPE-PEG-PFPE/ H_2O, **D)** FC770 + 2.4 % PFPE-PEG-PFPE/ H_2O + 600 mM NaCl and **E)** FC770 + 3.4 % PFPE-PEG-PFPE/ H_2O; Droplet formation in the dripping regime leading to highly monodisperse droplets. **F)** FC770 + 3.4 % PFPE-PEG-PFPE/ H_2O + 600 mM NaCl; Droplet generation in an early jetting regime with monodisperse droplets.

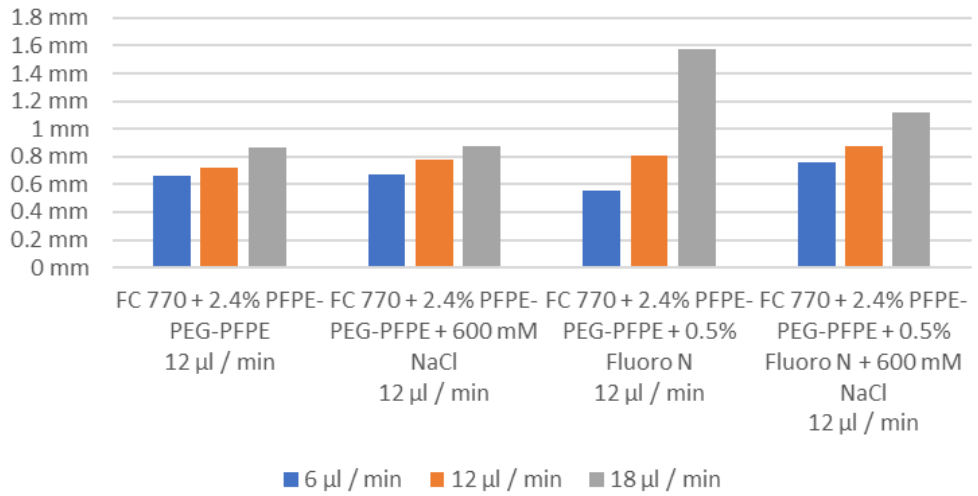

Figure 120: Droplet size as a function of different additives and the flow rate of the CP (legend) in µl/min in the VIM2b microreactor. H_2O was compartmentalized in FC770 + 2.4 % PFPE-PEG-PFPE as the standard. The addition of 600 mM NaCl to the water phase did not change the droplet sizes, validating that FC770 + PFPE-PEG-PFPE displayed a higher salt tolerance than tetradecane + Span 20. The addition of Fluoro N, a further surfactant, to the CP reduced the droplet surface tension leading to the coalescence of droplets, especially at higher flowrates.

V.4.2 Mixing in droplet flow format

One of the microfluidic systems' essential benefits is the rapid mixing of compounds within ms due to the turbulent flow inside the plug resulting from the Taylor flow around the droplets combined with specific microreactor patterns.[1,2,25] To highlight mixing efficiency in the here described microreactors experiments with colorized indicator solutions were designed. As for the negative control, 0.5 % phenolphthalein in 20 mM HEPES (pH 9) was coinjected with 0.1 M HCl, resulting in the decoloration from a deep purple to a transparent liquid post mixing after complete mixing. First, the two water-based liquids were introduced with a flow rate of 18 µl/min resulting in a laminar co-flow due to the low Re number. Owning to the laminar flow, mixing was driven purely by radial diffusion and occurred after around 6.9 mm, which equals a residence time of around 1 s in the VIM2 microreactor (Figure 121).

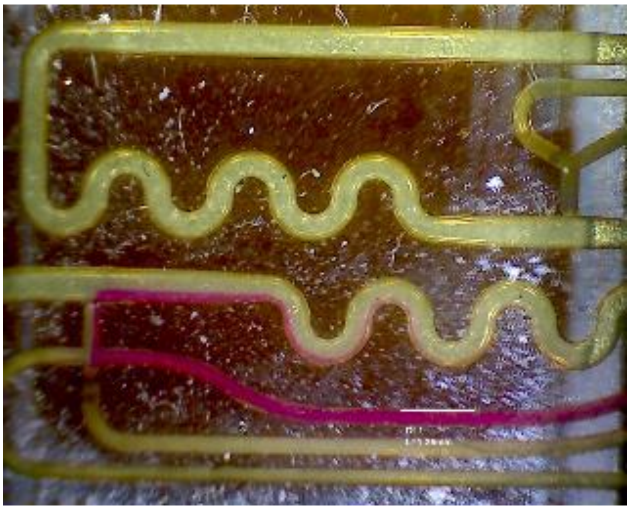

Figure 121: Laminar co-flow of 0.5 % phenolphthalein in 20 mM HEPES (pH 9) and 0.1 M HCL in the VIM2 microreactor. Radial diffusion leads to mixing the two water phases under 1 second, leading to the protonation and thereby discoloration of phenolphthalein.

In the second experiment, additionally to the water phase, tetradecane + 0.5 % Span 20 was injected with a flow rate of 48 µl/min resulting in droplet formation. The glass microreactors were fabricated with a short serpentine structure directly after droplet generation to enhance the mixing in droplets by introducing turbulence.[26] Tayler flow around the droplets resulted in fast mixing within the droplets after a travel time of only 3 mm, or a residence time of under 150 ms (Figure 122).

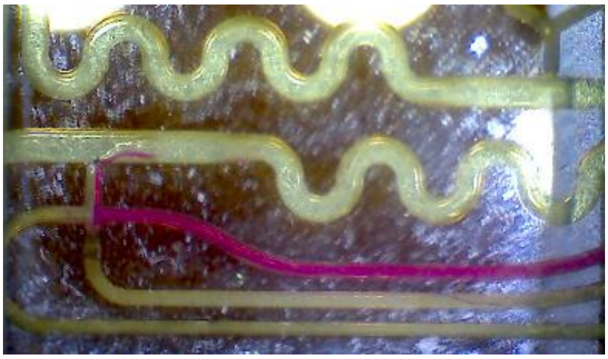

Figure 122: Droplet formation with tetradecane + 0.5 % Span 20 as the CP and a mixture of 0.5 % phenolphthalein in 20 mM HEPES (pH 9) and 0.1 M HCL as the DP in the VIM2 microreactor. Taylor dispersion leads to the fast mixing (<150 ms) of the two water phases, leading to phenolphthalein's protonation and discoloration.

This experiment was repeated using a high-resolution camera of a 5SE iPhone with 200 frames per second and mixing 0.67 mM $Fe(NO_3)$ and 2 mM KSCN within droplets to have higher accuracy.[123] The diffusion of these complexes resembles the actual diffusion time better than acid-base reactions, which can be misleading due to the fast proton travel. Mixing time in the droplets was estimated by the color change from a light yellow to an intense red and was calculated by dividing the traveled distance (from T-junction to complete mixing) by the channel's middle flow rate and allowed the calculation of rapid mixing in droplets within ms (Figure 124).

Figure 124: Mixing of 0.67 mM Fe(NO3) and 2 mM KSCN in droplets in tetradecane with 0.5 % SPAN 20. Droplet generation was recorded with 200 frames per second using the mobile camera of an iPhone 5 SE.

V.4.3 Encompertimentalization of TAD diluted FITC in droplets

After the previously listed evaluations of the different microreactors, surfactants, and additives, the TAD mediated dilution curve of fluorescein (3 µM) dispersed in FC770 + 2.4 % PFPE-PEG-PFPE was recorded with the following setup (Figure 125).

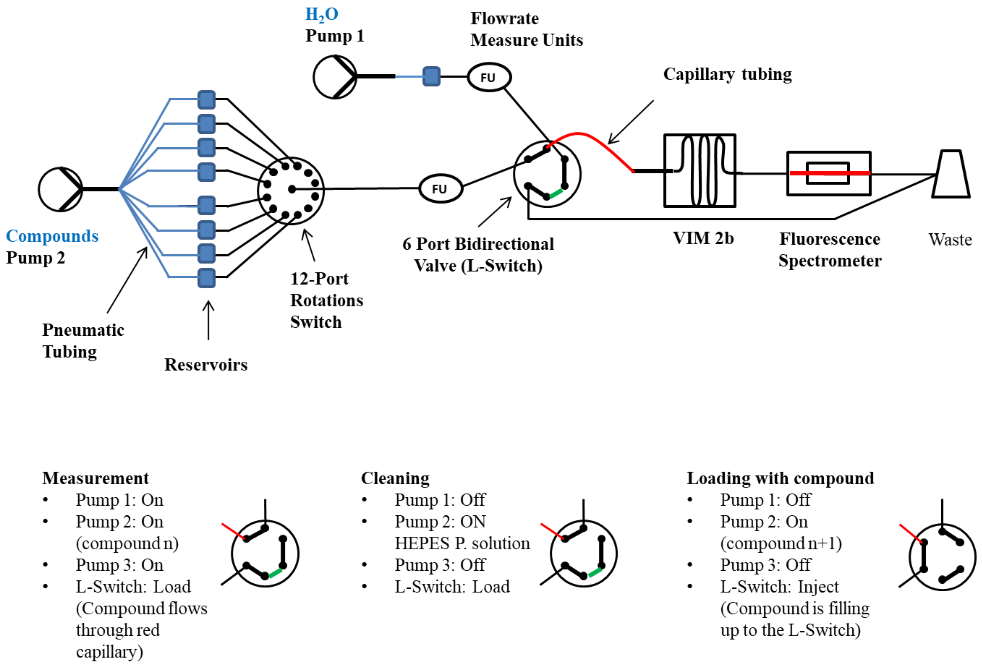

Figure 125: Schematic representation of the microfluidic system used for inflow compartmentalization of TAD diluted FITC. Following the initiation, pump 2 was set to the same flow rate as pump 1, and the L-Switch turned to the On-position. This led to the TAD of the FITC's compound margin in the designated (red) capillary and its subsequent mixing with the CP150-BO protein in the droplet microreactor. After the measurement, the system was cleaned with H_2O using pump1 and pump 2 switched to the respective reservoir. Legend for the various units is depicted in Figure 30.

The compartmentalization was successful and reproducible confirmed by four independent measurements including a version without droplet generation (Figure 127) with three technical replicates (Figure 126), respectively.

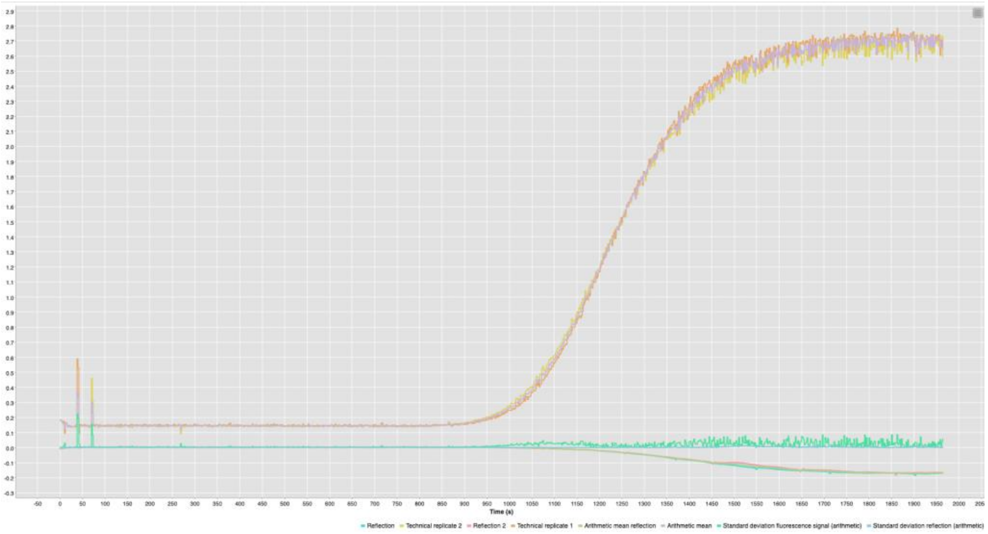

Figure 126: Three technical replicates of TAD mediated dilution of fluorescein (3 µM) (yellow, purple, and orange) dispersed in tetradecane + 0.5 % SPAN.

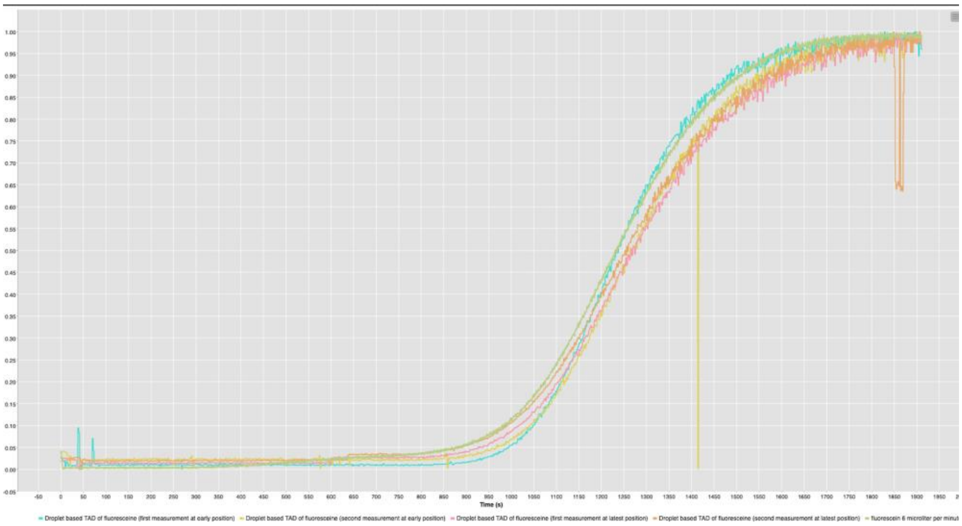

Figure 127: Four independent measurements of TAD mediated dilution of fluorescein (3 µM) and dispersion in tetradecane + 0.5 % SPAN. TAD without droplet generation (cyan) and the three TAD with droplet generation showed a high consensus verifying the method.

After the successful implementations of TAD to microfluidics, the CAM-mediated HBc assembly assay's adaptation to droplet flow was attempted.

V.4.4 CP150-BO assembly assay in droplet microfluidics

Before a dose-response measurement, the assembly of CP150-BO mixed with either 32 µM BAY 41-4109 compound or NVR-3-778 was measured at 35 s post droplet formation. Unfortunately, the HBc assembly reaction in droplets was incomplete, ranging from only 5 % - 19 % assembly activity, compared to the measured values in microtiter well format. As a reference for the early kinetics, the compounds and the protein were coinjected without the carrier oils leading to a laminar flow with diffusion-mediated slow mixing. Even at these conditions, the assembly reached 55 % (BAY 41-4109) and 33 % (NVR-3-778) confirming, that the slow assembly values are not due to the short residence times or system errors but the utilization of the CF (Figure 128).

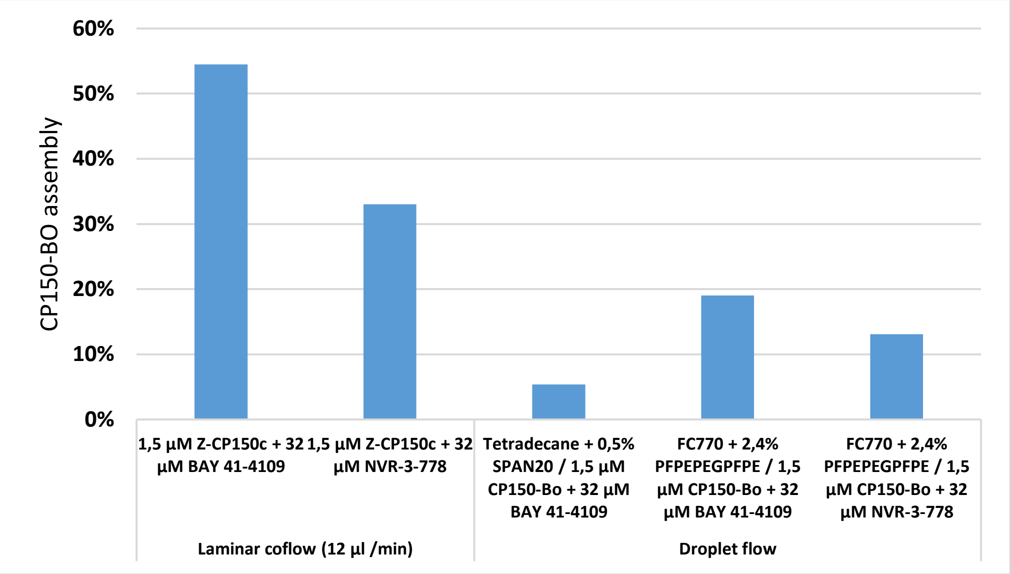

Figure 128: CP150-BO percentual assembly in the VIM2 microreactor using laminar co-flow (first two columns) and droplet flow (last three columns) at a residence time of 35 s. Overall flowrate of all the channels was 12 µl/min for every reaction (Laminar co-flow: protein 12 µl/min + compound with salt 12 µl/min; Droplet flow: CP 12 µl/min; DP: protein 6 µl/min + compound with salt 6 µl/min). The two different reference compounds, BAY41-4109, and NVR-3-778 were used at 32 µM concentration to initiate the compound assembly.

As a consequence of the incomplete HBc assembly, the methodology was re-evaluated and troubleshot. Different parameters were tested, starting with technical parameters, followed by the protein and compound activity, and physical parameters such as compound diffusion into the carrier and assembly kinetics. First, the flow rates and pump pressures were recorded during the measurements, not showing any anomalies. Next, the flow-through characteristics of the respective compounds and proteins were measured individually, which perfectly correlated with the displayed values during the reaction; hence a plugging in the system was ruled out. Theoretically, the compounds' diffusion into the carrier phase should be prevented by the hydrophobic and lipophobic characteristics of the fluorinated oils.[9] Furthermore, diffusion of the CAMs out of the DP as the sole reason for reduced assembly is questionable since, in the case of 32 µM BAY 41-4109, the assembly was reduced to 15 %, while the activity should reach 50 % even if more than half of the compound diffused out. As a further experiment for compound diffusion out of the droplet, the fluorescence signal of FITC was measured after the compartmentalization between the droplets (Figure 129 to Figure 131). As depicted in Figure 131, the signal was zero in the carrier phase, confirming that fluorescein was not leaving the DP. In summary, as it was showcased with various experiments, it is not likely that CAMs would leave the DP.

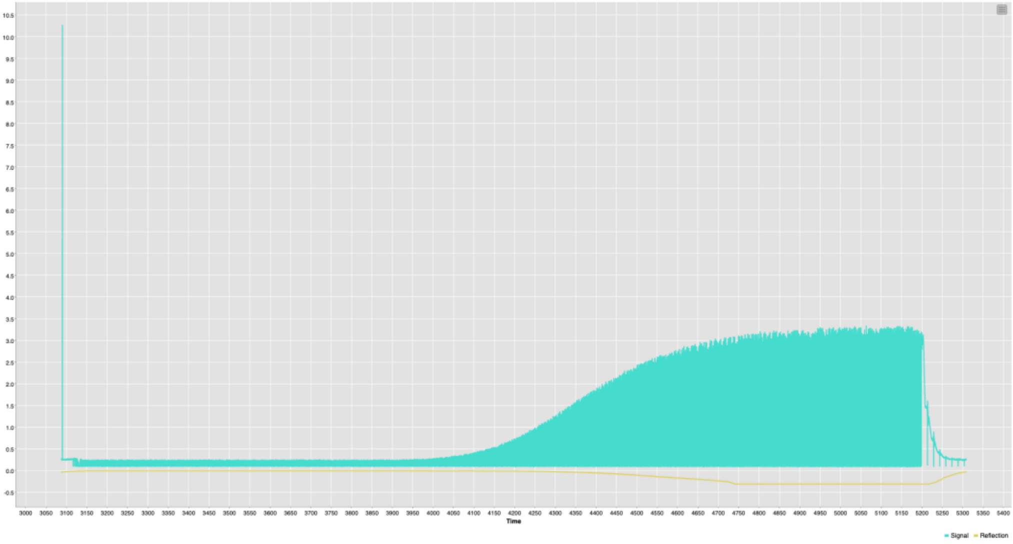

Figure 129: TAD mediated dilution of fluorescein in a 7 cm capillary with an ID of 1.4 mm at a flowrate of 6 µl/min followed by compartmentalization of the dye in FC770 + 2.4 % PFPE-PEG-PFPE.

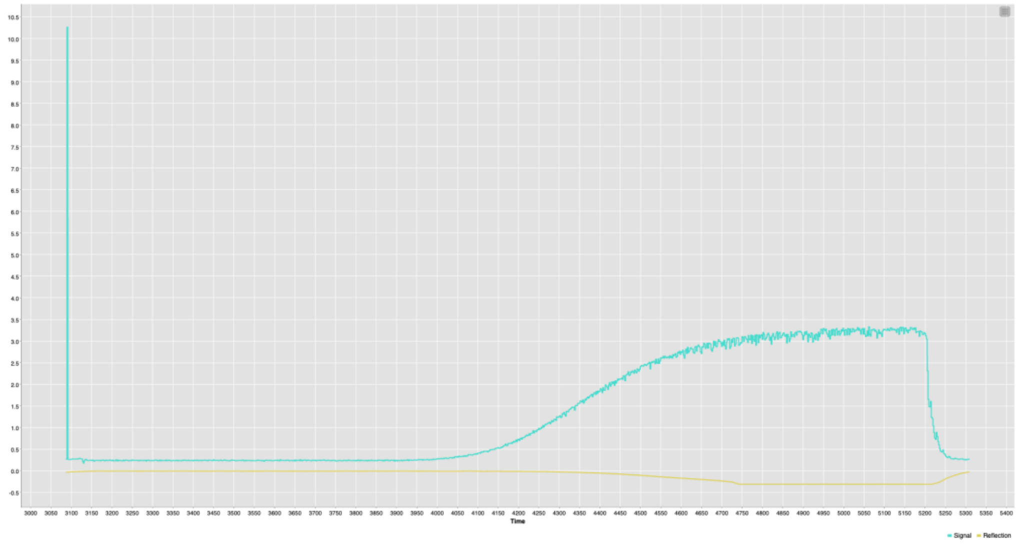

Figure 130: TAD mediated dilution of fluorescein in a 7 cm capillary with an ID of 1.4 mm at a flowrate of 6 µl/min followed by compartmentalization of the dye in FC770 + 2.4 % PFPE-PEG-PFPE. Only the maximas are depicted representing the DP phase of the liquid.

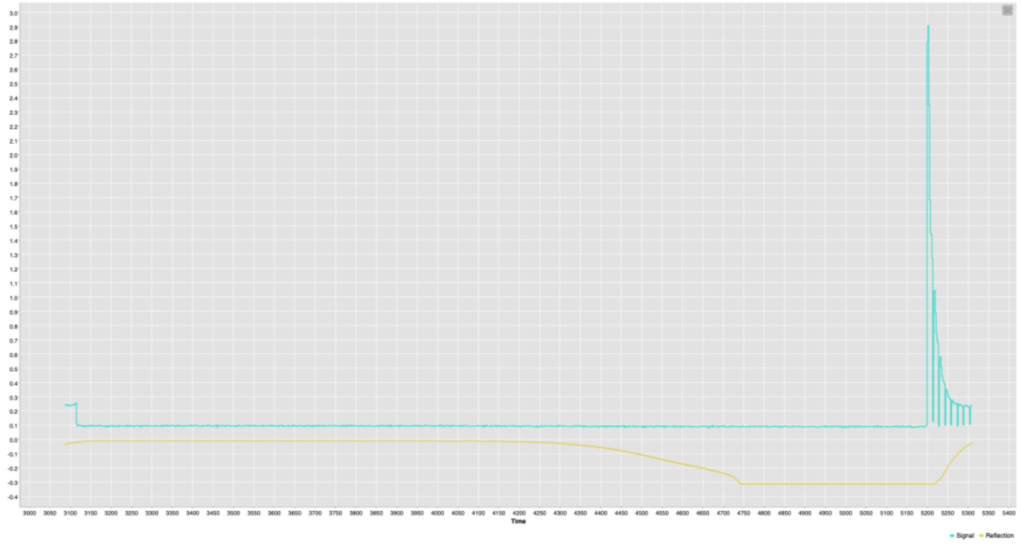

Figure 131: TAD mediated dilution of fluorescein in a 7 cm capillary with an ID of 1.4 mm at a flowrate of 6 µl/min followed by compartmentalization of the dye in FC770 + 2.4 % PFPE-PEG-PFPE. Only the minimums are depicted representing the CP phase of the liquid.

Next, the EC_{50} values (0.37) of the new HBc charge were tested in microtiter well plate format which was within the scope of anticipated values (Figure 137). Surprisingly, the addition of FC770 (Figure 138) or FC770 + 2.4 % PFPE-PEG-PFPE (Figure 139) to the respective wells did not interfere with the assay. A Premixing between protein and compound can be excluded since the carrier oils were first filled into the microtiter plate.

In contrast to the flow measurements, the observed assembly potency in the microtiter format might be related to a lower surface-to-volume ratio. A higher surface-to-volume ratio found in droplet microfluidics leads to more space for the HBc dimers to adsorb, which would limit the capsid's assembly potential. At the same time, reducing the droplet’s volume will facilitate its mixing properties. In this way, proteins might bind faster to the compound leading to an assembly instead of binding to the droplet interface. This hypothesis was evaluated using the tighter VIM 2b and WCA1b microreactor for the previously described assembly reaction (Figure 132 and Figure 133).

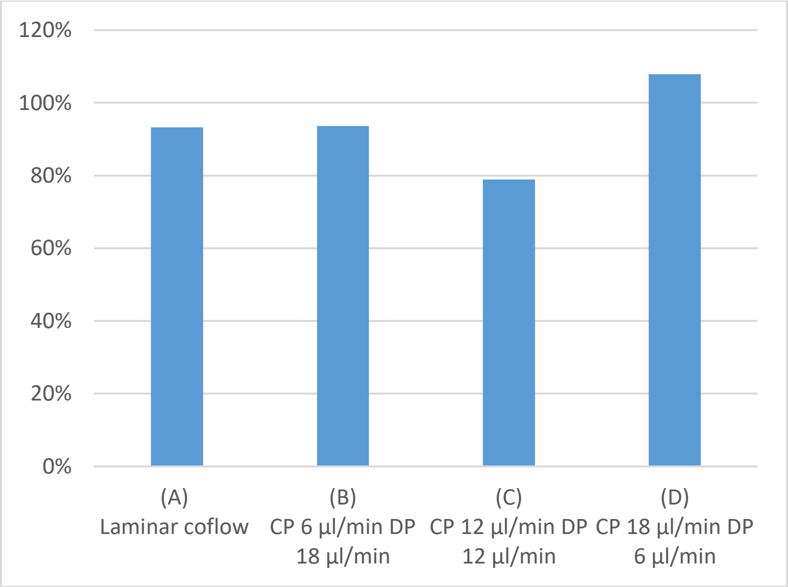

Figure 132: Capsid assembly in the VIM2b microreactor at 35 s reaction time using laminar co-flow (first column) and droplet microfluidics with different CP and DP flowrates. The overall flow rate for every measurement was 24 µl/min for comparative kinetic measurements. Despite enhanced mixing in droplets, the compartmentalization of the droplets did not have a strong positive effect on the assembly rate compared to the laminar coflow.

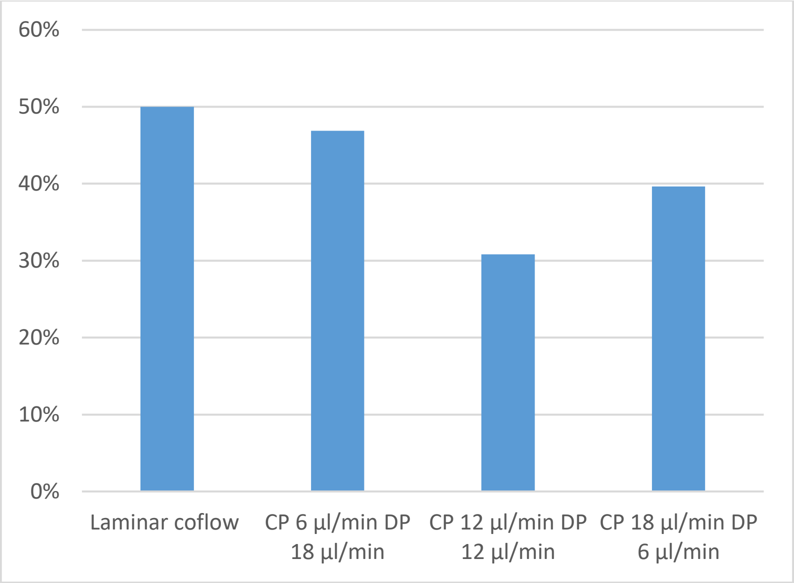

Figure 133: Capsid assembly in the WCA1B microreactor at 35 s reaction time using laminar co-flow (first column) and droplet microfluidics with different CP and DP flowrates. The overall flow rate for every measurement was 24 µl/min for comparative kinetic measurements. Despite enhanced mixing in droplets, the compartmentalization of the droplets did not have a strong positive effect on the assembly rate compared to the laminar coflow.

Compared to the VIM 2 microreactor with around 19 % assembly, the tighter microreactors showed a considerably higher assembly of around 85 % and 50 %, respectively. However, these values were still below the assembly achieved by laminar co-flow (85 %), leaving room for further improvement. Finally, BAY41-4109 and NaCl were premixed with CP150-BO in the 3D-serpentine micromixer before compartmentalization in droplets to demonstrate that the reduced signal observed in droplets microfluidics is due to an inhibition of the assembly reaction during droplets formation. Interestingly, the premixed HBc reactions in droplets showed the same assembly values as the ones measured in the continuous flow format. Furthermore, removing the 3D-Serpentine mixer before the droplet chip led to reduced HBc assembly of 40 % instead of 75 %. These outcomes prove that droplet-based microfluidics interferes with the assay by inhibiting the capsid assembly, likely due to adsorption of the CP150-BO dimers to the droplet interface. Premixing the compounds with the protein followed by the dispersion into the CP bypasses this problem, allowing the assembled capsids' compartmentalization and measurement of independent droplets at various kinetics on the chip (Figure 134).

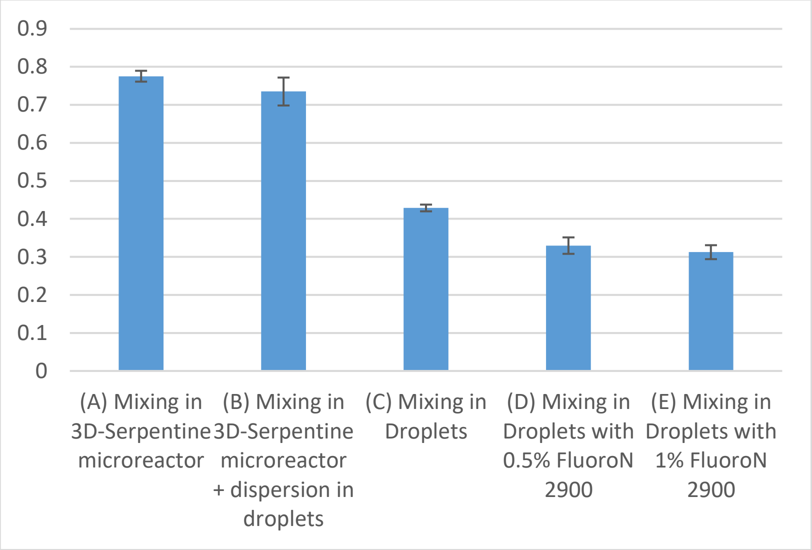

Figure 134: BAY 41-4109 mediated CP150-BO assembly in the WCA1B microreactor at 35 s residence time. The overall flow rate for every measurement was 24 µl/min for comparative kinetic measurements. (A) The protein and compounds were mixed in the 3D-Serpentine mixer and then transferred into the WCA1b microreactor without compartmentalization in droplets. (B) Reaction as described in A, but the resulting mixture was compartmentalized in FC770+2.4 % PFPE-PEG-PFPE. (C) Protein and compounds were directly compartmentalized mixed in FC770+2.4 % PFPE-PEG-PFPE. (D) As C, but 0.5 % FluoroN 2900 was added to the CP. (E) as C, but 1 % FluoroN 2900 was added to the CP. By premixing the CP150-BO protein with BAY 41-4109 followed by the compartmentalization, a significantly higher assembly was reached than without the premixing (B).

Different additives can be combined with a mixture to prevent protein adsorption to the droplet interface. As previously described, FluoroN 2900 is a fluorinated PFPE-PEG surfactant with a lower molecular mass than PFPE-PEG-PFPE. Therefore it should bind faster to the newly generated droplet interface, preventing protein adsorption. However, experiments revealed that the inhibition of protein assembly was not prevented by FLuoroN 2900 addition. Therefore, in future experiments, BSA could be evaluated as a sacrifice protein to prevent unwanted protein adsorption.

V.5 Conclusion

Droplet microfluidics and analytical methodologies underwent substantial developments in the last years, given various benefits compared to the continuous flow formats.[27] The compartmentalization of the reagents into small droplets of femtoliter to nanoliter size allows fast mixing, ultra-low sample consumption, and high throughput of discrete miniaturized reaction chambers.[20] In these assays, the droplets function as independent small reaction chambers, this allows the determination of fast kinetics based on the distance traveled by limiting TAD mediated compound dilutions post mixing. Many complex systems allow the handling, splitting, storing, sorting, and remixing between various droplets opening novel opportunities for specialized assays.[2,27,28] However, these complex formats often require specialized equipment and specifically trained presonnel. Moreover, even though droplet processing is faster than traditional robotics, the complex operations require the droplet's tracking or barcoding. Multiple downstream processes with different temperature conditions can also lead to size and stability variations during the reaction. Even in simpler systems, challenges might arise from droplet cross talk,[10,11] droplet coalescence or adsorption, or compound inactivities.[27] Therefore, this technology requires intense troubleshooting and is less reliable than many robotic systems used in microtiter plate formats.[28] Nonetheless, the unique benefits of droplet microfluidics technology have lead to its integration in various stages of drug discovery, especially in hit-to-lead development. High-throughput screening in microfluidic format has proven its value in numerous assays and has shown to be a valuable alternative to microtiter-based screening.[27] As an example, Miller et al. developed robust platforms able to generate high-resolution dose-response curves with up to 10,000 data points allowing the generation of high-resolution IC_{50} values unmatched by any microtiter format.[29]

Following these examples, the adaptation of the HBc assembly assay to the droplet format was addressed. The main intended benefit for was the prevention of TAD post mixing to reduce unwanted diffusion mediated dilutions, thus permitting the measurement of the assay at higher residence times (5-10 min.).

The project's first step included the selection and evaluation of microreactors and surfactants based on droplet size, reproducibility, and stability. The optimal droplet microreactor must have high biocompatibility and the suitable droplet generation method to produce highly reproducible monodisperse droplets in high throughput.[20] Droplet size was especially relevant; since it directly impacts the reagent consumption, throughput, and surface to volume effects.[20] Considering the material PC, COC and glass were considered, from which glass microreactors were chosen due to their higher optical transparency and stability. As for the design, the T-junction microreactors combined the best economic benefits with sufficient droplet frequency and reproducibility. (Active Droplet Manchip 2, VIM2, VIM2b, and WCa1b). The last two microreactors (VIM2b and WCa1b) had a tighter T-junction than VIM 2, making them ideal for a higher throughput of smaller droplets. This reduced the sample consumption and led to a higher monodispersity (Figure 115 and Figure 116). The WCa1b small channel size allowed generation of droplets with a higher monodispersity, while the more extended channel size increased the possible residence time up to 10 min with the flowrates used in previous experiments (between 5 - 15 μl/min per channel).

Several carrier oils and surfactant combinations were considered for the CF with the main focus being on droplet size reproducibility and biocompatibility. The combination of the fluorinated oil FC770 and a surfactant concentration of 2.4 % PFPE-PEG-PFPE showed the best results in terms of droplet generation, droplet monodispersity, and tolerance against higher salt concentrations, which are required for the biochemical assay (Figure 119 to Figure 120). Furthermore, FC770 + PFPE-PEG-PFPE combinations were described as one of the most biocompatible carrier phases due to the reduced protein adsorption to the droplet interface. [12,23]

The mixing of compounds was performed within ms, as demonstrated in the VIM 2 microreactor (Figure 124). Finally, with the optimal setup, the dispersion of a TAD-generated FITC dilution curve in droplets was successfully demonstrated in a reproducible matter (Figure 126 and Figure 127). However, the first attempts at mixing CAMs with HBc in droplets showed surprisingly low reaction rates even compared to the control of laminar co-flow between protein and compound (Figure 128). Multiple possible reasons were examined for the low reaction rates, such as droplet cross-talk (Figure 129 to Figure 131), protein and compound stability, and interactions between FC770 or PFPE-PEG-PFPE with the target protein (Figure 137 to Figure 139). In addition, HBc assembly is driven by hydrophobic interactions, which could also bind to the droplet interface.[30] Surprisingly, all of the above-described possibilities were experimentally disproven. Even more, in the microtiter-plate format, the addition of FC770 with surfactants did not influence the capsid assembly. Therefore, it was assumed that the impairment of the initial capsid assembly could be attributed to the increased SAV characteristics of microfluidic formats. The hysteris of HBc capsids can be used by premixing the HBc with CAMs before the compartmentalization in droplets.[31] This theory was successfully demonstrated with the mixing of BAY41-4109 and CP150-BO in the 3D Serpentine before entering the droplet chip, followed by the capsid's compartmentalization in droplets (Figure 134). This effect is not necessarily reproducible with compounds having slower kinetics since BAY41-4109 (32 µM) achieves the assembly reaction within seconds (IV.4.3 CP150-BO assembly kinetics as an indicator of the mode of action of CAMs), whereas slower CAMs could leave enough free HBc dimers to adsorb to the droplet interface, thereby limiting the assay's sensitivity. In this settings, BSA or other proteins/ compounds could be used to bind to the droplet surface prior to adding the CP150-BO and other reagents into the droplets.

In conclusion the various microreactors, oils, and surfactants were evaluated. The final setup produced droplets in a reproducible and calculatable manner, and mixing within droplets could be performed within ms. The compertimentalization of compounds was also demonstrated with no traceable droplet cross-talk. Despite initial difficulties with the HBc adaptation to the microfluidic format, the feasibility of BAY41-4109 mediated HBc was successfully demonstrated by premixing the solutions before the compartmentalization. Further studies will be required to standardize the technique, and the reaction should also be demonstrated with slower CAMs. Overall, a foundation has been laid for successful implementation of the HBc assay to droplet microfluidics.

V.6 References

1. Ismagilov, R. F. A Microfluidic System for Controlling Reaction N. *AngewandteChemie* 791–796 (2003).

2. Helen Song, Joshua D. Tice, and R. F. I. A Microfluidic System for Controlling Reaction Networks in Time**. *Angew. CHem. Int.*. **42**, 767 (2003).

3. Shang, L., Cheng, Y. & Zhao, Y. Emerging Droplet Microfluidics. *Chem. Rev.* **117**, 7964–8040 (2017).

4. Seemann, R., Brinkmann, M., Pfohl, T. & Herminghaus, S. Droplet based microfluidics. *Reports Prog. Phys.* **75**, (2012).

5. Priest, C., Herminghaus, S. & Seemann, R. Generation of monodisperse gel emulsions in a microfluidic device. *Appl. Phys. Lett.* **88**, 1–3 (2006).

6. Li, X., He, L., He, Y., Gu, H. & Liu, M. Numerical study of droplet formation in the ordinary and modified T-junctions. *Phys. Fluids* **31**, (2019).

7. Ambravaneswaran, B., Subramani, H. J., Phillips, S. D. & Basaran, O. A. Dripping-jetting transitions in a dripping faucet. *Phys. Rev. Lett.* **93**, 034501–1 (2004).

8. Utada, A. S., Fernandez-Nieves, A., Stone, H. A. & Weitz, D. A. Dripping to jetting transitions in coflowing liquid streams. *Phys. Rev. Lett.* **99**, 1–4 (2007).

9. Roach, L. S., Song, H. & Ismagilov, R. F. Controlling nonspecific protein adsorption in a plug-based microfluidic system by controlling interfacial chemistry using fluorous-phase surfactants. *Anal. Chem.* **77**, 785–796 (2005).

10. Chen, Y., Wijaya Gani, A. & Tang, S. K. Y. Characterization of sensitivity and specificity in leaky droplet-based assays. *Lab Chip* **12**, 5093–5103 (2012).

11. Etienne, G., Vian, A., Biočanin, M., Deplancke, B. & Amstad, E. Cross-talk between emulsion drops: How are hydrophilic reagents transported across oil phases? *Lab Chip* **18**, 3903–3912 (2018).

12. Holtze, C. *et al.* Biocompatible surfactants for water-in-fluorocarbon emulsions. *Lab Chip* **8**, 1632–1639 (2008).

13. Baret, J. C., Kleinschmidt, F., Harrak, A. El & Griffiths, A. D. Kinetic aspects of emulsion stabilization by surfactants: A microfluidic analysis. *Langmuir* **25**, 6088–6093 (2009).

14. Riechers, B. *et al.* Surfactant adsorption kinetics in microfluidics. *Proc. Natl. Acad. Sci. U. S. A.* **113**, 11465–11470 (2016).

15. Chen, Y., Wijaya Gani, A. & Tang, S. K. Y. Characterization of sensitivity and specificity in leaky droplet-based assays. *Lab Chip* **12**, 5093–5103 (2012).

16. Corcuera, A. *et al.* Novel non-heteroarylpyrimidine (HAP) capsid assembly modifiers have a different mode of action from HAPs in vitro GPA, PT, DBT. *Antiviral Res.* **158**, 135–142 (2018).

17. VANDYCK, Koen; HACHE, Geerwin; Yvonne, Paul; Stefaan, Julien;David, Craig;ROMBOUTS, Geert; VERSCHUEREN, Wim, Gaston; RABOISSON, Pierre, Jean-Marie, B. WO 2014/184350 A1. vol. 5 (2014).

18. Karl Deres, H. R.-W. Inhibition of Hepatitis B Virus Replication by Drug-Induced Depletion of Nucleocapsids. *Science (80-.).* **303**, 1829 (2003).

19. Wang, X. Y. *et al.* In vitro inhibition of HBV replication by a novel compound, GLS4, and its efficacy against adefovirdipivoxil-resistant HBV mutations. *Antivir. Ther.* **17**, 793–803 (2012).

20. Rosenfeld, L., Lin, T., Derda, R. & Tang, S. K. Y. Review and analysis of performance metrics of droplet microfluidics systems. *Microfluid. Nanofluidics* **16**, 921–939 (2014).

21. Chiu, F. W. Y. & Stavrakis, S. High-throughput droplet-based microfluidics for directed evolution of enzymes. *Electrophoresis* **40**, 2860–2872 (2019).

22. Wagner, O. *et al. Biocompatible fluorinated polyglycerols for droplet microfluidics as an alternative to PEG-based copolymer surfactants Supporting Information*. (2015).

23. Wagner, O. *et al.* Biocompatible fluorinated polyglycerols for droplet microfluidics as an alternative to PEG-based copolymer surfactants. *Lab Chip* **16**, 65–69 (2016).

24. Segaliny, A. I. *et al.* Functional TCR T cell screening using single-cell droplet microfluidics. *Lab Chip* **18**, 3733–3749 (2018).

25. Michelle R. Bringer, Cory J. Gerdts, Helen Song, J. D. T. and R. F. I. Microfluidic systems for chemical kinetics. *Phil. Trans. R. Soc. Lond. A* 1087–1104 (2004).

26. Tung, K. Y., Li, C. C. & Yang, J. T. Mixing and hydrodynamic analysis of a droplet in a planar serpentine micromixer. *Microfluid. Nanofluidics* **7**, 545–557 (2009).

27. Payne, E. M., Holland-Moritz, D. A., Sun, S. & Kennedy, R. T. High-throughput screening by droplet microfluidics: Perspective into key challenges and future prospects. *Lab Chip* **20**, 2247–2262 (2020).

28. Shembekar, N., Chaipan, C., Utharala, R. & Merten, C. A. Droplet-based microfluidics in drug discovery, transcriptomics and high-throughput molecular genetics. *Lab on a Chip* vol. 16 1314–1331 (2016).

29. Miller, O. J. *et al.* High-resolution dose-response screening using droplet-based microfluidics. *Proc. Natl. Acad. Sci. U. S. A.* **109**, 378–383 (2012).

30. Ceres, P. & Zlotnick, A. Weak protein-protein interactions are sufficient to drive assembly of hepatitis B virus capsids. *Biochemistry* **41**, 11525–11531 (2002).

31. Singh, S. & Zlotnick, A. Observed hysteresis of virus capsid disassembly is implicit in kinetic models of assembly. *J. Biol. Chem.* **278**, 18249–18255 (2003).

V.7 Attachment

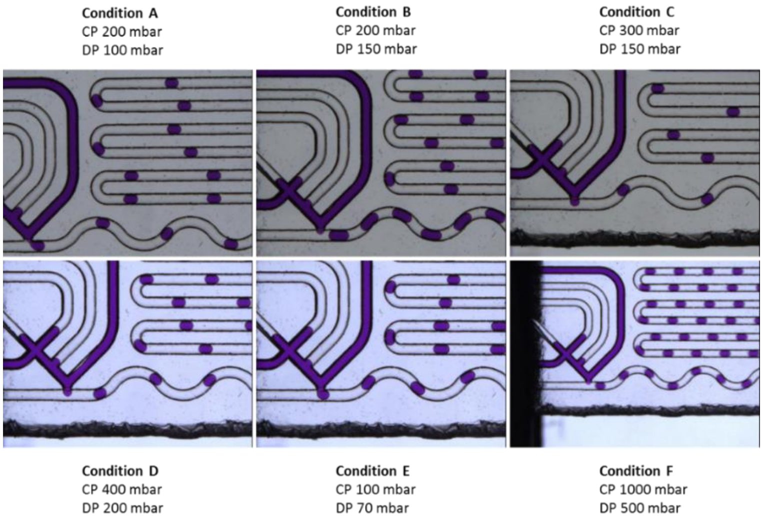

Figure 135: Equilibrated Active Droplet Manchip 2 Assay chip with different flow parameters for the continuous phase (CP) and disperse phase (DP). The figure displayes first calibration measurements to determine the droplet size and frequency as a function of the flowrates.

With the VIM2 microreactor, the droplet generation frequency was calculated as a function of different flow rates (Figure 136), and the effective residence time was depicted as a function of the flow rates for the VIM2 microreactor.

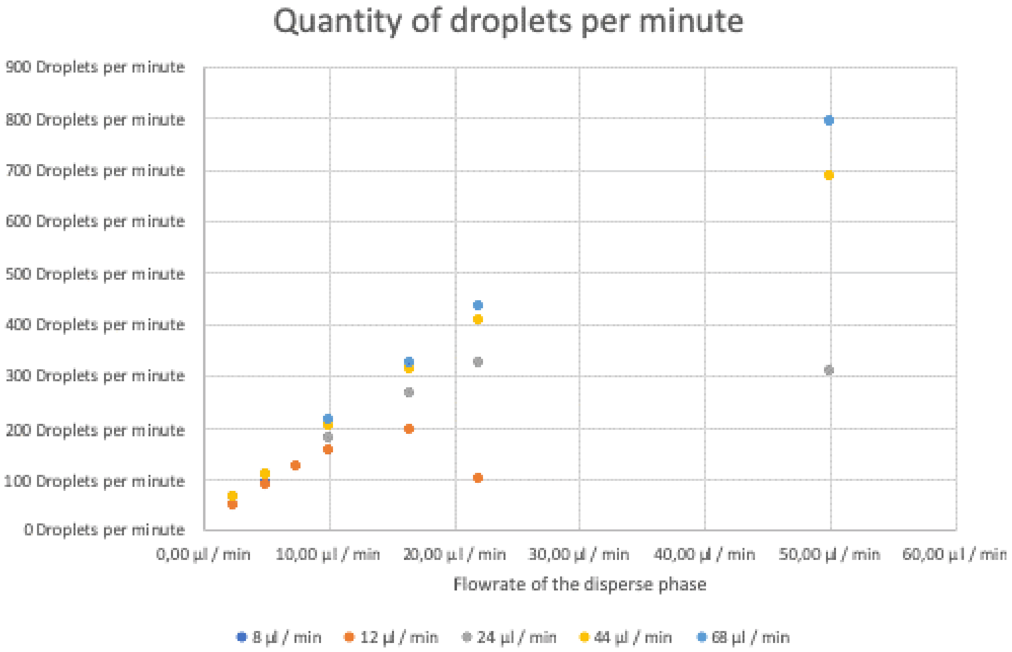

Figure 136: Droplet's frequency in the VIM2 microreactor as a function of the DP and CP phases' flow rates. Droplets were generated by mixing 0.67 mMol Fe (NO3) and 2 mMol KSCN in tetradecane with 0.5 % SPAN 20.

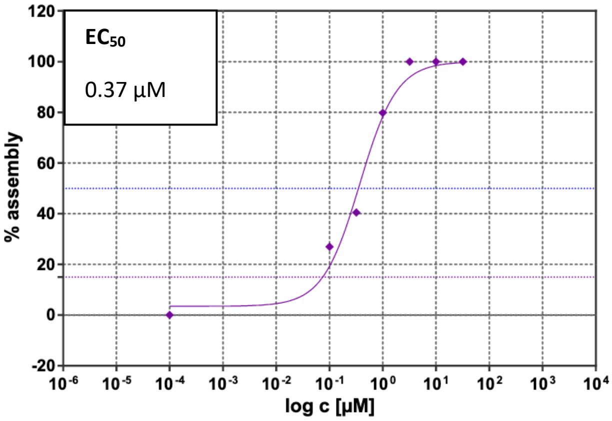

Figure 137: EC$_{50}$ value of the new CP150-BO charge mixed with BAY41-4109. Values were obtained in a standard microtiter plate format at 10 min post mixing.

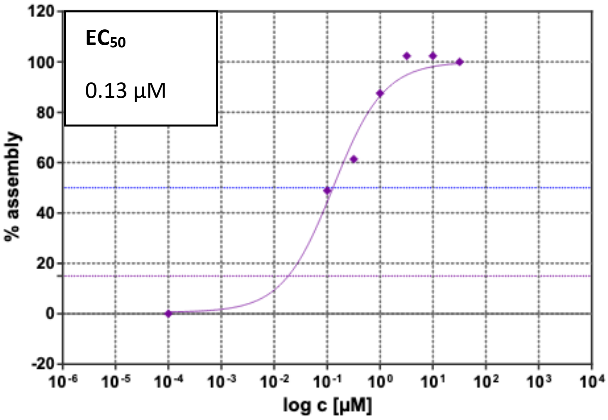

Figure 138: EC$_{50}$ value of the new CP150-BO charge mixed with BAY41-4109 in the presence of 50 % FC770. Values were obtained in a standard microtiter plate format at 10 min post mixing.

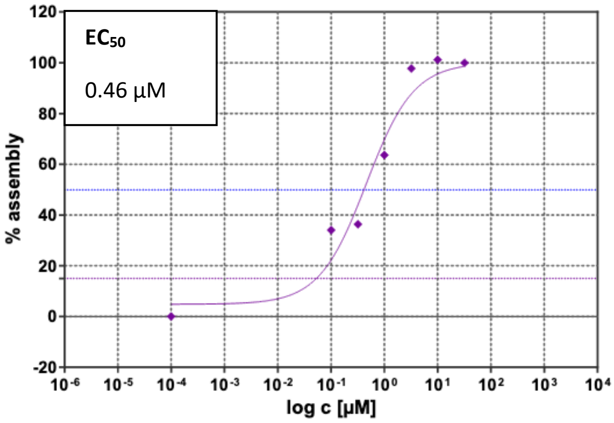

Figure 139: EC$_{50}$ value of the new CP150-BO charge mixed with BAY41-4109 in the presence of 50 % FC770 + 2.4 % PFPE-PEG-PFPE. Values were obtained in a standard microtiter plate format at 10 min post mixing.

General conclusion and future work

The inherent benefits of microfluidic systems, such as ease of automation, miniaturization, and tight control over physical parameters, have been emphasized in several individual academic success stories.[1–4] However, despite the academic advancements and the implementation of microfluidics by various start-ups, it has not yet achieved broad-scale application within the pharmaceutical industry. Some argue that the lack of microfluidic uses is partly due to the improvements made to other technologies thus weakening the advantages of microfluidic solutions.[5] Others emphasize the complexity of the systems combined with the task-specific specializations performed in academia that prevent more widespread use. This issue is often exacerbated by a lack of communication between the end-user and the engineering-based research, which could be circumvented in close collaborations.[6] Hence, it is essential to compare the designed microfluidic system with the current alternative technologies to determine whether the given application truly requires this type of solution. The areas in which microfluidic systems excel are preclinical studies using **organ-on-a-chip**, **diagnostic tools**, and **automated screening setups** in the hit-to-lead development cycle.

Organ-on-a-chip solutions harness cellular cultures in a 3D environment compared to the 2D Petri dishes and include all physical and chemical stimuli required for the cells.[7] A brilliant example was demonstrated by Huh et al. in which an alveoli-capillary barrier of a lung was simulated, which recreated the lung movement using vacuum pumps. By providing the epithelial cells with a blood and air current combined with 3D growth and physical stimuli, more precise information could be generated during a screening process.[8] In more complex setups, several different organs on a chip can be combined to a multi-tissue interaction or a human on a chip can, which can simultaneously screen multiple organ interactions of a single drug.[6,9] Given the high quality of the data obtained, organs on a chip could be used in preclinical studies to supplement the animal models or, in some cases, even to replace them, thereby strongly reducing the research expenses and offering the further advantages of reduced ethical limitations and enhanced public image/ support.[10]

As discussed in the introduction, microfluidic systems also excel in point-of-care applications given their flexibility, ease of automation, and parallelization.[11] Several self-contained systems have been introduced that could reach developing countries that were usually not reachable with other setups.[12] Point of care applications are by design economically affordable, which leads to more non-profit research in these areas.[6]

Lastly, microfluidic systems have seen a great number of automated systems in screening approaches.[1–4] The large amount of data obtained from these measurements also facilitates a more personalized therapy.[13] In the hit-to-lead development cycle, multiple systems have been introduced, combining synthesis with immediate evaluation of the compounds in biochemical assays.[14–18] A major benefit is the automation of complete screening cycles using feedback mechanisms to reduce the time required from 2-8 weeks (conventional approaches) to only several hours up to a day. Given these benefits, multiple start-ups emerged, determined to functionalize these technologies on a broader scale.[17,19–24] However, as mentioned before, most of the presented systems were highly complex and target-specific, making general implementation complicated. So far, the majority of the biochemical targets were enzymatic assays, thus leaving open the question of a more general setup for other assay types, such as protein-protein interactions or assembly reactions.

In this context, the VIRO-FLOW project was founded by specialists across the whole spectrum of related sciences, with the aim of developing a general microfluidic system to improve the time and resource-consuming SAR cycle. The multidisciplinary program was engaged in medicinal chemistry (including organic and computational chemistry), molecular biology, protein biochemistry, and continuous flow technology. The aim of the VIRO-FLOW project was to design a fully automated continuous flow platform to accelerate the hit to lead development of novel anti-HBV compounds. This process includes the drug synthesis in flow with inline detection of the compound’s chemical properties and biochemical activity. The ambition of the project was to evaluate the obtained data automatically and, using artificial intelligence or similar tools, calculate the most fitting structures for the following synthetic cascade. The automatization of the combined chemical and biochemical processes will lead to an iterative optimization cycle of biochemical activity for the newly generated compounds. Simultaneously the system would benefit from the previously described distinct features of continuous flow chemistry and biochemistry, leading to increased productivity, higher control of physical variables, and safer working conditions for toxic or runaway reactions. Furthermore, the reduced time and sample consumption required for the synthesis allows the more affordable exploration of new chemical space.[25]

The work presented here was performed as part of the VIRO-FLOW project with the principal aim of developing a microfluidic system for the screening of antiviral compounds combined with an interface to the organic synthesis. The microfluidic system was set up from modular devices obtained through intense research of the currently marketed solutions and the assay requirements. In this process, the flow generation and control, inflow dilution of compounds and subsequent mixing, and finally, the readout was considered and implemented. Furthermore, several automated rotational check valves were installed for advanced flow handling, which allowed the compound dilution using TAD and the sequential measurement of up to 8 compounds in 10 replicates, respectively. The devices were evaluated individually with respect to accuracy, reproducibility, and stability. Finally, the modules were connected, and the setup was automatized with protocols written in the MAT software (Figure 69). Several workflows were generated in KNIME to allow the comprehensive evaluation of the produced fluorescence data. With the protocols, unprocessed text data was converted into excel format, and the reproducibility of the assay was measured based on the technical replicates by calculating the standard deviations, the limits of detection and quantification, and the Z'-Factor for each individual measurement.

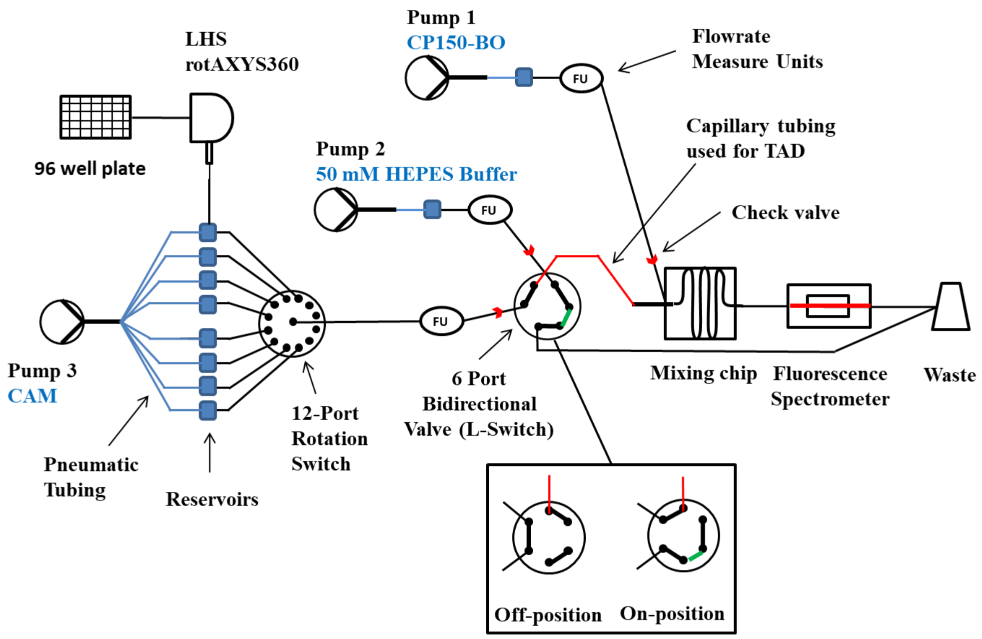

Figure 140: Schematic representation of the microfluidic system used for the screening and characterization of novel HBV CAMs. The compounds were transferred from a 96 well plate to the pressurized reservoirs (blue squares) with the LHS rotAXYS360. Afterward, the system was equilibrated by first loading the first compound until the L-Switch, which was set to the Off-position to remove compound excess into the waste. Simultaneously, Pump 2 and Pump 3 were running with identical flowrates allowing the mixing of 50 mM HEPES with CP150-BO in the mixing chip and thereby generating the baseline. Following the initiation, pump 3 was set to the same flowrate as pump 1, and the L-Switch turned to the On-position, allowing the TAD of the CAM's compound margin in the designated (red) capillary and its subsequent mixing with the CP150-BO protein. After the measurement, the system was cleaned with H_2O using pump 3 switched to the respective reservoir and 50 mM HEPES using pump 2. Legend for the various units is depicted in Figure 30.

Despite all the benefits, microfluidic processes have proven to be more complex than the regular microtiter assays, which was also the case in the system presented here.[26] Issues identified during the system's setup, operation, and maintenance often impaired data quality and reproducibility. Each problem was successfully solved, and troubleshooting guides were developed for the following issues:[26]

- Value deviations due to air bubbles
- Plugging of microreactors
- Unstable flow rates, backflow, and flow fluctuations
- Deviations and problems with the readout
- Protein stability during more extended measurements
- Protein or compound adsorption to the microreactors or channel walls
- Individual device failure

In conclusion, a fully automated fluorescence readout-based microfluidic system was established able to measure multiple compounds sequentially at various time points from a couple of seconds up to 15 min. The microfluidic system offered high reproducibility with standard deviations under 5 %, flexible kinetic measurements, and high accuracy in an automated manner. The seamless diversification for various biochemical targets was ensured by the flexibility of the modular design combined with the extension-oriented programming of the workflow and evaluation protocols.

Lastly, the microfluidic system was still a standalone module with maximal 8 sequential compound measurements. The direct integration of chemical synthesis inflow and subsequent evaluation in microfluidic screening systems, both biochemical and cellular, have been successfully demonstrated in various papers and was also part of the VIRO-FLOW project's ambition. However, an undertaking of this size often requires a team of experts and long setup times due to the complexity and multidisciplinary nature of the task. Here a more straightforward integration of the synthesis and screening was developed given the limited amount of time and resources available. Instead of a continuous flow interface, the system was equipped with an LHS used to transfer the compounds from up to 6 pieces of 96-well plates into the 7 sealed reservoirs of the microfluidic system. This stopped-flow solution is easily harmonized with synthetic platforms given the standard 96 well format as an interface. However, a fully automated synthesis, and screening platform requires further optimizations, mainly relating to the purification of the compounds, the exchange of solvents, and the accurate determination of final compound concentrations. In the future, the microfluidic assay presented here could be telescoped to a synthesis platform in this way combined with an automated evaluation of the drug activity. This upgrade is highly feasible given the modularity of the setup, which allows an easy exchange or extension of hardware. Furthermore, all protocols (automation and evaluation) were written in a way, that future modules could easily be included. Overall, the existing interface allowed a direct, automated transition between synthesis and screening. Hence, the complete system reduces cycle times and costs in early-stage drug discovery while offering remarkably higher data density and novel screening opportunities for faster reactions.

As a first target, the homogeneous HBc capsid assembly assay was adapted to the microfluidic flow format. The HBV core protein was an attractive target given the global need for an HBV cure and the fast reaction kinetics of HBc assembly processes.[32,33] The first objective was the screening of inflow dose-response curves followed by the evaluation of EC_{50} values. The required compound dilutions under continuous flow were addressed using convection-dominated TAD, and after the exhaustive analysis of capillary parameters and flow rates, reproducible dilution curves were generated with optimal hillslopes and a high number of data points (10 per s). Furthermore, compared to convection-diffusion-mediated TAD, the compound-specific diffusion was eliminated. Hence, the dose-response curves for compounds between 250-600 g/mol followed the same dilution pattern, allowing the use of the FITC's dilution curve was used as an encoder for all the CAMs (Figure 141). In case of compounds with higher molar mass, one can simply shorten the capillary used for the dilutions. Thereby the convection-dominated effects will increase, allowing the simple generation of encoder curves, but at the same time, the maximal number of data points will be reduced given the steeper dilution slopes.

The high-resolution dose-response curves were generated following the compound dilution for six reference- and two in-house compounds at 51 s post-inflow-mixing. Based on the results, the EC_{50} values were successfully calculated but were significantly higher than in the microtiter-based format due to the short residence times (Figure 142). The experiments were repeated at residence times of 5 min to gain more comparative results. Unfortunately, the CAMs' dilution deviated from the ideal convection-dominated TAD at higher residence times because the longer channel size amplified the diffusion-mediated effects of TAD. To maintain the convection-dominated TAD, the dilution must be inhibited after mixing.

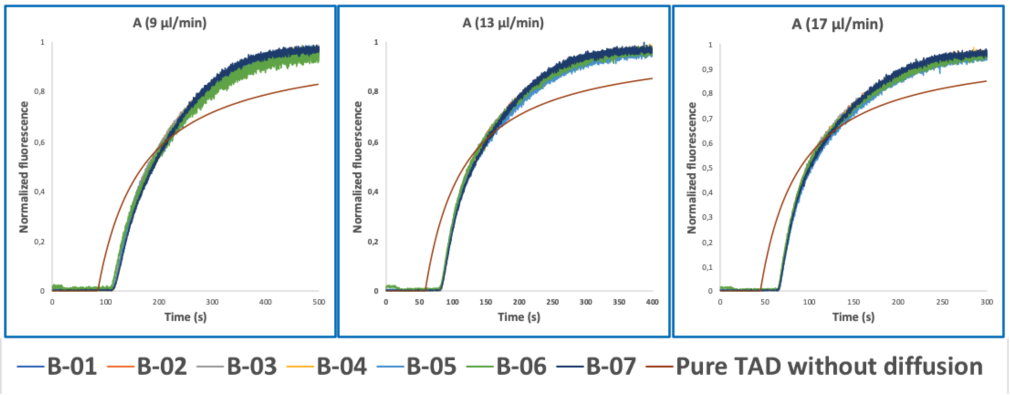

Figure 141: Normalized fluorescence spectra (y-axis) of the convection-dominated TAD in isopropanol of the BODIPY derivatives B-01 to B-07 (legend) in a 2.5 cm tubing with an ID of 1 mm followed by a 1.5 cm tubing with an ID of 0.75 mm as a function of time in s (x-axis). The dilution curves of all seven compounds aligned perfectly at the three different flow rates evaluated: 9 µl/min (A), 13 µl/min, and (C) 17 µl/min. TAD without diffusion was calculated using Equation 5.1 for the two short capillaries (ID 1 mm, L 2.5 cm; ID 0.75 mm, L 1.5 cm) and the microfluidic channel of the chip (ID 0.04 mm, L 3 cm). Measurements for each compound were repeated in three technical replicates.

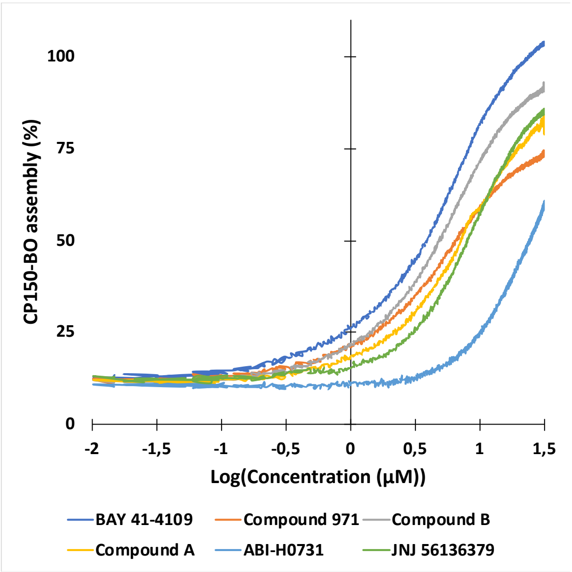

Figure 142: High-resolution dose-response curves for the six CAMs at 51 s post-mixing inflow. Compounds were diluted using TAD-mediated dispersion and mixed inflow as described in the Experimental section. CAM-N compounds had mostly incomplete CP150-BO assembly at 51 s, resulting in higher EC_{50} values. This was mainly evident for ABI-H0731, which yielded a non-sigmoidal assembly curve due to the incomplete reaction. GLS4 and NVR-3-778 were measured at 10 µM maximal concentration due to solubility issues, and so, were not displayed in this graph.

Droplet microfluidics is ideal for this challenge and can eliminate unwanted dilution by encapsulating the protein and compound together.[29] In this regard, the system was supplemented with T-junction droplet microfluidic chips. Mixing in droplets within ms and compartmentalization with non-detectable cross talk was demonstrated using fluorinated oil-based carrier phase with

PFPE-PEG-PFPE surfactants. Surprisingly, the HBc assembly was impaired in initial attempts, and after several rounds of troubleshooting, the problem was narrowed down to the partial adsorption of dimers to the droplet interface. This issue was circumvented by premixing the protein with the compound; however, more sophisticated solutions are required to realize the full potential of the droplet technology for the HBc assembly assay (Figure 134). The setup is currently able to switch between continuous and droplet flow measurements, which will facilitate the evaluation of biochemical assays in both formats. The adaptation of novel targets to the droplet format, such as enzymes, is a feasible undertaking for the future, especially given that some enzymes showed an enhanced activity linked to the droplet surface.[34]

Aside from the high-resolution dose-response curves, the microfluidic system enabled the measurement of fast assembly rates just 5 s post mixing. Building on this unique feature, the concentration-dependent kinetics of the CAMs were evaluated successfully at various time points ranging from 5 s to 120 s and concentrations of (1 µM, 10 µM, and 100 µM). Interestingly, compounds from class CAM-A displayed significantly faster assembly rates compared to CAM-Ns with profound differences at 10 µM and lower residence times of 7.7 s (Figure 143). This result is in line with the literature, showing that CAM-A mediated HBc assembly often leads to kinetic trapping due to disproportional acceleration of the nucleation step.[35,36]

As discussed in II.4 Results and Discussions, compounds from class A offered interesting behavior which could lead to benefits over the CAM-Ns, among others a seroclerence of HBc. Therefore, further research was conducted to develop an assay that can identify novel CAM-As.[37–44] Aside from the six reference CAMs, the two inhouse compounds, compound A and B, with unknown mode of action were classified using the microfluidic system. While compound A was successfully recognized as a CAM-N, compound B showed an in-between mode of action which was confirmed by Dr. Corcuera's cross-evaluation of the results with SEC and immunofluorescence.

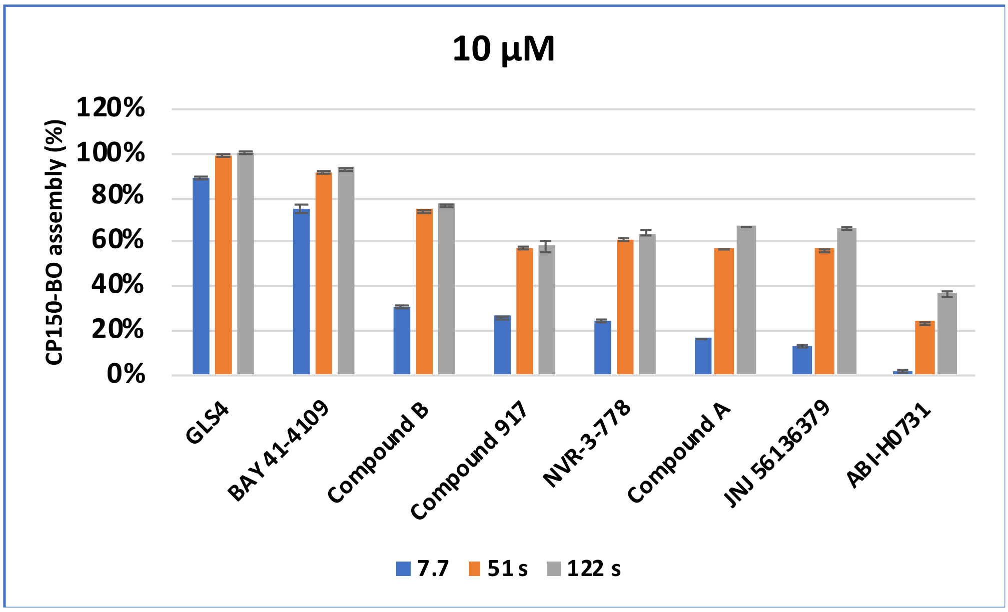

Figure 143: HBc assembly mediated by different CAMs at three incubation time points (7.7 s, 51.1 s and 122.7 s) and at 10 µM concentration. GLS4 and BAY 41-4109 both belong to CAM-A class, Compound B displayed an inbetween mode of action while the rest belongs to CAM-N. For each compound, the reaction was performed in duplicate.

It can be concluded that aside from the morphology of the assembled HBc products and the localization in cells, the aggressive assembly displayed by CAM-A compounds is a possible identification factor for the CAMs' mode of action. This is a notable finding considering the short screening times of a couple of minutes compared to the current methodologies, which require time consuming evaluations ranging from an hour up to a day.[33,43,53,45–52]

As an alternative to the microfluidic system, a simpler and faster screening method was envisioned in the microtiter format to differentiate between the CAM-A and -N. In initial attempts, a second screening step was telescoped to the microtiter plate assay based on the size or stability of the assembly products. This step was intended to remove the protein aggregates by filtration, selective proteinase mediated digestion, or selective detergence mediated disassembly. Unfortunately, despite early positive results, every attempt to differentiate the assembly products by modifying the HBc assay was unsuccessful. Therefore, the modification of the assay protein was addressed by changing CP150C for CAM-specific mutants. However, the final purification of the mutants proved to be very time-consuming. Meanwhile, novel results in cellular assay obtained by Dr. Corcuera suggested that the CP150C mutants were compound-specific rather than class-specific, and hence, this project was halted. On the other hand, HBc assembly was analyzed in other assay formats such as DLS, FA and FCS. The latter was not only able to determine concentration dependent assembly curves, but also generated information about the CAMs'mode of action by observing the product's morphology.

These technologies are quite expensive and complex, but an implementation of FCS or FA as a readout for microfluidic formats could be a feasible task for the future. In conclusion, the successful categorization of the CAMs' mode of action based on the compounds' kinetic is a feature currently unique to the microfluidic format. The major benefit is the short evaluation time of just 4 min compared to other analytical methods, usually requiring up to 1 h, -making microfluidics especially interesting for mode of action screening approaches.

In the future, further experiments can be conducted on the so far experimentally unexplored fast HBc assembly kinetics. Experiments in this direction were performed using resistive-pulse analysis-based microfluidic screening. However, mixing the HBc dimer with the salts was performed off-platform, and hence the results were obtained earliest after 10 min and latest after overnight incubation, which does not give insights into the very early nucleation steps.[33,51–53] The microfluidic system offers an excellent opportunity to study capsid kinetics for different viral or bacterial targets as well. Several interesting starting points are presented by viruses on which the assembly had already been studied, such as Cowpea chlorotic mottle virus (CCMV), HCMV, HIV, Human papillomavirus, Bacteriophages alphaviruses, retrovirus, and influenza.[54–59] Variations might arise from the different assembly mechanisms involving heterodimers.

In conclusion, with the presented results, the microfluidic system's feasibility, reproducibility, and accuracy were demonstrated in an automated fashion. The CAM-mediated HBc assembly was successfully integrated into the flow format, and high-resolution dose-response curves, kinetic data, and hints about the CAMs' mode of action were obtained and evaluated using protocols written in KNIME. The modular design of the microfluidic system will facilitate the simple reproduction of the data by other research groups and the extension of the system with further hardware. The generation of a kinetic measurement based on three residence times required only 4 min, while the high-resolution dose-response curves were around 25 min (12 min screening + 13 min cleanings). The cleaning step reduced compound traces down to single digit nanomolar compound concentrations and can be shortened depending on the assay's requirements. As a standalone module, the microfluidic system is more suited for hit-to-lead optimizations than initial screenings in which microtiter-based HTS systems outperform the sequential screening method. In this context, one has to consider the number of data points obtained, up to several 1,000 compared to the 8 from microtiter plate-based assays. With the higher data accuracy and density, more complicated drug-target interactions can be detected.[60] Furthermore, given the information on kinetics and mode of action, the screening platform provided a more complete CAM evaluation than a standard microtiter-based assay. This could be especially important given that HTS based assays are usually highly artificial, and activities mainly result from lipophilicity, often leading to significant differences between biochemical and cellular assays.[61] Finally, the simple adaptation of the microfluidic system to continuous flow synthesis will eliminate the screening time gap after the synthesis, reducing the overall time requirement for SAR cycles. This will be very useful for testing novel viral or bacterial targets in the future, including other capsid proteins and enzymes. Furthermore, the feasibility of the COVID-19's protease's adaptation of the microfluidic system was already considered, which could be performed with the existing hardware.? The previously introduced organ-on-a-chip are also possible and attractive complementation that could be inserted in the future after the biochemical assay or directly after synthesis inflow. The 3D environment in these modules can provide precise information, including ADME-T properties and phenotypic activity of the drug required to supplement or even replace the cellular and animal studies.

In the end, the microfluidic system presents a robust format for activity and kinetic measurements with the versatility to screen several possible targets. Hence, the presented benefits open new possibilities for early-stage DD by enhancing data quality and offering novel information to obtain an overall better understanding of the hit and thereby accelerate the lead identification process.

References

1. Schneider, G. Automating drug discovery. *Nat. Rev. Drug Discov.* **17**, 97–113 (2018).
2. Whitesides, G. M. The origins and the future of microfluidics. *Nature* **442**, 368–373 (2006).
3. Miller, O. J. *et al.* High-resolution dose-response screening using droplet-based microfluidics. *Proc. Natl. Acad. Sci. U. S. A.* **109**, 378–383 (2012).
4. Werner, M. *et al.* Seamless integration of dose-response screening and flow chemistry: Efficient generation of structure-activity relationship data of β-secretase (BACE1) inhibitors. *Angew. Chemie - Int. Ed.* **53**, 1704–1708 (2014).
5. Sackmann, E. K., Fulton, A. L. & Beebe, D. J. The present and future role of microfluidics in biomedical research. *Nature* **507**, 181–189 (2014).
6. Elvira, K. S. Microfluidic technologies for drug discovery and development: friend or foe? *Trends Pharmacol. Sci.* **42**, 518–526 (2021).
7. Benam, K. H. *et al.* Engineered in vitro disease models. *Annu. Rev. Pathol. Mech. Dis.* **10**, 195–262 (2015).
8. Huh, D. *et al.* Reconstituting organ-level lung functions on a chip. *Science (80-.).* **328**, 1662–1668 (2010).
9. Skardal, A. *et al.* Multi-tissue interactions in an integrated three-tissue organ-on-a-chip platform. *Sci. Rep.* **7**, 1–16 (2017).
10. Ma, C., Peng, Y., Li, H. & Chen, W. Organ-on-a-Chip: A New Paradigm for Drug Development. *Trends Pharmacol. Sci.* **42**, 119–133 (2021).
11. Samiei, E., Tabrizian, M. & Hoorfar, M. A review of digital microfluidics as portable platforms for lab-on a-chip applications. *Lab Chip* **16**, 2376–2396 (2016).
12. Boyd-Moss, M., Baratchi, S., Di Venere, M. & Khoshmanesh, K. Self-contained microfluidic systems: A review. *Lab Chip* **16**, 3177–3192 (2016).
13. Eduati, F. *et al.* A microfluidics platform for combinatorial drug screening on cancer biopsies. *Nat. Commun.* **9**, (2018).
14. Czechtizky, W. *et al.* Integrated synthesis and testing of substituted xanthine based DPP4 inhibitors: Application to drug discovery. *ACS Med. Chem. Lett.* **4**, 768–772 (2013).
15. Pant, S. M. *et al.* Design, Synthesis, and Testing of Potent, Selective Hepsin Inhibitors via Application of an Automated Closed-Loop Optimization Platform. *J. Med. Chem.* **61**, 4335–4347 (2018).
16. Werner, M. *et al.* Seamless integration of dose-response screening and flow chemistry: Efficient generation of structure-activity relationship data of β-secretase (BACE1) inhibitors. *Angew. Chemie - Int. Ed.* **53**, 1704–1708 (2014).

17. Baranczak, A. *et al.* Integrated Platform for Expedited Synthesis-Purification-Testing of Small Molecule Libraries. *ACS Med. Chem. Lett.* **8**, 461–465 (2017).

18. Baumann, M. Integrating continuous flow synthesis with in-line analysis and data generation. *Org. Biomol. Chem.* **16**, 5946–5954 (2018).

19. Parry, D. M. Closing the Loop: Developing an Integrated Design, Make, and Test Platform for Discovery. *ACS Med. Chem. Lett.* **10**, 848–856 (2019).

20. Wright, B. D. *et al.* Development of a high-throughput screening assay to identify inhibitors of the lipid kinase PIP5K1C. *J. Biomol. Screen.* **20**, 655–662 (2015).

21. Perrin, D., Frémaux, C., Besson, D., Sauer, W. H. B. & Scheer, A. A microfluidics-based mobility shift assay to discover new tyrosine phosphatase inhibitors. *J. Biomol. Screen.* **11**, 996–1004 (2006).

22. Samiei, E., Tabrizian, M. & Hoorfar, M. A review of digital microfluidics as portable platforms for lab-on a-chip applications. *Lab Chip* **16**, 2376–2396 (2016).

23. Lee, S. J. & Lee, S. Y. Micro total analysis system (μ-TAS) in biotechnology. *Appl. Microbiol. Biotechnol.* **64**, 289–299 (2004).

24. Dittrich, P. S., Tachikawa, K. & Manz, A. Micro total analysis systems. Latest advancements and trends. *Anal. Chem.* **78**, 3887–3907 (2006).

25. Plutschack, M. B., Pieber, B., Gilmore, K. & Seeberger, P. H. The Hitchhiker's Guide to Flow Chemistry â¥. *Chem. Rev.* **117**, 11796–11893 (2017).

26. Nys, G. & Fillet, M. Microfluidics contribution to pharmaceutical sciences: From drug discovery to post marketing product management. *J. Pharm. Biomed. Anal.* **159**, 348–362 (2018).

27. Beebe, D. J., Mensing, G. A. & Walker, G. M. Physics and applications of microfluidics in biology. *Annu. Rev. Biomed. Eng.* **4**, 261–286 (2002).

28. Du, G., Fang, Q. & den Toonder, J. M. J. Microfluidics for cell-based high throughput screening platforms-A review. *Anal. Chim. Acta* **903**, 36–50 (2016).

29. Payne, E. M., Holland-Moritz, D. A., Sun, S. & Kennedy, R. T. High-throughput screening by droplet microfluidics: Perspective into key challenges and future prospects. *Lab Chip* **20**, 2247–2262 (2020).

30. Lauschke, V. M., Hendriks, D. F. G., Bell, C. C., Andersson, T. B. & Ingelman-Sundberg, M. Novel 3D Culture Systems for Studies of Human Liver Function and Assessments of the Hepatotoxicity of Drugs and Drug Candidates. *Chem. Res. Toxicol.* **29**, 1936–1955 (2016).

31. Desai, B. *et al.* Rapid discovery of a novel series of Abl kinase inhibitors by application of an integrated microfluidic synthesis and screening platform. *J. Med. Chem.* **56**, 3033–3047 (2013).

32. Hepatitis B. https://www.who.int/news-room/fact-sheets/detail/hepatitis-b.

33. Zhou, J. *et al.* Characterization of Virus Capsids and Their Assembly Intermediates by Multicycle Resistive-Pulse Sensing with Four Pores in Series. *Anal. Chem.* **90**, 7267–7274

(2018).

34. Roach, L. S., Song, H. & Ismagilov, R. F. Controlling nonspecific protein adsorption in a plug-based microfluidic system by controlling interfacial chemistry using fluorous-phase surfactants. *Anal. Chem.* **77**, 785–796 (2005).

35. Endres, D. & Zlotnick, A. Model-based analysis of assembly kinetics for virus capsids or other spherical polymers. *Biophys. J.* **83**, 1217–1230 (2002).

36. Zlotnick, A., Johnson, J. M., Wingfield, P. W., Stahl, S. J. & Endres, D. A theoretical model successfully identifies features of hepatitis B virus capsid assembly. *Biochemistry* **38**, 14644–14652 (1999).

37. Stray, S. J. *et al.* A heteroaryldihydropyrimidine activates and can misdirect hepatitis B virus capsid assembly. *Proc. Natl. Acad. Sci. U. S. A.* **102**, 8138–8143 (2005).

38. Schlicksup, C. J. *et al.* Hepatitis B virus core protein allosteric modulators can distort and disrupt intact capsids. *Elife* **7**, 1–24 (2018).

39. Zhou, Z. *et al.* Heteroaryldihydropyrimidine (HAP) and Sulfamoylbenzamide (SBA) Inhibit Hepatitis B Virus Replication by Different Molecular Mechanisms. *Sci. Rep.* **7**, 1–12 (2017).

40. Berke, J. M. *et al.* Antiviral profiling of the capsid assembly modulator BAY41-4109 on full-length HBV genotype A-H clinical isolates and core site-directed mutants in vitro. *Antiviral Res.* **144**, 205–215 (2017).

41. Bourne, C. *et al.* Small-Molecule Effectors of Hepatitis B Virus Capsid Assembly Give Insight into Virus Life Cycle. *J. Virol.* **82**, 10262–10270 (2008).

42. Yang, L. *et al.* Treatment of Chronic Hepatitis B Virus Infection Using Small Molecule Modulators of Nucleocapsid Assembly: Recent Advances and Perspectives. *ACS Infect. Dis.* **5**, 713–724 (2019).

43. Corcuera, A. *et al.* Novel non-heteroarylpyrimidine (HAP) capsid assembly modifiers have a different mode of action from HAPs in vitro GPA, PT, DBT. *Antiviral Res.* **158**, 135–142 (2018).

44. Rouviere, C. P., Dousson, C. B., Tavis, J. E., Endres, D. & Zlotnick, A. HBV replication inhibitors. *Antiviral Res.* **179**, 104815 (2020).

45. Newman, M., Suk, F.-M., Cajimat, M., Chua, P. K. & Shih, C. Stability and Morphology Comparisons of Self-AssembledVirus-Like Particles from Wild-Type and Mutant Human Hepatitis B VirusCapsidProteins. *J. Virol.* **77**, 12950–12960 (2003).

46. Zlotnick, A., Aldrich, R., Johnson, J. M., Ceres, P. & Young, M. J. Mechanism of capsid assembly for an icosahedral plant virus. *Virology* **277**, 450–456 (2000).

47. Sauviller, S. *et al.* Development of a cellular high-content, immunofluorescent HBV core assay to identify novel capsid assembly modulators that induce the formation of aberrant HBV core structures. *J. Virol. Methods* **293**, 114150 (2021).

48. Uetrecht, C., Barbu, I. M., Shoemaker, G. K., Van Duijn, E. & Heck, A. J. R. Interrogating viral

capsid assembly with ion mobility-mass spectrometry. *Nat. Chem.* **3**, 126–132 (2011).

49. Tresset, G. *et al.* Norovirus capsid proteins self-assemble through biphasic kinetics via long-lived stave-like intermediates. *J. Am. Chem. Soc.* **135**, 15373–15381 (2013).

50. Borodavka, A., Tuma, R. & Stockley, P. G. Evidence that viral RNAs have evolved for efficient, two-stage packaging. *Proc. Natl. Acad. Sci. U. S. A.* **109**, 15769–15774 (2012).

51. Harms, Z. D., Selzer, L., Zlotnick, A. & Jacobson, S. C. Monitoring Assembly of Virus Capsids with Nanofluidic Devices. *ACS Nano* **9**, 9087–9096 (2015).

52. Kondylis, P. *et al.* Nanofluidic Devices with 8 Pores in Series for Real-Time, Resistive-Pulse Analysis of Hepatitis B Virus Capsid Assembly. *Anal. Chem.* **89**, 4855–4862 (2017).

53. Kondylis, P. *et al.* Competition between Normative and Drug-Induced Virus Self-Assembly Observed with Single-Particle Methods. *J. Am. Chem. Soc.* **141**, 1251–1260 (2019).

54. Zlotnick, A. & Katen, S. The thermodynamics of virus capsid assembly. *Methods Enzymol.* **6879**, 1–19 (2009).

55. Perotti, M. & Perez, L. Virus-like particles and nanoparticles for vaccine development against HCMV. *Viruses* **12**, 1–17 (2019).

56. Wang, M. *et al.* Quenching protein dynamics interferes with HIV capsid maturation. *Nat. Commun.* **8**, (2017).

57. Bartonova, V. *et al.* Residues in the HIV-1 capsid assembly inhibitor binding site are essential for maintaining the assembly-competent quaternary structure of the capsid protein. *J. Biol. Chem.* **283**, 32024–32033 (2008).

58. Zlotnick, A. Are weak protein-protein interactions the general rule in capsid assembly? *Virology* **315**, 269–274 (2003).

59. Stray, S. J., Johnson, J. M., Kopek, B. G. & Zlotnick, A. An in vitro fluorescence screen to identify antivirals that disrupt hepatitis B virus capsid assembly. *Nat. Biotechnol.* **24**, 358–362 (2006).

60. Cai, L. F., Zhu, Y., Du, G. S. & Fang, Q. Droplet-based microfluidic flow injection system with large-scale concentration gradient by a single nanoliter-scale injection for enzyme inhibition assay. *Anal. Chem.* **84**, 446–452 (2012).

61. Keserü, G. M. & Makara, G. M. The influence of lead discovery strategies on the properties of drug candidates. *Nat. Rev. Drug Discov.* **8**, 203–212 (2009).

ICIQ
Institut
Català
d'Investigació
Química

UNIVERSITAT
ROVIRA i VIRGILI